DEVELOPMENT OF ODOT GUIDELINES FOR THE USE OF GEOGRIDS IN AGGREGATE BASES

FINAL REPORT ~ FHWA-OK-12-04

ODOT SP&R ITEM NUMBER 2220

Submitted to:

John R. Bowman, P.E.
Planning & Research Division Engineer
Oklahoma Department of Transportation

Submitted by:

Kianoosh Hatami, Ph.D., P.Eng.
Tahsina Mahmood, Ph.D. Candidate
Musharraf Zaman, Ph.D., P.E.
Rouzbeh Ghabchi, Ph.D. Candidate
School of Civil Engineering and Environmental Science (CEES)
The University of Oklahoma

March 2012

TECHNICAL REPORT DOCUMENTATION PAGE

1. REPORT NO.	2. GOVERNMENT ACCESSION NO.	3. RECIPIENT=S CATALOG NO.
FHWA-OK-12-04		

4. TITLE AND SUBTITLE	5. REPORT DATE
Development of ODOT Guidelines for the Use of Geogrids in Aggregate Bases	March 2012
	6. PERFORMING ORGANIZATION CODE

7. AUTHOR(S)	8. PERFORMING ORGANIZATION REPORT
Kianoosh Hatami, Ph.D., P.Eng., Tahsina Mahmood, Ph.D. Candidate, Musharraf Zaman, Ph.D., P.E., Rouzbeh Ghabchi, Ph.D. Candidate	

9. PERFORMING ORGANIZATION NAME AND ADDRESS	10. WORK UNIT NO.
University of Oklahoma School of Civil Engineering and Environmental Science 202 W. Boyd Street, Room 334, Norman, OK 73019	11. CONTRACT OR GRANT NO. ODOT SP&R Item Number 2220

12. SPONSORING AGENCY NAME AND ADDRESS	13. TYPE OF REPORT AND PERIOD COVERED
Oklahoma Department of Transportation Planning and Research Division 200 N.E. 21st Street, Room 3A7 Oklahoma City, OK 73105	Final Report August, 2009 – March, 2012
	14. SPONSORING AGENCY CODE

15. SUPPLEMENTARY NOTES

16. ABSTRACT

A primary objective of the current study was to help ODOT expand its selection of approved geogrid products for base reinforcement applications by producing measured data on selected geogrids and a dense-graded base aggregate commonly used in ODOT roadway projects. The study involved in-isolation and in-aggregate laboratory testing of several base reinforcement geogrid products from major geosynthetic suppliers. In-isolation tests included rib strength and junction strength tests, and in-aggregate tests included pullout and plate load tests. Field-scale installation damage tests were also performed. Test results on different geogrids in this study were aimed to quantify the significance of the geogrids in-isolation properties on their in-aggregate response under controlled conditions.

17. KEY WORDS	18. DISTRIBUTION STATEMENT
Geogrid, pavement, aggregate, strength, pullout test, cyclic plate load test, installation damage	No restrictions. This publication is available from the Planning & Research Div., Oklahoma DOT.

19. SECURITY CLASSIF. (OF THIS REPORT)	20. SECURITY CLASSIF. (OF THIS PAGE)	21. NO. OF PAGES	22. PRICE
Unclassified	Unclassified	210	N/A

SI* (MODERN METRIC) CONVERSION FACTORS

APPROXIMATE CONVERSIONS TO SI UNITS				
SYMBOL	**WHEN YOU KNOW**	**MULTIPLY BY**	**TO FIND**	**SYMBOL**
LENGTH				
in	inches	25.4	millimeters	mm
ft	feet	0.305	meters	m
yd	yards	0.914	meters	m
mi	miles	1.61	kilometers	km
AREA				
in^2	square inches	645.2	square millimeters	mm^2
ft^2	square feet	0.093	square meters	m^2
yd^2	square yard	0.836	square meters	m^2
ac	acres	0.405	hectares	ha
mi^2	square miles	2.59	square kilometers	km^2
VOLUME				
fl oz	fluid ounces	29.57	milliliters	mL
gal	gallons	3.785	liters	L
ft^3	cubic feet	0.028	cubic meters	m^3
yd^3	cubic yards	0.765	cubic meters	m^3
NOTE: volumes greater than 1000 L shall be shown in m^3				
MASS				
oz	ounces	28.35	grams	g
lb	pounds	0.454	kilograms	kg
T	short tons (2000 lb)	0.907	megagrams (or "metric ton")	Mg (or "t")
TEMPERATURE (exact degrees)				
°F	Fahrenheit	5 (F-32)/9 or (F-32)/1.8	Celsius	°C
ILLUMINATION				
fc	foot-candles	10.76	lux	lx
fl	foot-Lamberts	3.426	$candela/m^2$	cd/m^2
FORCE and PRESSURE or STRESS				
lbf	poundforce	4.45	newtons	N
lbf/in^2	poundforce per square inch	6.89	kilopascals	kPa

APPROXIMATE CONVERSIONS FROM SI UNITS				
SYMBOL	**WHEN YOU KNOW**	**MULTIPLY BY**	**TO FIND**	**SYMBOL**
LENGTH				
mm	millimeters	0.039	inches	in
m	meters	3.28	feet	ft
m	meters	1.09	yards	yd
km	kilometers	0.621	miles	mi
AREA				
mm^2	square millimeters	0.0016	square inches	in^2
m^2	square meters	10.764	square feet	ft^2
m^2	square meters	1.195	square yards	yd^2
ha	hectares	2.47	acres	ac
km^2	square kilometers	0.386	square miles	mi^2
VOLUME				
mL	milliliters	0.034	fluid ounces	fl oz
L	liters	0.264	gallons	gal
m^3	cubic meters	35.314	cubic feet	ft^3
m^3	cubic meters	1.307	cubic yards	yd^3
MASS				
g	grams	0.035	ounces	oz
kg	kilograms	2.202	pounds	lb
Mg (or "t")	megagrams (or "metric ton")	1.103	short tons (2000 lb)	T
TEMPERATURE (exact degrees)				
°C	Celsius	1.8C+32	Fahrenheit	°F
ILLUMINATION				
lx	lux	0.0929	foot-candles	fc
cd/m^2	candela/m^2	0.2919	foot-Lamberts	fl
FORCE and PRESSURE or STRESS				
N	newtons	0.225	poundforce	lbf
kPa	kilopascals	0.145	poundforce per square inch	lbf/in^2

*SI is the symbol for the International System of Units. Appropriate rounding should be made to comply with Section 4 of ASTM E380.

Table of Contents

List of Figures

List of Tables

Acknowledgements

This study was financially supported by the Oklahoma Department of transportation (ODOT) (Grant No. SPR 2220) and the Oklahoma Transportation Center (OTC) (Grant No. OTCREOS 9.1-23). The geogrids were donated by Tensar Corporation, Synteen Technical Fabrics, Inc., TenCate Geosynthetics, Maccaferri, Inc. and Strata Global Geosolutions. An initial quantity of the aggregates was donated by Dolese Bros. Co., a member of the Oklahoma Aggregate Association (OKAA). The compactor equipment for the installation damage tests was loaned by the Haskell Lemon Company. The authors would also like to acknowledge the contribution of Mr. Michael Schmitz at the OU Fears Laboratory in fabricating the test boxes and setting up the testing stations for this project and those of the following undergraduate research assistants: Jesse Berdis, Max Newton, Derek Reid, Kyle Olson, Evan Burns, Brandi Dittrich, Carlos Chang, Thai Dinh, Alex Haluska, Grayson Niemeyer, Carl Walkup, Chris Barclay, Juan Pereira, Mariam Edwar, Nicholas Ibarguen, Adam Burke, Jeremy Lakes (Graduate Student at ECE) in setting up and carrying out the tests described in this report.

1. Introduction

It has been shown that geogrids, when properly installed as aggregate base and/or subgrade reinforcement, can help to improve the service life and performance of roads and highways and help reduce their repair and maintenance costs (e.g., Perkins 1999, Leng and Gabr 2002, Perkins et al. 2004, Giroud and Han 2004, Gabr et al. 2006, Aran 2006, Holtz et al. 2008, Kwon and Tutumluer 2009). The existing specifications manual of the Oklahoma Department of Transportation (ODOT 2009) only endorses a very limited number of geogrids for base reinforcement and needs to be updated to include a wider range of products that are currently available on the market. However, there are currently no universally accepted guidelines for the acceptance and specification of geogrids for base reinforcement and subgrade stabilization applications. Alzamora and Anderson (2012) highlighted challenges that different State DOTs and research institutions face in establishing a direct connection between index properties of geogrids and their field performance. Nevertheless, careful measurement of geogrids index properties and their in-aggregate performance in controlled laboratory conditions is essential in order to develop empirical correlations with field performance and input properties that are needed to develop mechanistic models for the design of reinforced base pavements.

Therefore, a primary objective of the current study was to help ODOT expand its selection of approved geogrid products for base reinforcement applications by producing measured data on selected geogrids and a dense-graded base aggregate commonly used in ODOT roadway projects. The study involved in-isolation and in-aggregate laboratory testing of several base reinforcement geogrid products from major geosynthetic suppliers. The in-isolation tests included rib strength and junction strength tests, and the in-aggregate tests included pullout and plate load tests on reinforced aggregate models involving selected geogrid products. Field-scale installation damage tests were also performed to investigate the survivability of the selected geogrids during simulated construction. A primary objective of the laboratory and field tests on different geogrids in this study was to quantify the significance of the geogrids in-isolation properties on their in-aggregate response under controlled conditions.

2. In-isolation testing of geogrids

2.1. A review of geogrids used in the U.S. and classification of geogrid products

2.1.1. Venders' data

As a first step of this study, a survey was carried out on a wide range of commonly available geogrids on the market in order to identify candidate products for ODOT's new geogrid specifications. Candidate geogrids were initially screened from the 2009 issue of the Geosynthetics Specifier's Guide (IFAI 2009) on the basis of their aperture size and rib strength at 5% strain. Tensar BX1100 and BX1200 geogrids which are primarily used in ODOT projects are referred to as the control geogrids in this study. These geogrids are referred to as Type-1 and Type-2 geogrids, respectively in the ODOT specifications manual.

Several geogrid producers and suppliers were contacted for additional information on their products. A database of surveyed geogrids and their selected properties (aperture size, rib strength at 5% strain and ultimate strength) is given in Appendix A. **Figure 1** shows a histogram of geogrid products available on the market based on their machine direction (MD) rib strength at 2% strain, which is used in specifications published by several U.S. State DOTs (see **Section 2.1.2.** DOT agencies data). The rib strength at 2% strain has been recommended as a serviceability criterion in previous studies (e.g. Christopher et al. 2008). The histogram in **Figure 1** was produced based on a survey of 113 geogrids from available sources.

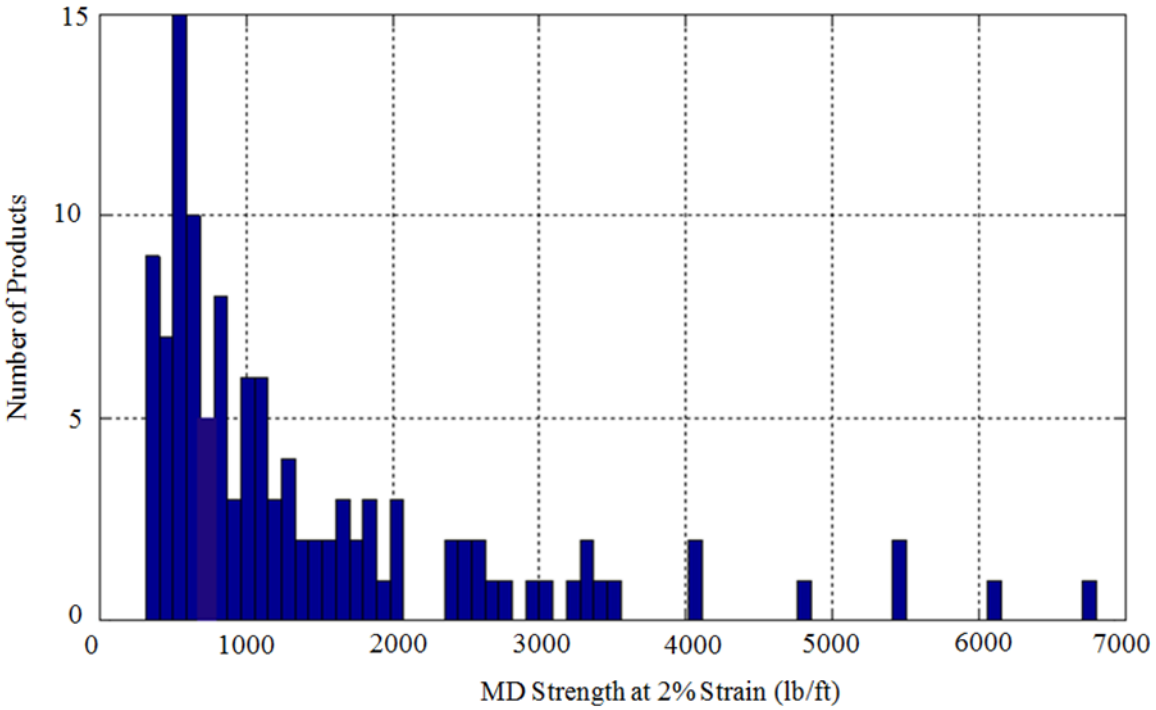

Figure 1. Distribution of MD strength at 2% rib strain of all geogrids available on the market

Among these 113 geogrids surveyed, 66 geogrids were biaxial. Since this study was focused on bi-axial geogrids used for base reinforcement, the distribution of MD rib strength at 2% strain of bi-axial geogrids as a subset of what is shown in **Figure 1** is shown in **Figure 2**.

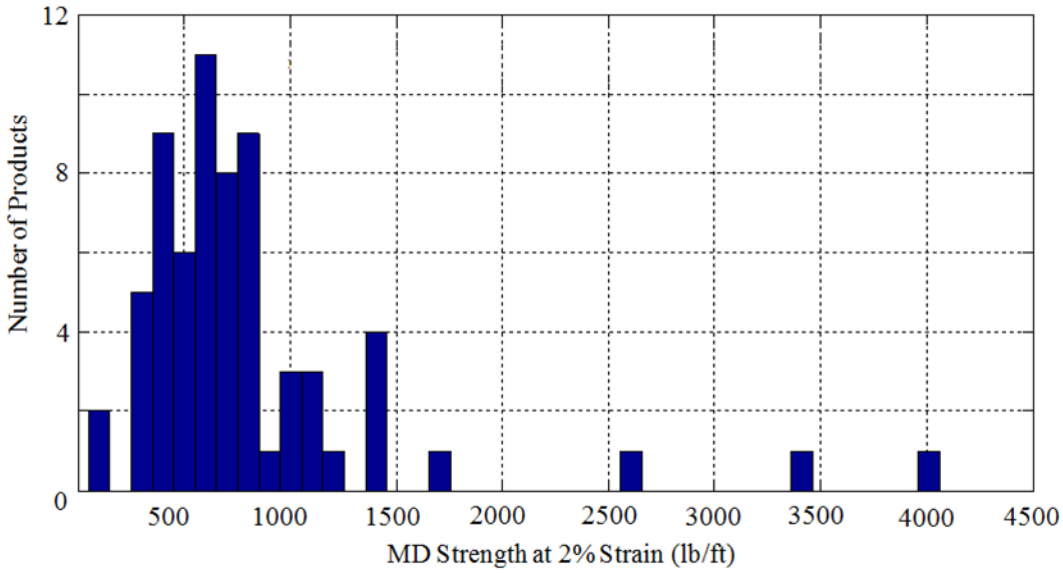

Figure 2. Distribution of MD strength at 2% rib strain of bi-axial geogrids available on the market

Among the 66 geogrids represented in **Figure 2**, a total of 31 geogrids were found to have either an aperture size or a 5%-strain rib strength value comparable to those of ODOT Type-1 and ODOT Type-2 geogrids as given in **Table 1.** The geogrid products discussed in this report are classified as extruded and non-extruded geogrids (EGG and NEGG, respectively). The NEGG category, in turn, includes woven and knitted geogrids (WGG and KGG, respectively).

Table 1. List of candidate geogrids with either aperture size or 5%-strain tensile strength comparable to those of ODOT Type-1 and Type-2 geogrids

Product Name	Aperture Size (in)		Strength @ 5% Strain (lb/ft)	
	MD	XD	MD	XD
ACE GG30-ll	1.00	1.12	1027.40	NP
ACE GG300-ll	1.00	1.20	8219.16	NP
BX1100*	1.00	1.32	582.19	917.81
BX 1120	1.00	1.32	582.19	917.81
BX1200**	1.00	1.32	808.22	1342.46
BX-1220	1.00	1.32	808.22	1342.46
BX 1500	1.00	1.24	1198.63	1369.86
BX 4100	1.00	1.32	547.94	719.18
BX-4200	1.00	1.32	719.18	1000.00
Fornit 20	0.60	0.60	753.42	1095.89
Fortrac 35	0.80	0.80	890.41	NA
LBO 202	1.12	1.52	650.68	924.66
MacGrid EB2	1.68	2.00	616.44	917.81
MacGrid EB3	1.68	2.00	924.66	1342.46
MacGrid WB1	1.00	1.32	1041.09	787.67
MacGrid WB2	1.00	1.32	1041.09	1130.13
MacGrid WB3	1.00	1.00	863.01	979.45
MacGrid WG3	1.00	1.12	1027.40	NP
MacGrid WG5	0.96	1.12	1917.80	NA
MacGrid WG8	0.96	1.12	2739.72	NA
Mirafi BXG 11	1.02	1.02	917.81	917.81
Mirafi BXG 12	1.02	1.02	917.81	1349.31
Miragrid 3XT	0.88	1.00	1054.79	NA
MS 220	1.68	2.00	616.44	919.18
MS 330	1.68	2.00	924.66	1342.46
MS 500	2.40	2.40	924.66	1342.46
SF 11	1.00	1.00	1041.09	787.67
SF 12	1.00	1.00	1041.09	1363.01
SF13	1.00	1.00	1041.09	1164.38
SF 15	1.00	1.00	1198.63	1369.86
StrataGrid SG150	1.02	0.96	623.29	424.66

Note: * ODOT Type-1 Geogrid; ** ODOT Type-2 Geogrid; NA: Not Applicable;
NP: Not Provided; products in green cells were ultimately selected for testing in this study.

Based on the above survey and the selection criteria illustrated in **Figure 3**, a total of eight geogrids were selected as a final set for testing in this study (**Table 2**). Dimensional and 5%-strain rib strength properties of these geogrid products (tested in this study) found from manufacturer datasheet are presented in **Table 3**.

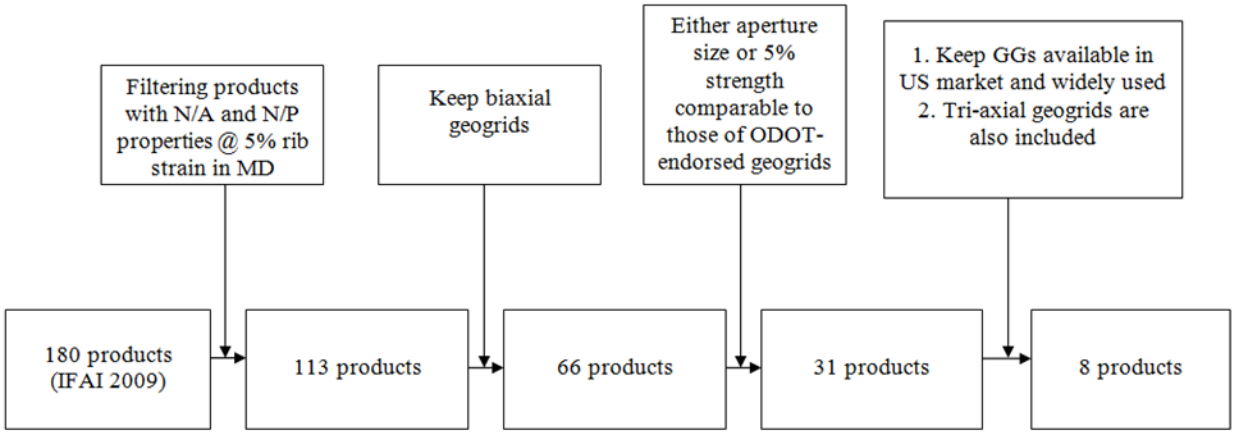

Figure 3. Procedure used to select geogrid products for testing in this study (Note: EGG - Extruded Geogrid; NEGG - Non Extruded Geogrid)

Table 2. List of selected geogrid products tested in this study

Commercial Name	Designation in this report	Fabrication Category	Manufacturer	Grid Structure	Polymer
BX1200	EGG1	EGG	Tensar	BX	PP
EB2	EGG2		Maccaferri	BX	
TX140	EGG3		Tensar	TX	
TX160	EGG4		Tensar	TX	
BXG11	WGG1	NEGG	TenCate-Mirafi	BX	PET
BXG12	WGG2		TenCate-Mirafi	BX	
SF11	WGG3		Synteen	BX	
SG150	KGG1		Strata	BX	

Notes: PP: Polypropylene, PET: Polyester, BX: Biaxial, TX: Triaxial

Table 3. Selected properties of geogrid products listed in Table 2 from manufacturers' datasheets

Geogrid	Aperture Size (in)		Strength @ 5% Strain (lb/ft)	
	MD	XD	MD	XD
EGG1	1	1.3	808.22	1342.46
EGG2	1.7	2	616.44	917.81
WGG1	1	1	917.81	917.81
WGG2	1	1	917.81	1349.31
WGG3	1	1	1041.09	787.67
KGG1	1	1	623.29	424.66

Geogrid	Rib Pitch (in)			Mid-rib Depth (in)			Mid-rib Width (in)			Rib Shape	Aperture Shape
	Longitudinal	Diagonal	Transverse	Longitudinal	Diagonal	Transverse	Longitudinal	Diagonal	Transverse		
EGG3(*)	1.6	1.6	-	-	0.048	0.048	-	0.044	0.044	Rectangular	Triangular
EGG4(*)	1.6	1.6	-	-	0.064	0.056	-	0.04	0.048	Rectangular	Triangular

(*) included in the final set due to ODOT's interest

2.1.2. DOT agencies data

Table 4 shows a list of all 50 State DOTs in the United States that were surveyed with respect to their geogrid specifications. This survey revealed that those DOTs that have specifications for base reinforcement geogrids specify MD rib strength values at 2% elongation which vary between 68.5 lb/ft and 205.5 lb/ft. This range represents 62% of the biaxial geogrid products surveyed (i.e. 41 out of 66 products) within the lower end of tensile strength values (**Figure 3** and **Figure 2**). Stronger geogrids (especially of uniaxial type) are primarily used for reinforced soil walls, embankments and steepened slopes, which are outside the scope of this study. Based on the above survey, the geogrids listed in **Table 2** were grouped into categories shown in **Figure 4**. The 25-lb split value for junction strength shown in **Figure 4** was selected based on the Holtz et al. (2008) requirement for minimum ultimate junction strength of geogrids. The split value for the 2%-strain rib strength was selected such that ODOT Type-1 and ODOT Type-2

geogrids represent the weak rib (W_R) and strong rib (S_R) categories, respectively, with respect to this index property.

Table 4. State DOTs providing geogrid specifications for base reinforcement

State	Specs.	No Specs.	Info. Source
Alabama		✓	🖱
Alaska*	✓		✉
Arizona		✓	🖱
Arkansas		✓	✉
California		✓	🖱
Colorado		✓	🖱
Connecticut		✓	🖱
Delaware		✓	🖱
Florida*	✓		🖱
Georgia		✓	🖱
Hawaii		✓	🖱
Idaho		✓	🖱
Illinois		✓	🖱
Indiana	✓		🖱
Iowa		✓	🖱
Kansas	✓		🖱
Kentucky	✓		🖱
Louisiana		✓	✉
Maine		✓	🖱
Maryland		✓	✉
Massachusetts		✓	✉
Michigan		✓	✉
Minnesota	✓		🖱
Mississippi		✓	🖱
Missouri		✓	🖱
Montana		✓	🖱
Nebraska		✓	🖱
Nevada		✓	🖱
New Hampshire		✓	🖱
New Jersey		✓	🖱
New Mexico		✓	🖱
New York		✓	🖱
North Carolina		✓	🖱
North Dakota		✓	🖱
Ohio	✓		🖱
Oklahoma*	✓		🖱
Oregon	✓		🖱
Pennsylvania		✓	🖱
Rhode Island	✓		🖱
South Carolina		✓	🖱
South Dakota		✓	🖱
Tennessee	✓		🖱
Texas	✓		🖱
Utah		✓	🖱
Vermont	✓		🖱
Virginia		✓	🖱
Washington		✓	🖱
West Virginia		✓	🖱
Wisconsin*	✓		🖱
Wyoming	✓		🖱

🖱 DOT Agency Website

✉ Correspondence with Agency

* States that Endorse Specific Products

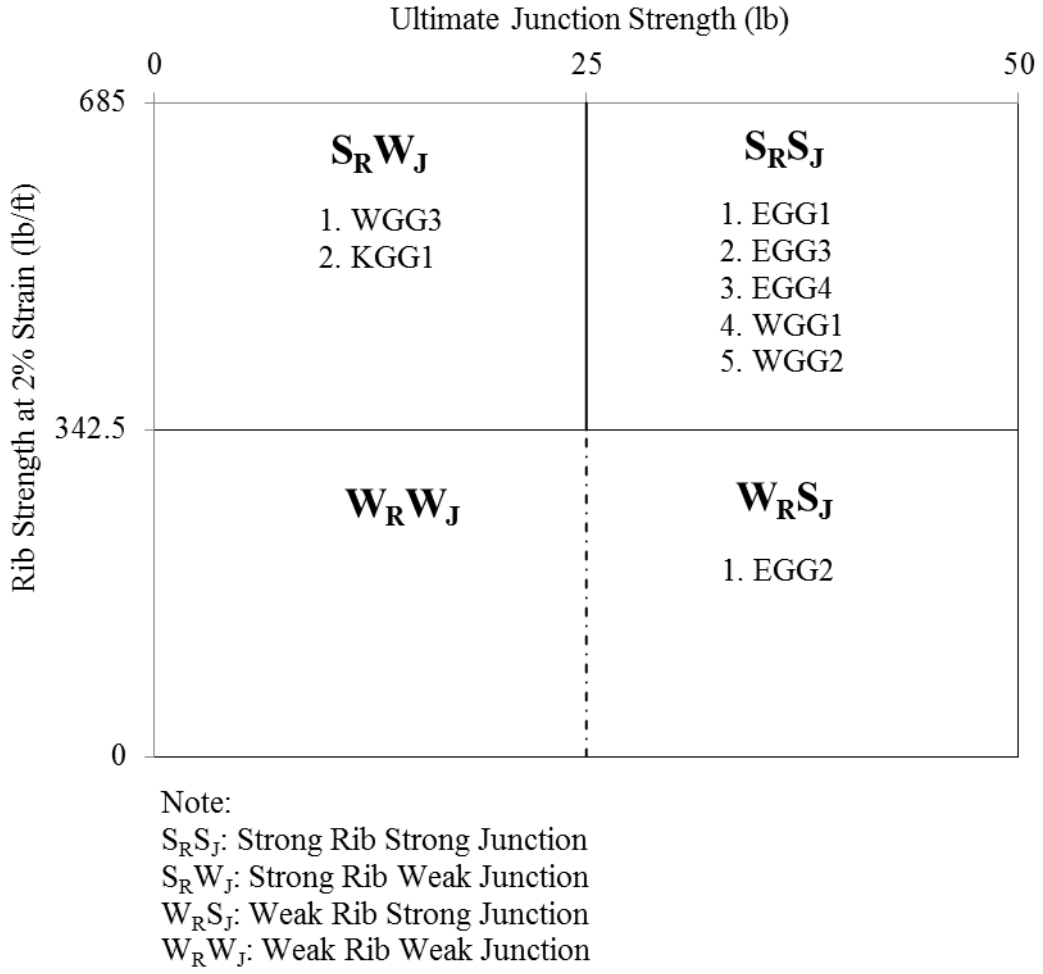

Figure 4. Classification of the geogrid products used in the study

2.1.3. Geogrid properties

A few recent studies have been aimed at developing a correlation between index properties of geogrids and their field performance (e.g. Perkins et al. 2004, Chehab et al. 2007, Christopher et al. 2008, Tang et al. 2008).

Perkins et al. (2004) developed numerical models and testing methods to determine input parameters for the geogrid reinforcement and its interaction with the aggregate and subgrade materials. The testing methods included tensile tests for evaluating direction dependent, non-linear elastic constants for the reinforcement and cyclic pullout tests for evaluating a stress-dependent interface shear resilient modulus. Perkins et al. (2004) carried out wide-width tensile tests according to ASTM D4595 with a cyclic loading protocol on three geosynthetic

reinforcement products. They studied the influences of the geogrids elastic tensile modulus, equivalent isotropic modulus and Poisson's ratio on the elastic response of reinforced pavement models. Their cyclic pullout test results showed that the interface shear modulus was dependent on the normal and shear stress on the interface.

Chehab et al. (2007) studied the effects of aperture size, tensile strength at 2% strain, ultimate tensile strength, junction strength and flexural rigidity of geogrids on rutting performance of small-scale roadway models. They performed Accelerated Pavement Tests (APT) on a 7.3 ft × 12 ft test pit. The pit was originally 14 ft deep but was backfilled with aggregate. The densely-compacted aggregate layer served as a bedrock-like support. The top 16 inches was considered as the pavement section. They used aggregate as subgrade and base material. They selected a Type-2A aggregate base conforming to the PennDOT specifications. An asphalt slab was constructed on the top of base layer. They presented a series of correlations between the geogrid index properties and the rutting performance of their reinforced models. Chehab et al. (2007) concluded that adequate ultimate junction strength is essential for the geogrid to develop high pullout resistance. Overall, good correlations were found between geogrid tensile strength and junction strength properties and results of their interface shear and pullout tests.

Christopher et al. (2008) suggested that rib strength at 2% strain is a suitable value for geogrid design for base reinforcement at service-level conditions. They concluded that junction strength at 2% strain should therefore be used as an appropriate value to achieve a consistent design.

Tang et al. (2008) examined the correlations between index properties such as the aperture size, wide-width tensile strength and junction strength of four geogrid products and their bench-scale interface test and pullout test results. They found that junction and tensile strength properties of geogrids at small strains showed strong correlations with their in-aggregate performance. They observed that the pullout coefficient of interaction factors increased with the junction strength and the rib tensile strength at 2% strain of the geogrids tested.

Cuelho and Perkins (2009) constructed field test sections to evaluate the performance of several geosynthetics for subgrade stabilization application. A sandy clay soil was prepared as a weak roadbed material to a CBR strength of approximately 1.8, and an 8-inch-thick aggregate layer was compacted over the geosynthetic reinforcement. They examined the effects of the tensile strength at 2% strain, 5% strain and the ultimate tensile strength on the rutting performance of geogrid-reinforced roadway test sections. Cuelho and Perkins (2009) acknowledged that a number of geosynthetic properties may be working together to stabilize a subgrade. However, they attributed a majority of the stabilization benefit to the geosynthetics ability to support loads in a direction transverse to the applied load, i.e. their cross-machine direction. A direct comparison between tensile strength in the cross-machine direction at 2% and 5% strain was made to investigate whether. Cuelho and Perkins (2009) concluded that the observed rutting in

their test models was related to the tensile strength of the geosynthetic in the cross machine direction and an increase in the 2%-strain and 5%-strain tensile strength values in the cross machine direction would reduce the amount of rutting and hence a better pavement performance.

The above studies have revealed the significance of geogrid mechanical properties on their in-aggregate performance. However, the influence of individual index properties of geogrids on their in-aggregate performance is still not well understood and requires further study. Furthermore, the influence of the geogrid index properties on their in-aggregate performance also depends on the properties of the aggregate. Therefore, this study is aimed at producing experimental data which are specific to aggregate types that are commonly used in highway projects in Oklahoma. Nevertheless, the methodology adopted in this study as described in this report is applicable to other aggregate types in future studies. Based on the survey of previous studies, the geogrid properties that are important to their in-aggregate performance are summarized in **Table 5**. Selected geogrid properties of interest in this study are listed in **Table 6**.

Table 5. List of geogrid properties examined for base reinforcement applications in related previous studies

Mechanical Properties (MD and XD)	Webster (1992)	Giroud and Hann (2004)	Chehab et al. (2007)	Tang et al. (2008)	Cuelho and Perkins (2009)	Current Study
Ultimate Rib Strength			√	√	√	√
Rib Strength at 2%Elongation			√	√	√	√
Rib Strength at 5%Elongation					√	√
Junction Strength	√		√	√		√
Tensile Modulus		√				
Aperture Size	√		√	√		
Flexural Rigidity			√	√		
Aperture Stability Modulus		√			√	
Rib Thickness	√					
Rib Cross-Section Shape	√					

Table 6. Geogrid properties of interest in this study

Mechanical Properties (MD and XD)	Fabrication Technique
Ultimate Rib Strength Rib Strength at 2% Strain Rib Strength at 5% Strain Ultimate Junction Strength	Extruded Non Extruded (Woven and Knitted)

2.2. Junction strength tests

2.2.1. Fabrication of junction strength testing clamps for extruded and non-extruded geogrids

A total of eighty (80) junction strength tests were carried out on geogrids listed in **Figure 4** in both MD and XD direction according to the GRI GG2 test method. A minimum of five replicate samples of each product were prepared and tested. In these tests, a junction clamp firmly gripped the transverse ribs on each side of the junction (**Figure 5**) and the specimen was subjected to a monotonic tensile load until the junction failed. In addition to obtaining junction strength values for the geogrid products, these tests helped us evaluate the performance of the fabricated clamps and apply necessary modifications to improve their performance. Due to the manufacturing technique and comparatively low junction strength, the strain magnitudes of the non-extruded geogrids (NEGG) were low. Therefore it was decided to report only the ultimate junction strength of these products. Digital imagery technique was used to determine the strain in extruded geogrid (EGG) products (Wang 2009).

Figure 6 and **Figure 7** show the tensile testing machine and an example output plot from the in-isolation tests, respectively. **Figure 8** shows different failure modes observed in the junction tests carried out on the extruded geogrid (EGG) products.

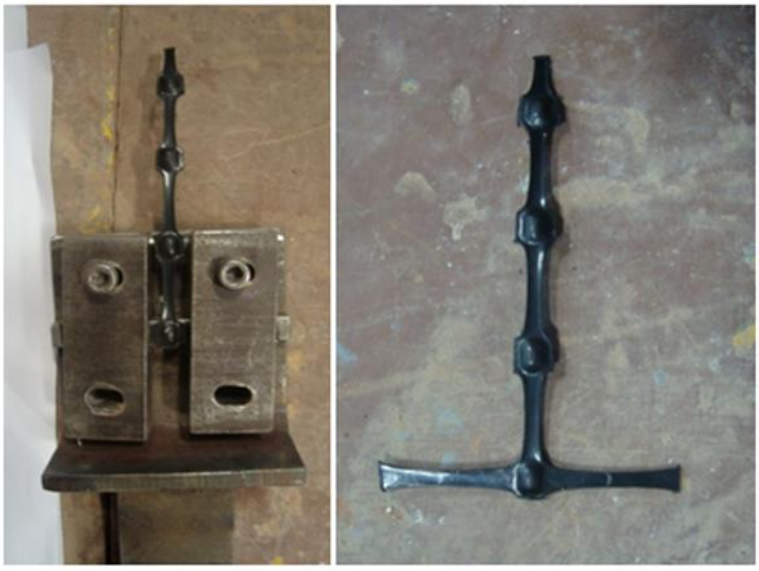

Figure 5. Clamp and example test specimen used in junction tests (junctions in the specimen shown are one inch apart from each other)

Figure 6. Tensile testing frame for testing rib and junction strength of geogrid specimens

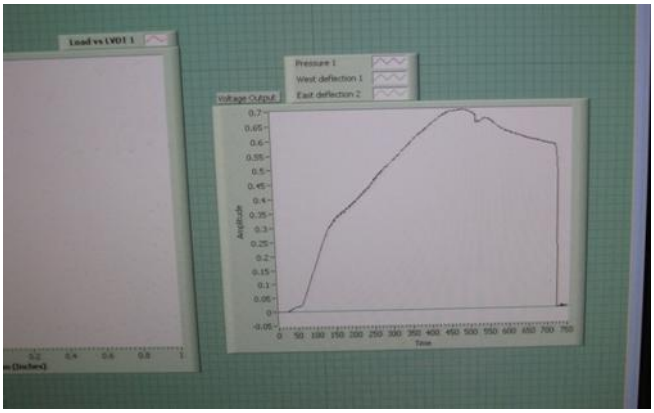

Figure 7. Specimen failure as captured on the data acquisition system screen

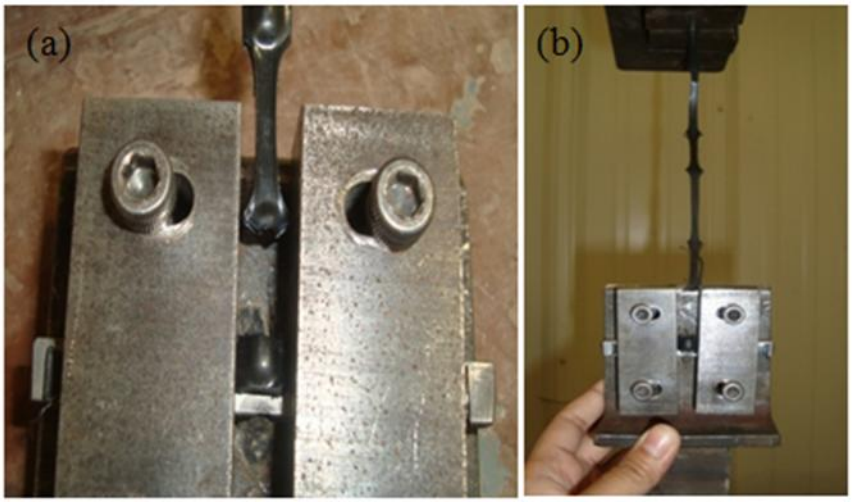

Figure 8. Different failure modes observed in junction testing of extruded geogrids: (a) Brittle failure (b) Ductile failure

2.2.2. Junction strength test results

Samples of the eight (8) different geogrids examined in this study (**Table 2** and **Table 3**) are shown in **Figure 9** through **Figure 16,** respectively. **Figure 17** shows an EGG4 geogrid specimen in the junction test setup before and after failure.

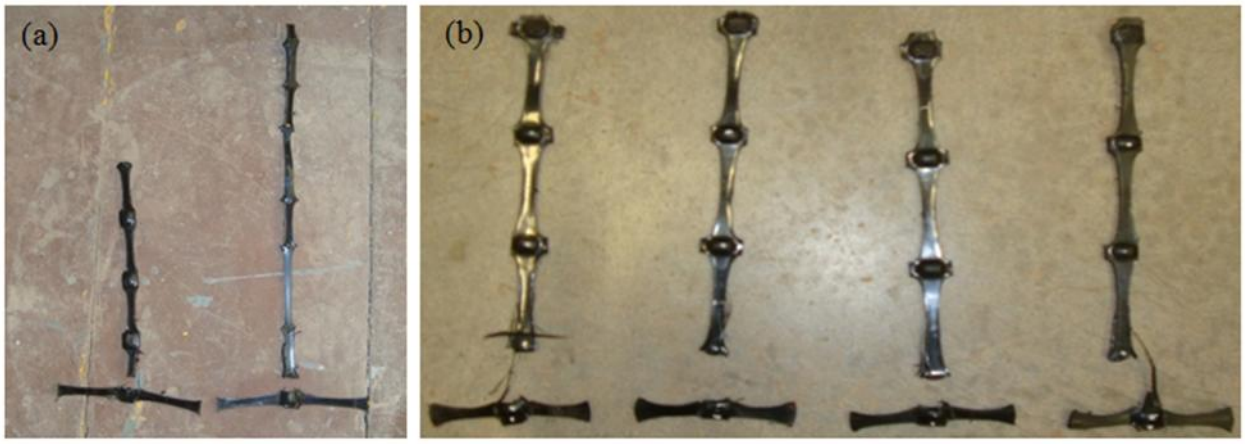

Figure 9. EGG1 geogrid junction strength specimens after the test in (a) MD and, (b) XD

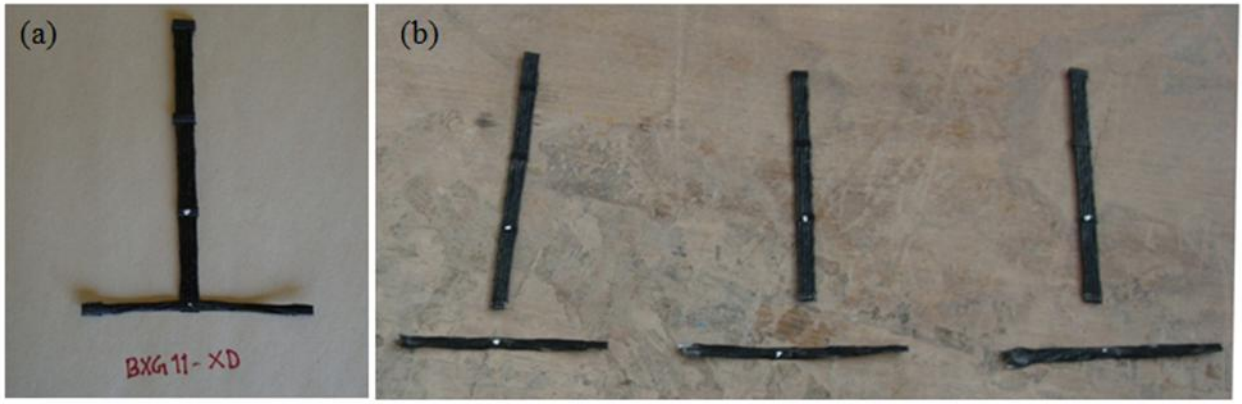

Figure 10. WGG1 geogrid junction strength specimens in XD: (a) before failure, (b) after failure

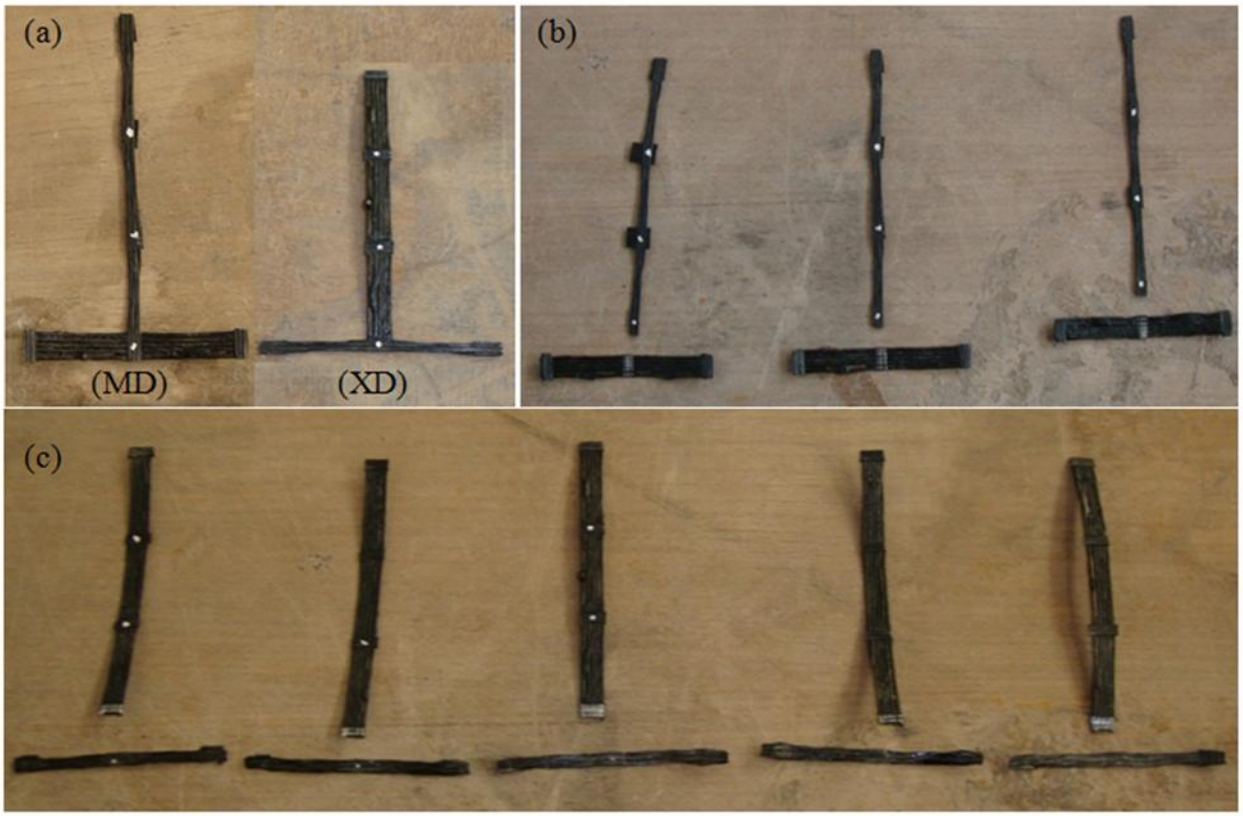

Figure 11. WGG2 geogrid junction strength specimens: (a) before the test, (b) after failure (MD), (c) after failure (XD)

Figure 12. WGG3 geogrid junction strength specimens (a) before the test, (b) after failure (MD), (c) after failure (XD)

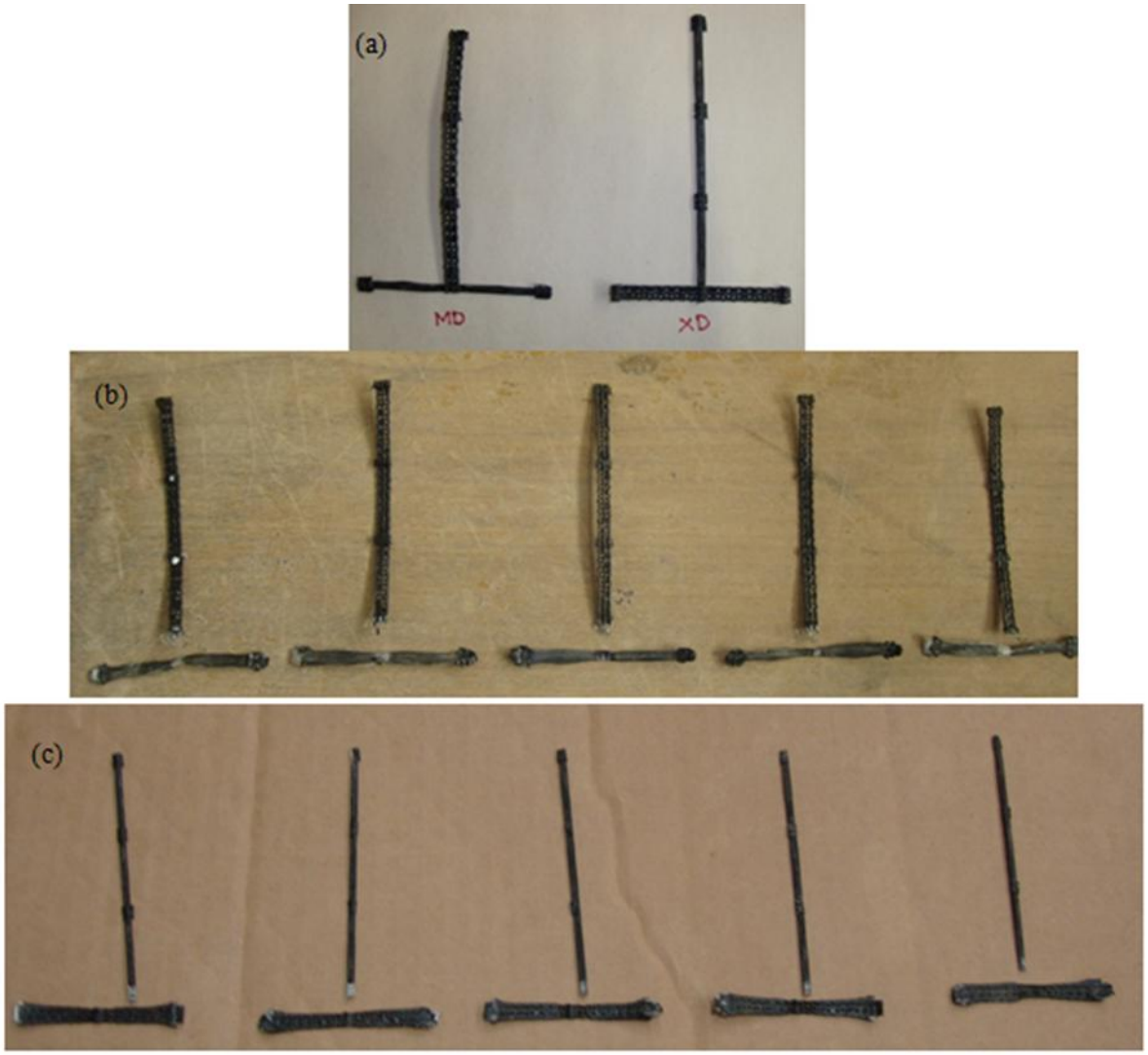

Figure 13. KGG1 geogrid junction strength specimens: (a) before the test, (b) after failure (MD), (c) after failure (XD)

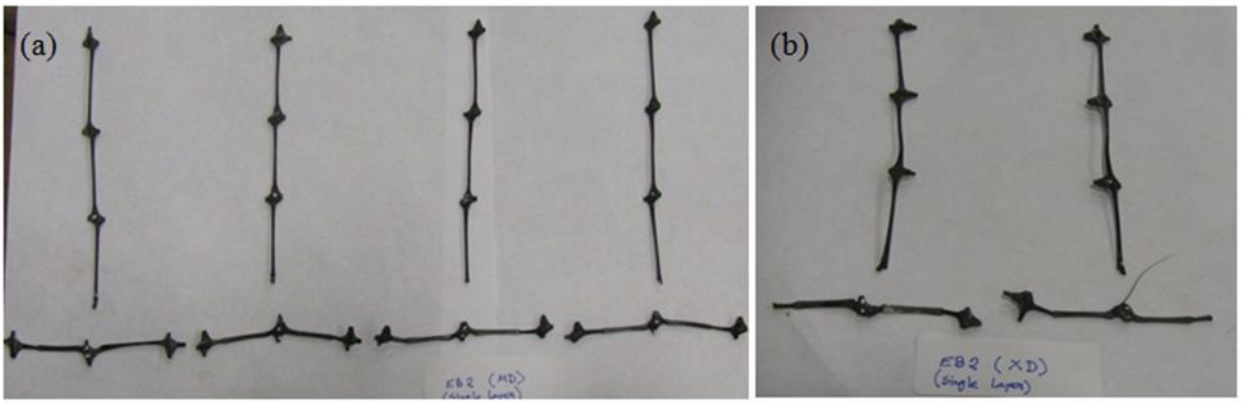

Figure 14. EGG2 (single layer) geogrid junction strength specimens after the test: (a) in MD and (b) in XD

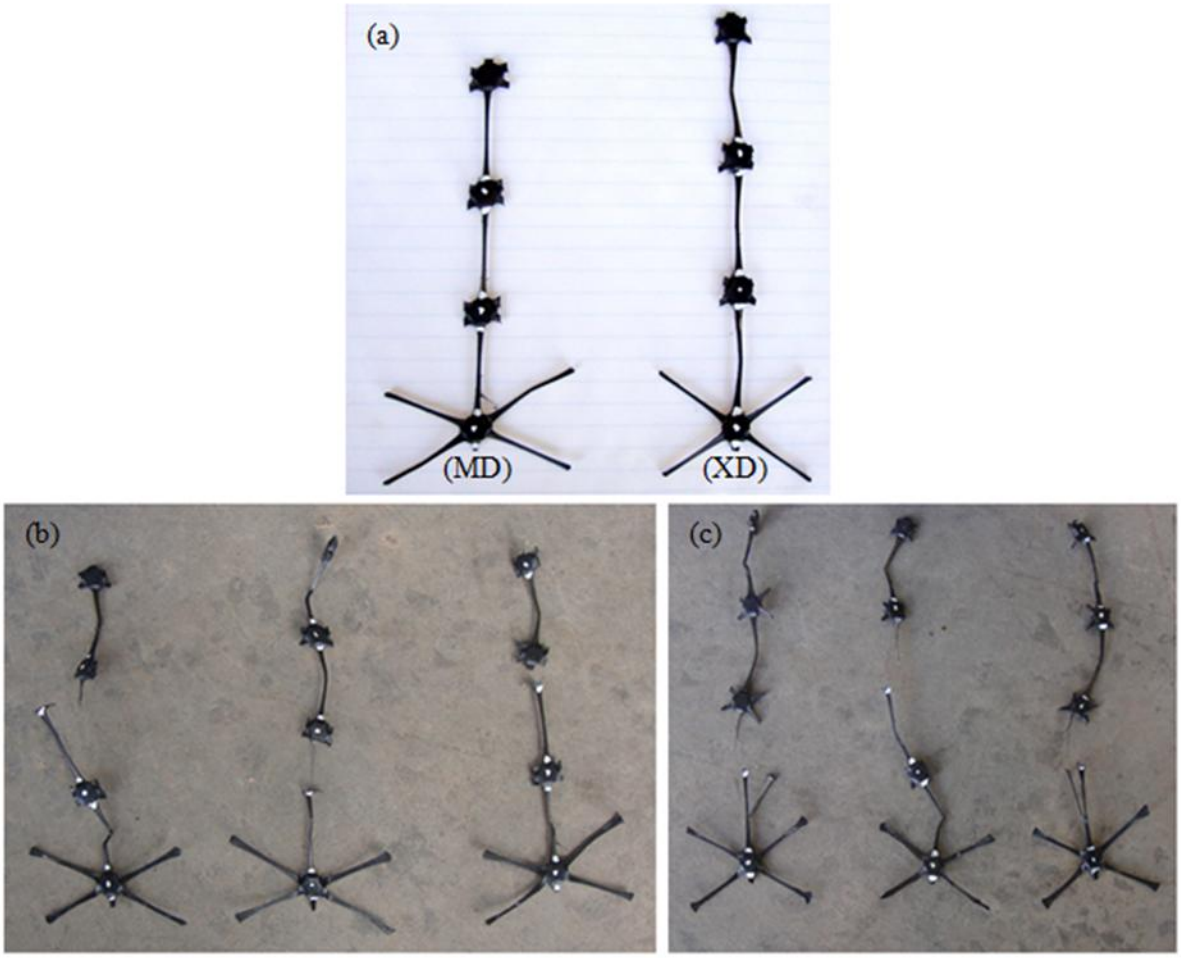

Figure 15. EGG3 geogrid junction strength specimens: (a) before the test, (b) after failure (MD), (c) after failure (XD)

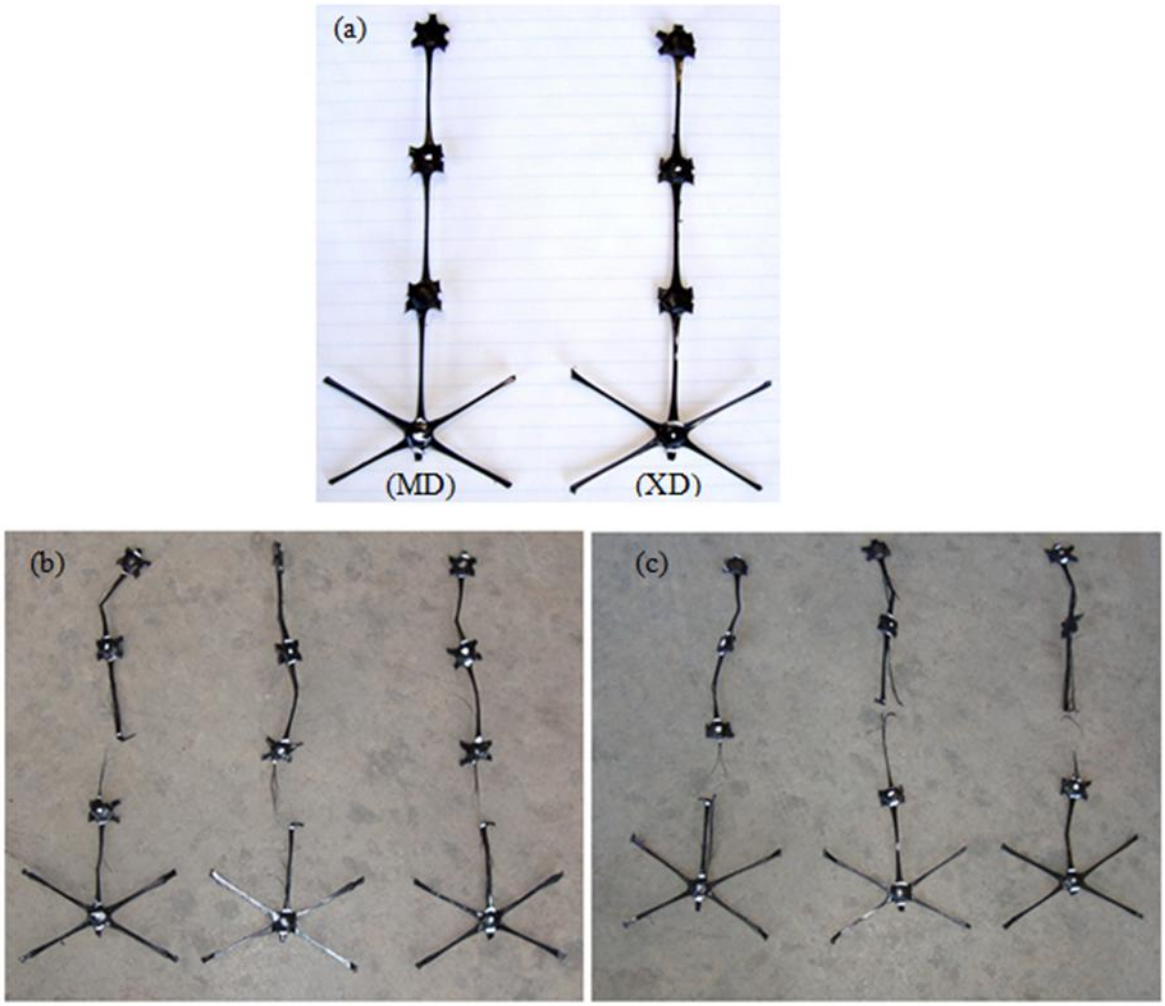

Figure 16. EGG4 geogrid junction strength specimens: (a) before the test, (b) after failure (MD), (c) after failure (XD)

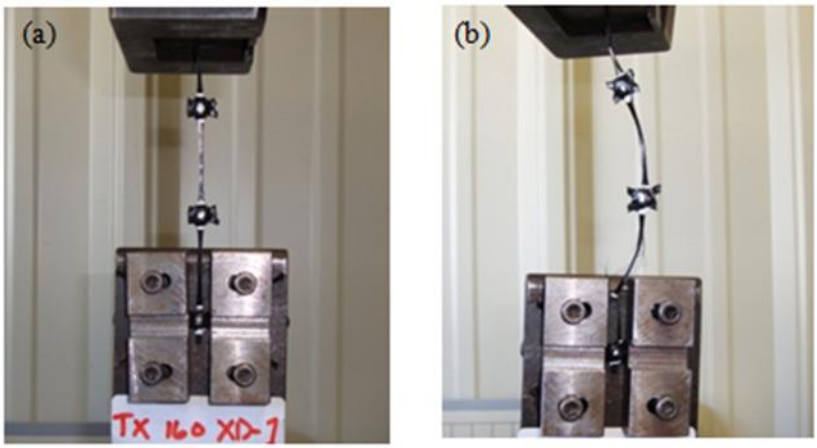

Figure 17. EGG4 geogrid specimen in junction strength test: (a) before the test, (b) after failure

Junction test results for the eight (8) different types of geogrids investigated (**Table 2**) are shown in **Figure 18** through **Figure 33**. In the cases of EGG3 and EGG4 geogrids in **Figure 30** through **Figure 33**, the "MD" notation refers to the ribs that are situated at 30^{o} from the machine direction due to their triangular configurations. The test results for each geogrid product tested are summarized in **Table 7** and **Table 8**. In the results shown in these figures and tables, the outlier data points were discarded such that all the remaining data will fall within ±5% of the mean value.

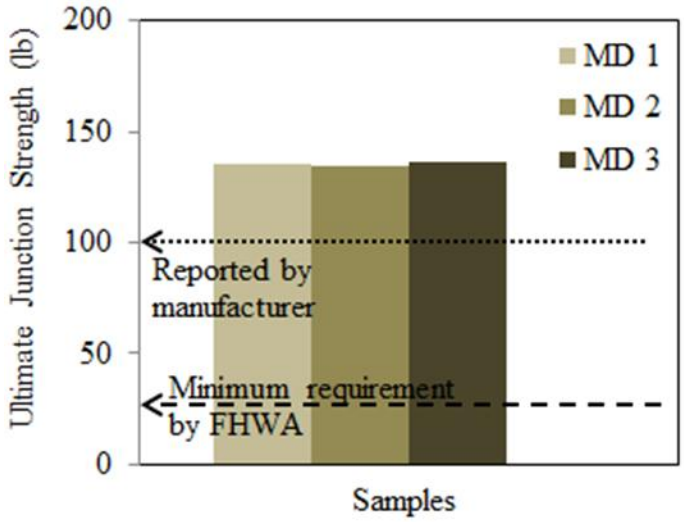

Figure 18. Junction strength variation in different EGG1 test specimens (MD)

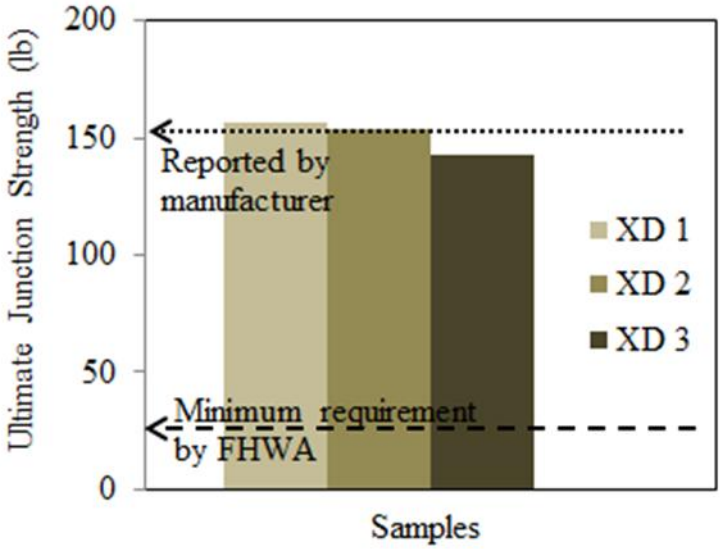

Figure 19. Junction strength variation in different EGG1 test specimens (XD)

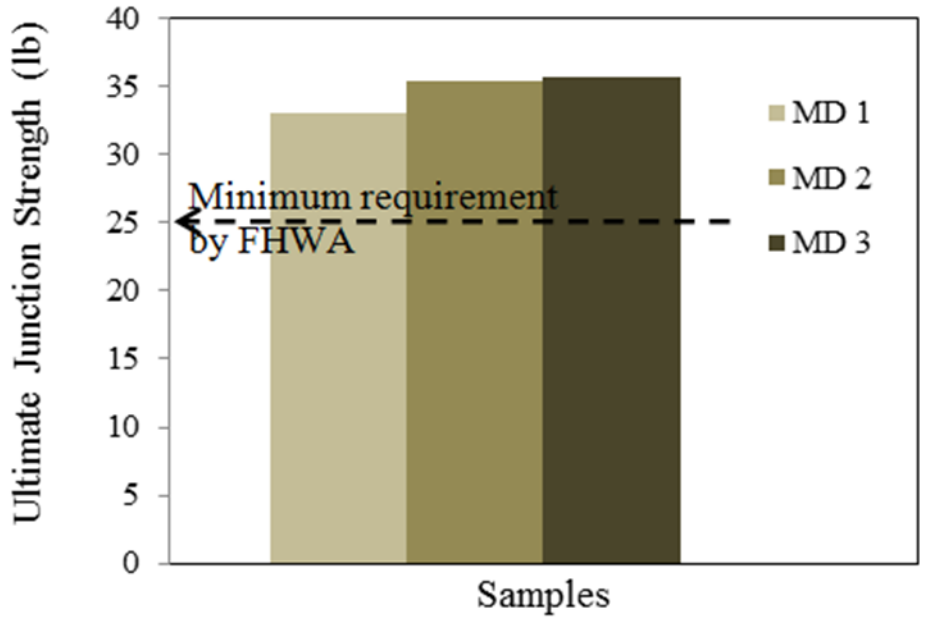

Figure 20. Junction strength variation in different WGG1 test specimens (MD)

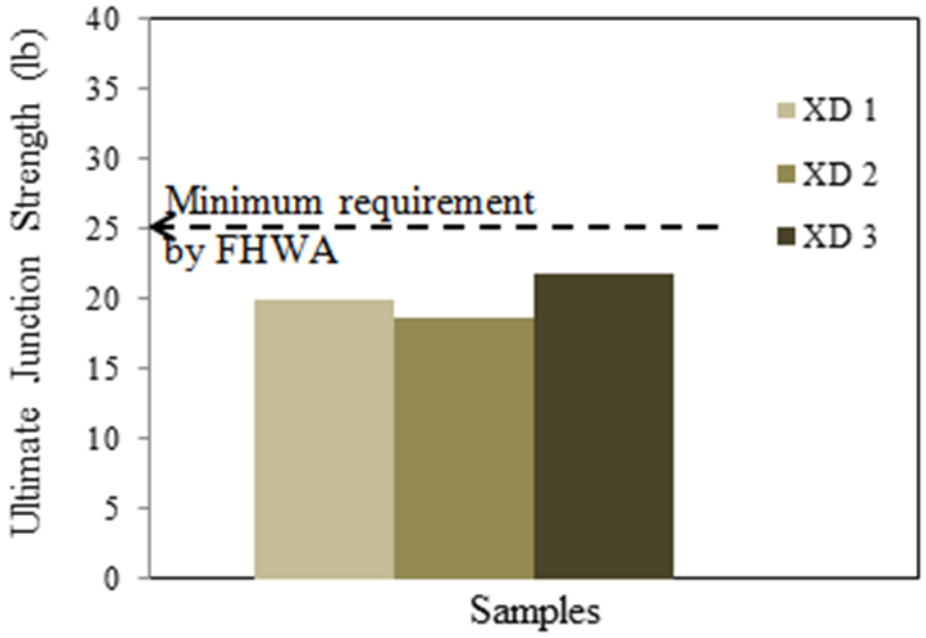

Figure 21. Junction strength variation in different WGG1 test specimens (XD)

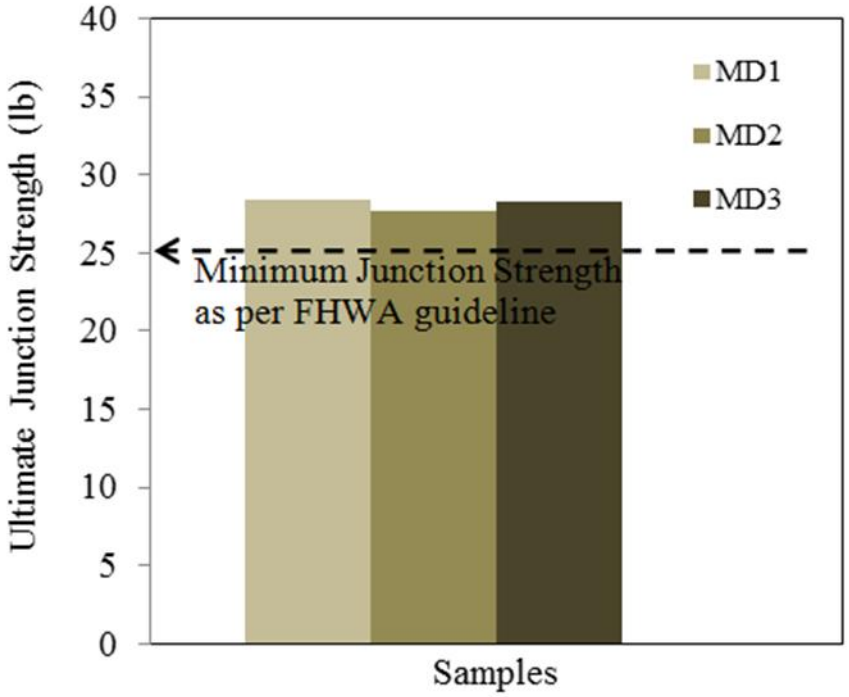

Figure 22. Junction strength variation in different WGG2 test specimens (MD)

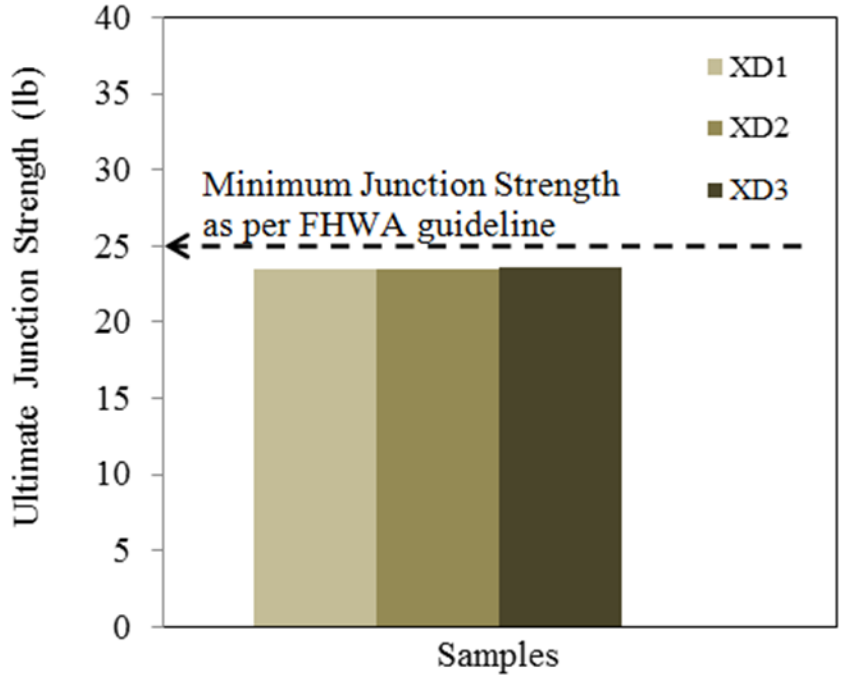

Figure 23. Junction strength variation in different WGG2 test specimens (XD)

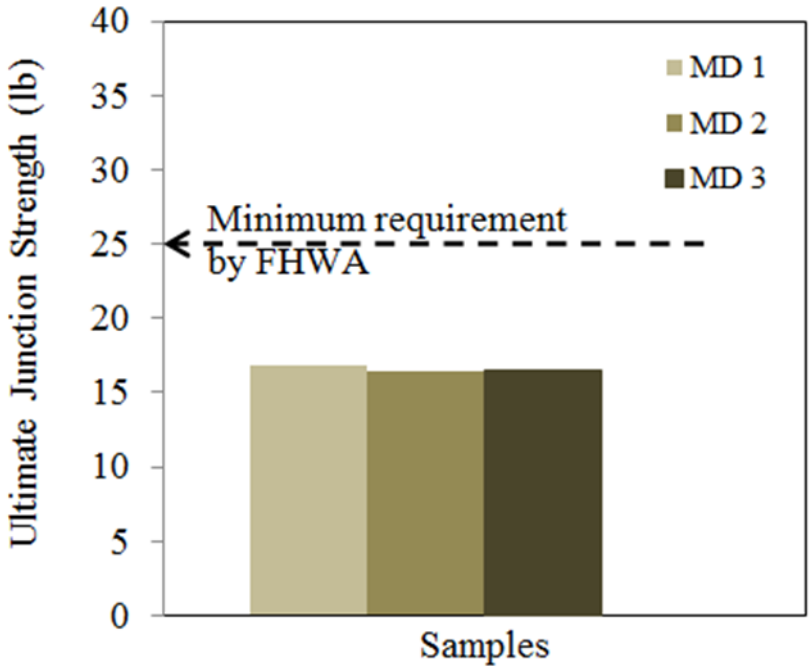

Figure 24. Junction strength variation in different WGG3 test specimens (MD)

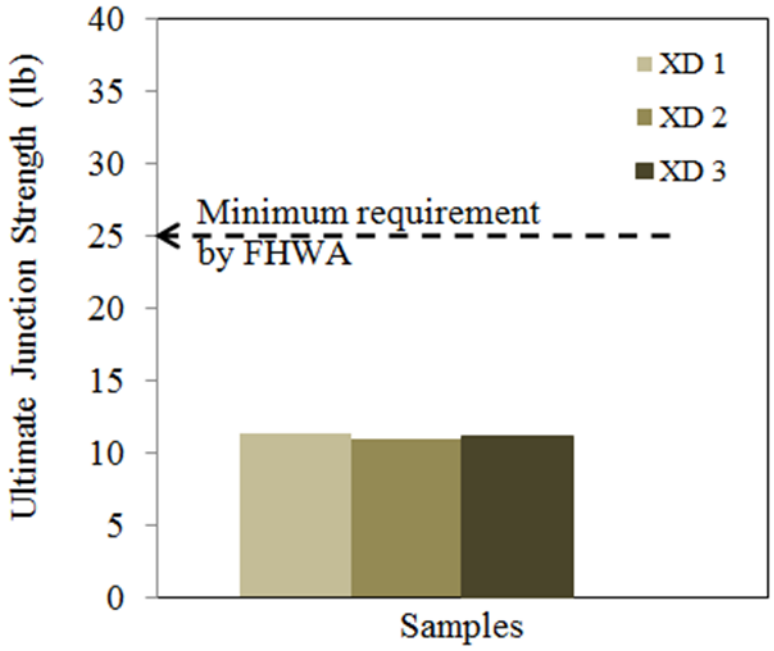

Figure 25. Junction strength variation in different WGG3 test specimens (XD)

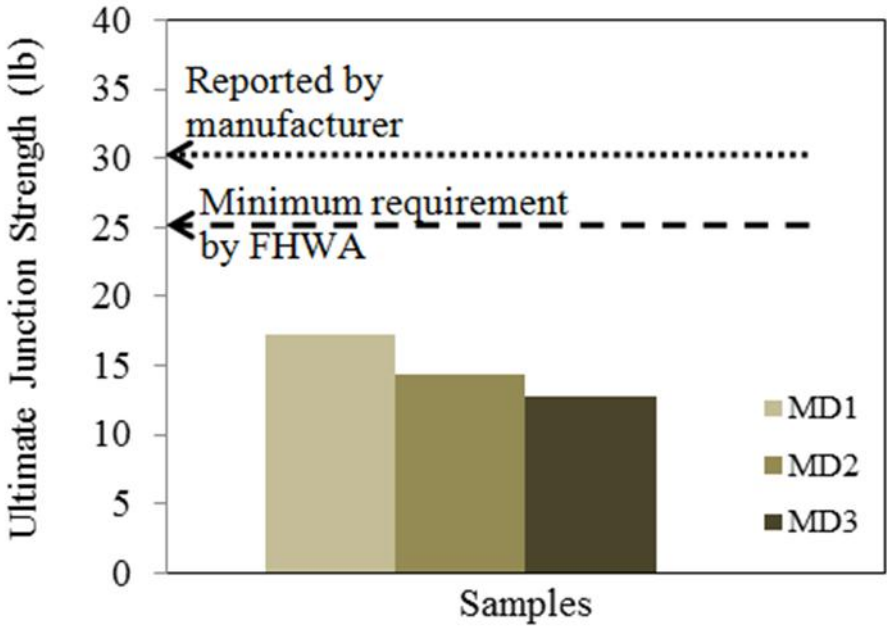

Figure 26. Junction strength variation in different KGG1 test specimens (MD)

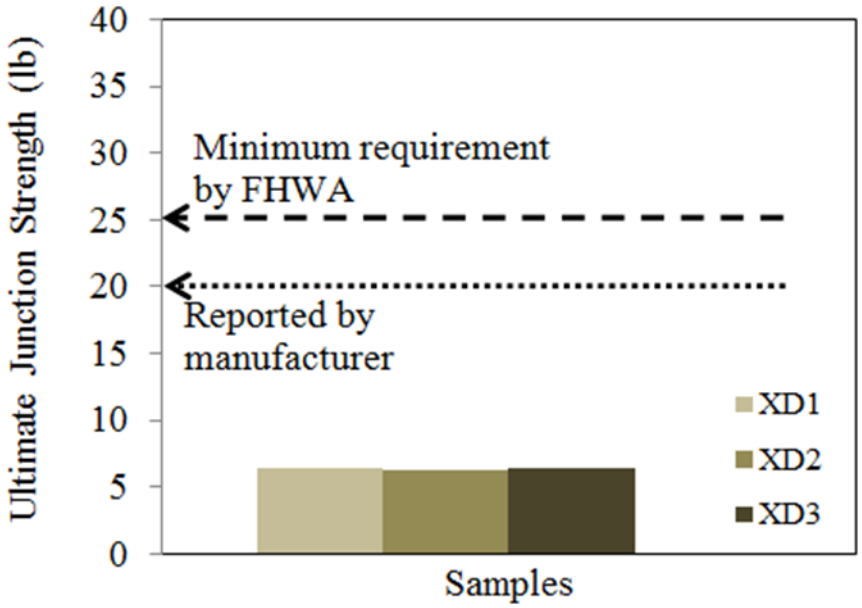

Figure 27. Junction strength variation in different KGG1 test specimens (XD)

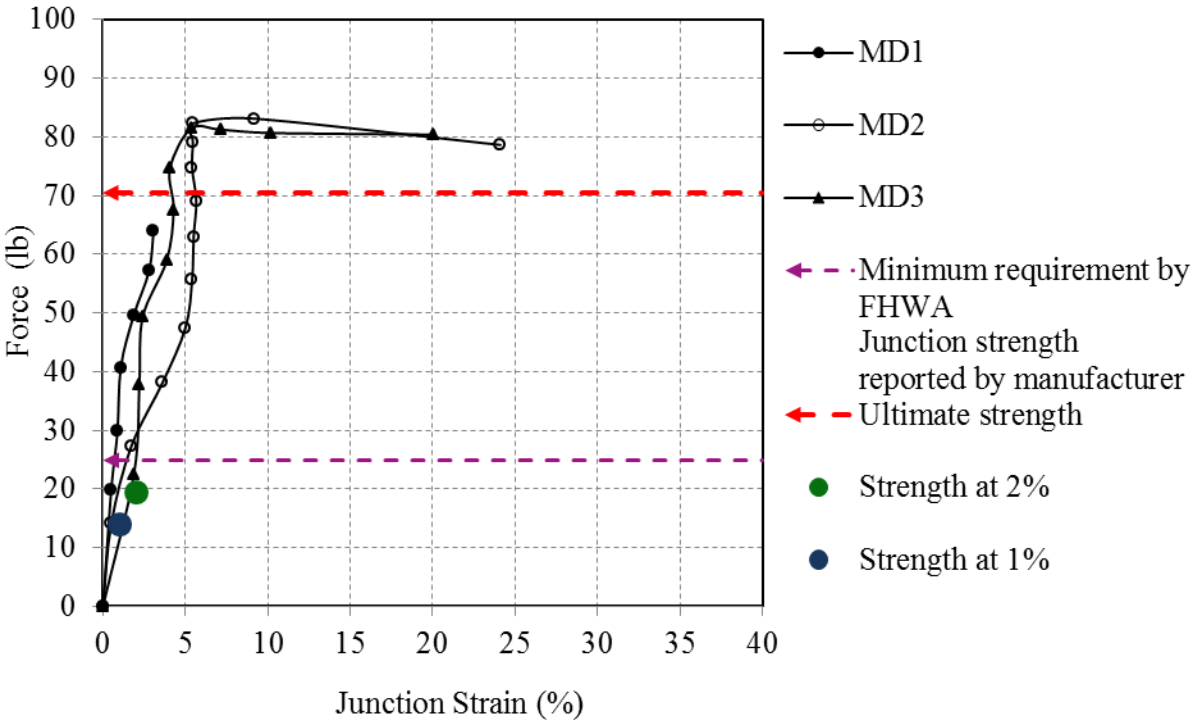

Figure 28. Load-strain responses of EGG2-single layer specimens (MD)

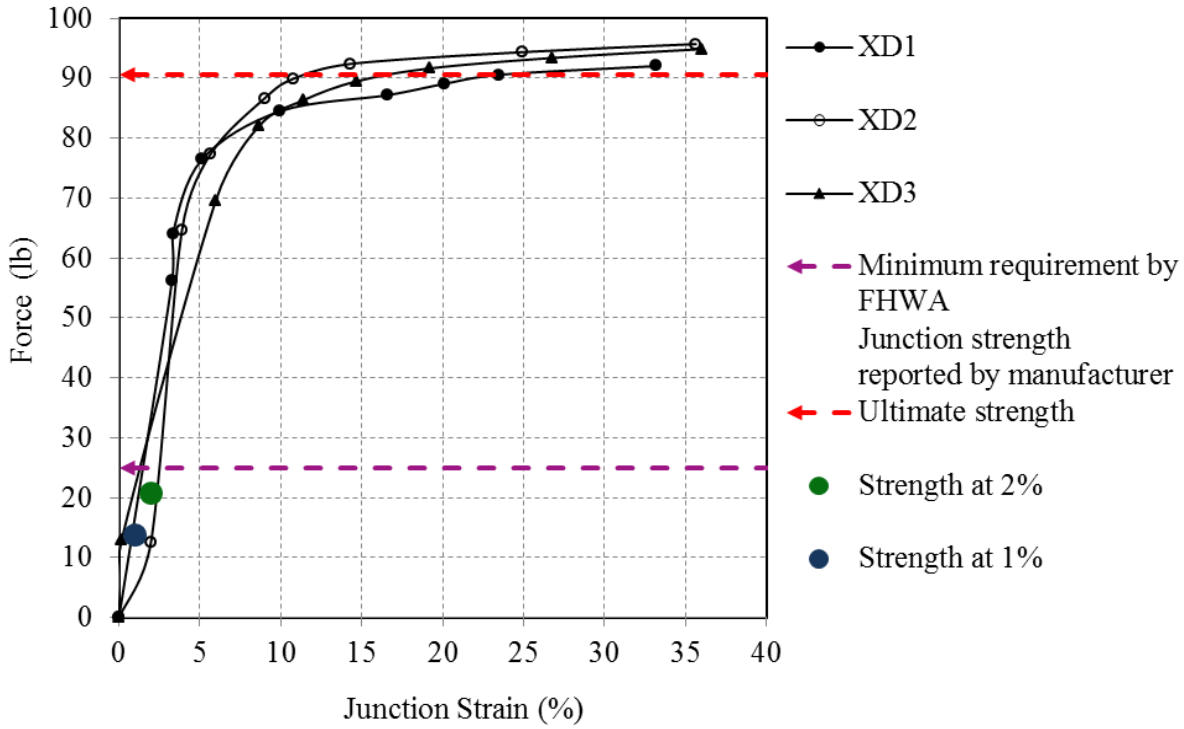

Figure 29. Junction strength variation in different samples of EGG2-single layer (XD)

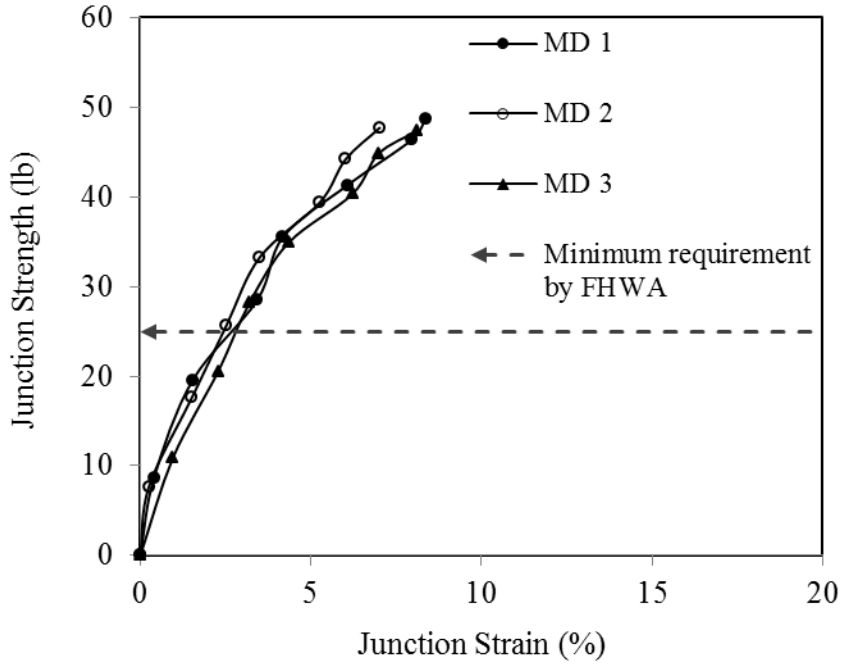

Figure 30. Junction strength test results of EGG3 geogrid in MD ribs (30 ° from machine direction)

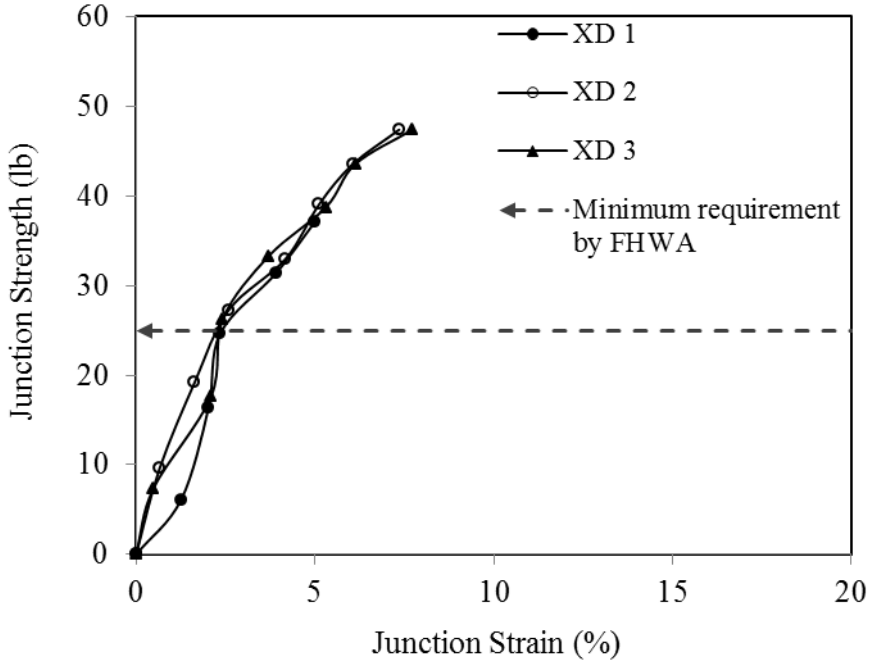

Figure 31. Junction strength test results for EGG3 in XD

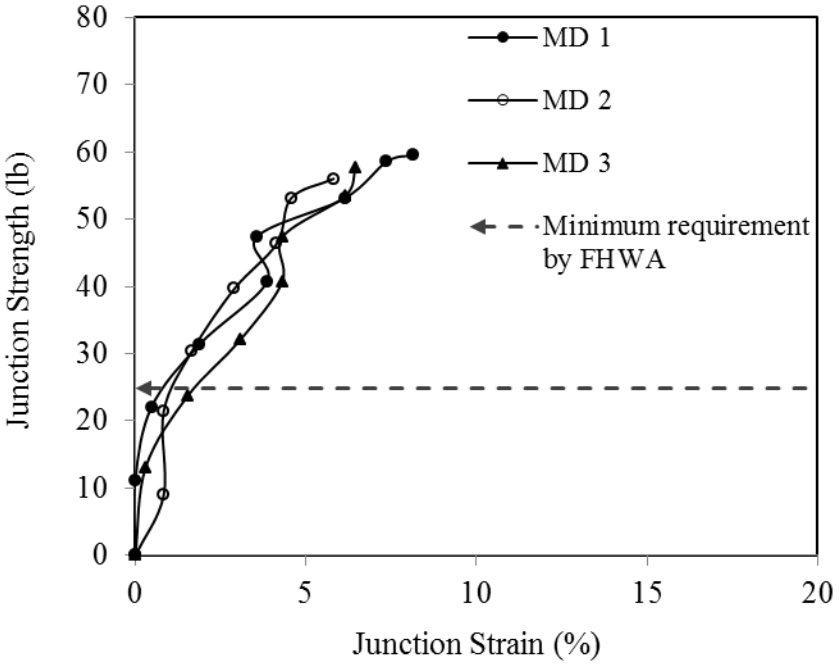

Figure 32. Junction strength test results of EGG4 geogrid in MD (30^{o} from machine direction)

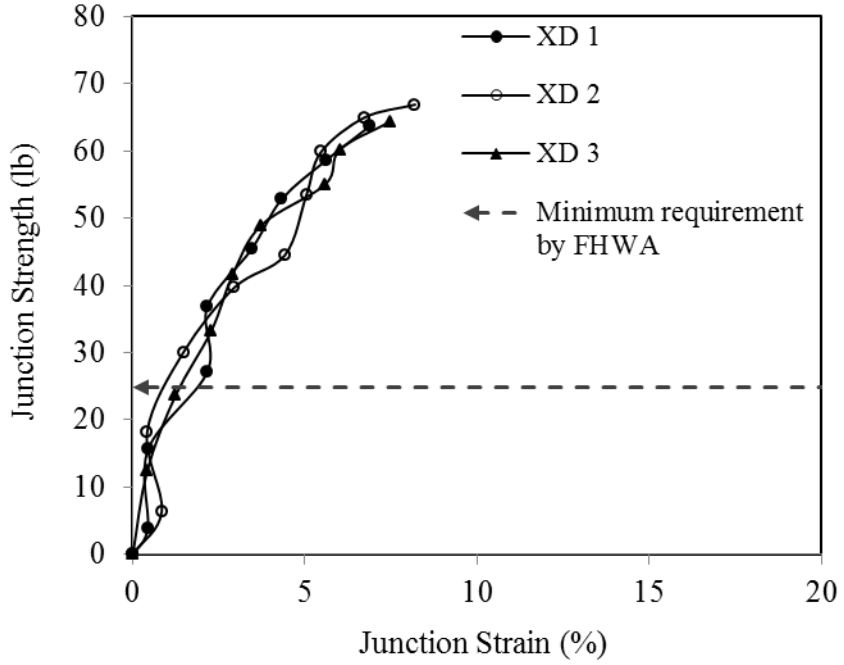

Figure 33. Junction strength test results for EGG4 in XD

Table 7. Summary of junction strength test results in machine direction (MD)

Geogrid	Type	Junction Strength in Machine Direction (lb)								
		1	2	3	4	5	Mean (μ)	Standard Deviation (σ)	Co-efficient of Variation, COV (%)	MARV value from manufacturer
EGG1	S_RS_J Biaxial Extruded	134.99	134.88	[132]	135.89		135.25	0.45	0.33	101.52
WGG1	S_RS_J Biaxial Woven	[41.27]	35.63	35.39	33.04		34.69	1.17	3.37	30.00
WGG2	S_RS_J Biaxial Woven	28.26	28.27	27.67	28.35	[39.9]	28.14	0.27	0.97	30.00
WGG3	S_RW_J Biaxial Woven	16.79	16.39	16.47	16.37	16.38	16.48	0.16	0.96	59.40
KGG1	S_RW_J Biaxial Knitted	17.29	10.24	14.41	12.81		13.69	2.56	18.68	30.50
EGG2 (single layer)	W_RS_J Biaxial Extruded	[63.84]	82.95	81.38	82.92	79.40	81.66	0.73	0.90	70.53
EGG3	S_RS_J Triaxial Extruded	47.21	47.21	48.33			47.58	0.53	1.11	NP
EGG4	S_RS_J Triaxial Extruded	56.20	56.20	58.45			56.95	1.06	1.86	NP

Cell background color key:

- Junction meets minimum Holtz et al. (2008) requirement
- Junction does not meet minimum Holtz et al. (2008) requirement

[---] Outlier value

NP Not provided by the manufacturer

Table 8. Summary of junction strength test results in cross machine direction (XD)

Geogrid	Type	Junction Strength in Cross-Machine Direction (lb)								
		1	2	3	4	5	Mean (μ)	Standard Deviation (σ)	Co-efficient of Variation, COV (%)	MARV value from manufacturer
EGG1	S_RS_J Biaxial Extruded	156.31	153.63	[125.60]	142.64		150.86	5.92	3.92	152.67
WGG1	S_RS_J Biaxial Woven	19.85	18.57	21.77	[28.81]		20.06	1.32	6.55	30.00
WGG2	S_RS_J Biaxial Woven	23.53	23.45	[38.63]	23.60		23.53	0.06	0.27	30.00
WGG3	S_RW_J Biaxial Woven	11.33	10.93	[6.44]	11.12		11.13	0.16	1.47	47.60
KGG1	S_RW_J Biaxial Knitted	6.72	6.72	6.72	6.40		6.64	0.14	2.09	20.30
EGG2 (single layer)	W_RS_J Biaxial Extruded	95.73	90.92	90.64	94.88	97.64	93.96	2.75	2.93	90.64
EGG3	S_RS_J Triaxial Extruded	47.21	47.21	44.96			46.46	1.06	2.28	NP
EGG4	S_RS_J Triaxial Extruded	67.44	65.19	65.19			65.94	1.06	1.61	NP

Cell background color key:

- Junction meets minimum Holtz et al. (2008) requirement
- Junction does not meet minimum Holtz et al. (2008) requirement

[---] Outlier value

NP Not provided by the manufacturer

2.3. Rib strength tests

Several preliminary tensile strength tests were carried out on selected geogrids according to the ASTM D6637 test protocol. However, the existing clamping mechanism for single rib specimens was found to be problematic; either the specimens would pull out of the clamps or the measured tensile strength values for different specimens were not consistent. Therefore, new clamps were fabricated to improve the test results as described in the following sections.

The new clamps were successfully tried on both ODOT Type-1 and Type-2 geogrids. Afterwards, these clamps were used to carry out a total of 80 in-isolation rib strength tests to determine the 2%-strain, 5%-strain and ultimate tensile strength values of the geogrids listed in **Table 2** and **Table 3** in both machine (MD) and cross-machine (XD) directions. Five tests were carried out in MD and five in XD for each geogrid products.

2.3.1. Fabrication of rib strength testing clamps for extruded geogrids

Two 4 inches × 4 inches × 0.2 inch steel plates were fabricated as rib strength test clamps. In order to grip the geogrid ribs properly, a clamping system was developed that utilized frictional and interlocking forces using two layers of sandpapers mounted on the inside edges of each clamp. A piece of No. 100 wood sandpaper was fixed on the edge of the clamp using superglue as a permanent frictional layer. A 1 inch × 1 inch piece of sandpaper was placed on the middle of each fixed sandpaper layer as a disposable pad as shown in **Figure 34**. These pieces were replaced after each test because they would lose their roughness during testing.

Figure 34. Rib strength test clamp for extruded geogrids and accessories

Specimen preparation in our procedure for rib strength testing of geogrids included the following steps:

1. A piece of geogrid was cut with the length of two or more aperture sizes depending on the aperture size. Then, the initial length of the geogrid specimen was measured and its junctions were marked using a white marker, as shown in **Figure 34**. According to ASTM D6637 test standard, each specimen should consist of 3 junctions or 12 in long.

2. Clamp bolts were inserted into the holes and 1 in by 1 in pieces of sandpaper were placed and aligned on the two clamps as shown in **Figure 35(a)**. The test specimen and additional dummy (spacer) pieces of geogrid were placed on the clamps at equal distances from the center of the bolts as shown in **Figure 35(b)**. Spacer pieces of geogrid were used to keep the clamp plates parallel to each other which would help increase the grip of the clamp on the specimen during the application of tensile load.

3. Two additional small pieces of sandpaper were placed on the specimen inside the clamp. During the assembly of the clamps, each nut was uniformly tightened one turn at a time until the geogrid was completely secured in the clamps [**Figure 36(a)**].

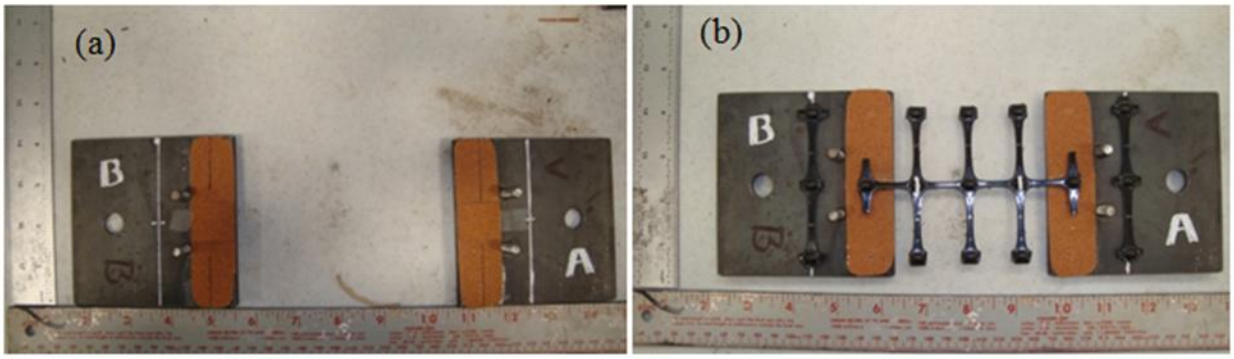

Figure 35. (a) Sandpapers mounted on test clamps (b) Alignment of test specimen and spacer pieces on clamps

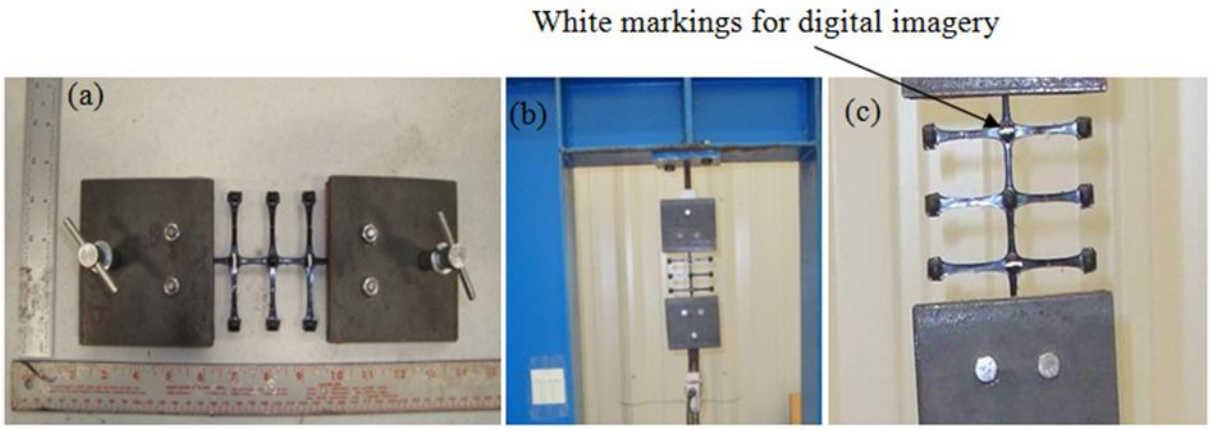

Figure 36. (a) Geogrid specimen secured in the clamps, (b) test setup mounted on the tension frame, (c) view from digital camera, ready to record the specimen deformation.

4. The clamps and specimen assembly were carefully transported to and mounted on the testing frame as shown in **Figure 36(b)**. A digital camera (camcorder) was set up to record the specimen deformation during the test as shown in **Figure 36(c)**. The view frame of the camera was zoomed on the specimen such that the size of the specimen image was as large as possible and yet, the two white marks on the specimen remained within the viewing range during the entire test until specimen failed.

5. The camcorder, the electric motor attached to the moving clamp and the data acquisition system were started simultaneously. The test continued until the specimen failed. This new clamping system was found to significantly improve the test success rate for extruded geogrids that offer very low surface friction. Only a minimum portion of the geogrid ribs needed to be placed inside the clamps.

6. The ASTM D6637 test protocol recommends placing three junctions across the width of the geogrid specimen inside the clamp. However, it was observed that placing three junctions in the clamped area prevents adequate pressure concentration on the middle junction, which results in increased risk of the test rib sliding out of the clamps. Our new procedure requires the placement of only one junction in a highly frictional clamped area (**Figure 35b**) which proved to be very effective in securing the specimen in its place throughout the test.

7. In all rib strength tests performed on the EGG1 specimens in the machine direction (MD), the specimens failed at the locations of mid-span junctions, and the test was unable to capture the failure of the ribs. It was concluded that the ribs in machine direction are stronger than the junctions. This is explained by the fact that extruded geogrids such as EGG1 are manufactured using a punch-and-drawing technique. The ribs are stretched parts of the perforated polymer sheet during the manufacturing process, which in contrast to the junctions, experience strain hardening. As a result, the ribs become stronger than the junctions. We discussed our observations with Tensar representatives and they acknowledged that failure of the mid-span junctions may likely occur while testing the rib samples. Nevertheless, the failure load recorded regardless of the location of the rupture in the mid-span is typically reported as the rib strength value. It therefore appears that using two aperture size-long specimens in the rib strength tests according to the ASTM D6637 test procedure makes it very difficult to measure the rib strength without rupturing the junction [**Figure 36(b)** and **Figure 37(a)**].

8. In order to investigate the influence of specimen size on junction failure as stated above and to eliminate any possible boundary effects (i.e. proximity of the failed junction to the clamps), samples with five aperture size length were tested. It was observed that the specimens still failed at their mid-span junction as shown in **Figure 37(b)**. This observation confirmed that the reason for junction failure in rib strength tests was indeed due to weaker junctions as compared to the ribs regardless of the specimen size. It also confirmed that the clamping system was robust and

consistently resulted in failure at the specimen mid-span as opposed to a location near the clamps. The specimens tested in the cross-machine direction (XD) all failed at the connection between the ribs and junctions [**Figure 37(c)**].

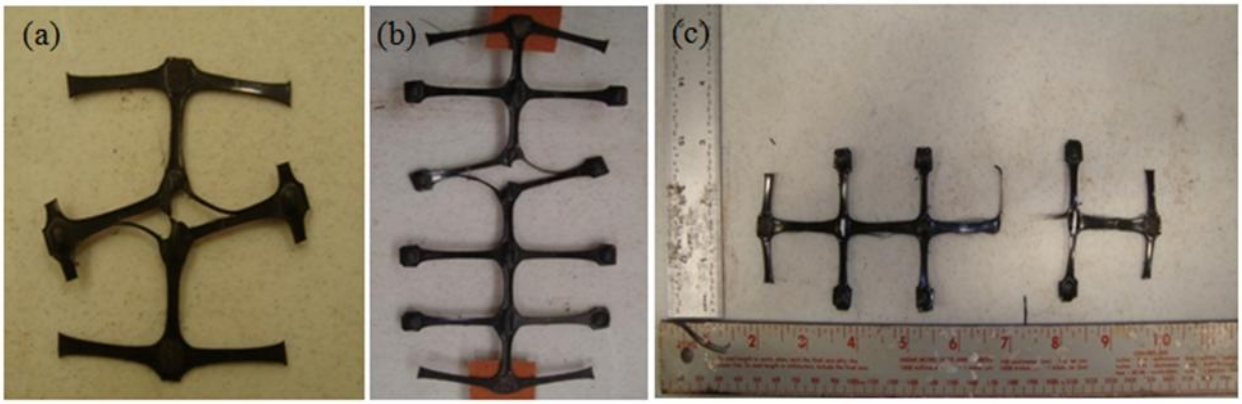

Figure 37. (a),(b) Two and five aperture size-long specimens which failed at their junctions in rib strength tests, (c) Specimen failed in cross-machine direction

In addition to conventional biaxial geogrids, recently introduced triaxial products (EGG3 and EGG4) by Tensar were investigated. Currently, there are no standard test protocols for sample preparation, clamping requirements and in-isolation testing of triaxial products. ASTM D6637 test standard was followed for this purpose, which was originally developed for uniaxial and biaxial geogrids. **Figure 38** shows the geogrid samples prepared for the rib test according to ASTM D6637. **Figure 39** and **Figure 40** show the rib test setup for the EGG3 and EGG4 geogrids respectively, before and after failure.

In the case of EGG3 and EGG4 products, rib strength tests were carried out in the directions along the diagonal (MD) and transverse (XD) ribs. After comparing the measured results and the test data supplied by Tensar with the criteria given in **Figure 4**, both the EGG3 and EGG4 geogrids were classified in the strong rib and strong junction category.

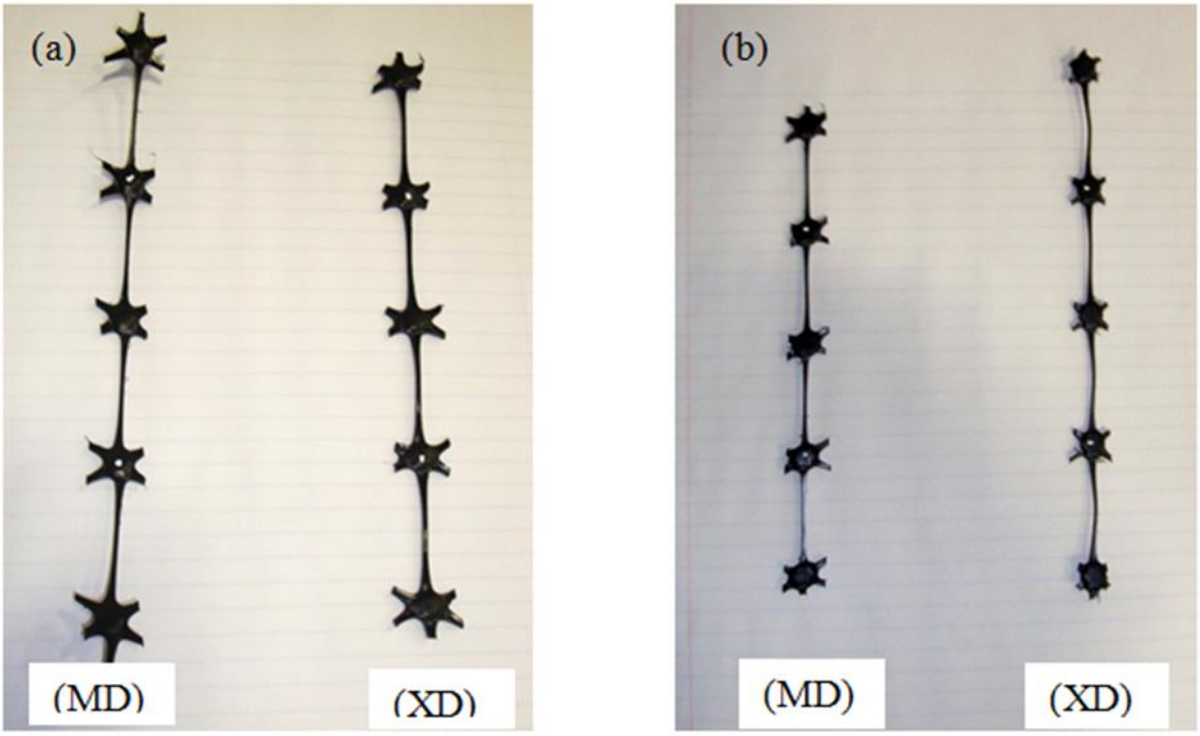

Figure 38. Geogrid specimens for rib strength tests (a) EGG3 specimens and (b) EGG4 specimens

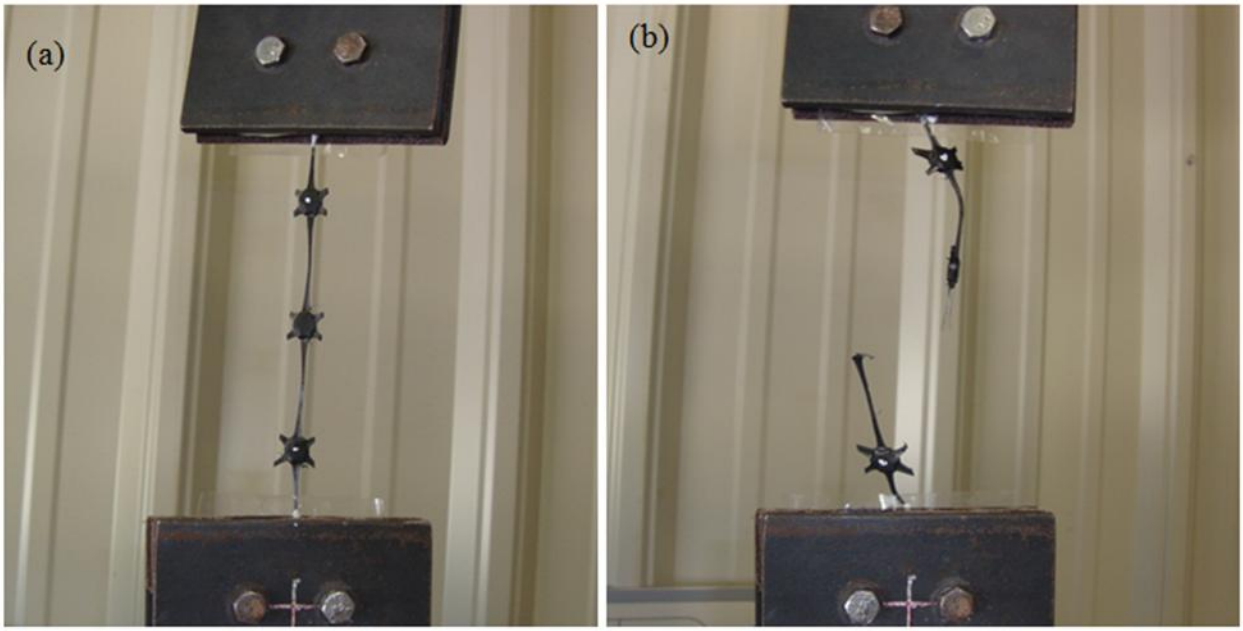

Figure 39. EGG3 geogrid sample for rib strength tests, (a) before the test, (b) after failure

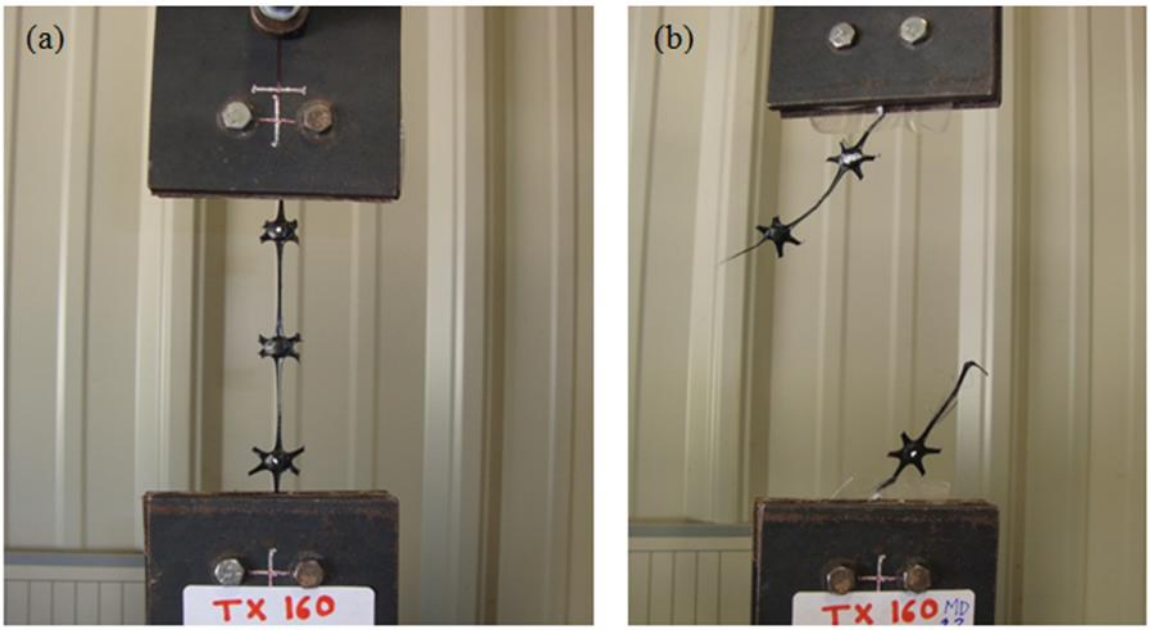

Figure 40. EGG4 geogrid sample for rib strength tests, (a) before the test, (b) after failure

2.3.2. Fabrication of rib strength testing clamps for non-extruded geogrids

When PVC-coated polyester (PET) geogrids were tested using the above test setup, it was observed that in some specimens polyester yarns were pulled out of the PVC coating leaving a piece of the coating in the clamp. Based on this observation, a new clamping system was developed for non-extruded geogrids as shown in **Figure 41** and **Figure 42**. These clamps helped mitigate stress concentrations at the geogrid-clamp connections and therefore, prevent immature failure of the specimen. This type of clamp is comparable to Capstan clamps and roller grips discussed in the ASTM D4595 test protocol (ASTM 2009).

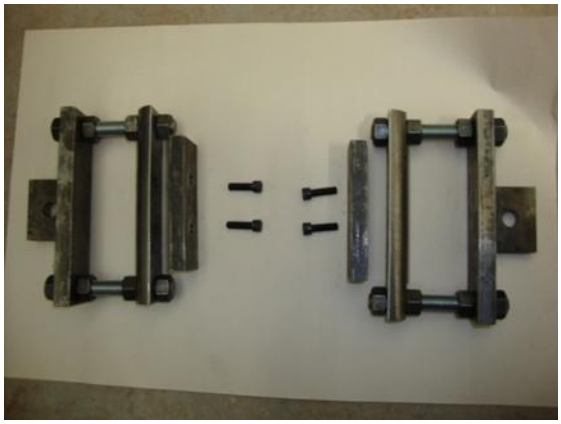
Figure 41. Clamping system fabricated to test non-extruded geogrids

Figure 42. Rib strength testing of non-extruded geogrid in progress

2.3.3. Rib strength test results

Load-strain test results for the geogrids listed in **Table 2** and **Table 3** are shown in **Figure 43** through **Figure 58.**

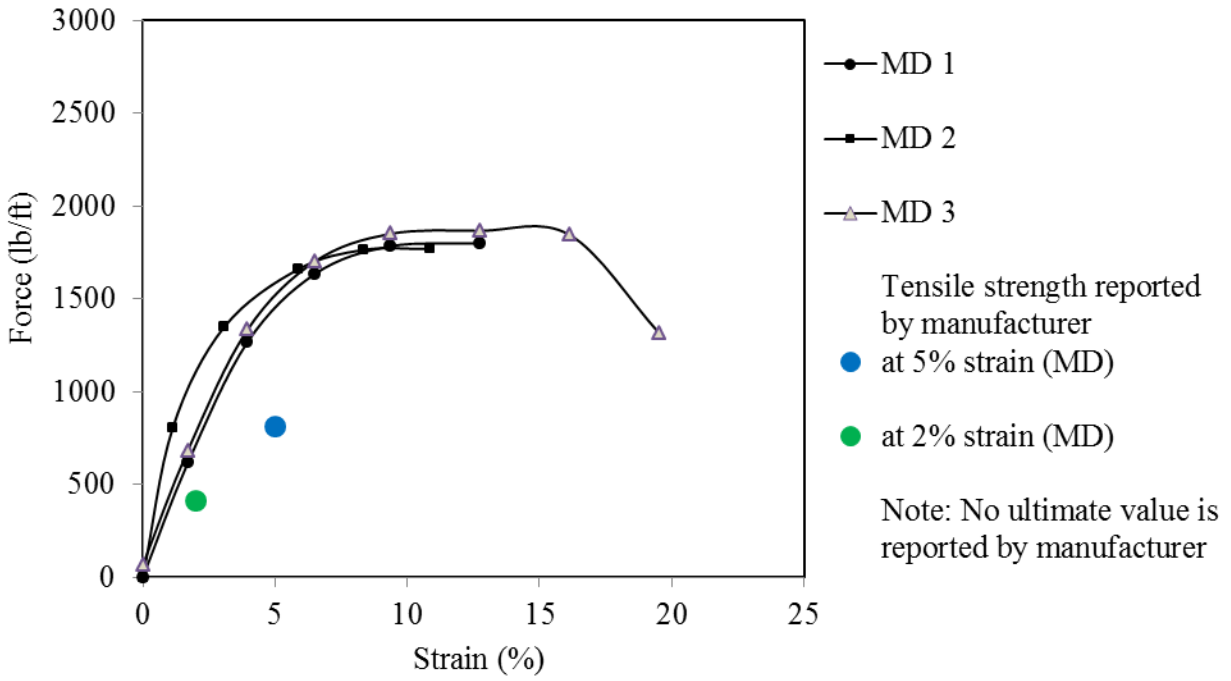

Figure 43. Tensile strength test results of EGG1 geogrid in machine direction

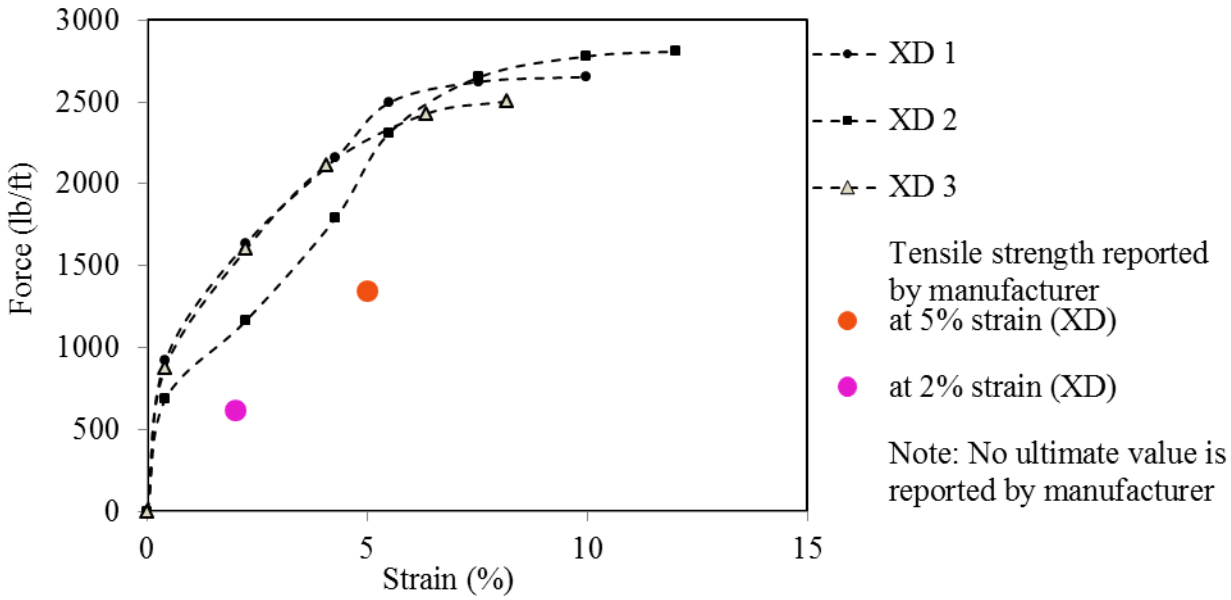

Figure 44. Tensile strength test results of EGG1 geogrid in cross-machine direction

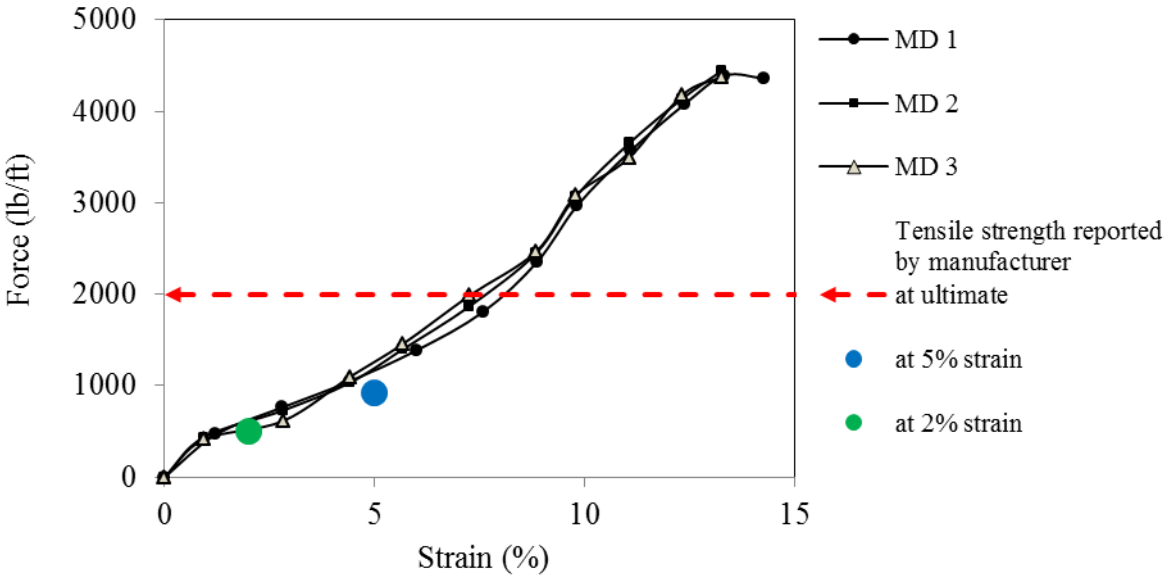

Figure 45. Tensile strength test results of WGG1 geogrid in machine direction

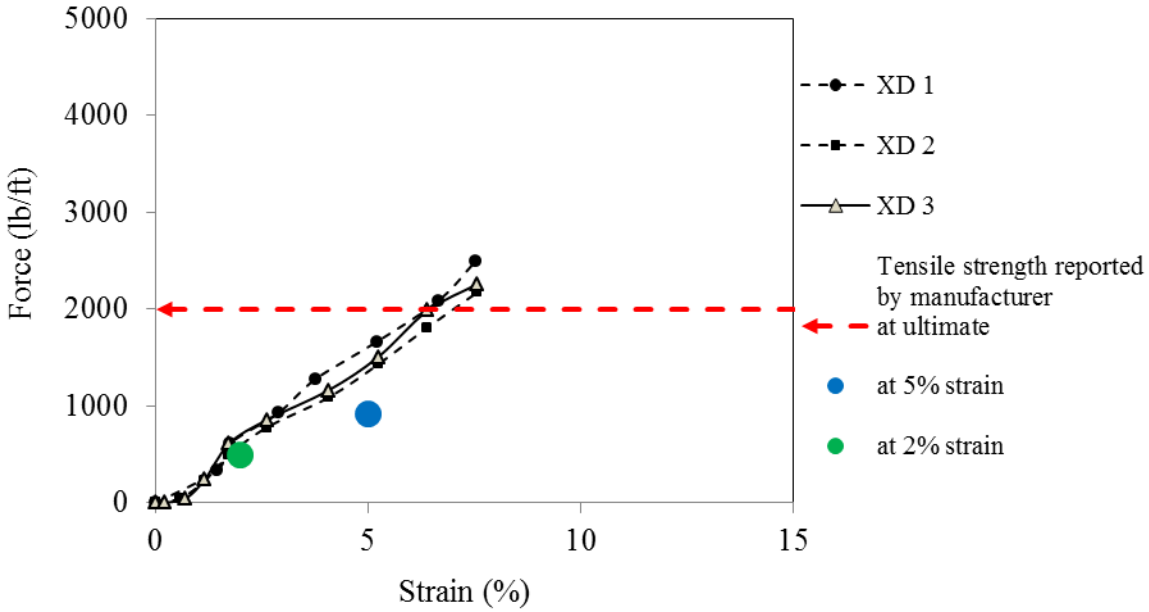

Figure 46. Tensile strength test results of WGG1 geogrid in cross-machine direction

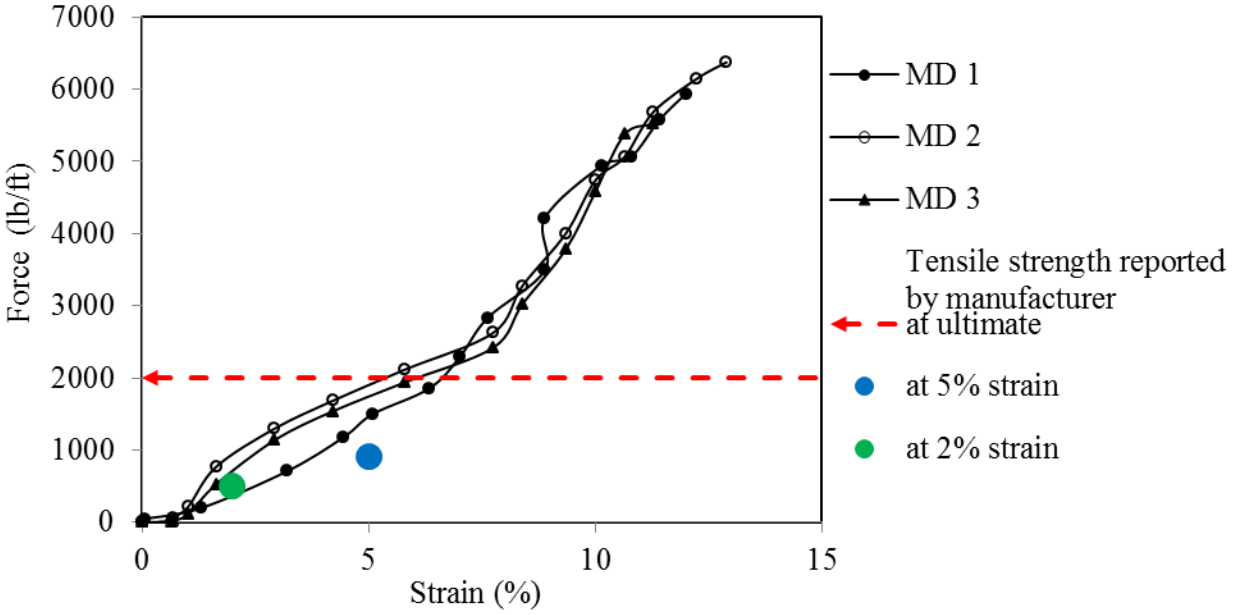

Figure 47. Tensile strength test results of WGG2 geogrid in machine direction

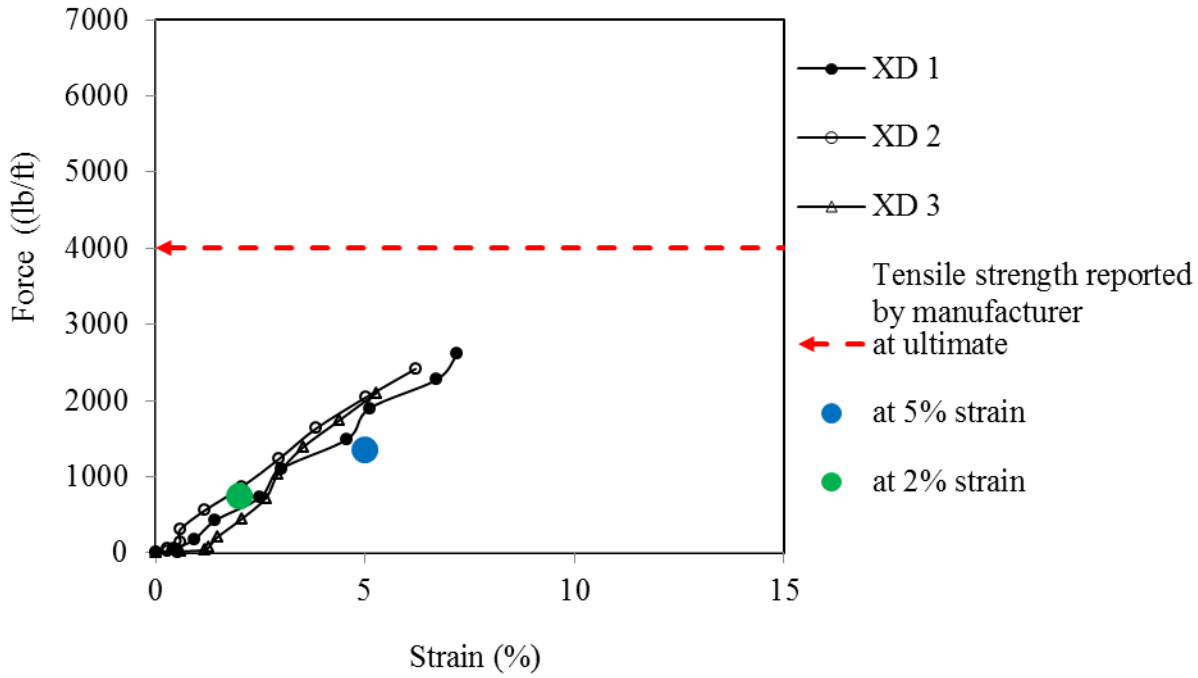

Figure 48. Tensile strength test results of WGG2 geogrid in cross-machine direction

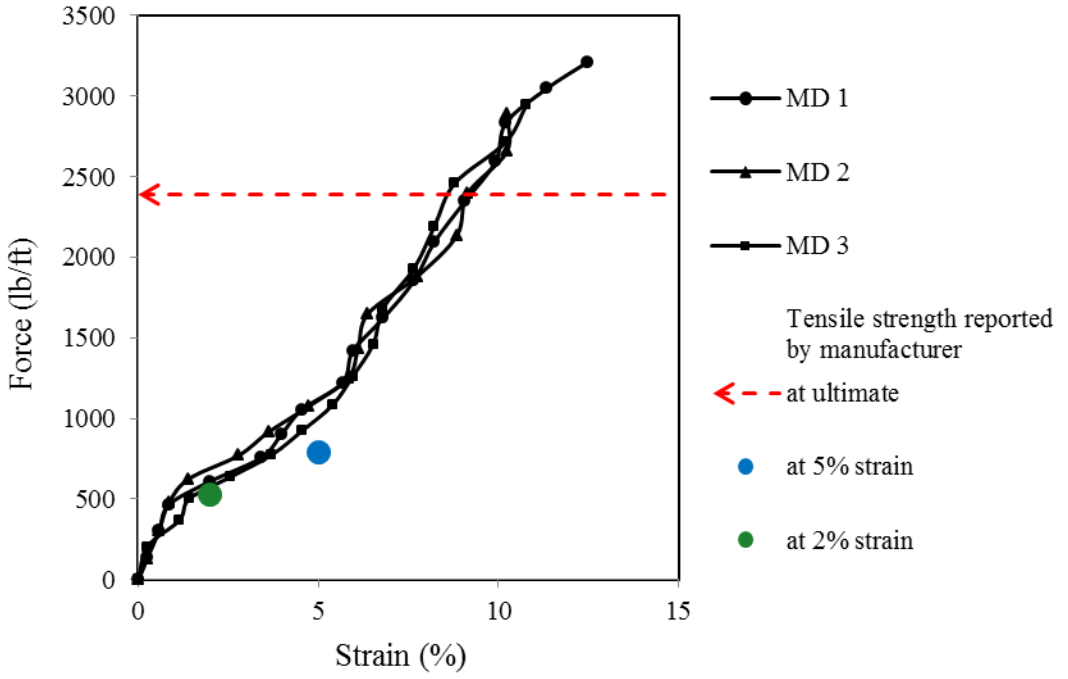

Figure 49. Tensile strength test results of WGG3 geogrid in machine direction

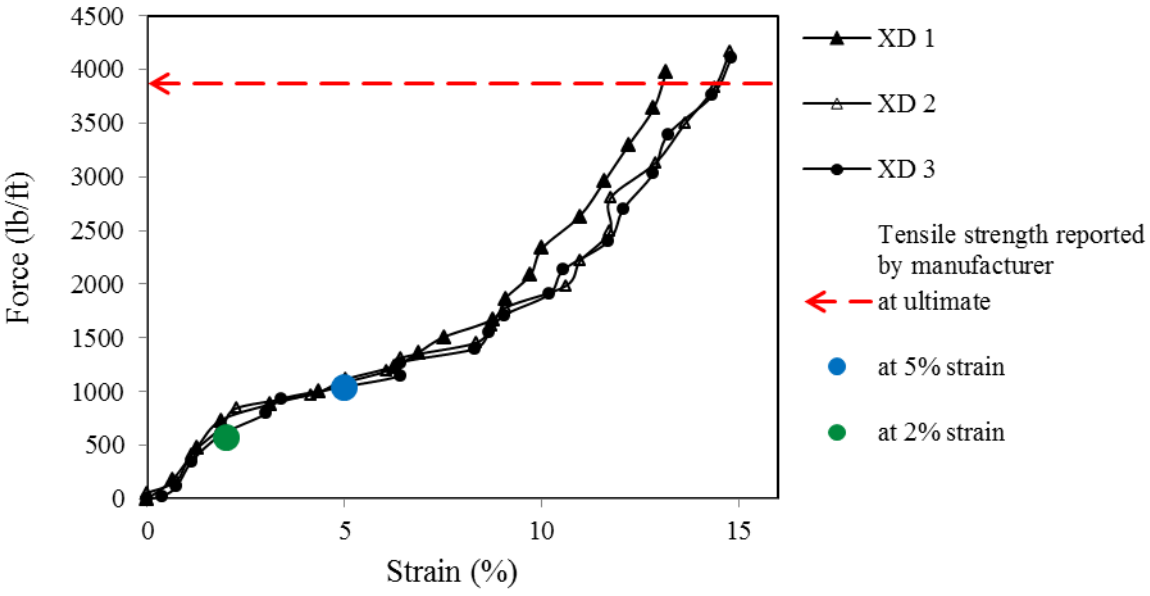

Figure 50. Tensile strength test results of WGG3 geogrid in cross-machine direction

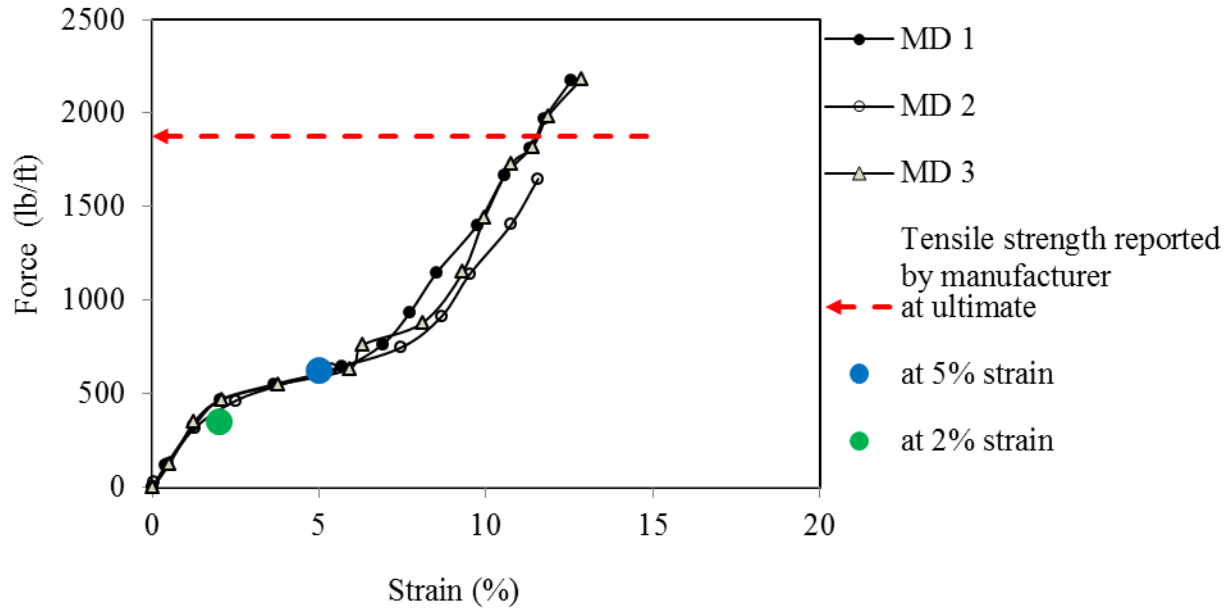

Figure 51. Tensile strength test results of KGG1 geogrid in machine direction

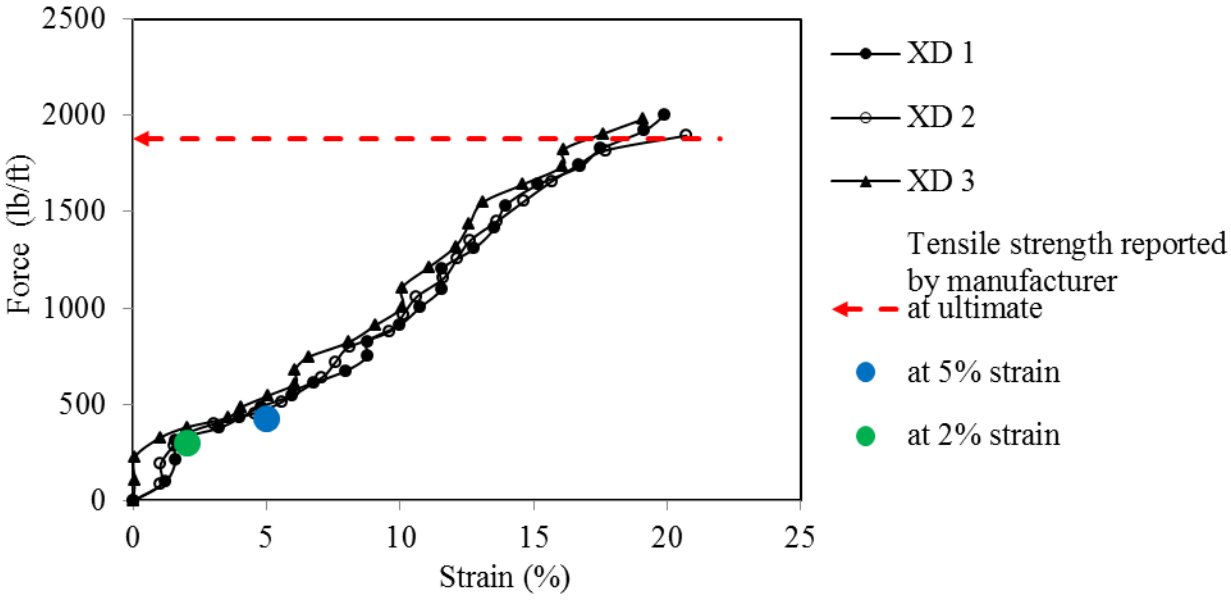

Figure 52. Tensile strength test results of KGG1 geogrid in cross-machine direction

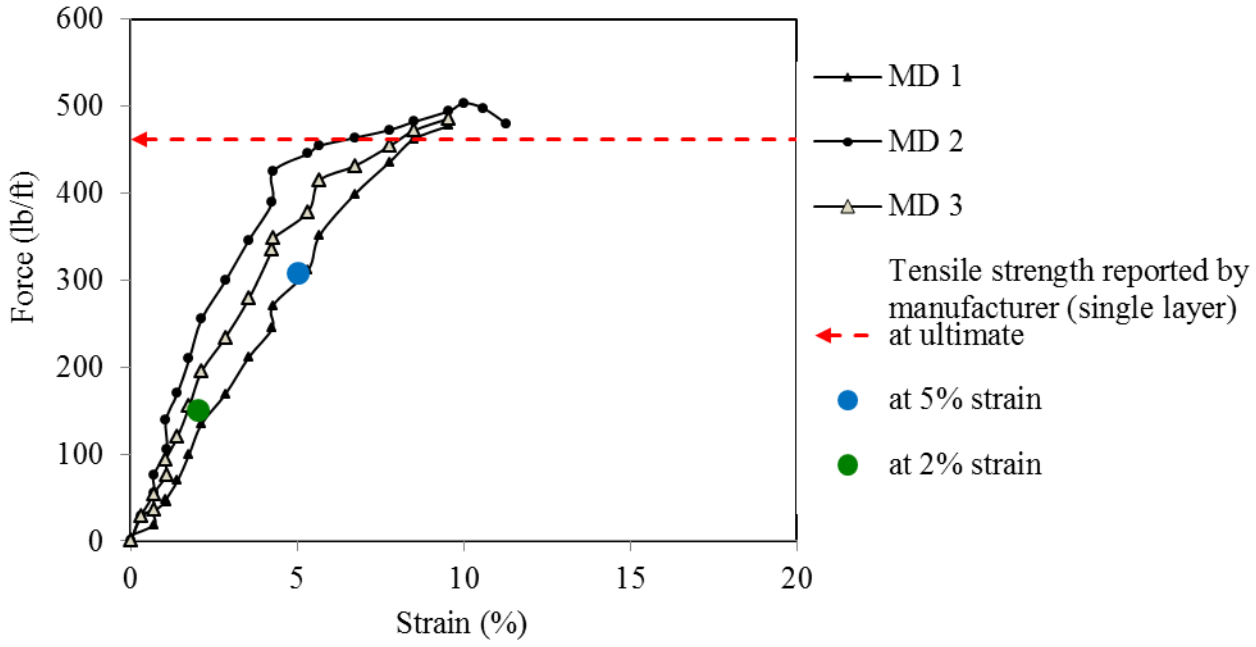

Figure 53. Tensile strength test results of EGG2 (single layer) geogrid in machine direction

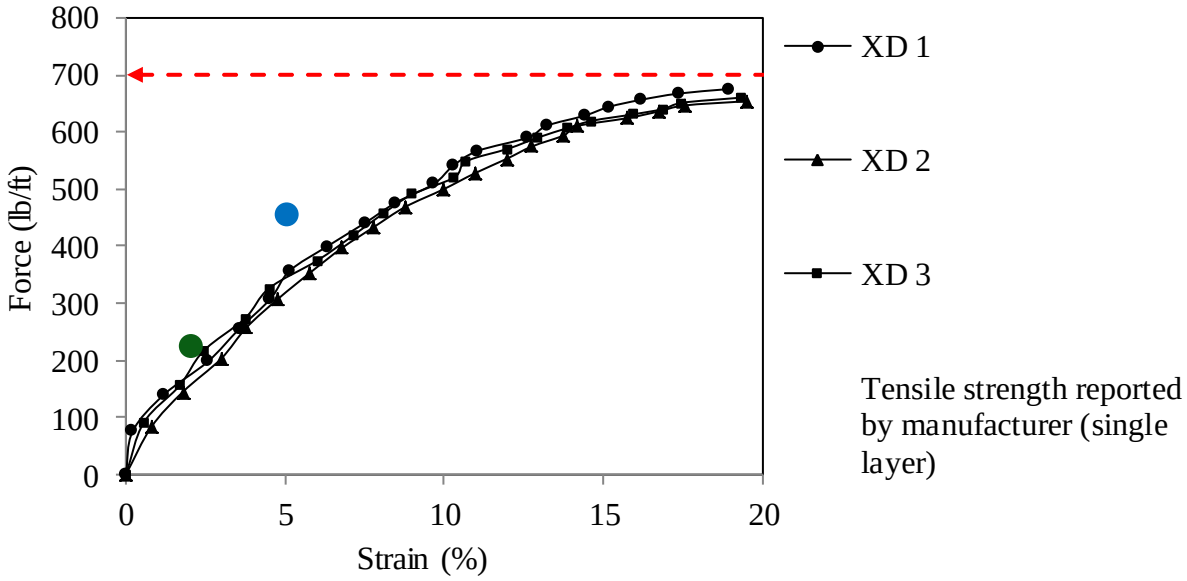

Figure 54. Tensile strength test results of EGG2 (single layer) geogrid in cross-machine direction

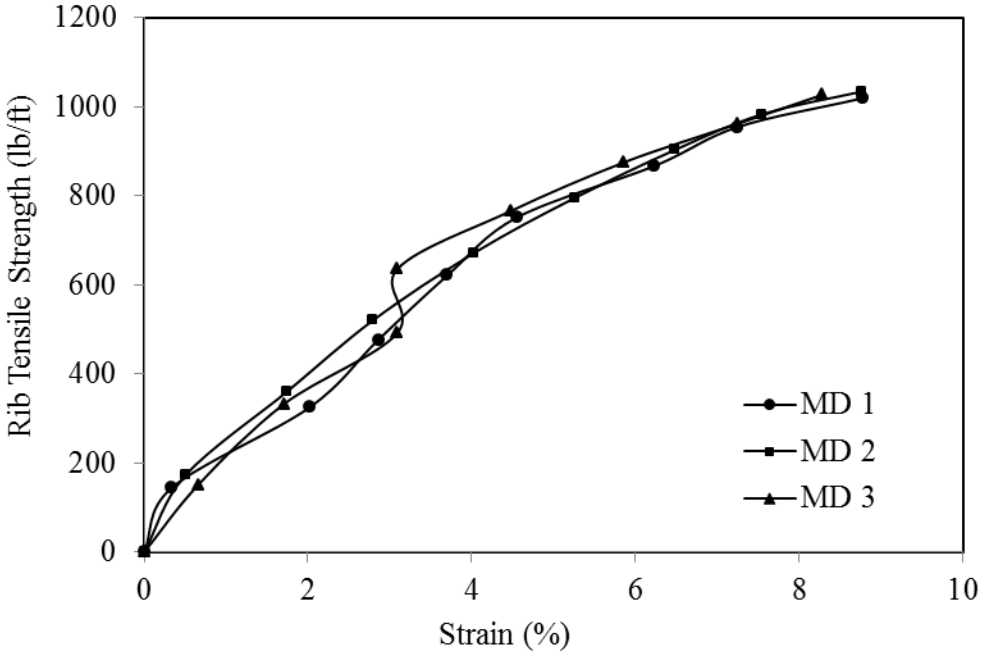

Figure 55. Tensile strength test results of EGG3 geogrid in machine direction

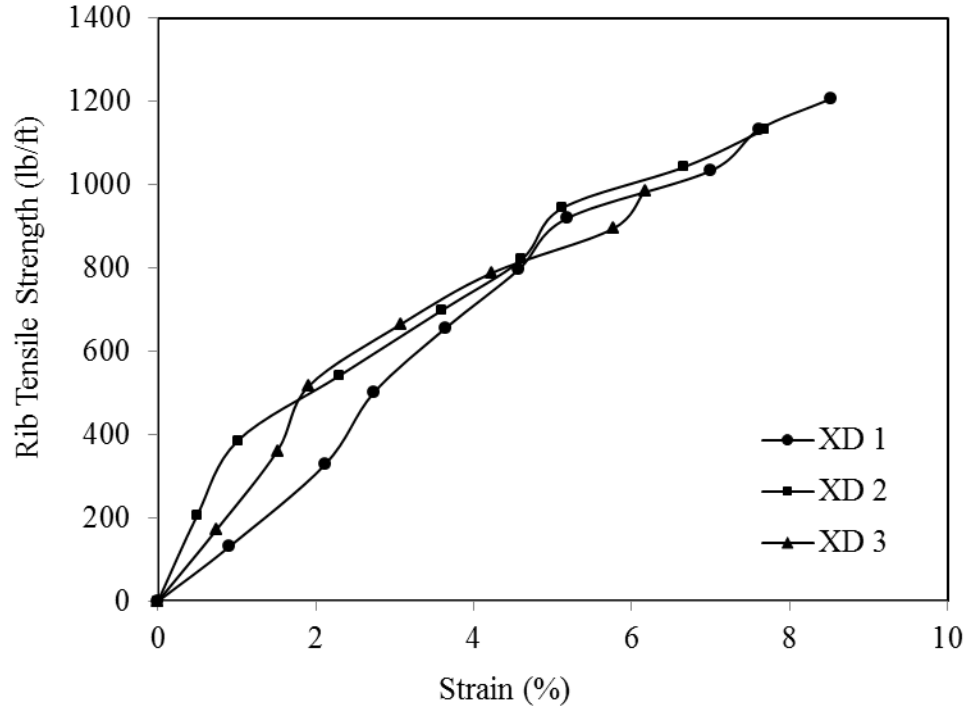

Figure 56. Tensile strength test results of EGG3 geogrid in cross-machine direction

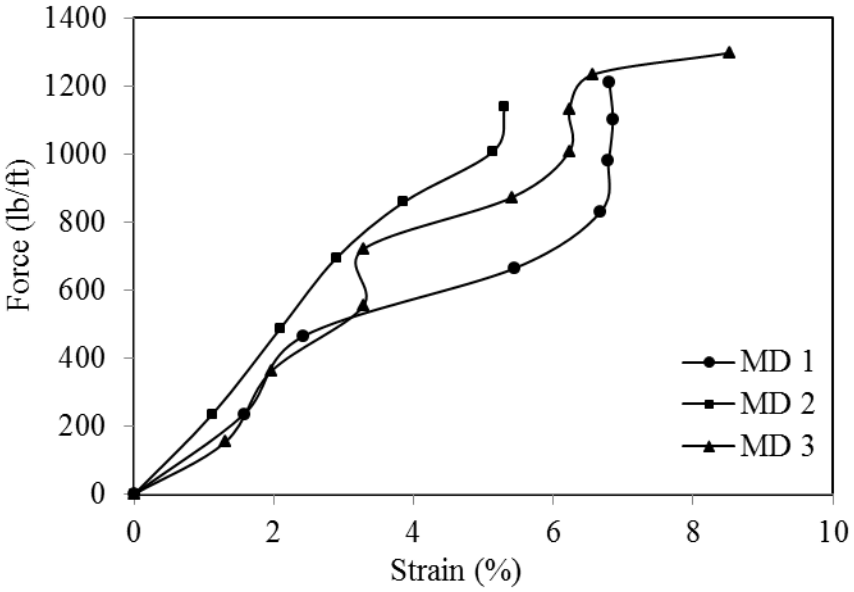

Figure 57. Tensile strength test results of EGG4 geogrid in machine direction

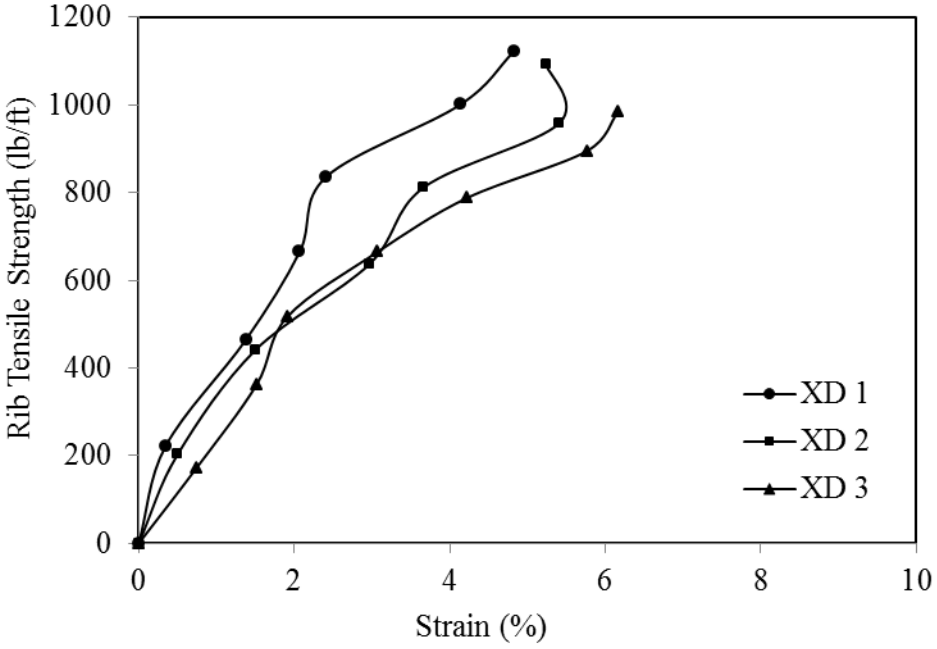

Figure 58. Tensile strength test results of EGG4 geogrid in cross-machine direction

Rib tensile strength values at 2% strain in MD and XD are summarized in **Table 9** and **Table 10**, respectively. In **Table 9**, the 2% rib strength values of the extruded biaxial geogrids (i.e. EGG1, WGG1, WGG2 and EB2) from our lab tests are slightly higher than the MARV (Minimum Average Roll Value) values reported by the corresponding manufacturers. This is not unexpected because the MARV values theoretically represent two standard deviations below the mean value of a large population of samples with an assumed bell-curve distribution (e.g. Koerner 2005). The FHWA guidelines (Holtz et al. 2008) also stipulate that the test results from any sampled roll in a lot should meet or exceed the minimum values reported by the manufacturers. The overall summary of the rib strength test results for all geogrids tested are given in **Table 9** through **Table 14**.

Table 9. Summary of rib tensile strength values at 2% strain in machine direction

Geogrid	Type	2% Rib Strength in Machine Direction (lb/ft)						
		MD 1	MD 2	MD 3	Mean (μ)	Standard Deviation (σ)	Co-efficient of Variation, COV (%)	MARV value from manufacturer
EGG1	S_RS_J Biaxial Extruded	698.63	1095.89	753.42	849.31	175.78	20.70	410.96
WGG1	S_RS_J Biaxial Woven	616.44	616.44	595.89	609.59	9.69	1.59	500.00
WGG2	S_RS_J Biaxial Woven	[1301]	958.90	684.93	821.92	136.99	16.67	500.00
WGG3	S_RW_J Biaxial woven	616.44	684.93	582.19	627.85	42.71	6.80	527.40
KGG1	S_RW_J Biaxial Knitted	410.96	479.45	479.45	456.62	32.29	7.07	349.31
EGG2 (single layer)	W_RS_J Biaxial Extruded	125.34	239.73	171.23	178.77	47.00	26.29	150.68
EGG3	S_RS_J Triaxial Extruded	335.62	356.16	397.26	363.01	25.63	7.06	NP
EGG4	S_RS_J Triaxial Extruded	479.45	342.47	376.71	399.54	58.21	14.57	NP

Notes (see **Figure 4**):
S_RS_J: Strong Rib Strong Junction
S_RW_J: Strong Rib Weak Junction
W_RS_J: Weak Rib Strong Junction
NP: Not provided by the manufacturer
[---] Outlier value

Table 10. Summary of rib tensile strength values at 2% strain in cross machine direction

Geogrid	Type	2% Rib Strength in Cross-Machine Direction (lb/ft)							
		XD 1	XD 2	XD 3	XD 4	Mean (μ)	Standard Deviation (σ)	Co-efficient of Variation, COV (%)	MARV value from manufacturer
EGG1	S_RS_J Biaxial Extruded	1506.85	1520.54	1095.89		1374.43	197.04	14.34	616.44
WGG1	S_RS_J Biaxial Woven	616.44	684.93	684.93		662.10	32.29	4.88	500.00
WGG2	S_RS_J Biaxial Woven	821.92	547.94	410.96	[205]	593.61	170.85	28.78	746.57
WGG3	S_RW_J Biaxial woven	753.42	753.42	890.41		799.09	64.58	8.08	575.34
KGG1	S_RW_J Biaxial Knitted	376.71	377.40	376.03	376.71	376.71	0.48	0.13	301.37
EGG2 (single layer)	W_RS_J Biaxial Extruded	178.08	152.74	178.08		169.63	11.95	7.04	226.03
EGG3	S_RS_J Triaxial Extruded	308.22	500.00	527.40		445.20	97.51	21.90	NP
EGG4	S_RS_J Triaxial Extruded	513.70	513.70	630.14		552.51	54.89	9.93	NP

Notes:
S_RS_J: Strong Rib Strong Junction
S_RW_J: Strong Rib Weak Junction
W_RS_J: Weak Rib Strong Junction
NP: Not provided by the manufacturer
[---] Outlier value

Table 11. Summary of rib tensile strength values at 5% strain in machine direction

Geogrid	Type	5% Rib Strength in Machine Direction (lb/ft)						
		MD 1	MD 2	MD 3	Mean (μ)	Standard Deviation (σ)	Co-efficient of Variation, COV (%)	MARV value from manufacturer
EGG1	S_RS_J Biaxial Extruded	1458.90	1589.04	1643.83	1563.92	77.56	4.96	808.22
WGG1	S_RS_J Biaxial Woven	1164.38	1232.87	1232.87	1210.04	32.29	2.67	917.81
WGG2	S_RS_J Biaxial Woven	[2328]	1917.80	1780.82	1849.31	68.49	3.70	917.81
WGG3	S_RW_J Biaxial woven	1013.70	1109.59	1109.59	1077.62	45.20	4.19	787.67
KGG1	S_RW_J Biaxial Knitted	616.44	623.29	616.44	618.72	3.23	0.52	623.29
EGG2 (single layer)	W_RS_J Biaxial Extruded	301.37	438.36	363.01	367.58	56.02	15.24	308.22
EGG3	S_RS_J Triaxial Extruded	767.12	787.67	808.22	787.67	16.78	2.13	NP
EGG4	S_RS_J Triaxial Extruded	616.44	821.92	993.15	810.50	154.00	19.00	NP

Notes:
S_RS_J: Strong Rib Strong Junction
S_RW_J: Strong Rib Weak Junction
W_RS_J: Weak Rib Strong Junction
NP: Not provided by the manufacturer
[---] Outlier value

Table 12. Summary of rib tensile strength values at 5% strain in cross machine direction

Geogrid	Type	5% Rib Strength in Cross-Machine Direction (lb/ft)							
		XD 1	XD 2	XD 3	XD 4	Mean (μ)	Standard Deviation (σ)	Co-efficient of Variation, COV (%)	MARV value from manufacturer
EGG1	S_RS_J Biaxial Extruded	2273.97	2410.95	2054.79		2246.57	146.69	6.53	1342.46
WGG1	S_RS_J Biaxial Woven	1630.13	1369.86	1506.85		1502.28	106.31	7.08	917.81
WGG2	S_RS_J Biaxial Woven	1849.31	1917.80	2054.79	2054.79	1969.17	88.98	4.52	938.35
WGG3	S_RW_J Biaxial Woven	1082.19	1089.04	1095.89		1089.04	5.59	0.51	1041.09
KGG1	S_RW_J Biaxial Knitted	513.70	479.45	547.94	527.40	517.12	24.93	4.82	424.66
EGG2 (single layer)	W_RS_J Biaxial Extruded	356.16	315.07	342.47		337.90	17.09	5.06	458.90
EGG3	S_RS_J Triaxial Extruded	821.92	890.41	924.66		878.99	42.71	4.86	NP
EGG4	S_RS_J Triaxial Extruded	821.92	924.66	1130.13		958.90	128.14	13.36	NP

Notes:
S_RS_J: Strong Rib Strong Junction
S_RW_J: Strong Rib Weak Junction
W_RS_J: Weak Rib Strong Junction
NP: Not provided by the manufacturer

Table 13. Summary of ultimate rib tensile strength values in machine direction

Geogrid	Type	Ultimate Rib Strength in Machine Direction (lb/ft)						
		MD 1	MD 2	MD 3	Mean (μ)	Standard Deviation (σ)	Co-efficient of Variation, COV (%)	MARV value from manufacturer
EGG1	S_RS_J Biaxial Extruded	1798.63	1767.12	1849.31	1805.02	33.86	1.88	NP
WGG1	S_RS_J Biaxial Woven	4383.55	4445.88	4315.06	4381.50	53.43	1.22	2000.00
WGG2	S_RS_J Biaxial Woven	2513.01	2876.71	2097.94	2495.88	318.16	12.75	2000.00
WGG3	S_RW_J Biaxial woven	3210.27	2894.51	2943.14	3015.98	138.81	4.60	2390.41
KGG1	S_RW_J Biaxial Knitted	2191.78	2260.27	2054.79	2168.95	85.43	3.94	1876.71
EGG2 (single layer)	W_RS_J Biaxial Extruded	477.40	502.05	410.96	463.47	38.47	8.30	461.64
EGG3	S_RS_J Triaxial Extruded	1027.40	1027.40	1034.24	1029.68	3.23	0.31	NP
EGG4	S_RS_J Triaxial Extruded	1164.38	1232.87	1301.37	1232.87	55.92	4.54	NP

Notes:
S_RS_J: Strong Rib Strong Junction
S_RW_J: Strong Rib Weak Junction
W_RS_J: Weak Rib Strong Junction
NP: Not provided by the manufacturer

Table 14. Summary of ultimate rib tensile strength values in cross machine direction

Geogrid	Type	Ultimate Rib Strength in Cross-Machine Direction (lb/ft)							
		XD 1	XD 2	XD 3	XD 4	Mean (μ)	Standard Deviation (σ)	Co-efficient of Variation, COV (%)	MARV value from manufacturer
EGG1	S_RS_J Biaxial Extruded	2503.42	2652.73	2739.72		2631.96	97.58	3.71	NP
WGG1	S_RS_J Biaxial Woven	2494.52	2173.97	1917.80		2195.43	235.93	10.75	2000.00
WGG2	S_RS_J Biaxial Woven	3082.19	2415.06	2607.53	2808.21	2728.25	247.15	9.06	3999.99
WGG3	S_RW_J Biaxial woven	3972.59	4168.48	4105.47		4082.18	81.65	2.00	3869.85
KGG1	S_RW_J Biaxial Knitted	1890.41	2027.39	1917.80	1917.80	1938.35	52.61	2.71	1876.71
EGG2 (single layer)	W_RS_J Biaxial Extruded	675.34	654.11	660.27		663.24	8.92	1.34	702.05
EGG3	S_RS_J Triaxial Extruded	958.90	1130.13	1198.63		1095.89	100.82	9.20	NP
EGG4	S_RS_J Triaxial Extruded	958.90	1095.89	1130.13		1061.64	73.98	6.97	NP

Notes:
S_RS_J: Strong Rib Strong Junction
S_RW_J: Strong Rib Weak Junction
W_RS_J: Weak Rib Strong Junction
NP: Not provided by the manufacturer

3. Pullout tests

3.1. General

Geogrids used in aggregate base reinforcement applications can be subjected to significant compaction-induced stresses during the construction stage. Pullout tests can provide a methodic means to study geogrid-aggregate interactions at different stress levels under controlled conditions. In addition, pullout tests can help to isolate the tensile performance of geogrids in the anchorage zone outside the pressure bulb of the tire from its out-of-plane membrane behavior when the geogrid is subjected to the vertical load of traffic (Hatami et al. 2011a).

3.2. Fabrication of a new pullout box

A new pullout test box with the dimensions 6 ft (H) × 3 ft (W) × 2.5 ft (H) was fabricated in the OU Fears laboratory to carry out pullout tests on geogrids in aggregates (**Figure 59**).

Figure 59. One of the two pullout test boxes at the OU Fears laboratory

3.3. Pullout test setup and procedure

A total of 33 pullout tests were carried out on the eight geogrid products listed in **Table 2** and **Table 3** as per the ASTM D6706 test protocol (ASTM 2009). The pullout tests were carried out in ODOT Type-A aggregate which is a widely used dense-graded aggregate in ODOT projects. Most of the tests were carried out at 69 psf, 138 psf and 240 psf overburden pressures. Additional tests were carried out at other overburden pressures (e.g. 101 psf and 112 psf) to improve the accuracy of the results. These overburden pressures on the geogrid-aggregate interface were primarily due to the weight of a compacted aggregate layer of different thicknesses on the top of the interface in the pullout box. The overburden pressures 69 psf, 101 psf, 112 psf and 138 psf were generated using aggregate thicknesses of 6 inches, 9 inches, 10 inches and 12 inches, respectively. In the case of the 240 overburden pressure, an airbag was used on the top of a 12 inch-thick aggregate layer to apply the additional pressure needed. These pressure levels resemble field conditions (outside the tire pressure bulb) where pullout (as opposed to geogrid rupture) would be the likely failure mechanism. Pullout tests on biaxial and triaxial geogrid specimens were carried out in the machine direction. However, due to the distinctive geometry of triaxial products (i.e. EGG3 and EGG4), the MD geogrid ribs are actually at 30^{o} angles diagonally from the machine direction on both sides (**Figure 78**).

Different steps of the pullout tests are depicted in **Figure 60** through **Figure 69**. The pullout force was applied to the geogrid specimen using a 4.5-kip, servo-controlled hydraulic actuator. The geogrid specimen was connected to the actuator through a roller clamp (**Figure 69**). Displacement of the geogrid specimen was measured and recorded in four different locations along their length using wire potentiometers (**Figure 64**).

Figure 60. Pullout test box before placing the aggregate

Figure 61. Compacted aggregate in the pullout box (the 8 inch-wide lower steel sleeve can be seen in the foreground)

Figure 62. Drilling the geogrid junctions to connect the extensometers

Figure 63. Connecting wires to geogrid specimen

Figure 64. Tell-tale wires connected to wire potentiometers

Figure 65. A separator geotextile is placed on the top of the aggregate

Figure 66. An earth pressure cell is placed on a 1 inch sand layer on the top of the aggregate

Figure 67. Air bag is used (if necessary) to generate additional overburden pressure on the geogrid-aggregate interface

Figure 68. The pullout test box is closed before the test

Figure 69. The geogrid is connected to the roller clamp

Figure 70 through **Figure 82** show condition of geogrid products related to some pullout tests.

Figure 70. EGG1 geogrid after pullout test

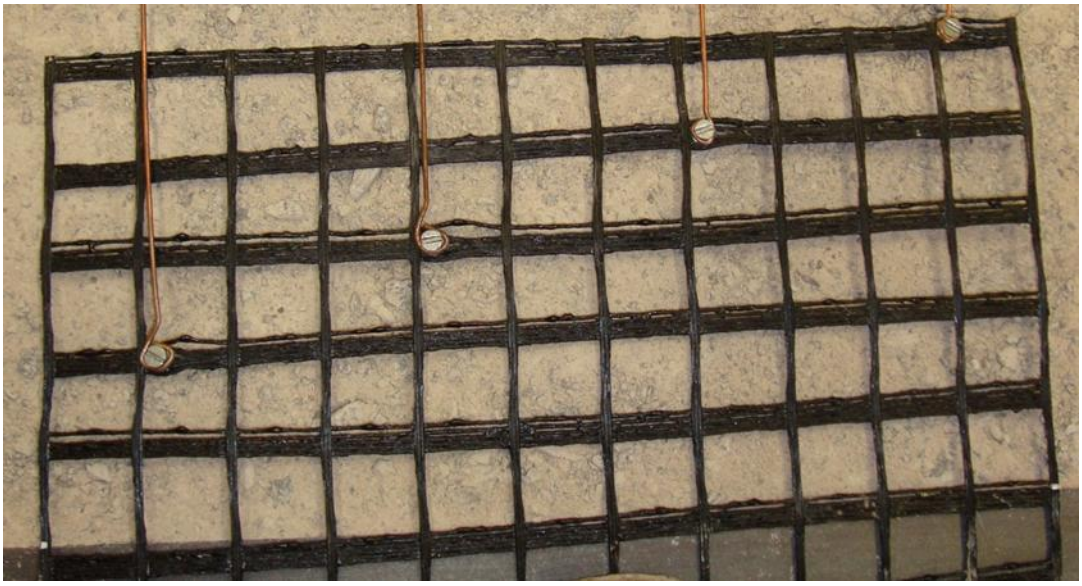

Figure 71. WGG2 geogrid before pullout test

Figure 72. WGG2 geogrid after pullout test

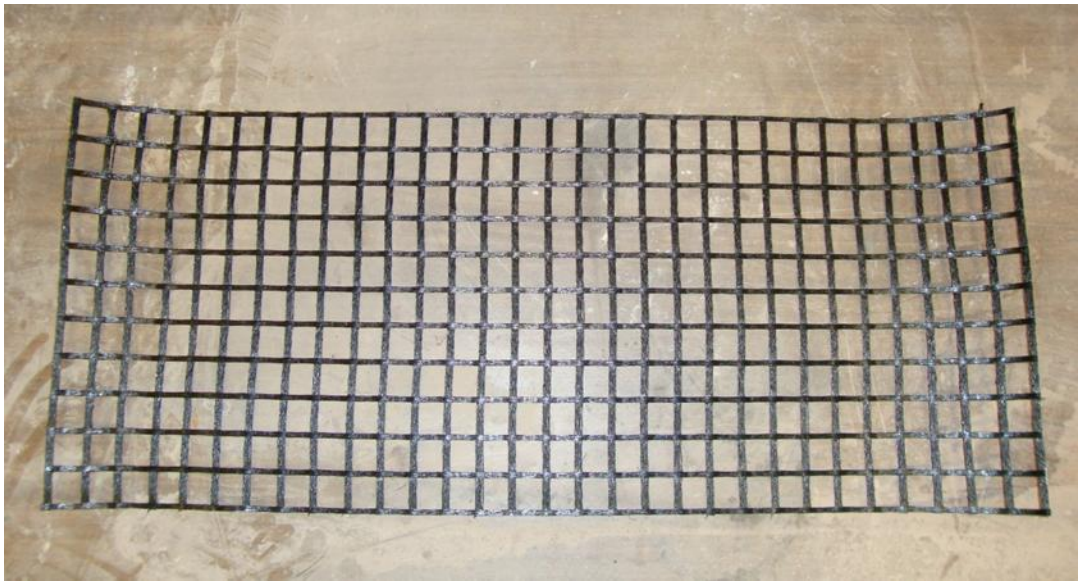

Figure 73. WGG3 geogrid before pullout test

Figure 74. WGG3 geogrid after pullout test

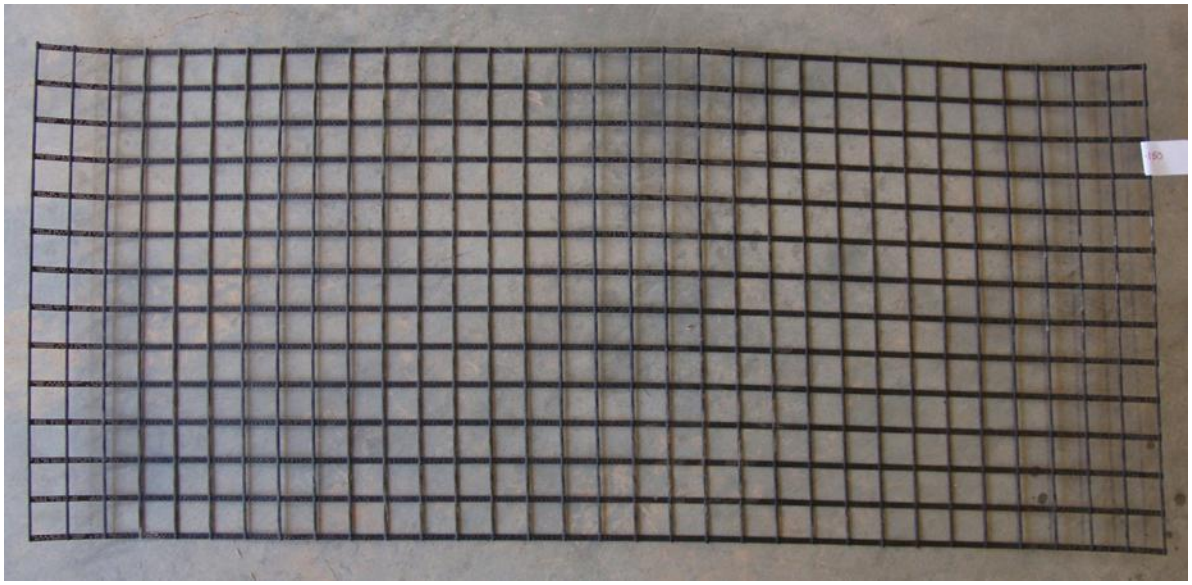

Figure 75. KGG1 geogrid before pullout test

Figure 76. KGG1 geogrid after pullout test

Three pullout tests were carried out on EGG2 (single layer) geogrid with a 2-ft embedded length at 69 psf, 101 psf and 138 psf overburden pressures (**Figure 77**).

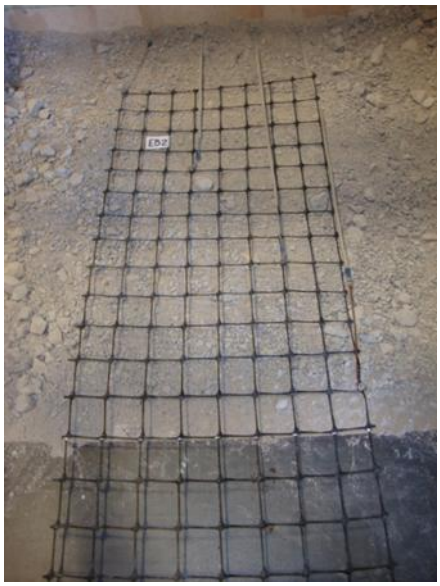

Figure 77. EGG2 geogrid before pullout test

Four pullout tests were carried out on EGG3 geogrid specimens (**Figure 78**). Three of the tests were carried out on 2-ft-long specimens subjected to 69 psf, 101 psf and 138 psf overburden pressures. One repeat test was carried out at 69 psf overburden pressure to improve the accuracy of the test data.

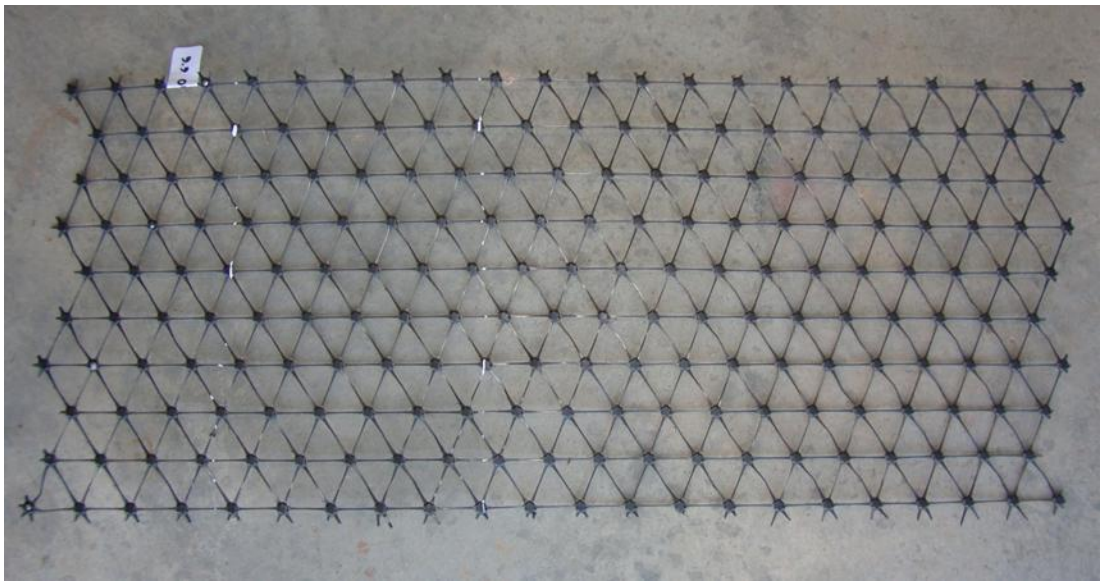

Figure 78. EGG3 geogrid before pullout test

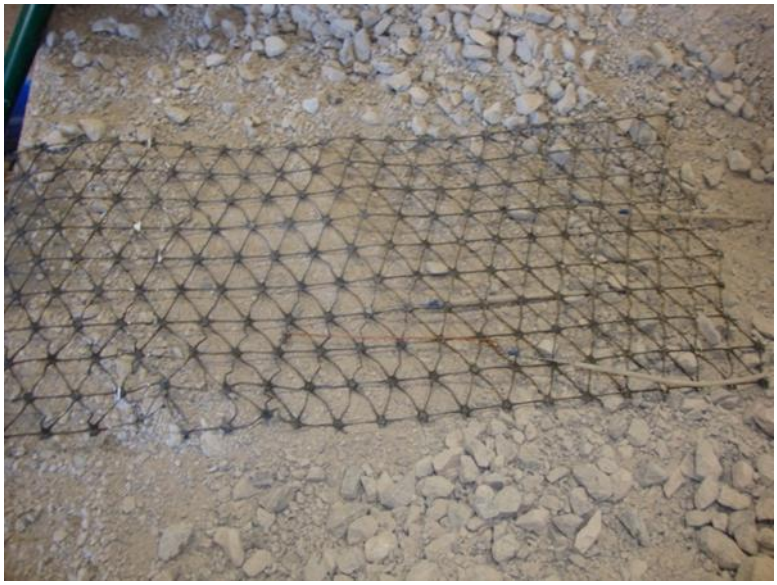

Figure 79. EGG3 geogrid after pullout test

Figure 80 shows an EGG4 geogrid sample which is prepared for pullout test. **Figure 81** and **Figure 82** show the condition of geogrid specimens after pullout tests subjected to 69 psf and 138 psf overburden pressures, respectively.

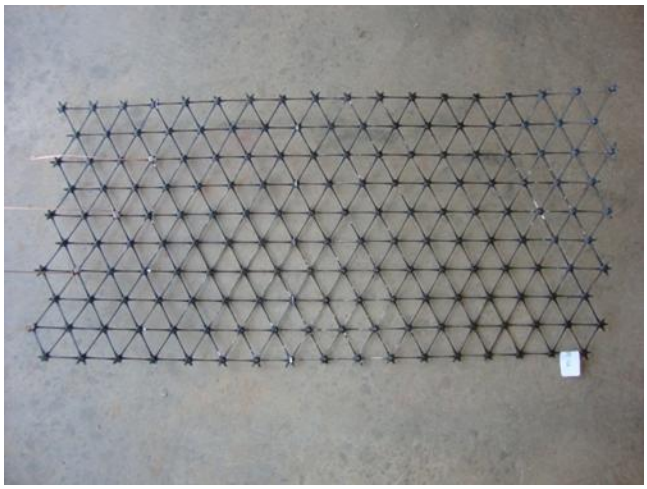

Figure 80. EGG4 geogrid before pullout test

Figure 81. EGG4 geogrid after pullout test subjected to 69 psf overburden pressure

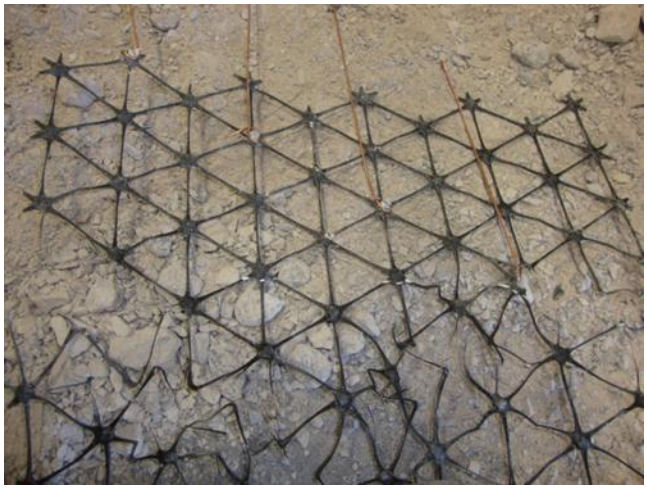

Figure 82. EGG4 geogrid after pullout test subjected to 138 psf overburden pressure

Two additional pullout tests were carried out on 2-ft-long (embedment length) EGG1 and WGG1 geogrid specimens at 69 psf overburden pressure. A summary of all pullout tests on geogrid products in this study is given in **Table 15**.

Table 15. Summary of pullout tests on geogrids in this study

Geogrid	Type	Pressure on Geogrid (psf)	Equivalent Aggregate Thickness (in)
EGG1	S_RS_J Biaxial Extruded	69	6
		138	12
		240	21
WGG1	S_RS_J Biaxial Woven	69	6
		138	12
		240	21
WGG2	S_RS_J Biaxial Woven	69	6
		103	9
		113	10
		138	12
		240	21
WGG3	S_RW_J Biaxial Woven	69	6
		103	9
		138	12
		240	22
KGG1	S_RW_J Biaxial Knitted	69	6
		138	12
		240	21
EGG2 (single layer)	W_RS_J Biaxial Extruded	69	6
		103	9
		138	12
EGG3	S_RS_J Triaxial Extruded	69	6
		103	9
		138	12
EGG4	S_RS_J Triaxial Extruded	69	6
		103	9
		138	12

Notes: S_RS_J: Strong Rib Strong Junction (**Figure 4**)
S_RW_J: Strong Rib Weak Junction
W_RS_J: Weak Rib Strong Junction

3.4. Pullout test results and analysis

Pullout responses of the geogrid products listed in **Table 15** subjected to different confining pressures are shown in **Figure 83** through **Figure 108**.

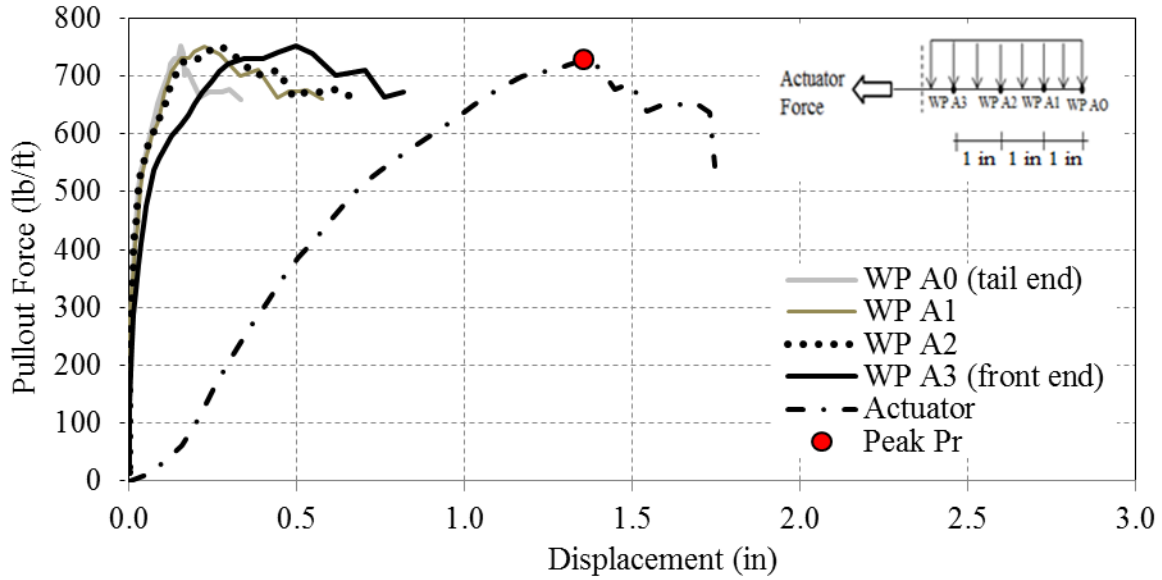

Figure 83. Pullout response results of EGG1 geogrid in ODOT Type-A aggregate subjected to 69 psf overburden pressure (WP: Wire-line Potentiometers)

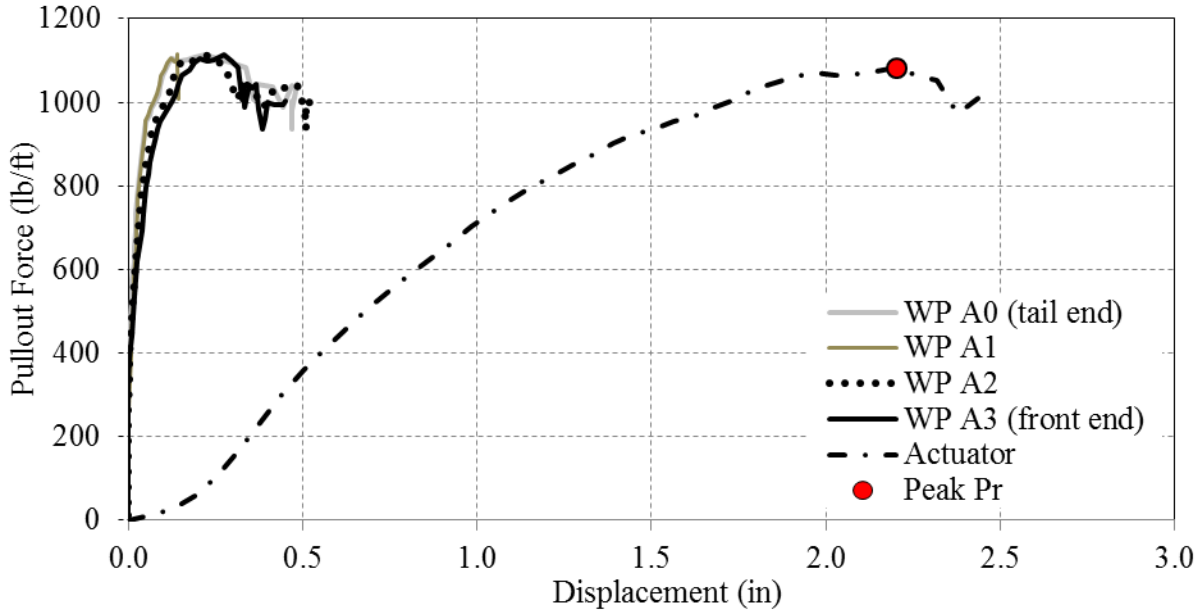

Figure 84. Pullout response results of EGG1 geogrid in ODOT Type-A aggregate subjected to 138 psf overburden pressure

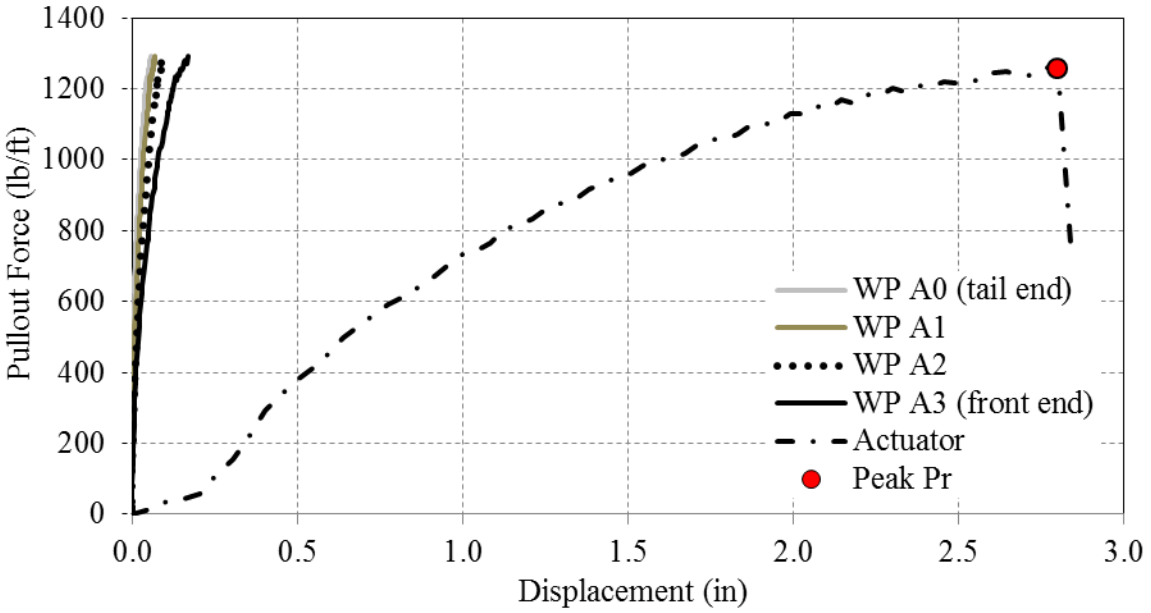

Figure 85. Pullout response results of EGG1 geogrid in ODOT Type-A aggregate subjected to 240 psf overburden pressure

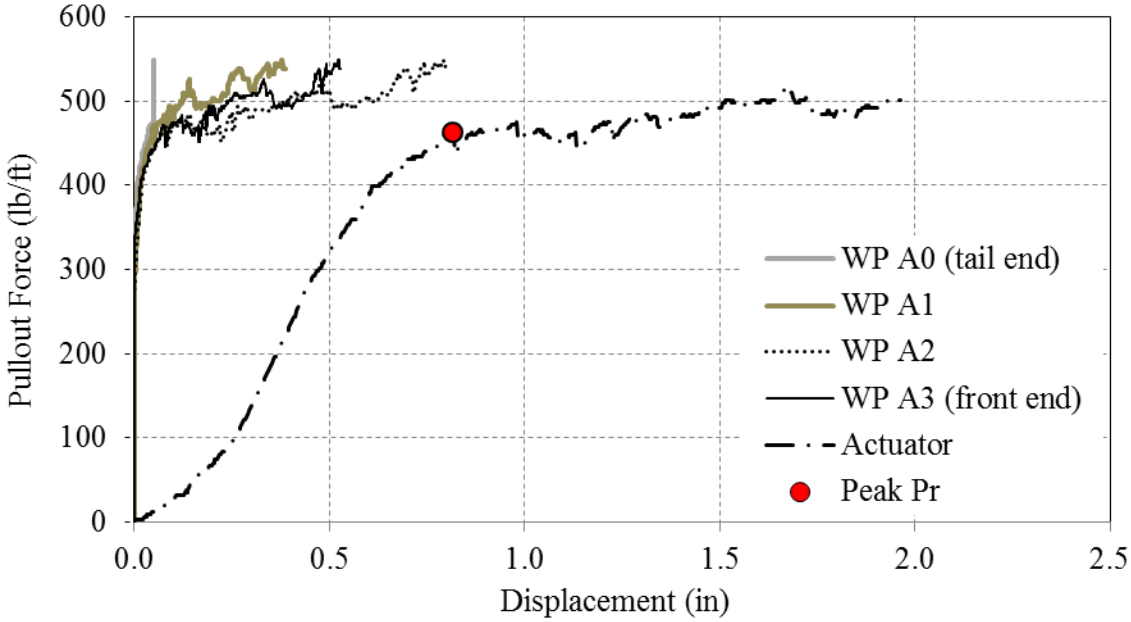

Figure 86. Pullout response results of WGG1 geogrid in ODOT Type-A aggregate subjected to 69 psf overburden pressure

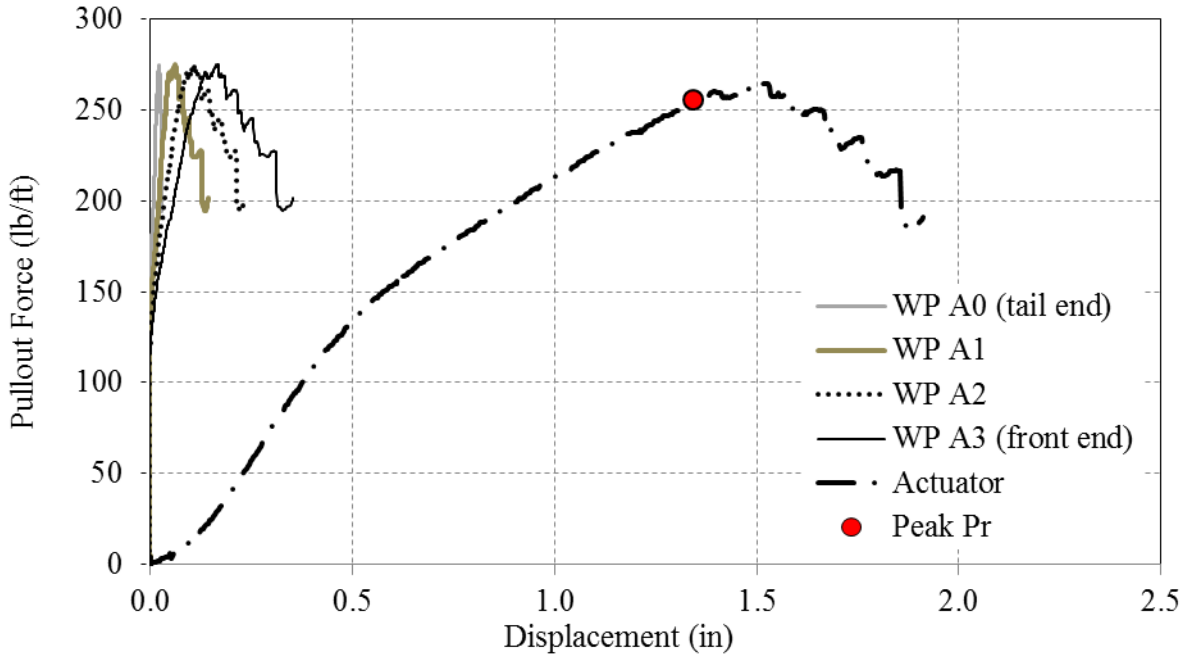

Figure 87. Pullout response results of WGG1 geogrid in ODOT Type-A aggregate subjected to 138 psf overburden pressure

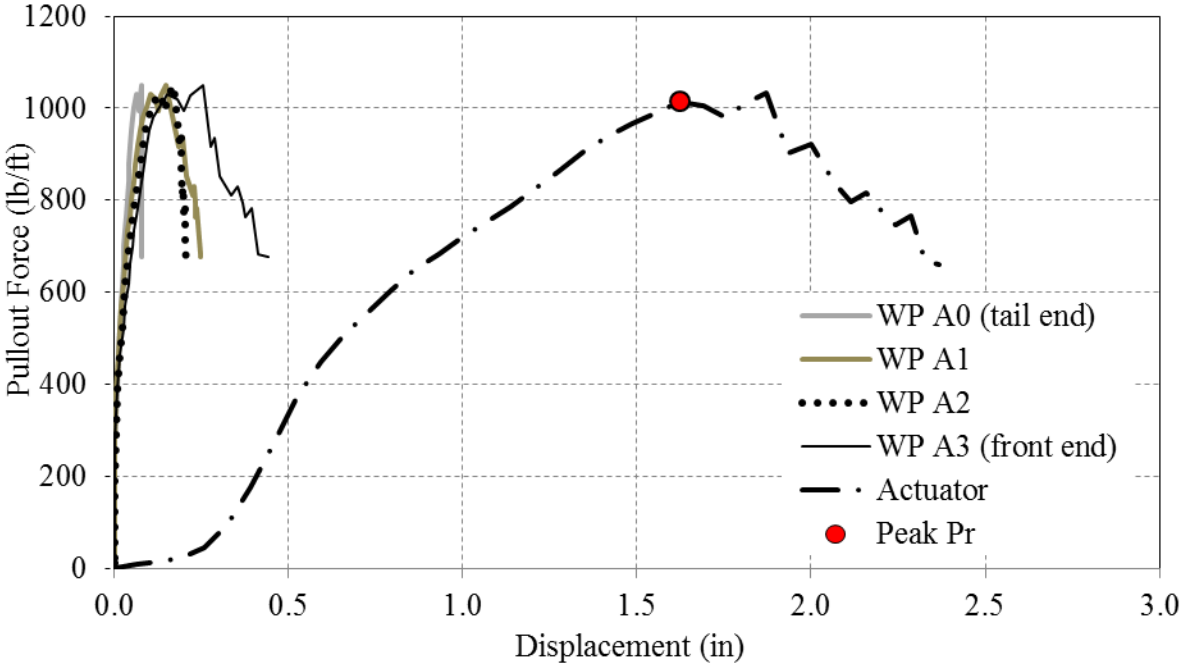

Figure 88. Pullout response results of WGG1 geogrid in ODOT Type-A aggregate subjected to 240 psf overburden pressure

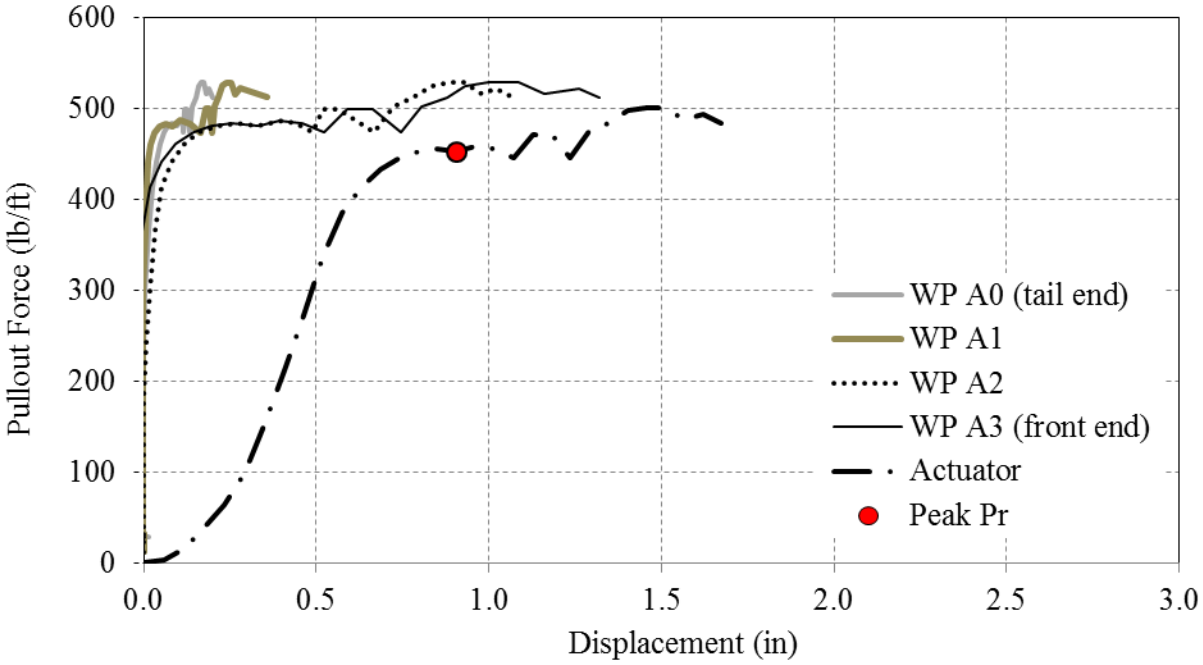

Figure 89. Pullout response results of WGG2 geogrid in ODOT Type-A aggregate subjected to 69 psf overburden pressure

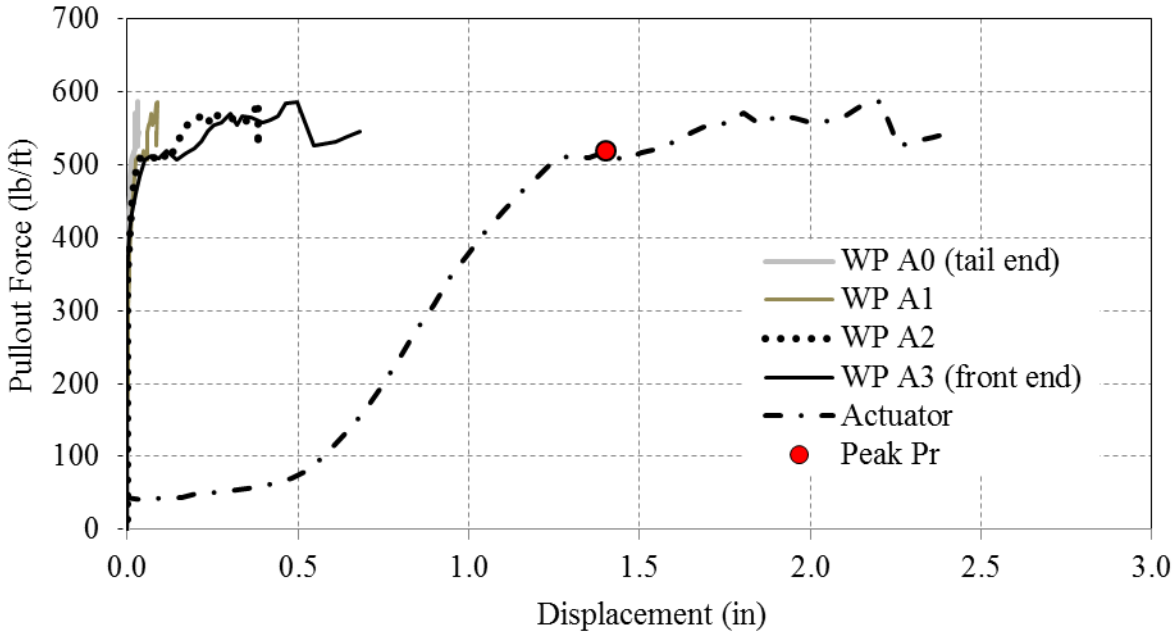

Figure 90. Pullout response results of WGG2 geogrid in ODOT Type-A aggregate subjected to 103 psf overburden pressure

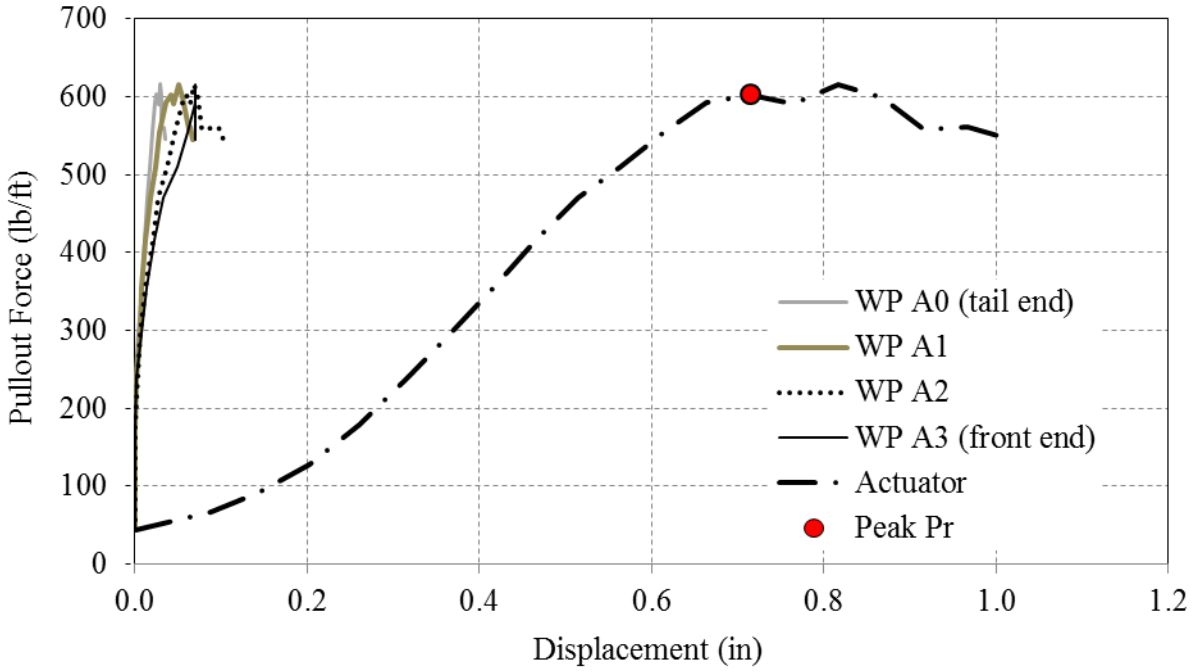

Figure 91. Pullout response results of WGG2 geogrid in ODOT Type-A aggregate subjected to 138 psf overburden pressure

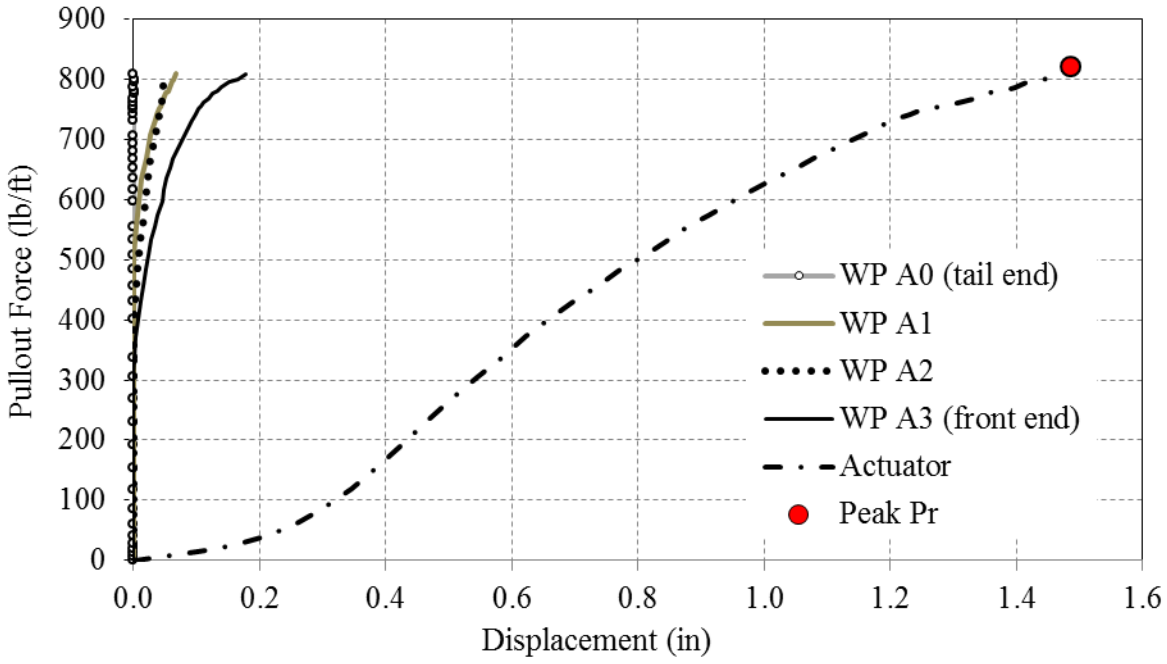

Figure 92. Pullout response results of WGG2 geogrid in ODOT Type-A aggregate subjected to 240 psf overburden pressure

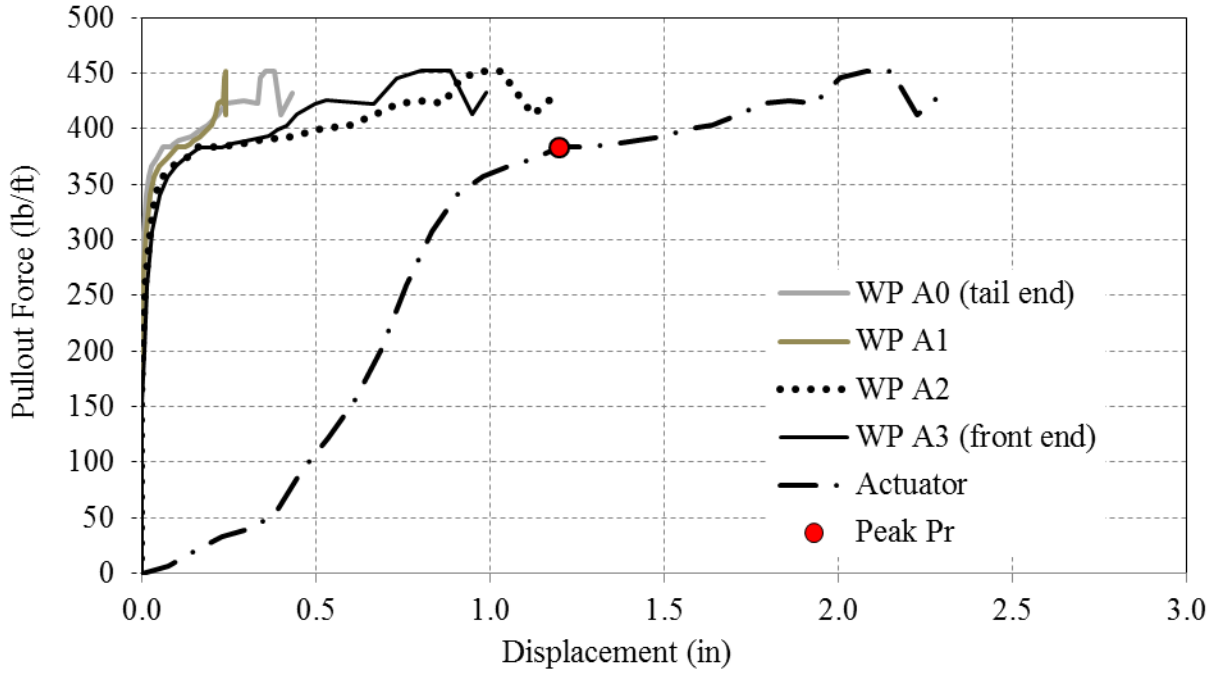

Figure 93. Pullout response results of WGG3 geogrid in ODOT Type-A aggregate subjected to 69 psf overburden pressure

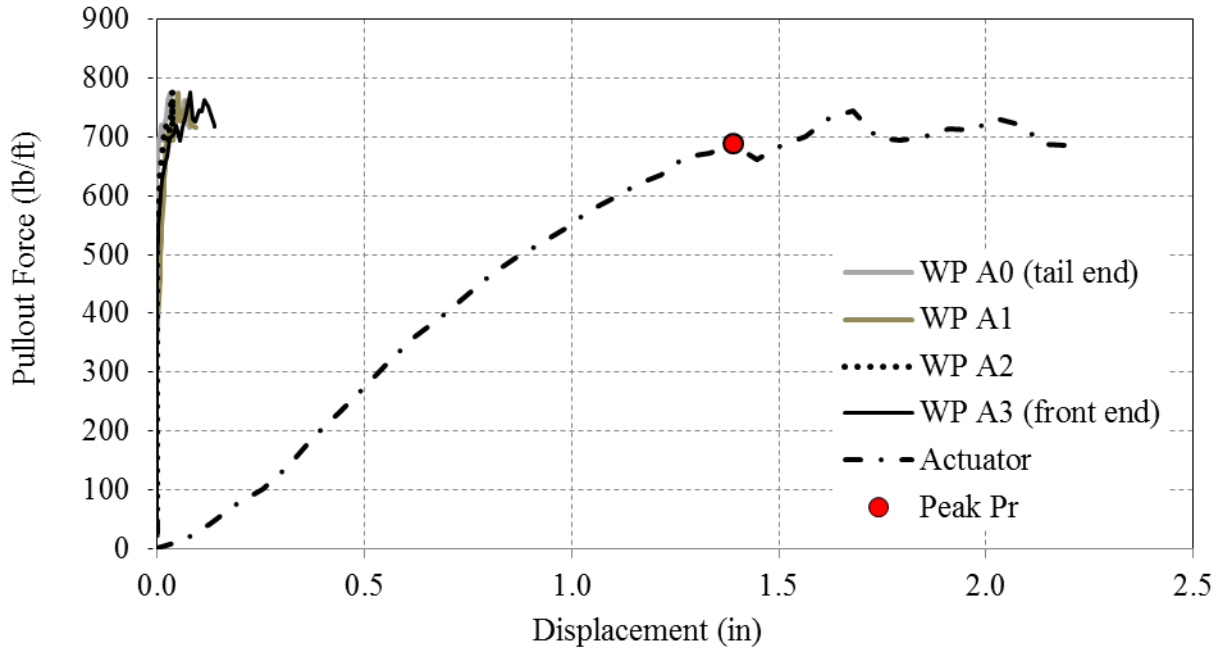

Figure 94. Pullout response results of WGG3 geogrid in ODOT Type-A aggregate subjected to 138 psf overburden pressure

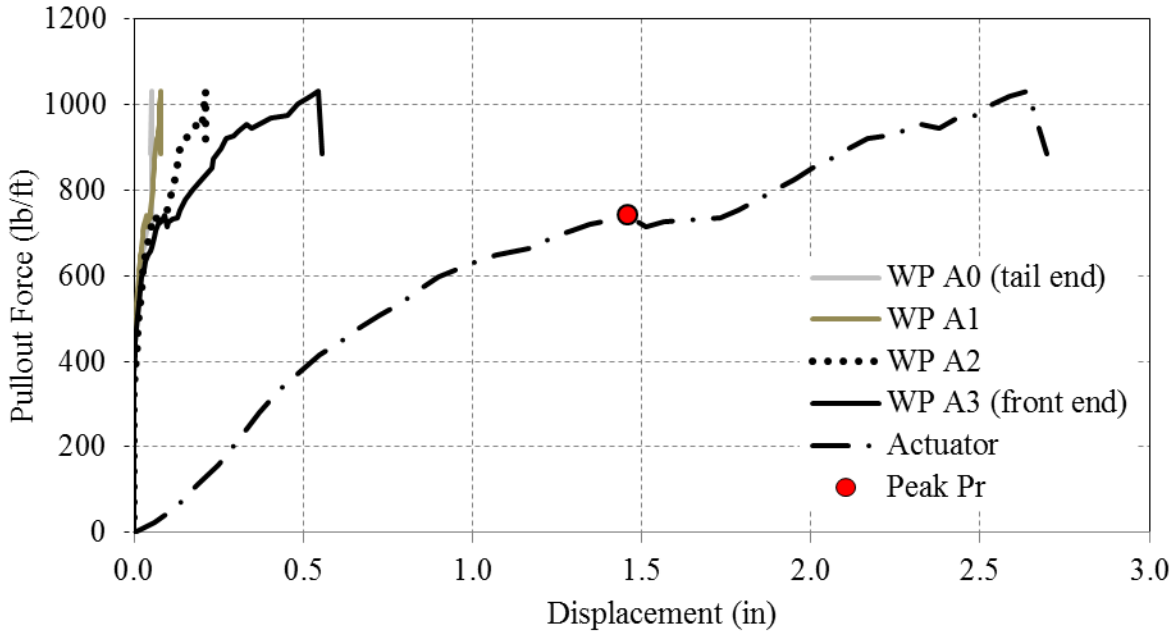

Figure 95. Pullout response results of WGG3 geogrid in ODOT Type-A aggregate subjected to 240 psf overburden pressure

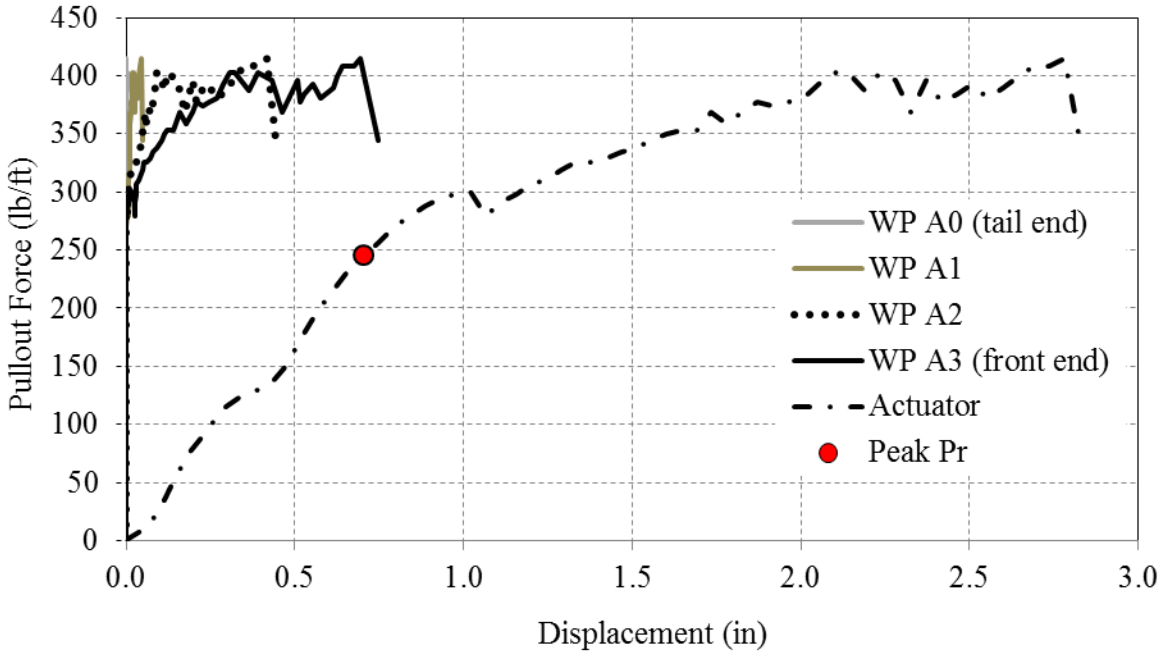

Figure 96. Pullout response results of KGG1 geogrid in ODOT Type-A aggregate subjected to 69 psf overburden pressure

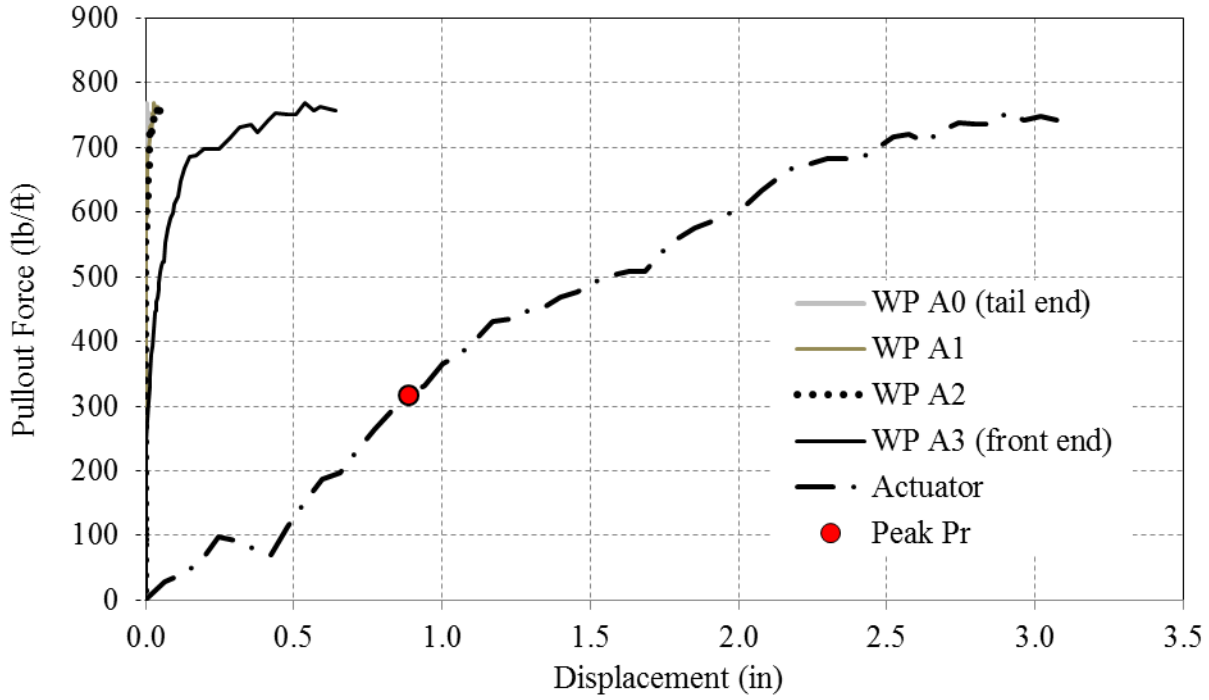

Figure 97. Pullout response results of KGG1 geogrid in ODOT Type-A aggregate subjected to 138 psf overburden pressure

After the pullout test on the KGG1 geogrid at 240 psf overburden pressure was completed (**Figure 98),** it was noticed that some junctions (especially those connected to the brass wires) had been ruptured. However, no ribs were found to have been ruptured. This failure pattern for the KGG1 geogrid is consistent with its classification in **Figure 4** as a comparatively weak-junction but strong-rib geogrid (**Section 2.1.2.** DOT agencies data**.**).

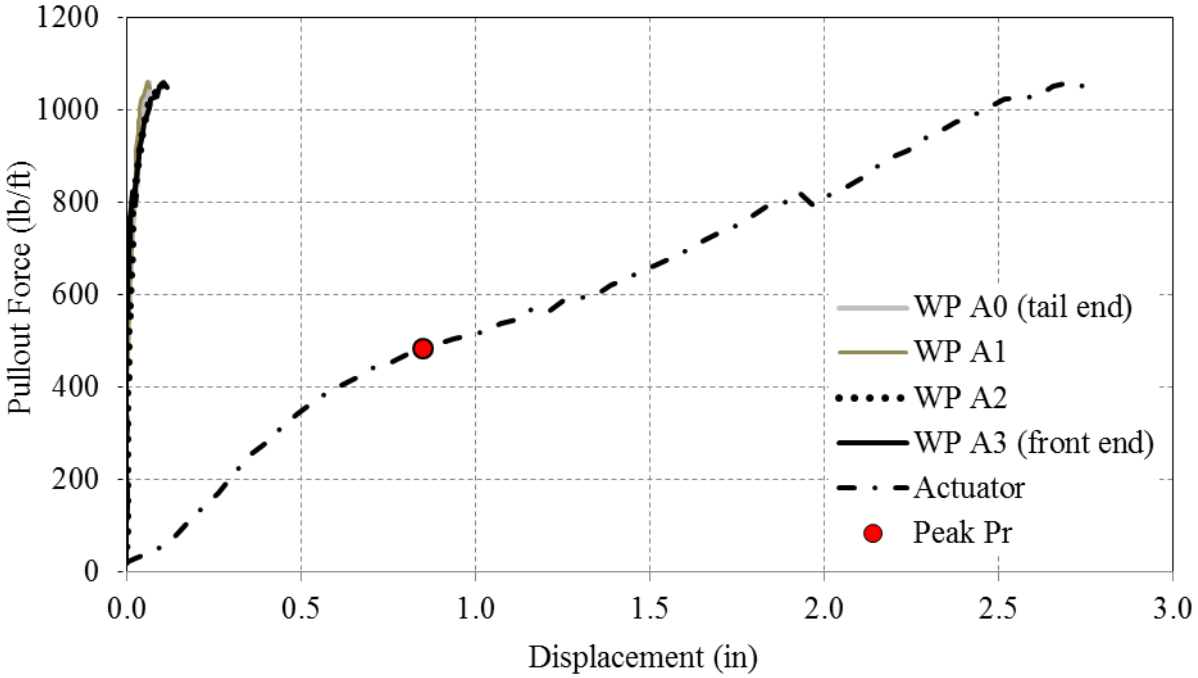

Figure 98. Pullout response results of KGG1 geogrid in ODOT Type-A aggregate subjected to 240 psf overburden pressure

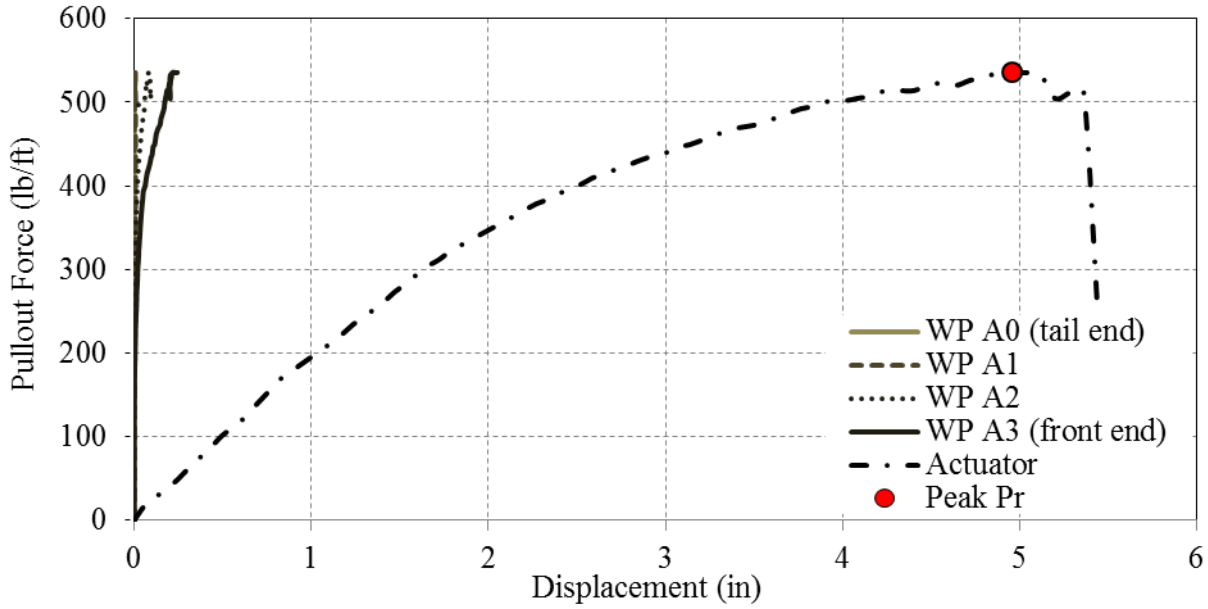

Figure 99. Pullout response results of EGG2 (single layer) geogrid in ODOT Type-A aggregate subjected to 103 psf overburden pressure

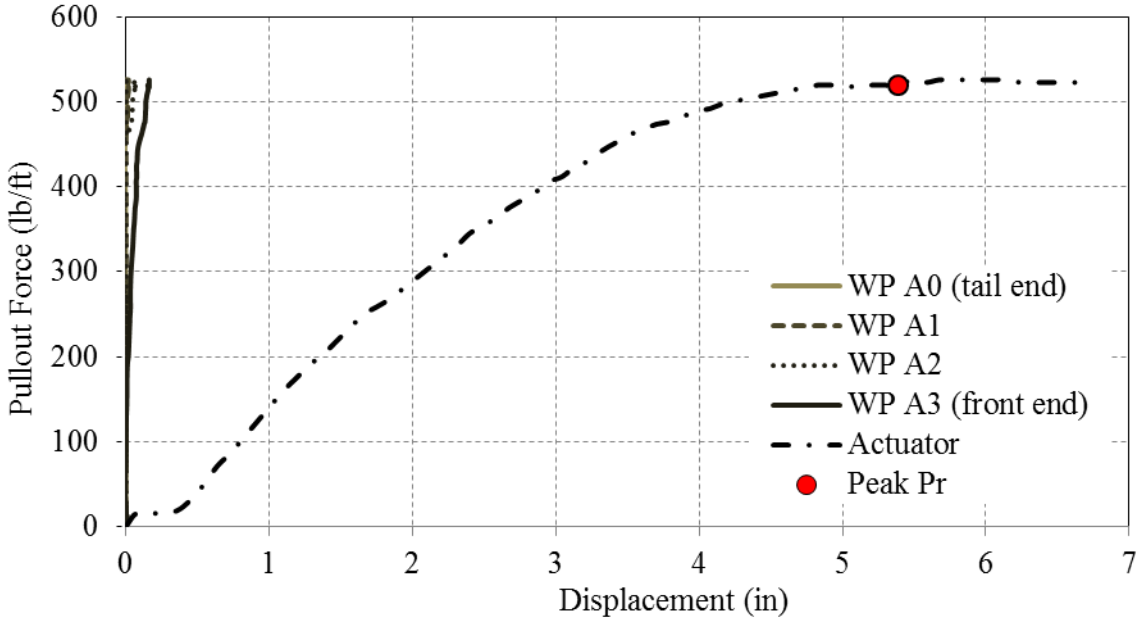

Figure 100. Pullout response results of EGG2 (single layer) geogrid in ODOT Type-A aggregate subjected to 138 psf overburden pressure

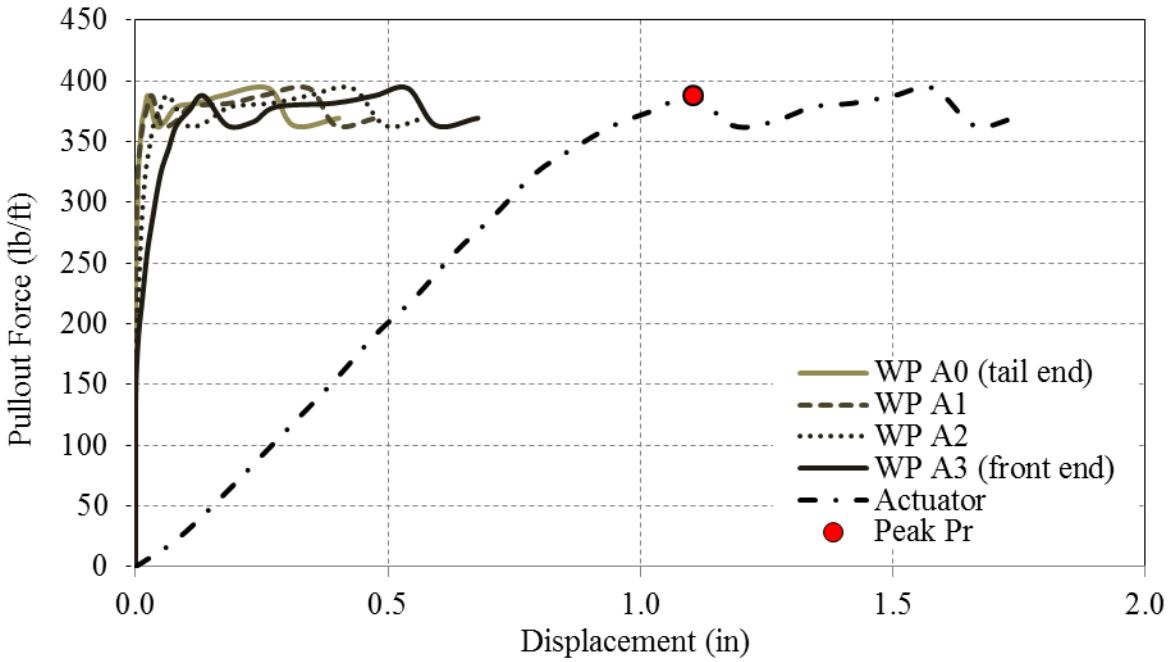

Figure 101. Pullout response results of EGG4 geogrid in ODOT Type-A aggregate subjected to 69 psf overburden pressure

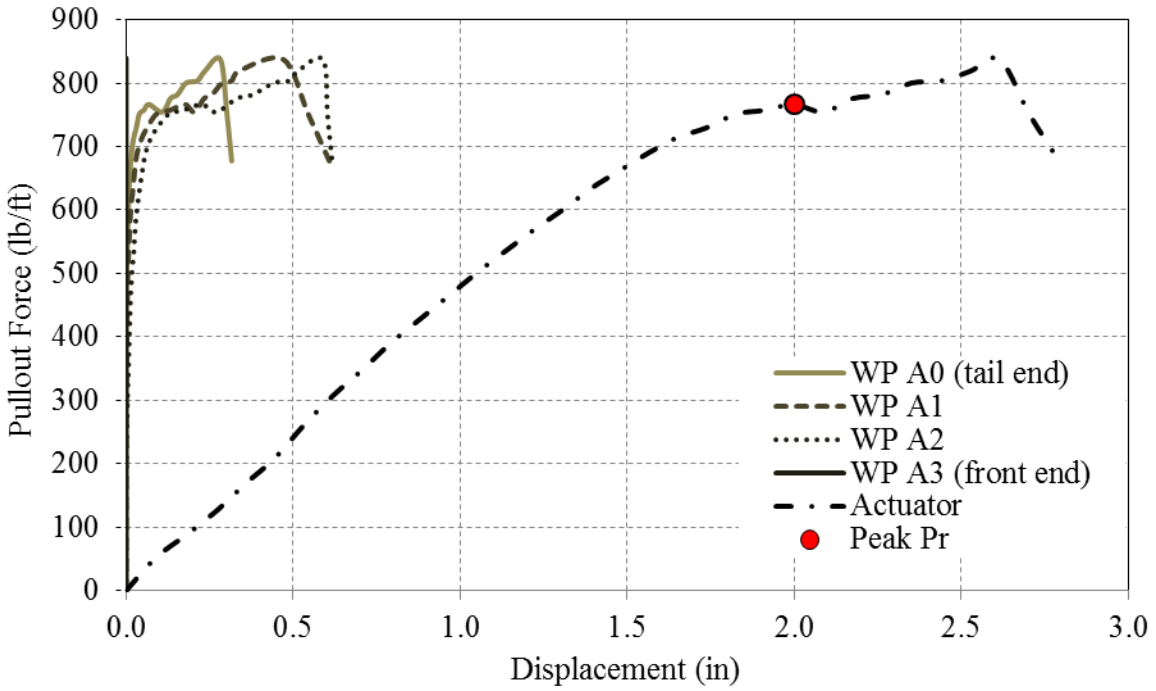

Figure 102. Pullout response results of EGG4 geogrid in ODOT Type-A aggregate subjected to 103 psf overburden pressure

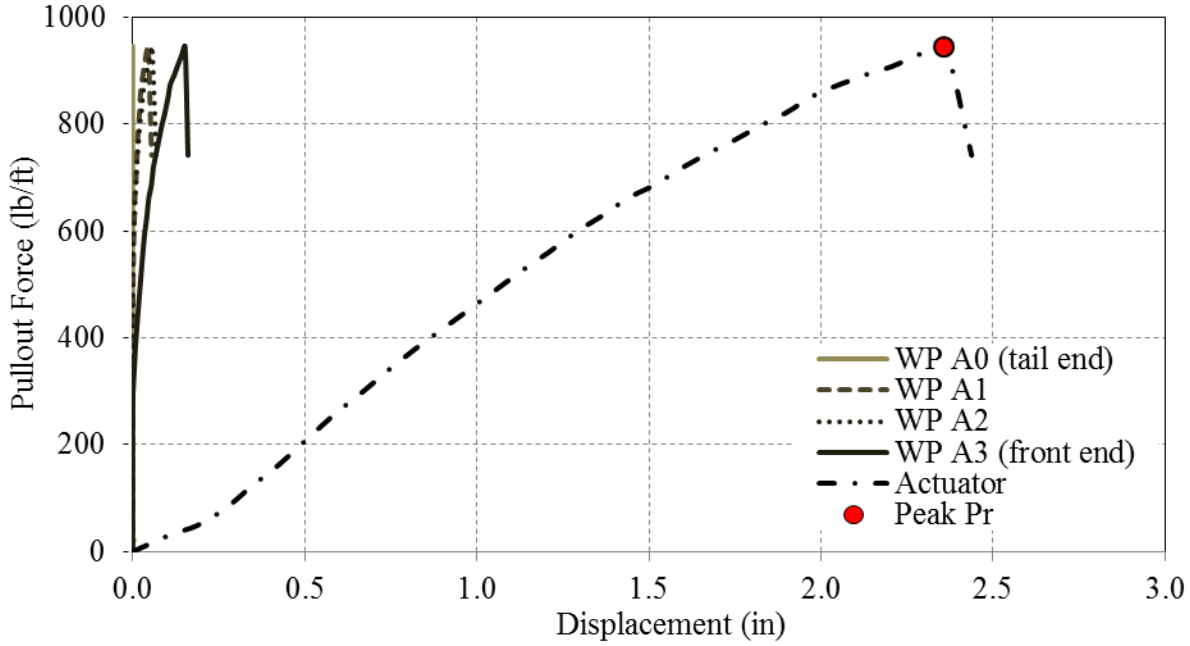

Figure 103. Pullout response results of EGG4 geogrid in ODOT Type-A aggregate subjected to 138 psf overburden pressure

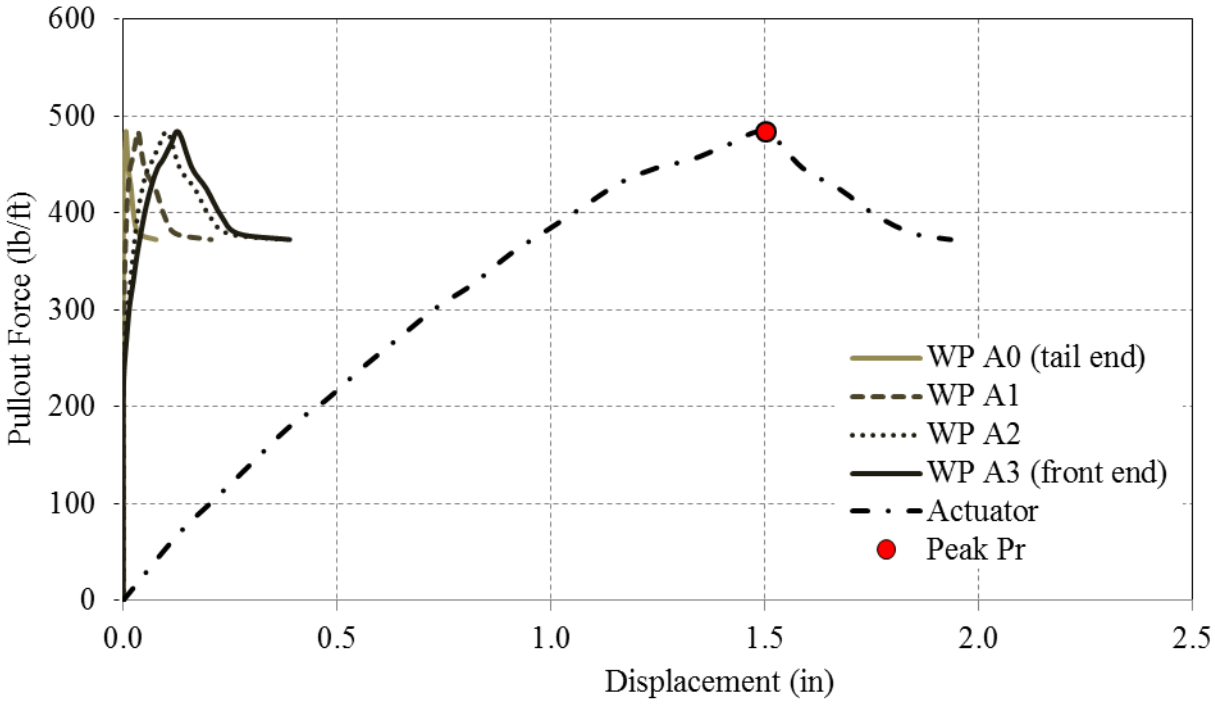

Figure 104. Pullout response results of EGG3 geogrid in ODOT Type-A aggregate subjected to 69 psf overburden pressure

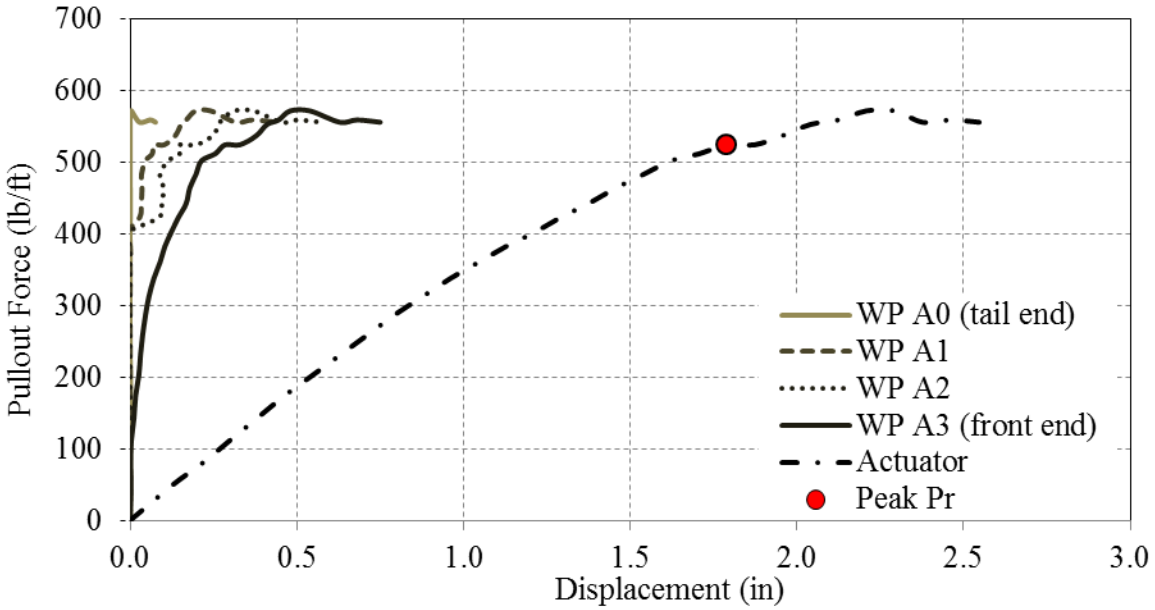

Figure 105. Pullout response results of EGG3 geogrid in ODOT Type-A aggregate subjected to 69 psf overburden pressure (2 ft embedment length)

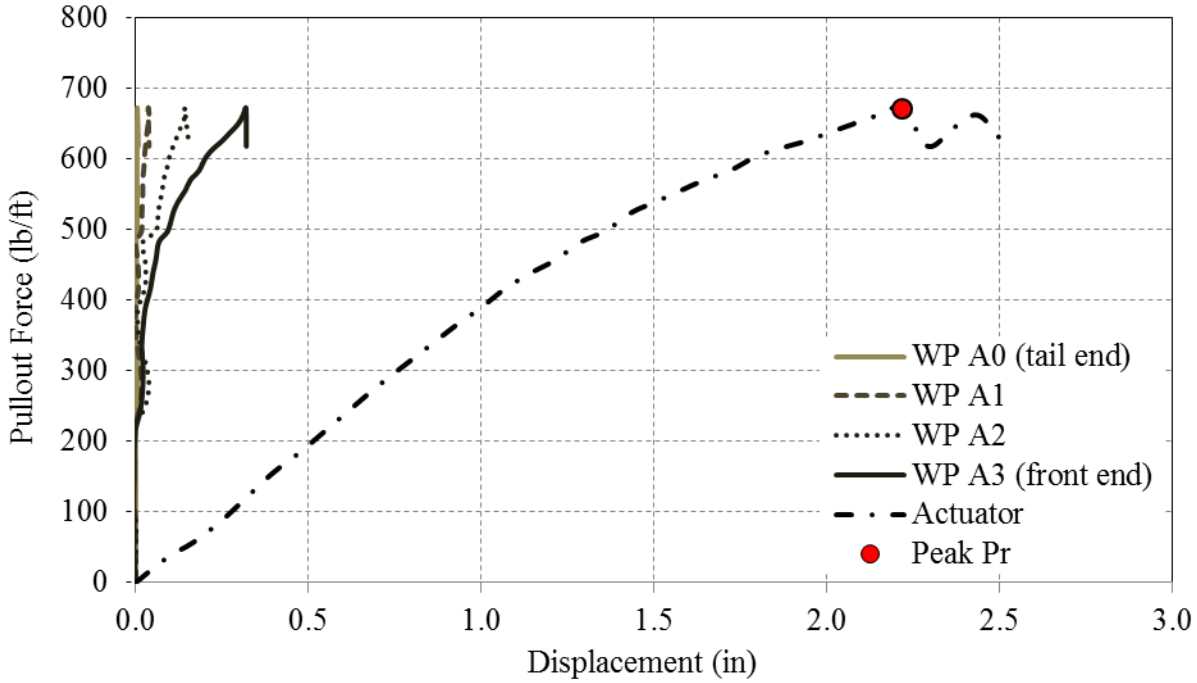

Figure 106. Pullout response results of EGG3 geogrid in ODOT Type-A aggregate subjected to 103 psf overburden pressure (2 ft embedment length)

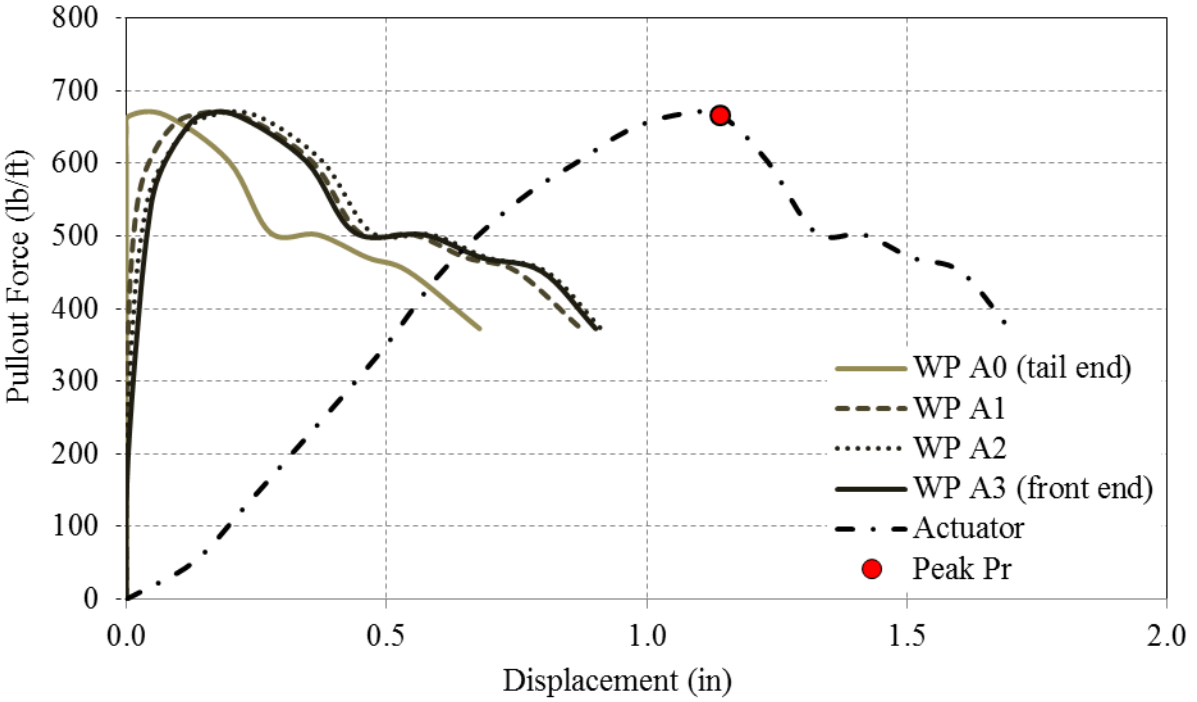

Figure 107. Pullout response results of EGG1 geogrid in ODOT Type-A aggregate subjected to 69 psf overburden pressure (2 ft embedment length)

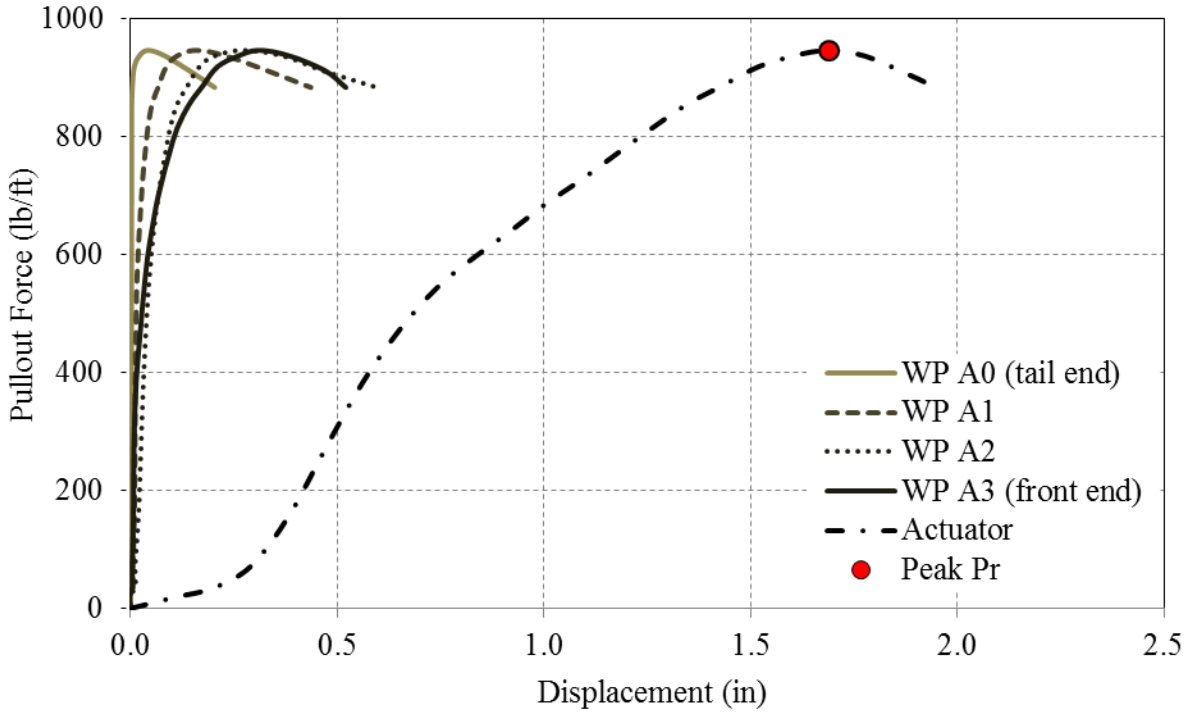

Figure 108. Pullout response results of WGG1 geogrid in ODOT Type-A aggregate subjected to 69 psf overburden pressure (2 ft embedment length)

3.5. Determination of peak pullout resistance

According to ASTM D6706, "the ultimate pullout resistance is the maximum pullout resistance measured during a pullout test". However, obtaining consistent pullout test data and getting a well-defined peak for geogrids in aggregates is challenging due to significant interlocking between these materials. In the pullout test data presented in this report, the ultimate pullout resistance, P_r, for each test case had to be determined by inspection. In several cases, it was determined as the first hump in the pullout response curve that preceded a plateau, followed by subsequent peaks or a monotonic increase in the pullout load. These strain-hardening features at larger displacements were attributed to the likely influence of the front boundary condition and were therefore dismissed. The magnitude of the peak pullout resistance, P_r, is reported in terms of the load per unit reinforcement width.

3.6. Relationship between peak pullout resistance and overburden pressure

Values of the peak pullout resistance as a function of overburden pressure are plotted in **Figure 109** through **Figure 116**. As was pointed out in the previous section, obtaining consistent pullout test data for geogrids in aggregates is fairly challenging due to significant interlocking effects

between these materials. However, the pullout response data for all geogrids as shown in **Figure 109** through **Figure 116** overall show reasonable trends in the form of a linear relationship between the pullout resistance and the overburden pressure.

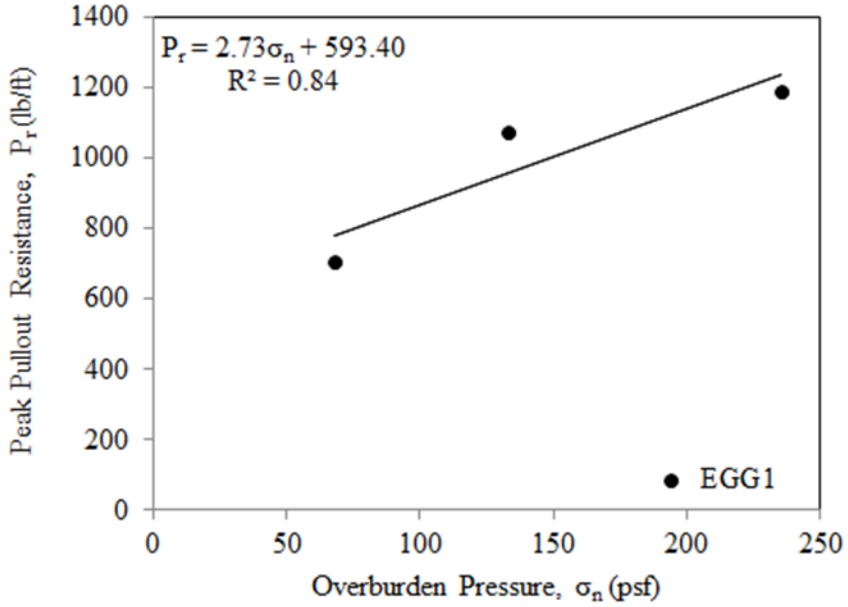

Figure 109. Variation of peak pullout resistance with overburden pressure for EGG1 geogrid in ODOT Type-A aggregate

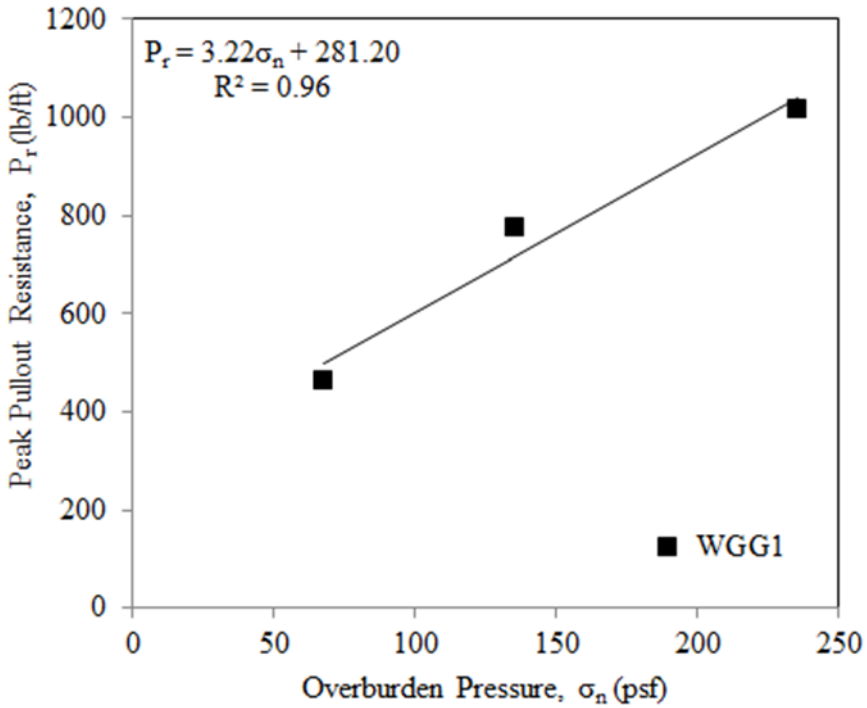

Figure 110. Variation of peak pullout resistance with overburden pressure for WGG1 geogrid in ODOT Type-A aggregate

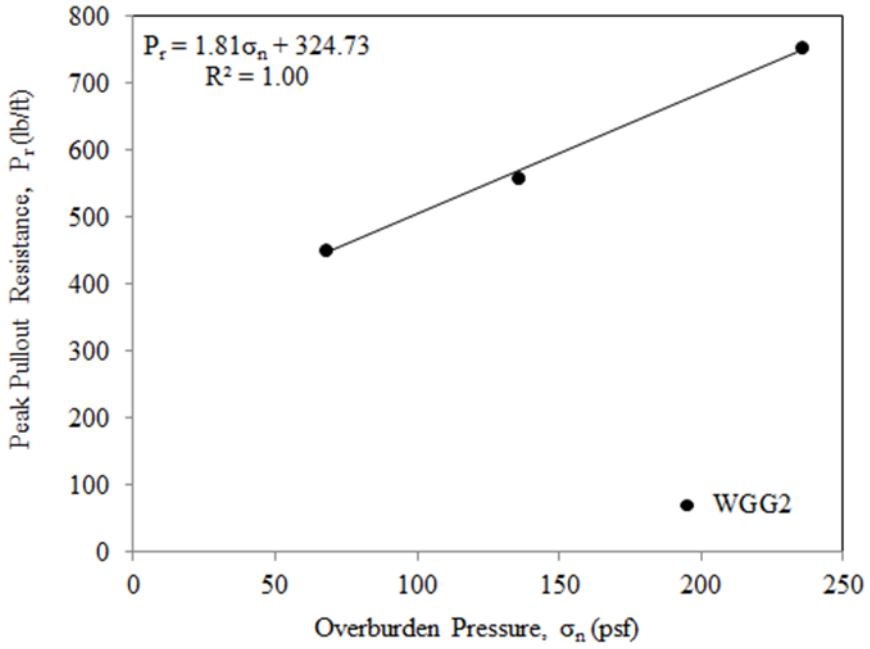

Figure 111. Variation of peak pullout resistance with overburden pressure for WGG2 geogrid in ODOT Type-A aggregate

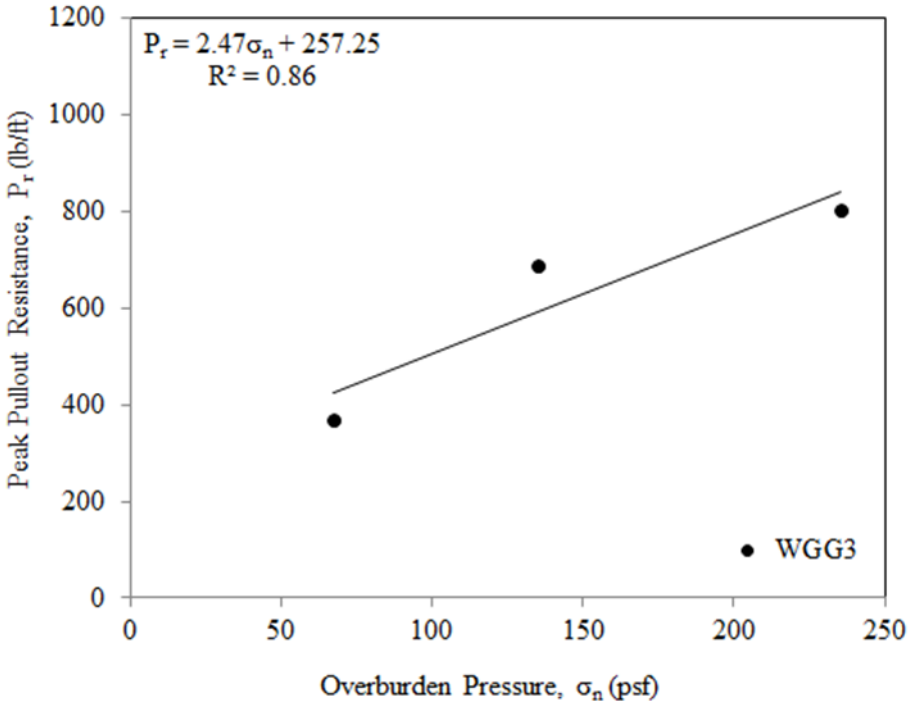

Figure 112. Variation of peak pullout resistance with overburden pressure for WGG3 geogrid in ODOT Type-A aggregate

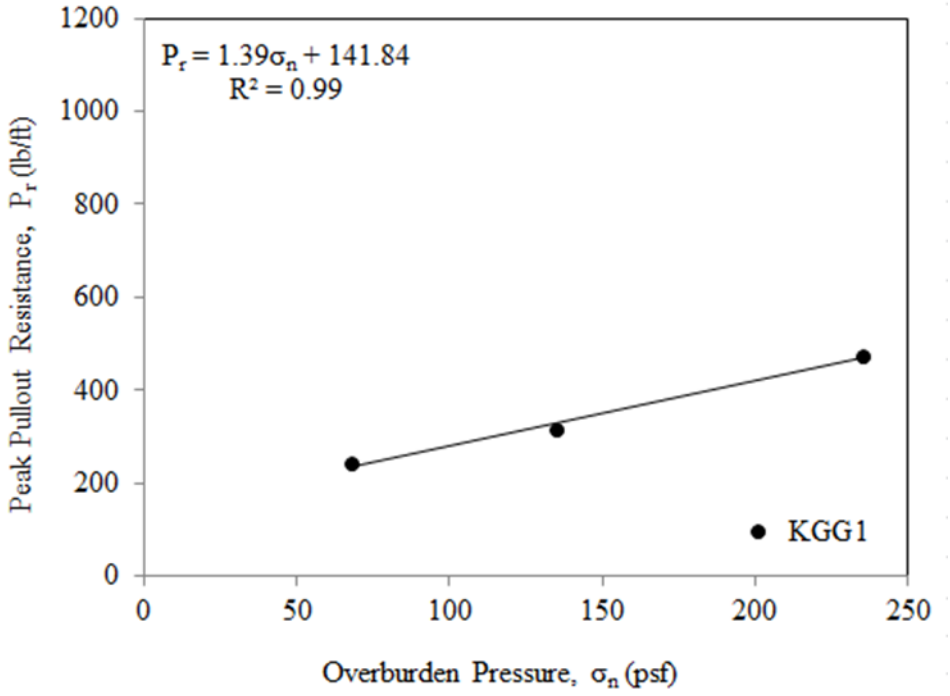

Figure 113. Variation of peak pullout resistance with overburden pressure for KGG1 geogrid in ODOT Type-A aggregate

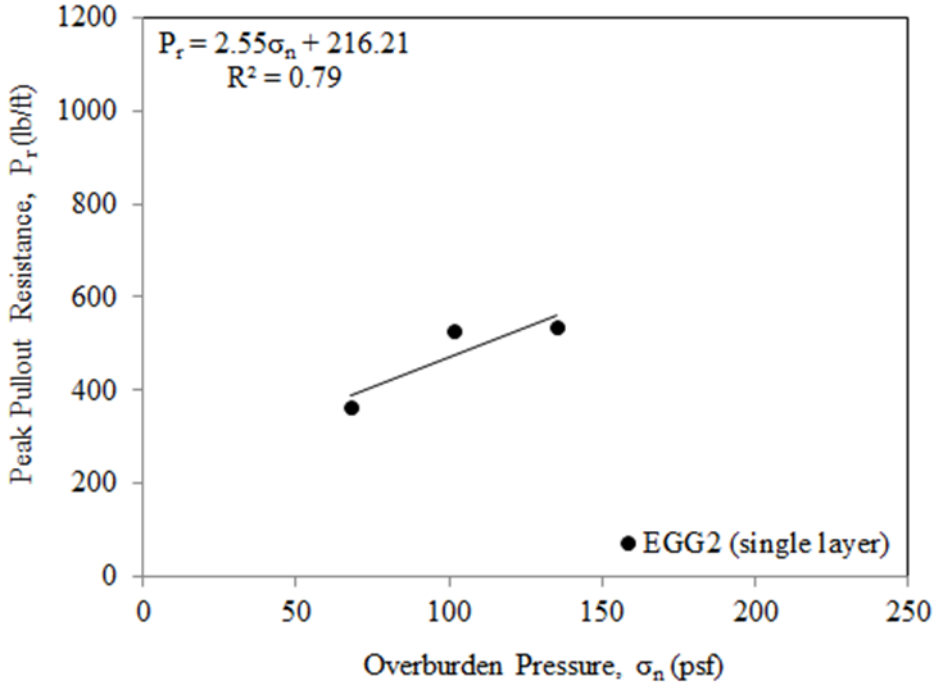

Figure 114. Variation of peak pullout resistance with overburden pressure for EGG2 (single layer) geogrid in ODOT Type-A aggregate

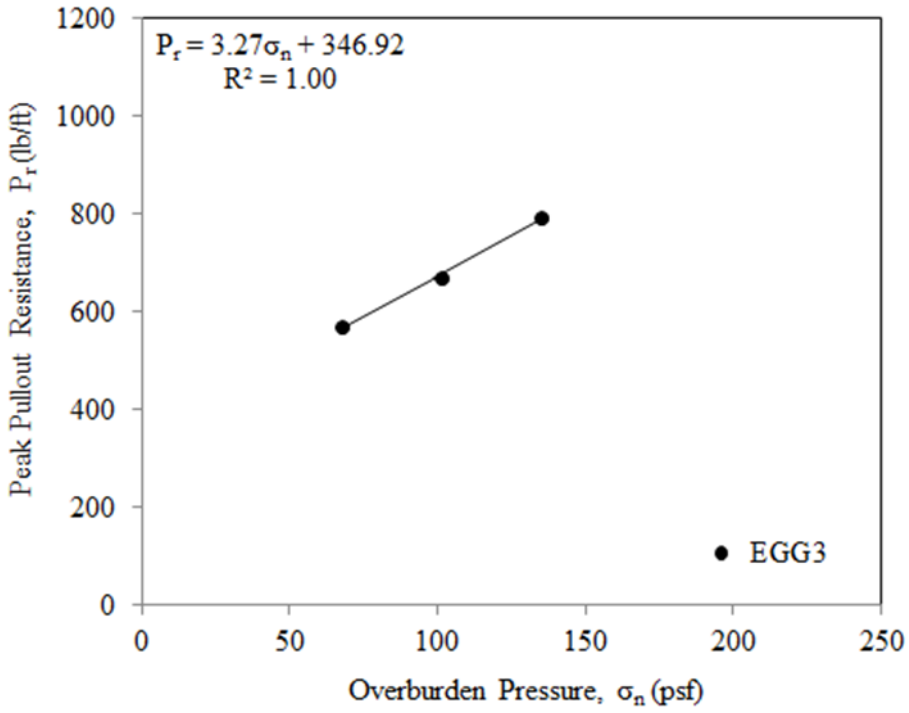

Figure 115. Variation of peak pullout resistance with overburden pressure for EGG3 geogrid in ODOT Type-A aggregate

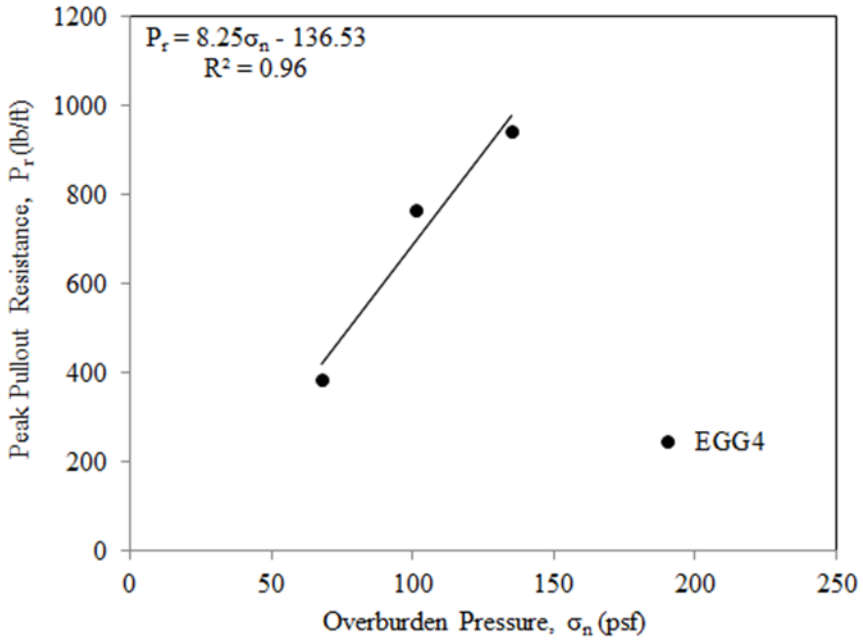

Figure 116. Variation of peak pullout resistance with overburden pressure for EGG4 geogrid in ODOT Type-A aggregate

Figure 118 shows the relationships between the peak pullout resistance and the overburden pressure (σ_n) for all extruded geogrids (EGG). It is noticed that the stronger EGG4 geogrid exhibits a greater pullout resistance and interlocking characteristics (i.e. greater slope) than the EGG3 geogrid. However, the pullout performance of EGG1 is still quite competitive in comparison with the newer EGG3 and EGG4 products. In addition, the pullout resistance of single-layer EGG2 geogrid is nearly half of that for EGG1. Since in practice EGG2 is used as a double-layer geogrid (**Figure 117**), its pullout performance could be comparable to that of EGG1. However, this hypothesis needs to be investigated by pullout testing of double layer (i.e. intact) EGG2 specimens.

Figure 117. EGG2 geogrid

Figure 119 compares the relationship between the peak pullout resistance, P_r, and the overburden pressure, σ_n, for non-extruded geogrids (NEGG) as compared with that for EGG1 (i.e. ODOT Type-2 geogrid). It can be observed that for the range of overburden pressures examined, the WGG2 and SF11 geogrids show comparable pullout performance in ODOT Type-A aggregate. In addition, EGG1 shows greater pullout resistance as compared to all NEGG products tested. The peak P_r - σ_n relationships from pullout tests on all geogrids examined in this study are summarized in **Figure 120**.

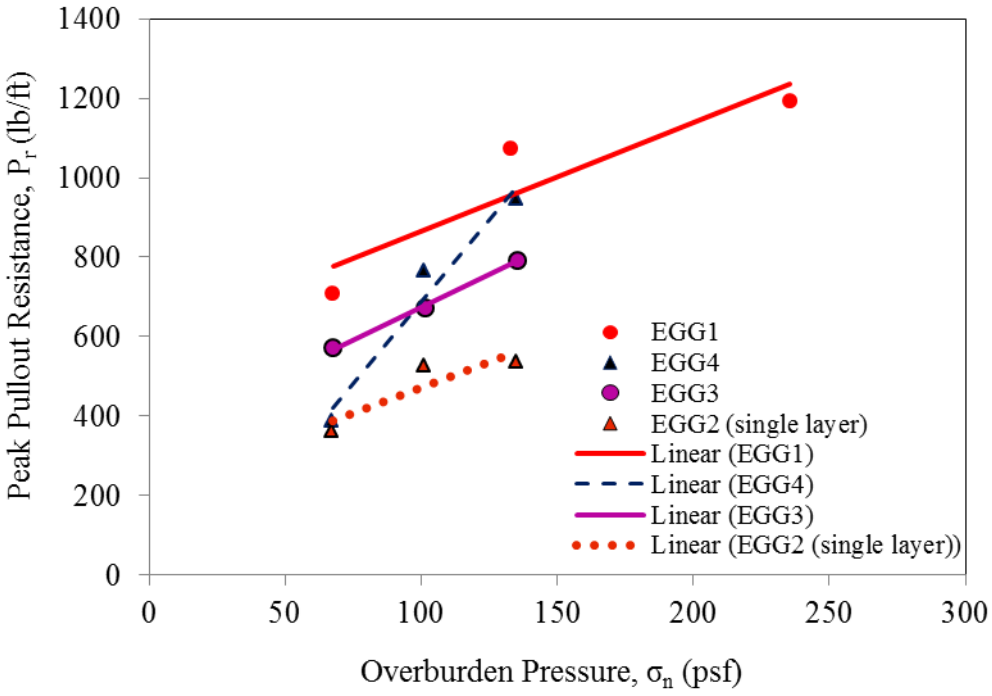

Figure 118. Peak pullout resistance of extruded geogrids tested in this study in comparison to that of EGG1

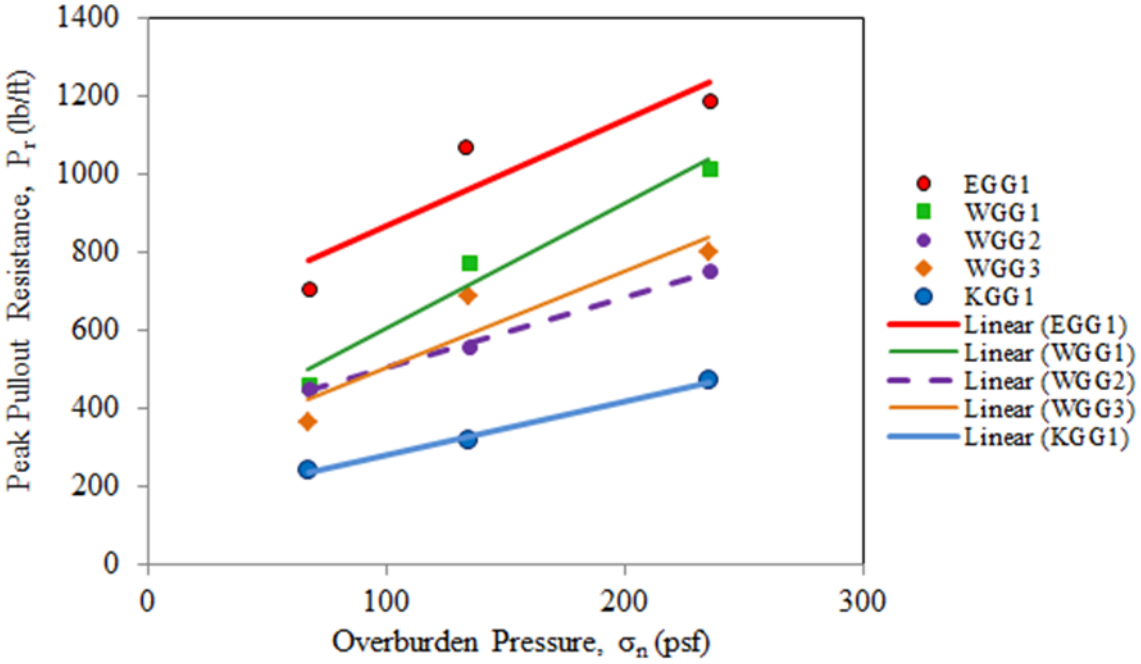

Figure 119. Peak pullout resistance of non-extruded geogrids tested in this study in comparison to that of EGG1

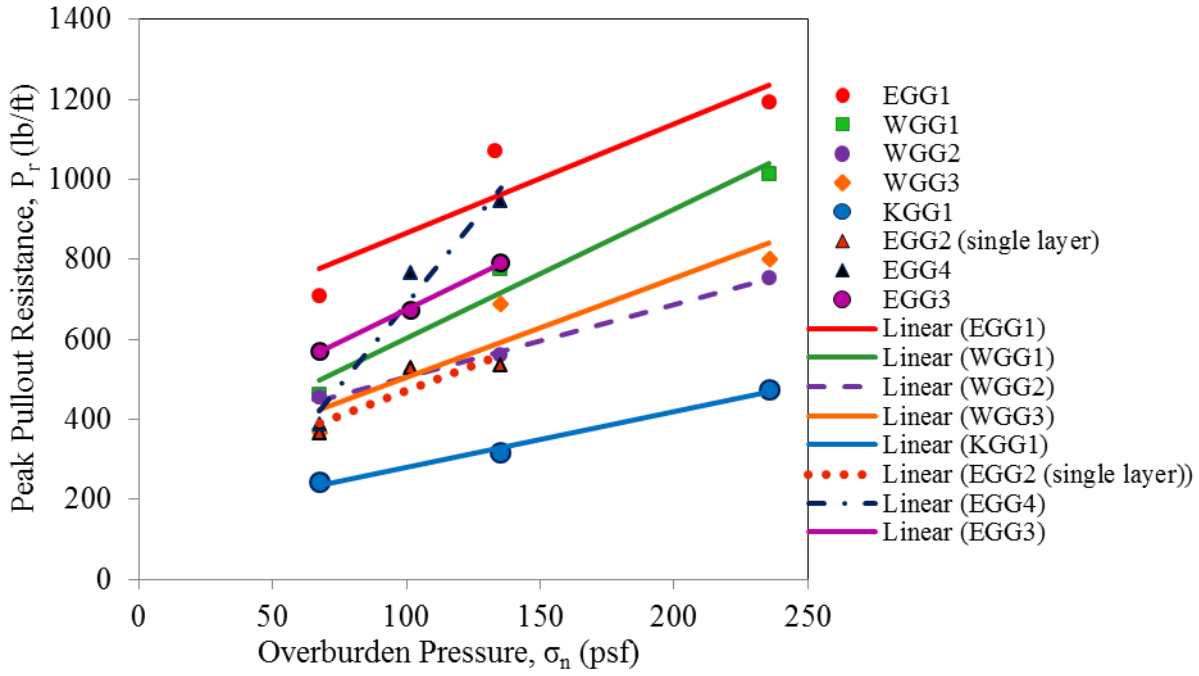

Figure 120. Peak pullout resistance of EGG and NEGG products tested in this study as a function of the overburden pressure

4. Installation damage tests

4.1. General

Stresses on geogrid reinforcement can be especially high during construction when geogrids are subjected to significant loading by the construction equipment. Therefore, survivability tests such as installation damage are important for the selection of suitable geogrids for a given project. In this study, two large-scale field installation damage tests were carried out on the extruded and non-extruded geogrids listed in **Table 2** in conformance with the ASTM D5818 test protocol to investigate their survivability during construction. According to the ASTM D5818 standard:

"6.4 Installation Procedure:
6.4.1 The soil subgrade or initial lift on which the geosynthetic(s) will be placed shall be constructed to specified conditions of soil type, moisture content and compaction. Construction equipment used should be the same as to be used to construct overlying lifts, unless otherwise requested. The geosynthetic should be installed in accordance with project specific procedures. When project specific procedures and/or materials are not known, representative equipment, materials and procedures should be used and thoroughly documented."

4.2. Summary of the installation damage test procedure

The following steps were taken to run the installation damage tests. Additional details of the installation damage procedure are given in the subsequent sections.

Step 1: A suitable site was selected for the test bed. Factors that were taken into consideration for this purpose included the evenness of the site surface and its proximity to the laboratory.
Step 2: The size of the test bed area and its depth were determined (**Section 4.3.** Size of the test bed area).
Step 3: The boundaries of the test area were marked and the surface vegetation was removed.
Step 4: Two 15 ft-long concrete beams were placed on the two sides of the cleared area. Soil was placed and compacted against the outside wall of each beam in order to support and secure it in place.
Step 5: An area near the test bed was cleared and prepared to store new aggregate.
Step 6: 24,000 lbs of ODOT Type-A aggregate was purchased.
Step 7: Four steel plates were purchased to help with exhumation of geogrid specimens after they were installed in the aggregate. 40 inches-long chains were attached to each steel plate which facilitated lifting of the plates during the exhumation process.

Step 8: Different alternatives for the compaction equipment were examined and a compactor was selected.

Step 9: Steel plates were placed side-by-side along the test bed and were covered with six inches of aggregate. An aggregate ramp was built on both ends of the test bed so that the compactor equipment could access the main test area (**Figure 140**). The aggregate was compacted to 90% maximum dry density (as recommended in ASTM D5818) using 4 passes of the 15.5-kip steel drum compactor on the top of the aggregate. The number of passes for the compaction equipment was determined following the information reported in TRI (2006).

Step 10: Four geogrid specimens were prepared and placed in the test bed on the top of the first aggregate lift (**Figure 147**).

Step 11: The second six-inch aggregate layer was placed and compacted in the test bed.

Step 12: The density of the aggregate in each lift was measured based on the as-placed thickness of the aggregate. In addition, a balloon testing apparatus was used to take additional density measurements (**Section 4.9.** Key steps in the field installation damage tests**).**

Step 13: Once the construction of the reinforced base model was completed, a forklift was used to lift the steel plates from underneath the base layer and tilt them to expose the geogrids. Afterwards, the aggregates on the top of the geogrid specimens were carefully removed and the specimens were taken to the laboratory for inspection and testing.

Step 14: The second installation damage test was carried out on four other geogrid products.

Step 15: In-isolation tests were carried out on damaged geogrid specimens to determine installation damage factors for their rib and junction strength properties.

4.3. Size of the test bed area

A schematic site plan for installation damage tests outside the Fears laboratory at OU is shown in **Figure 121**. Selected data related to this site include:

Size of the test area: 12 ft (L) × 8 ft (W) (excluding the ramp sections)
Total length of the test section (including the ramp sections) = 24 ft
Ramp slope = 3H : 1V
Length of the extended area for the compactor movement = 3 ft
Length of the ramp = 3 ft
Length of the side concrete beams = 15 ft
Height of the side concrete beams = 1.5 ft
Height of the test section = 1 ft

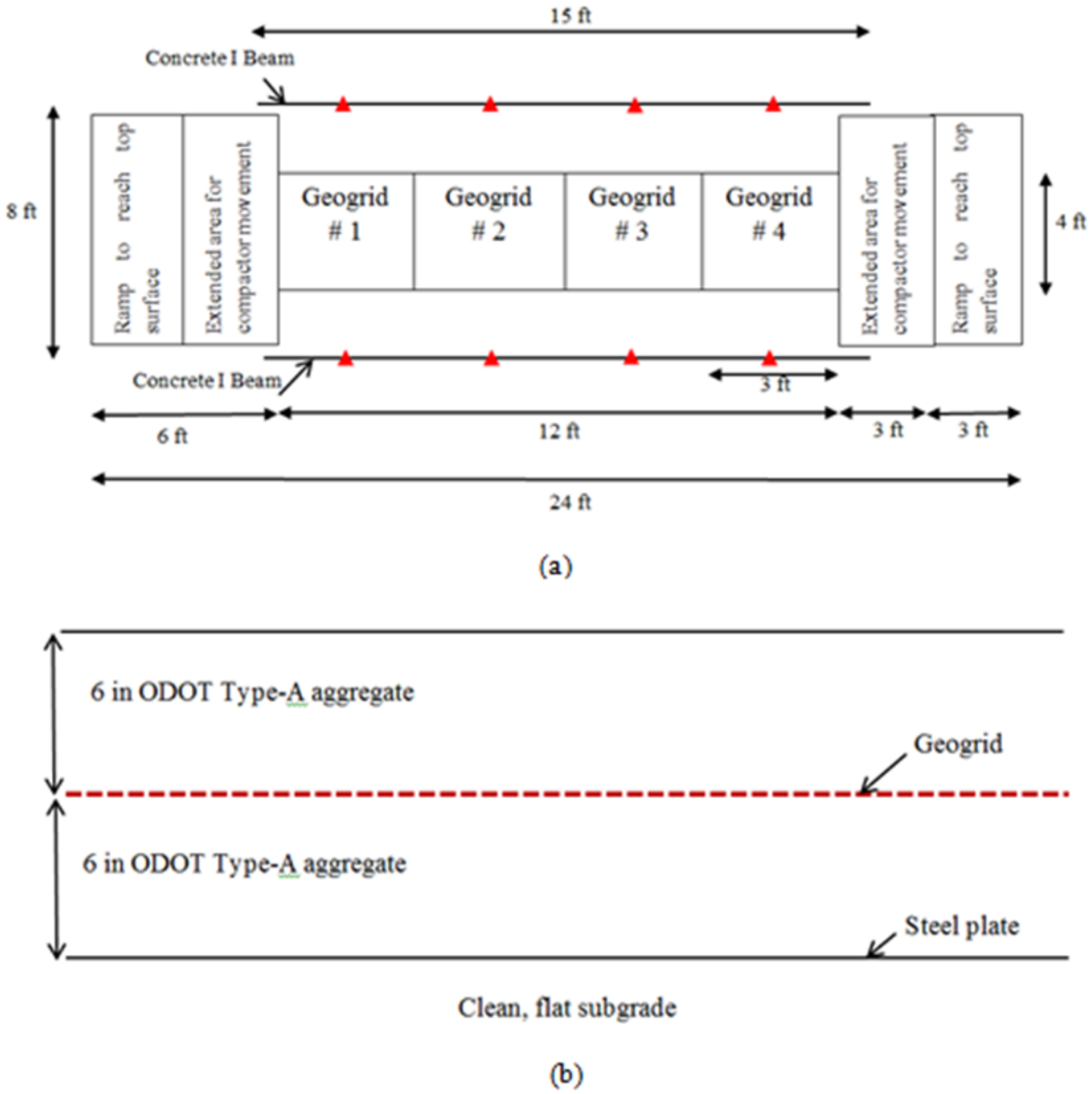

Figure 121. Schematic diagrams of the test bed for installation damage tests: (a) Plan view (Note: Solid triangles indicate the locations where the thickness of the aggregate layer was measured), (b) Elevation view (indicating the thicknesses of aggregate layers)

4.4. Geogrid sampling and specimen preparation

Eight 3 ft × 4 ft geogrid specimens (one from each geogrid product) were prepared for the installation damage tests as shown in **Figure 122** through **Figure 131**.

Figure 122. Geogrid sample preparation

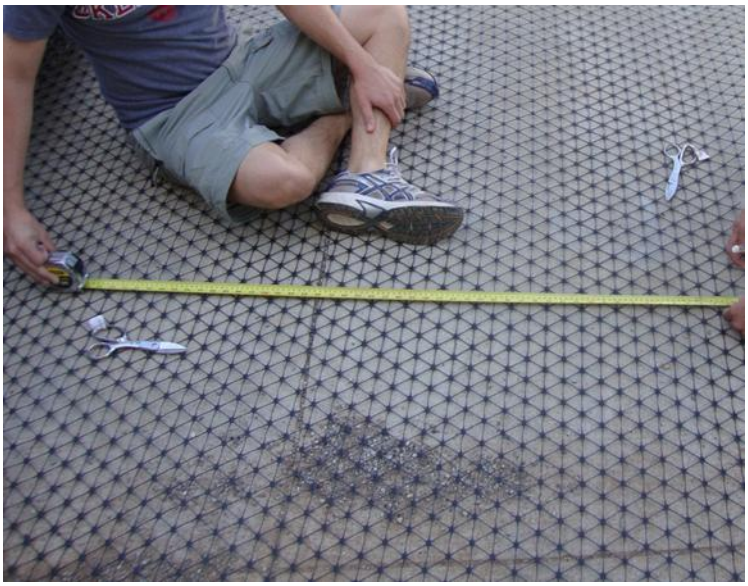

Figure 123. Preparing EGG4 geogrid specimen for installation damage tests

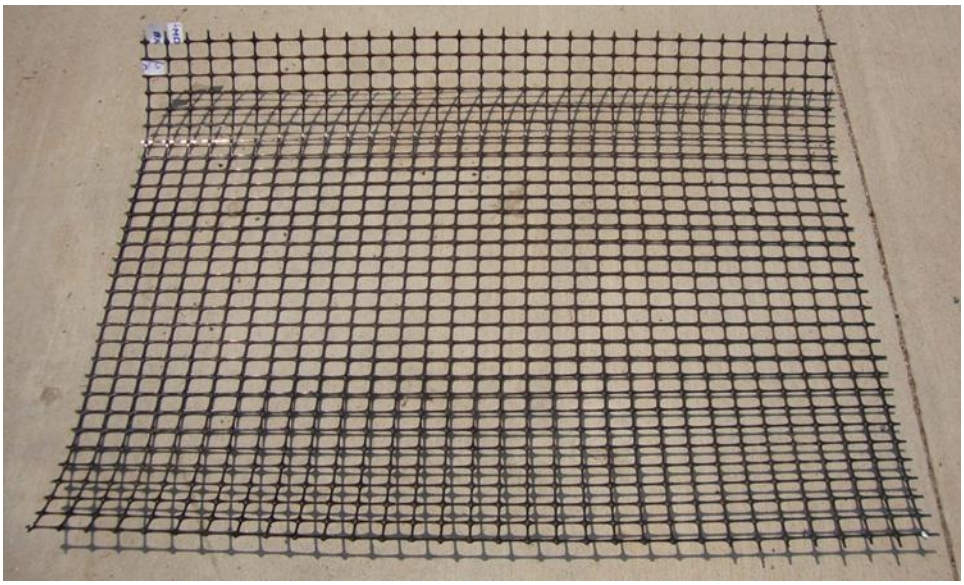

Figure 124. EGG1 geogrid specimen prepared for installation damage tests

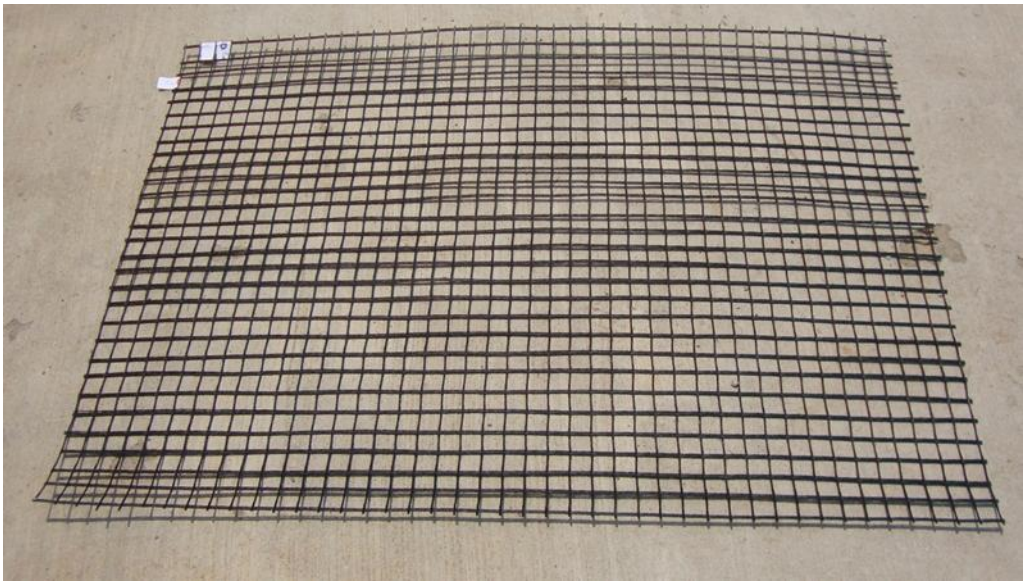

Figure 125. WGG1 geogrid specimen prepared for installation damage tests

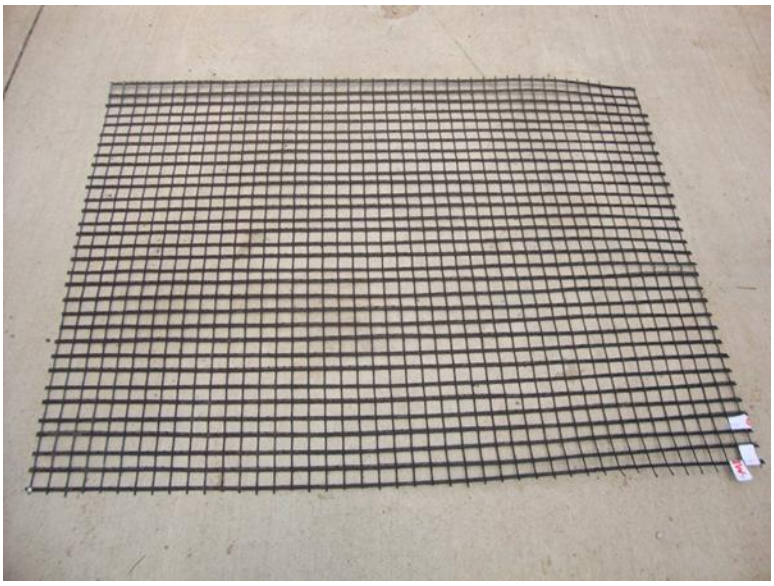

Figure 126. WGG2 geogrid specimen prepared for installation damage tests

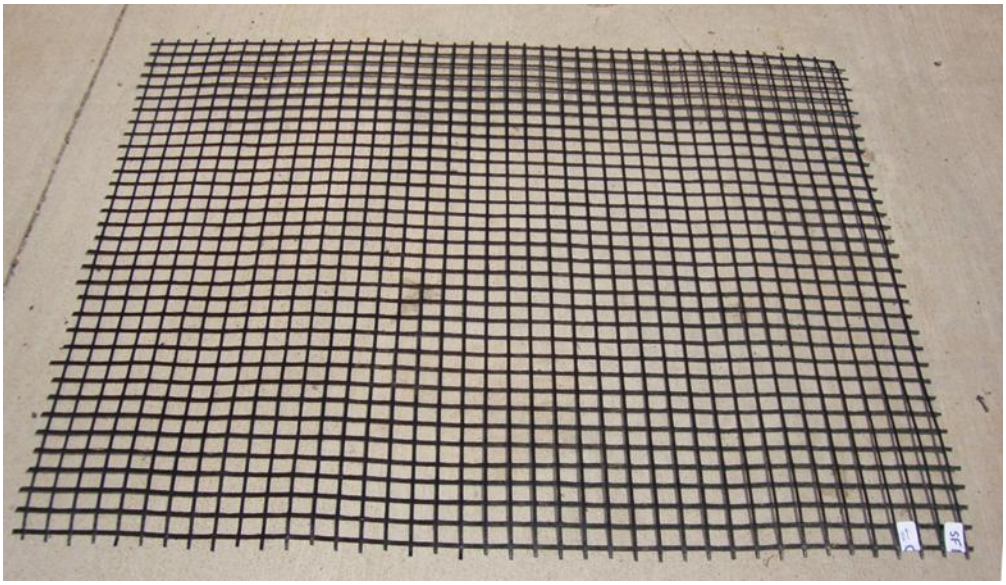

Figure 127. WGG3 geogrid specimen prepared for installation damage tests

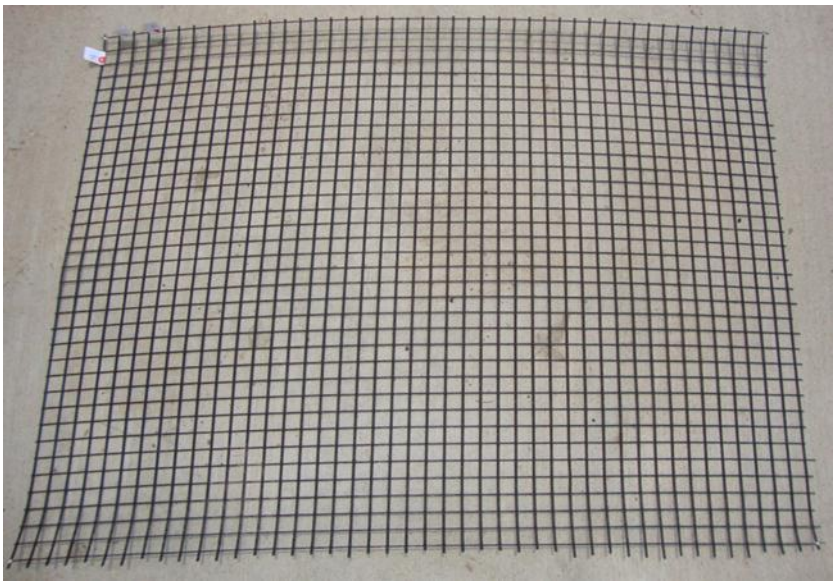

Figure 128. KGG1 geogrid specimen prepared for installation damage tests

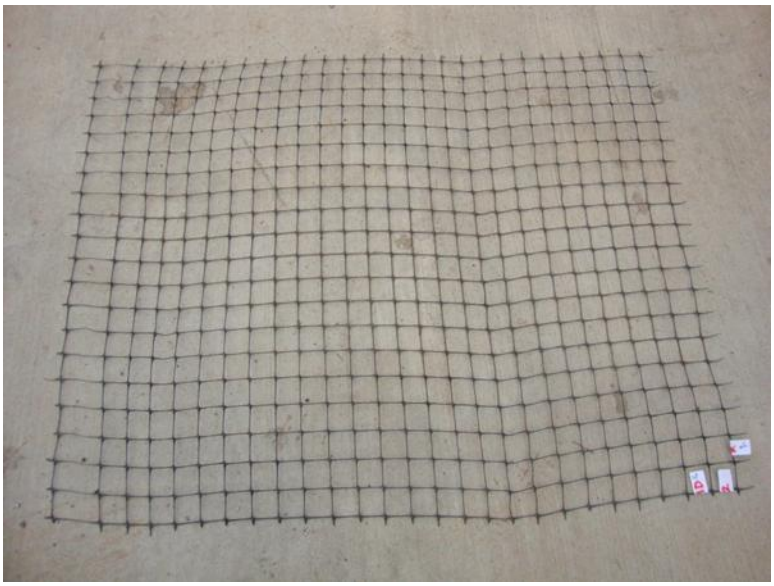

Figure 129. EGG2 single layer geogrid specimen prepared for installation damage tests

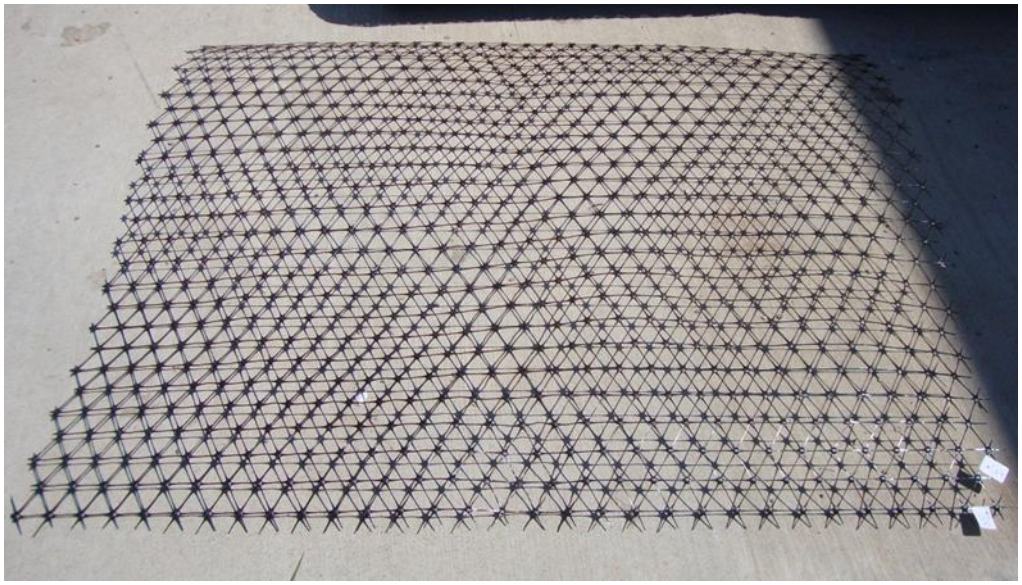

Figure 130. EGG3 geogrid specimen prepared for installation damage tests

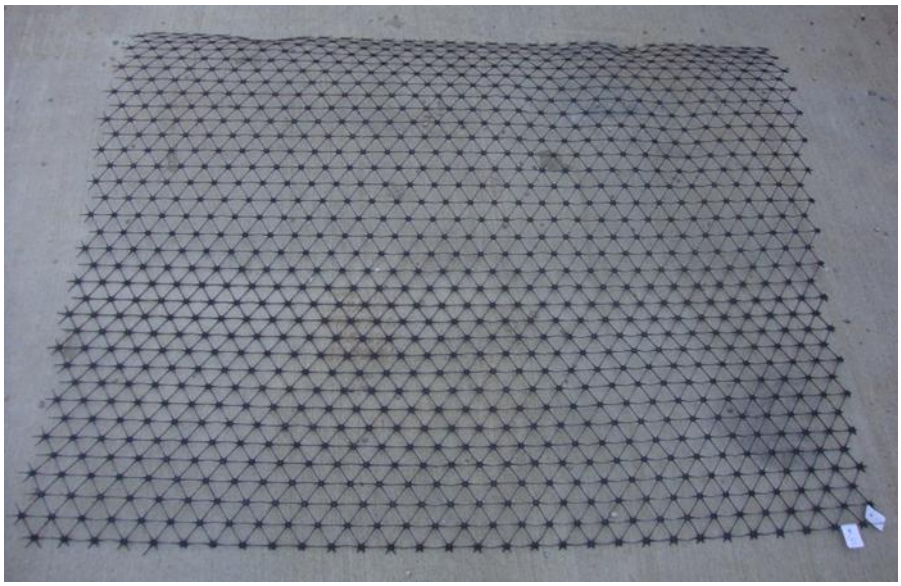

Figure 131. EGG4 geogrid specimen prepared for installation damage tests

The selected size of the geogrid specimens is comparable to that used in earlier similar studies (e.g. TRI 2006 and Jeon and Bouazza 2008). It is also in agreement with the ASTM D5818 guidelines which state that: "*The amount of geosynthetic to install in and retrieve from a test section is a function of the type and number of laboratory tests to be conducted for assessment of damage. An amount of material sufficient to obtain 20 tests on representative specimens for each type of test should be installed for each set of installation conditions*."

Two rounds of installation damage tests were carried out in this study. The extruded (EGG) and non-extruded (NEGG) geogrid specimens listed in **Table 2** were tested in the first and the second rounds of installation damage tests, respectively. The machine direction of each geogrid specimen was placed parallel to the running direction of the compaction equipment according to the ASTM D5818 test standard.

4.5. Equipment

A steel-wheeled vibratory roller compactor was used to compact the aggregates in the installation damage test bed. The compactor weight was more than 11 kips, as recommended in ASTM D5818. Different companies in Oklahoma and Texas were contacted and the specifications and the rental and transportation costs of the available choices for the compactor equipment were compared to select a suitable compactor for the tests. Fortunately, a local company (Haskell Lemon) had a suitable compactor (**Figure 132**) and was able to loan it to the research team of this project. The compactor (Volvo Model SD70D) was a single-drum vibratory roller compactor with the specifications as given in **Table 16**.

Figure 132. Compaction equipment (Source: http://www.volvo.com)

Table 16. Compactor Specifications

Weight	15.56 kips
Recommended minimum weight of the compactor (ASTM D5818)	11 kips
Width	6.17 ft
Length	16.6 ft
Height	9.46 ft
Width of the roller drum	5.5 ft
Degree of compaction (ASTM D5818)	90% maximum dry unit weight from Modified

A forklift tractor (**Figure 133**) with a lifting capacity of 4 kips was used to lift the steel plates from underneath the aggregate layer in the test bed and initiate the exhumation process.

Figure 133. The forklift which was used in this study to lift the steel plates from underneath the geogrid specimens

A front-loader “bobcat” tractor was used to spread the aggregate in the test bed (**Figure 134**).

Figure 134. The front-loader tractor used in this study

4.6. Steel plates

Four steel plates were placed underneath the aggregate layer in the test bed on the cleared subgrade. Lifting chains were attached to the plates along one edge to facilitate their lifting and tilting during the exhumation process of the geogrid samples from underneath the compacted aggregate (**Figure 135** and **Figure 136**). The specifications of the steel plates are given in **Table 17**.

Figure 135. Steel plates with lifting chains

Figure 136. Moving of the steel plates from the lab to the test site

Table 17. Specifications of the steel plates used in the installation damage test bed

Number of steel plates	4
Length	3.5 ft
Width	4.5 ft
Thickness	0.5 in
Weight	244.8 lb

4.7. Measuring density of compacted aggregate

There are a number of ASTM standards for measuring the in-situ density of soils and aggregates as follows:

1. ASTM D 1556-07 "Standard Test Method for Density and Unit Weight of Soil in Place by Sand-Cone Method"

   This test method is not suitable for soils consisting of unbound granular materials, soils containing appreciable amounts of coarse-grained material larger than 1.5 in, and granular soils having high void ratios. Therefore, sand cone method was not used in our tests.

2. ASTM D 4914-08 "Standard Test Methods for Density and Unit Weight of Soil and Rock in Place by the Sand Replacement Method in a Test Pit"

   This test method is primarily suitable for rock, which is defined as aggregates that typically contain particles larger than 3 inches. Since ODOT Type-A particles are significantly smaller than 3 inches, this method was not used to measure the as-placed density of the aggregates.

3. ASTM D 2167-08 "Standard Test Method for Density and Unit Weight of Soil in Place by the Rubber Balloon Method"

This test method is recommended for aggregates. Therefore, we used this method to measure the in-situ unit weight of the ODOT Type-A aggregate that we used in our installation damage tests (**Section 4.11.** Obtaining representative test specimens from exhumed samples).

4.8. Site preparation

A 24 ft × 8 ft area was marked outside the Fears laboratory on the OU south campus. The marked area was cleared of the existing vegetation and two concrete beams were placed on its side boundaries and secured in place by placing and compacting soil against the outside walls of the beams (**Figure 137** through **Figure 140**).

Figure 137. Test site for the installation damage tests of geogrids outside the Fears Laboratory

Figure 138. Marking the boundaries of the test site

Figure 139. Clearing the test area from existing vegetation

Figure 140. Concrete beams placed on both sides of the test section with soil support on the outside

4.9. Key steps in the field installation damage tests

Prior to the placement of aggregates, a grid was drawn on the inside wall of each beam using a red marker. Each grid was comprised of horizontal and vertical lines at six-inch intervals. For each lift, after more than six inches of aggregate was placed in the test bed and compacted, its final thickness was measured at eight locations along the length of the test section using a ruler (**Figure 141**). For this purpose, the lift thickness was calculated by measuring the distance between the aggregate surface and the marked horizontal line on the beam sidewall immediately above it. The compaction of each aggregate lift was carried out using four passes of the compaction equipment (TRI 2006).

Figure 141 through **Figure 153** illustrate the key steps followed to carry out the installation damage tests.

Figure 141. Four steel plates were placed in the test bed to facilitate the exhumation process of the geogrids after they were covered by compacted aggregate

Figure 142. Aggregate was taken from a nearby stockpile using a front-loader tractor

Figure 143. Spreading ODOT Type-A aggregate in the test bed

Figure 144. First layer of aggregate in the test bed before compaction

Figure 145. Compacting the first layer of aggregate with a vibratory roller compactor

The as-placed unit weight of the aggregate in each lift was measured according to ASTM D2167-08 using a model HM-310 Voluvessel densometer (**Figure 146**), which was found to vary between 130 lb/ft^3 and 135 lb/ft^3. Comparison of these values with the maximum unit weight of the ODOT Type-A aggregate used in the study (with a maximum dry unit weight equal to 146.5 lb/ft^3 from the modified proctor tests according to the AASHTO T 180-01 test method) indicated that the unit weight of the aggregate in the test bed was consistently greater than 90% of its maximum modified Proctor value during the tests.

The aggregate moisture content was also determined according to the ASTM D4643 test method. The moisture content values were in the range between 0.25% and 0.30%, which meant that the aggregate was in an essentially dry condition.

Figure 146. Measuring the in-situ density of aggregates according to ASTM D2167-08: (a) Model HM-310 Voluvessel Rubber Balloon densometer, (b) The densometer in use on the test bed

Figure 147. Four extruded geogrids are placed on the first layer of compacted aggregate

Figure 148. Spreading the second layer of aggregate in the test bed

Figure 149. Compacting the second layer of aggregate with the vibratory roller compactor

Figure 150. The top (second) layer of aggregate in the test bed after compaction

To exhume the geosynthetic specimens, the forklift tractor was used to lift the chains that were attached to one edge of the steel plates underneath the compacted aggregate. Each plate was lifted and tilted to an angle of nearly 45^{o} from horizontal using the lifting chains (**Figure 151** and **Figure 152**). Afterwards, the upper part of the aggregate on the top of the geogrid was initially removed using a shovel (**Figure 153**). However, deeper aggregate closer to the geogrid was carefully removed by hand. If necessary, the plate was struck with a mallet to loosen the fill and facilitate the exhumation process without any contact with the geogrid.

Figure 151. Connecting lifting chains to the forklift

Figure 152. Tilting of steel plates from underneath the compacted aggregate

Figure 153. Tilting of steel plates and removing of aggregates to facilitate exhumation process

The data for the two installation damage tests are summarized in **Table 18**.

Table 18. Summary of installation damage tests on geogrids in ODOT Type-A aggregate

Test No.	Geogrid	First Lift				Second Lift			
		Unit Weight (lb/ft^3)	Moisture Content (%)	No. of Passes	Final Thickness (in)	Unit Weight (lb/ft^3)	Moisture Content (%)	No. of Passes	Final Thickness (in)
1	EGG1, EGG2, EGG3, EGG4	133	0.25	4	5.8	130	0.25	4	6.3
2	WGG1, WGG2, WGG3, KGG1	135	0.3	4	6	132	0.3	4	6.2

4.10. Geogrid samples after exhumation

The geogrid samples after exhumation were brought to the laboratory where they were cleaned using a soft brush. Afterwards, the samples were tagged and stored in a secure place in the laboratory. Photographs of geogrid samples after exhumation are shown in **Figure 154** through **Figure 161**.

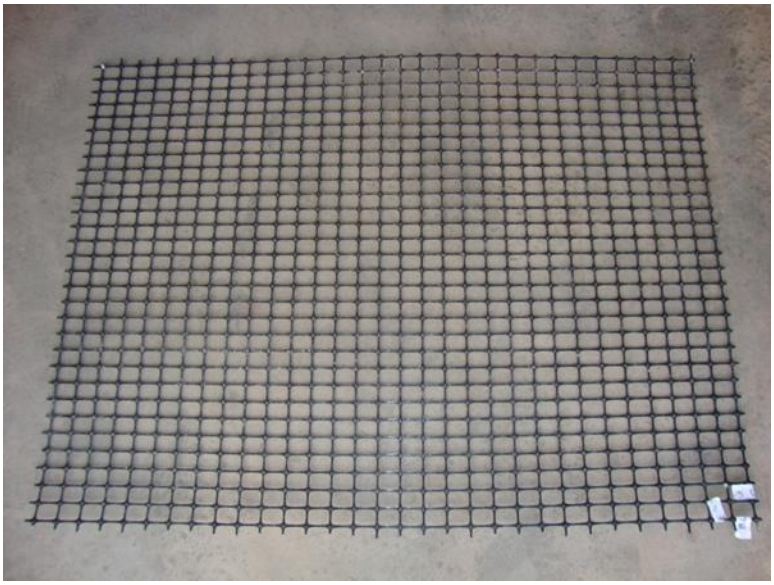

Figure 154. EGG1 geogrid specimen after exhumation

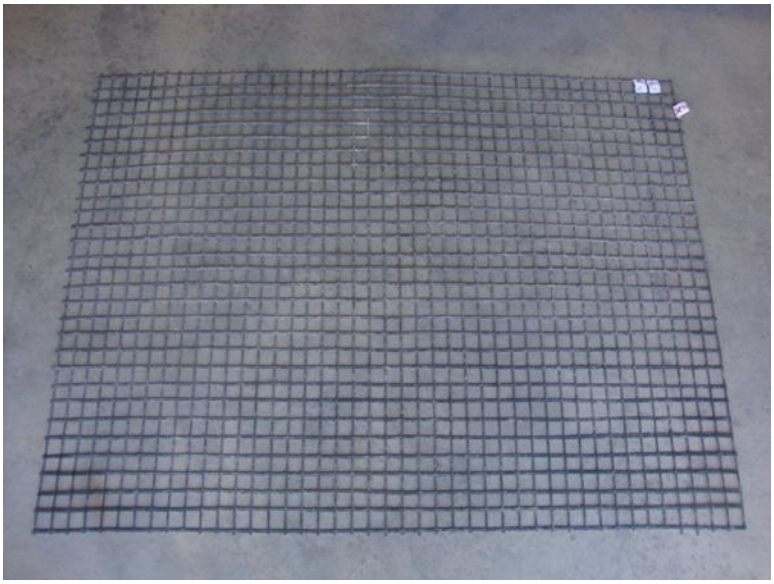

Figure 155. WGG1 geogrid specimen after exhumation

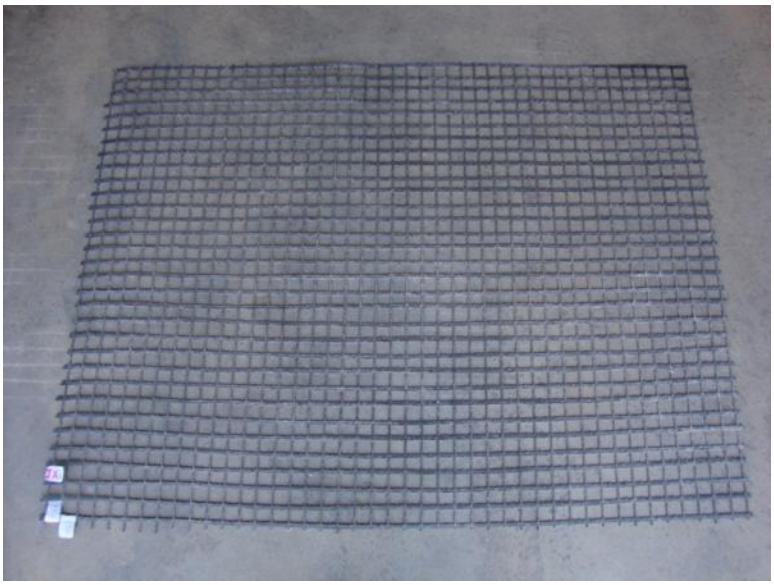

Figure 156. WGG2 geogrid specimen after exhumation

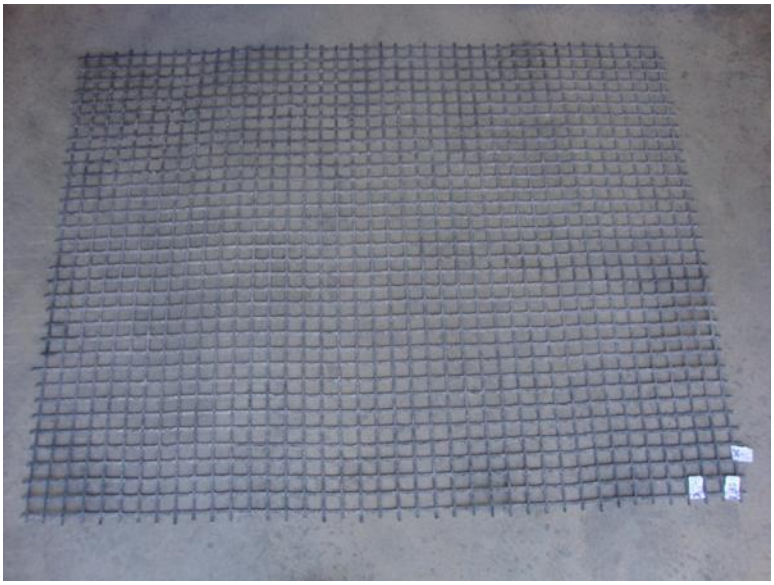

Figure 157. WGG3 geogrid specimen after exhumation

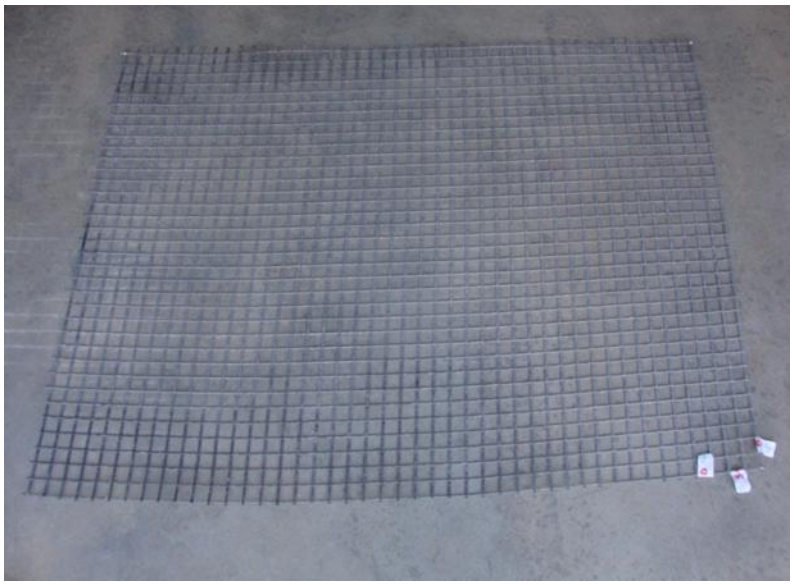

Figure 158. KGG1 geogrid specimen after exhumation

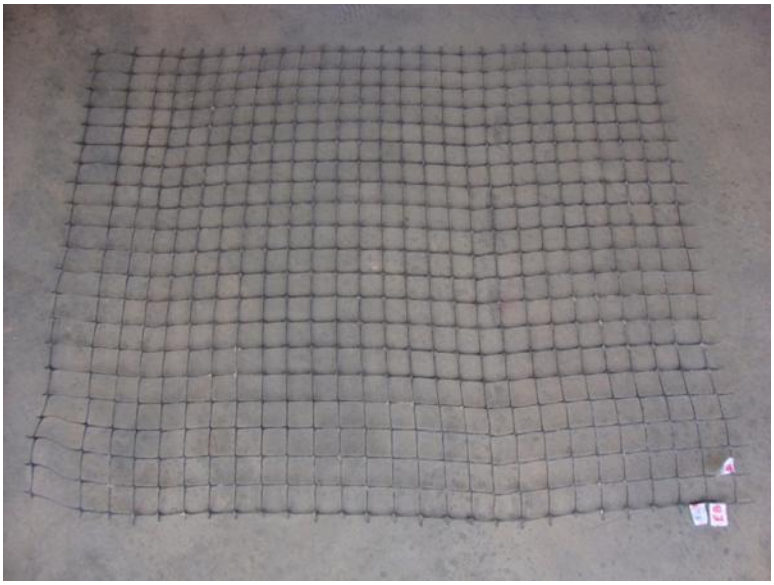

Figure 159. EGG2 single layer geogrid specimen after exhumation

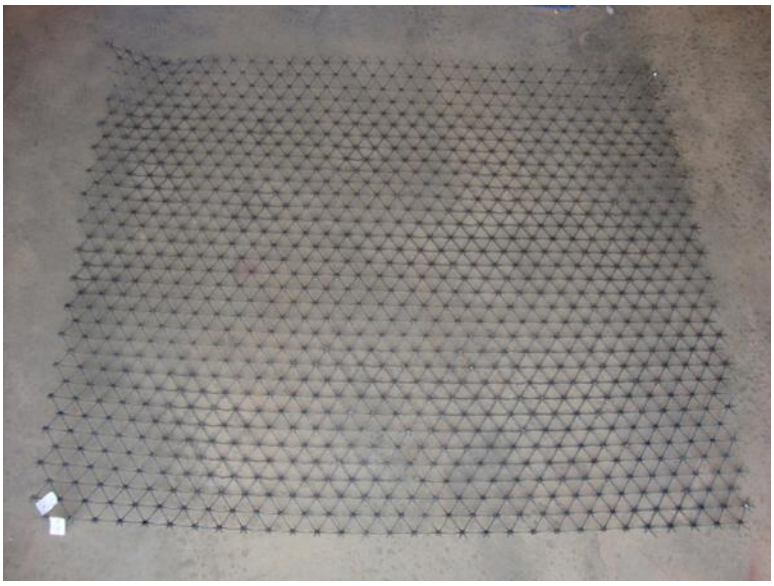

Figure 160. EGG3 geogrid specimen after exhumation

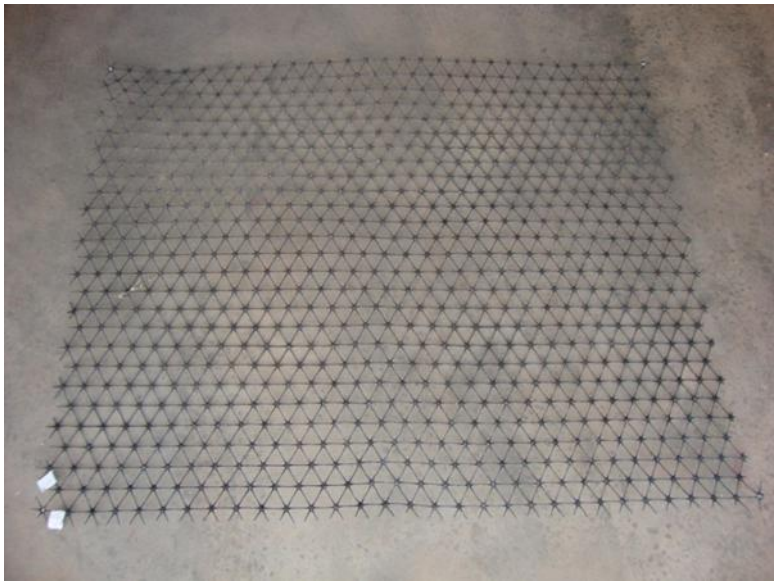

Figure 161. EGG4 geogrid specimen after exhumation

4.11. Obtaining representative test specimens from exhumed samples

Following the ASTM D5818 test standard, areas of the geosynthetic samples that were damaged *during removal* were identified, spray painted and designated as being non-representative of installation damage. Consequently, these parts of the geogrids were excluded from sampling for installation damage evaluation. The "non-representative area of installation damage" for EGG1,

KGG1, EGG2- single layer, EGG3 and Egg4 geogrid samples, painted in red, are shown in **Figure 162** through **Figure 166**.

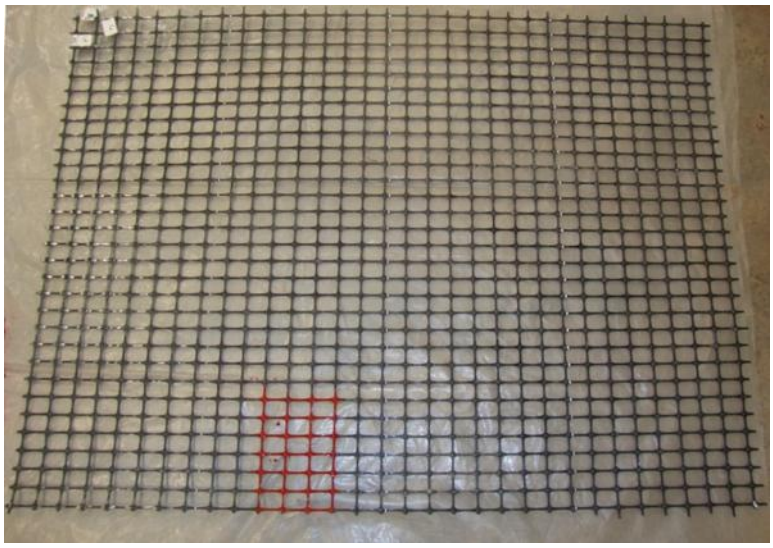

Figure 162. EGG1 geogrid sample with marked damaged area

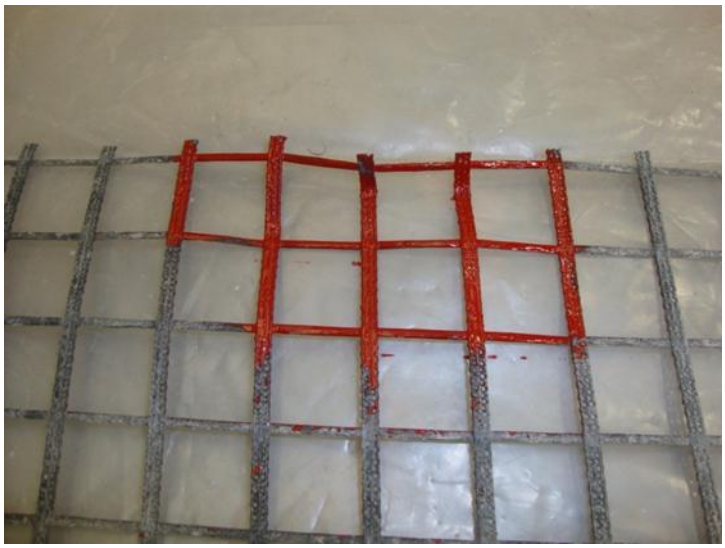

Figure 163. KGG1 geogrid sample with marked damaged area

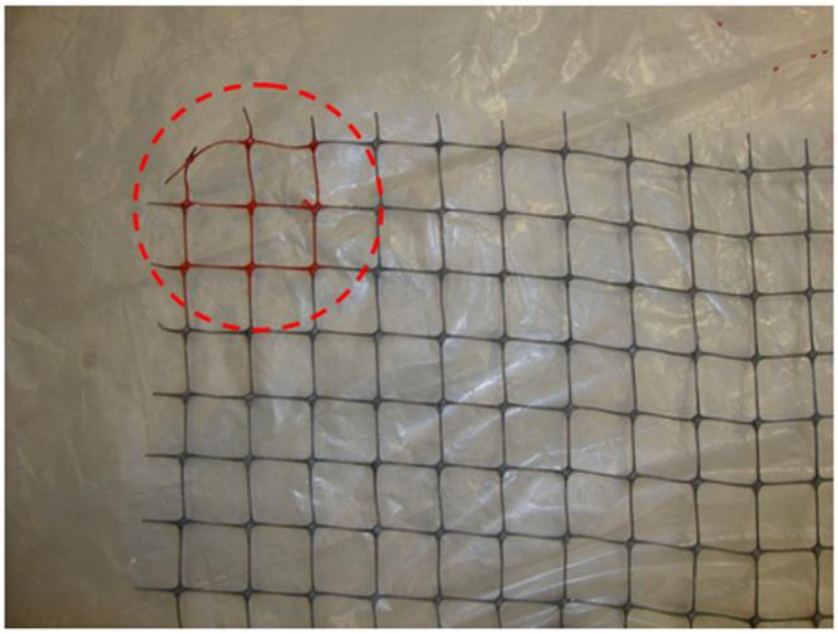

Figure 164. EGG2 single layer geogrid sample with marked damaged area

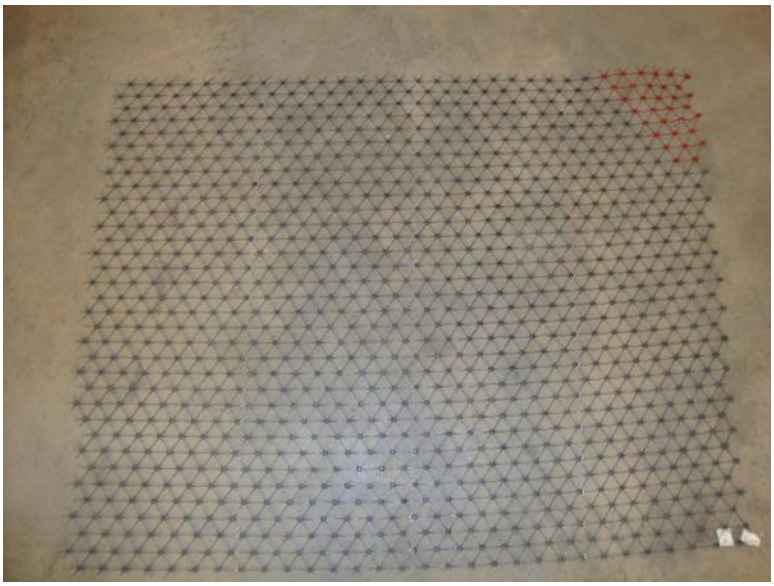

Figure 165. EGG3 geogrid sample with marked damaged area

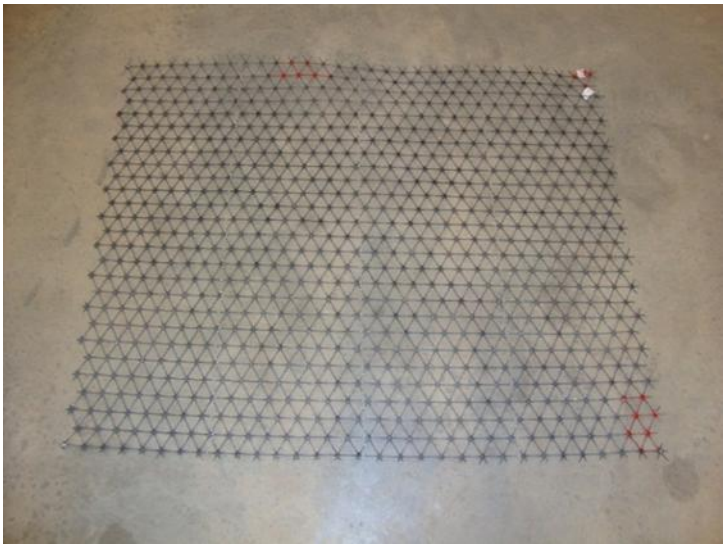

Figure 166. EGG4 geogrid sample with marked damaged area

Following the ASTM D5818 test protocol and the TRI (2006) sampling procedure guidelines, each exhumed geogrid sample was divided into four sections (indicated as Sections A, B, C and D in **Figure 167**). This was done in order to obtain representative specimens from the entire area of geogrid samples and thereby, eliminate any potential bias in specimen selection. Eight specimens were cut out from each section for in-isolation tests. As a result, a total of thirty two (32) representative specimens were obtained to carry out rib and junction strength tests in both machine and cross-machine directions (MD and XD) (**Figure 167**).

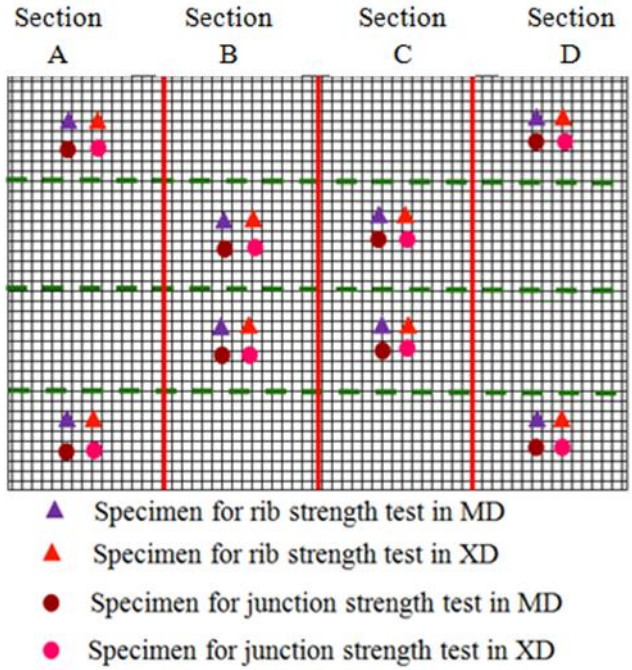

Figure 167. Layout of specimens obtained from each geogrid sample

4.12. Junction strength tests on damaged geogrid specimens

A total of eighty (80) junction strength tests (i.e. five in MD and five in XD for each of the final eight geogrid products that were shortlisted in **Table 2**) were carried out on damaged geogrid specimens according to the GRI GG2 test method. Due to the fabrication method of the non-extruded geogrids (NEGG), the magnitude of the junction strain before failure was very low. Therefore, only the ultimate junction strength of the NEGG products was determined (**Section 2.2.1.** Fabrication of junction strength testing clamps for extruded and non-extruded geogrids). However, digital imagery technique (Wang 2009, Hatami et al. 2011a) was used to determine the local strain in each junction for extruded geogrid (EGG) products. **Figure 168** shows damaged EGG1 geogrid specimens that were prepared for junction strength tests.

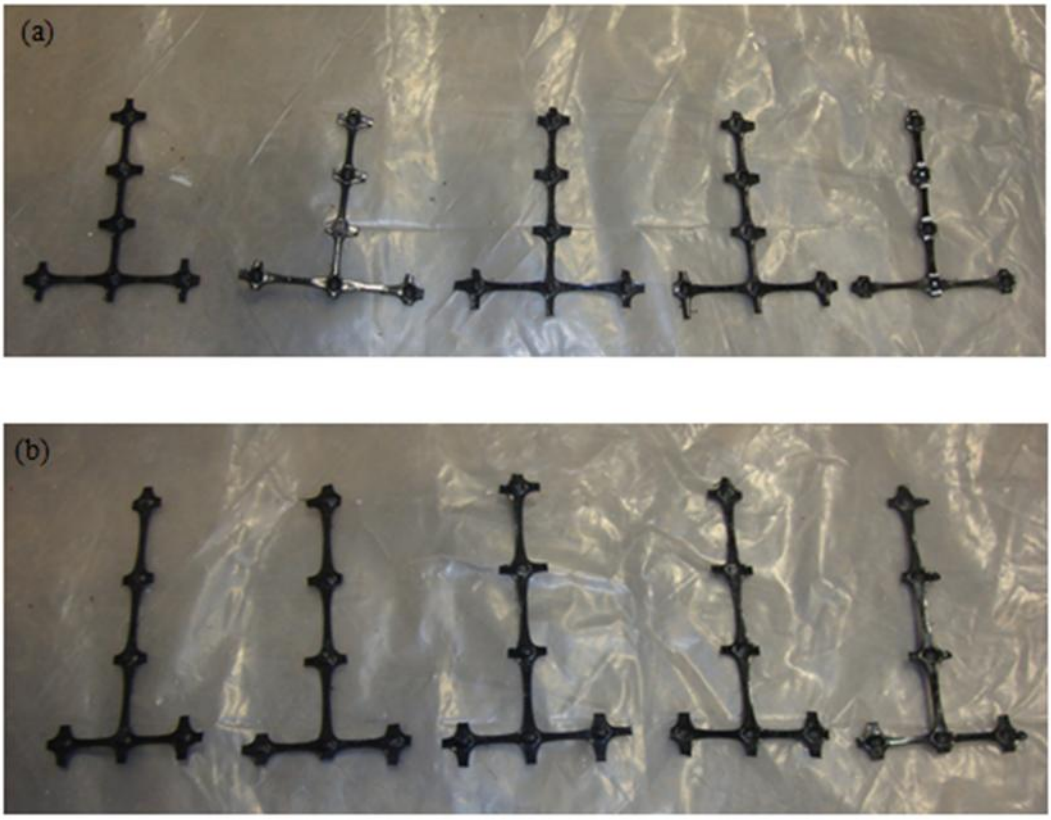

Figure 168. Damaged EGG1 geogrid junction strength test specimens before the test: (a) MD specimens, (b) XD specimens

4.13. Rib strength tests on damaged geogrid specimens

A total of eighty (80) rib strength tests (i.e. five in MD and five in XD for each of the final eight geogrid products that were shortlisted in **Table 2**) were carried out according to the ASTM D 6637 test standard. The gauge length on each specimen was marked and a non-contact digital imagery technique (Wang 2009, Hatami et al. 2011a) was used to measure the rib extension of extruded geogrids (**Figure 173**).

Figure 169 and **Figure 170** show damaged specimens of the EGG2 geogrid (single layer) before and after the rib strength tests. **Figure 171** and **Figure 172** show images of a KGG1 test specimen before and after the tests.

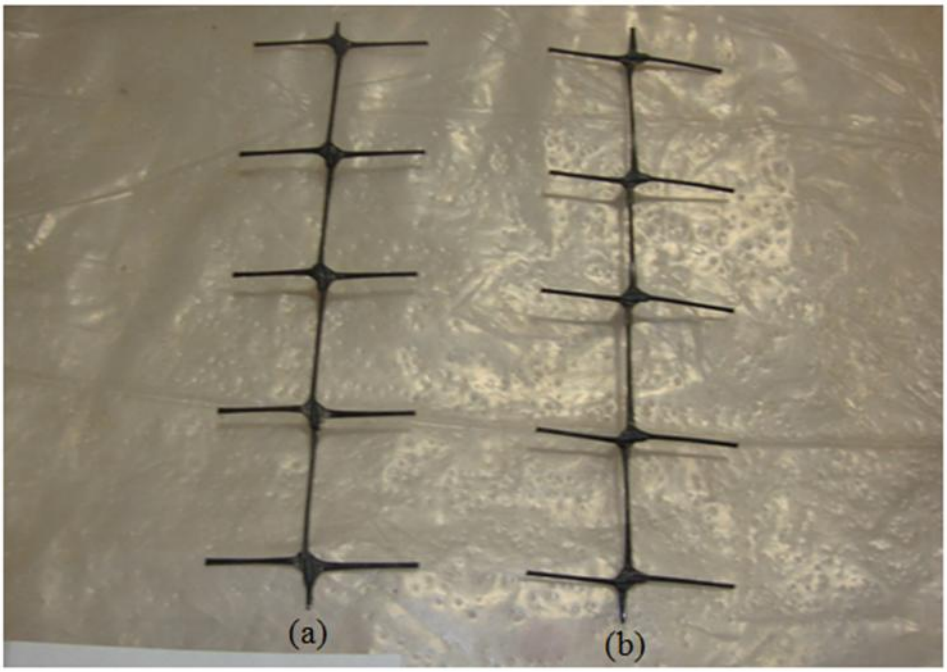

Figure 169. Damaged EGG2 (single layer) geogrid rib strength test specimens before the test: (a) MD, (b) XD

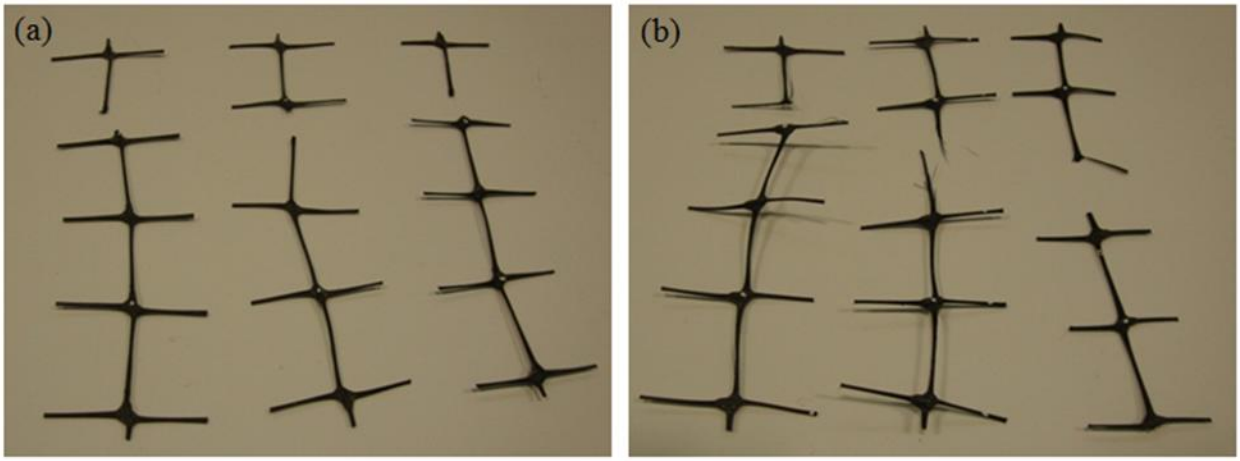

Figure 170. Damaged EGG2 (single layer) geogrid rib strength test specimens after the test: (a) machine direction, (b) cross-machine direction

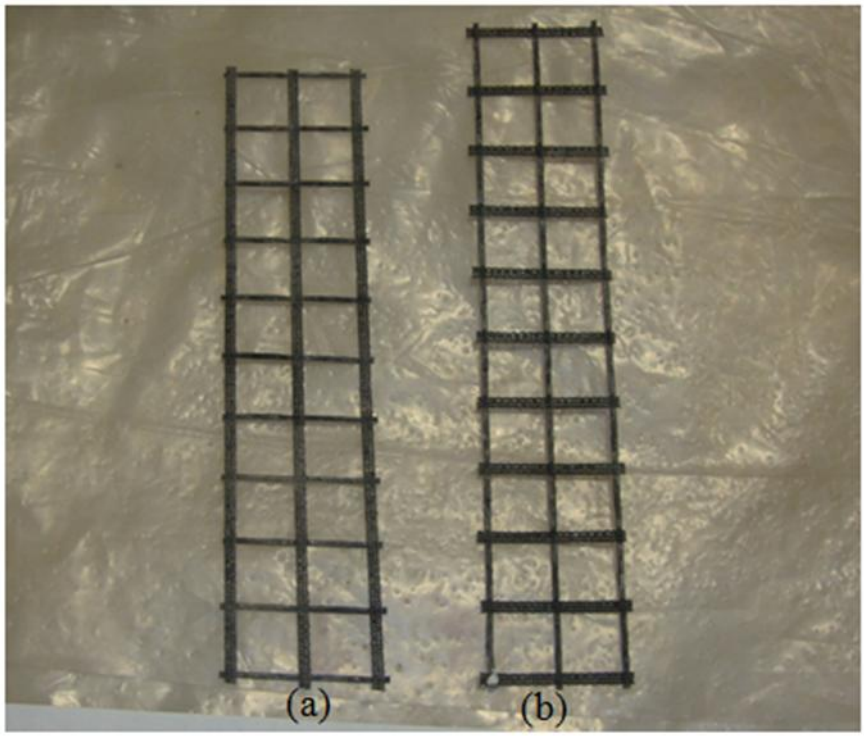

Figure 171. Damaged KGG1 geogrid rib strength test specimens before the test: (a) machine direction, (b) cross-machine direction

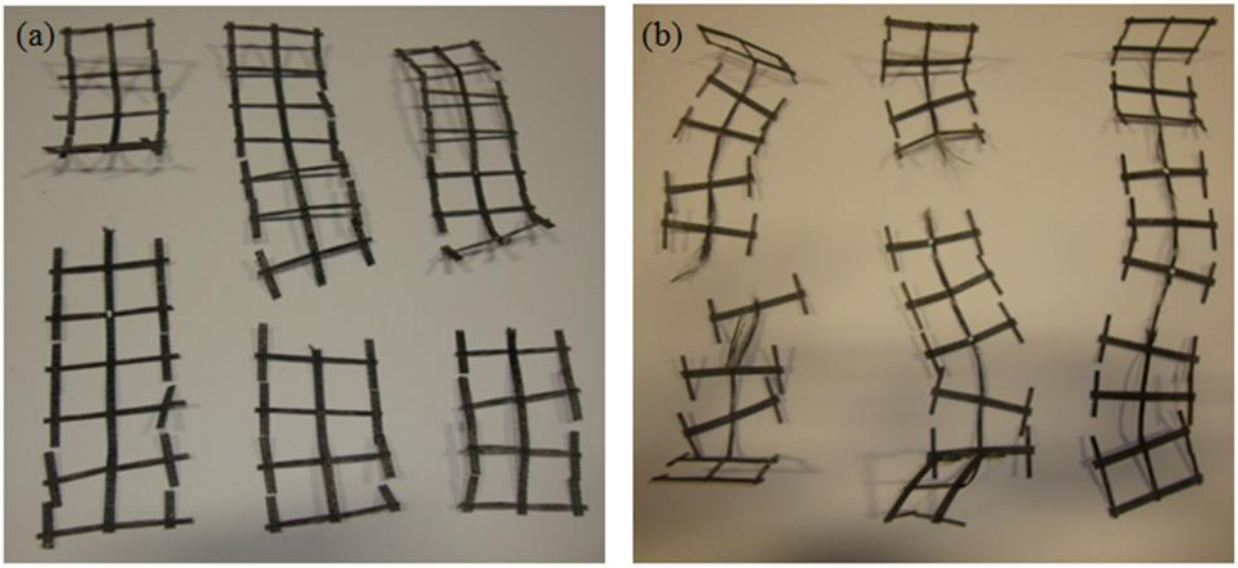

Figure 172. Damaged KGG1 geogrid rib strength test specimens after the test: (a) machine direction, (b) cross-machine direction

The EGG and NEGG specimens were tested using the clamping systems described in **Sections 2.3.1.** Fabrication of rib strength testing clamps for extruded geogrids and **2.3.2.** Fabrication of rib strength testing clamps for non-extruded geogrids, respectively. **Figure 173** and **Figure 174** show the rib strength test setup for the EGG and NEGG products, respectively.

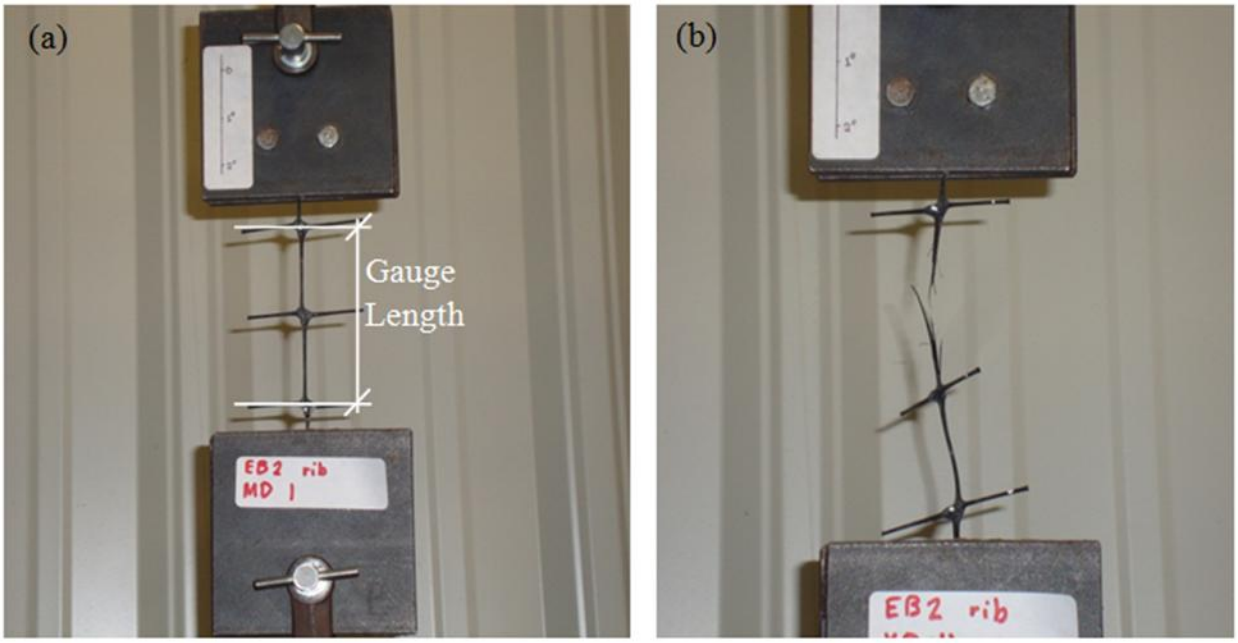

Figure 173. Rib strength testing of an extruded [EGG2 (single layer)] geogrid product: (a) before the test, (b) after the test

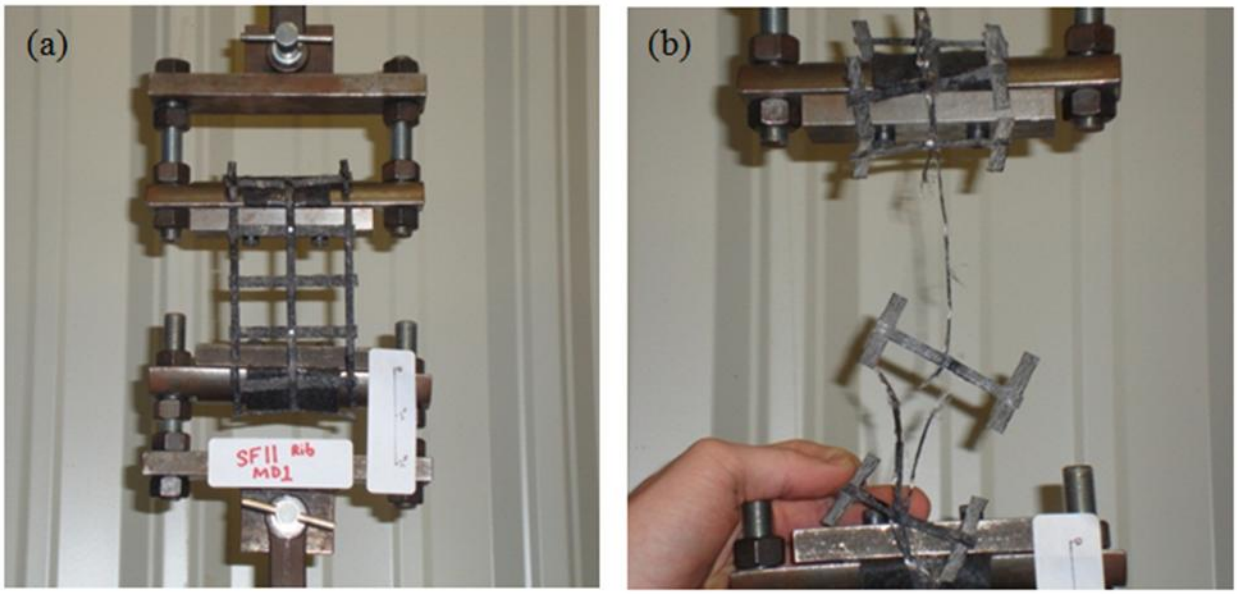

Figure 174. Rib strength testing of a non-extruded (WGG3) geogrid product: (a) before the test, (b) after the test

4.14. Installation damage reduction factors

The retained properties (e.g. rib strength and junction strength) of geogrid specimens, after they were carefully exhumed from the test bed, were compared with the corresponding values of virgin specimens (**Section 2.2.2.** Junction strength test results and **2.3.3.** Rib strength test results). Installation damage reduction factors for the eight geogrids tested in ODOT Type-A aggregate are listed in **Table 19**.

Koerner (2005) reports a range of recommended installation damage reduction factors (RF_{ID}) for unpaved roads, which vary between 1.1 and 2 for geotextiles. In our study, the range of installation damage factors for geogrids was found to vary between 1 and 2. The RF_{ID} values for the rib tensile strength at 2% strain were found to be larger than those for the ultimate strength. Overall, larger RF_{ID} values were obtained for extruded geogrid products as compared to non-extruded geogrid products. The EGG3 and EGG4 products overall showed greater RF_{ID} values compared to other products tested.

The installation damage factors for the EGG1 and EGG2 geogrids were compared with the values provided by the manufacturers. Manufacturers' data on installation damage factors were not found for other geogrid products. According to the manufacturers' data, the installation damage factors for EGG1 and EGG2 are 1.16 (86%) and 1.11 (90%) respectively, when used with gravel. These values are comparable with the values reported in **Table 19**. However, it should be noted that the geogrids RF_{ID} values depend on the type of materials/aggregate used in the tests. In addition, RF_{ID} values are reported for ultimate strength values only, whereas the results given in **Table 19** indicate that different RF_{ID} values should be used for different index properties of geogrids. However, such data are typically not available for low-strain rib tensile strength or junction strength of geogrid products.

Table 19. Installation damage factors of the geogrids tested in this study

Geogrid		Installation Damage Reduction Factors (RF_{ID})							
		RF_{ID} for rib strength at 2% strain		RF_{ID} for rib strength at 5% strain		RF_{ID} for ultimate rib strength		RF_{ID} for ultimate junction strength	
		MD	XD	MD	XD	MD	XD	MD	XD
EGG	EGG1 (ODOT Type-2)	1.7	1.3	1.2	1.1	1.1	1.1	1.0	1.0
	EGG2 (single layer)	1.3	1.2	1.1	1.2	1.0	1.0	1.0	1.0
	EGG3	1.1	1.5	1.3	1.5	1.6	1.8	1.0	1.0
	EGG4	1.1	1.2	1.1	1.2	1.4	1.3	1.0	1.0
NEGG	WGG1	1.0	1.0	1.0	1.3	1.5	1.1	1.0	1.0
	WGG2	1.1	1.0	1.3	1.1	1.0	1.0	1.0	1.0
	WGG3	1.3	1.0	1.0	1.2	1.0	1.0	1.3	1.0
	KGG1	2.0	1.1	1.2	1.0	1.0	1.0	1.1	1.0

5. Laboratory testing of aggregates

5.1. Gradation analysis

ODOT Type-A aggregates were purchased from Dolese's quarry in Oklahoma City and transported to the Fears laboratory at OU. The use of Type-A aggregates in this study was based on the feedback from Mr. Jeff Dean at ODOT who noted that these aggregates are currently the most commonly used type of aggregates in ODOT projects. Sieve tests were performed on the aggregates at the OU Fears and Broce Laboratories according to the ASTM C136-06 test standard (**Figure 175**).

Figure 175. Sieve analysis equipment at the OU Broce Lab

Two representative gradation curves from the sieve analyses are shown in **Figure 176**. It is observed that gradation curves from the two trials are reasonably close to each other and both fall within the upper and lower limits of the range defining ODOT Type-A aggregates (ODOT 2009). These aggregates were used in the pullout and plate load tests carried out in this study. The sieve analysis of aggregates was repeated after every four pullout tests to ensure that their gradation curve fell within the upper and lower limits of the ODOT Type-A aggregate. If that was not the case, the aggregates were discarded and new aggregates were used for the following tests.

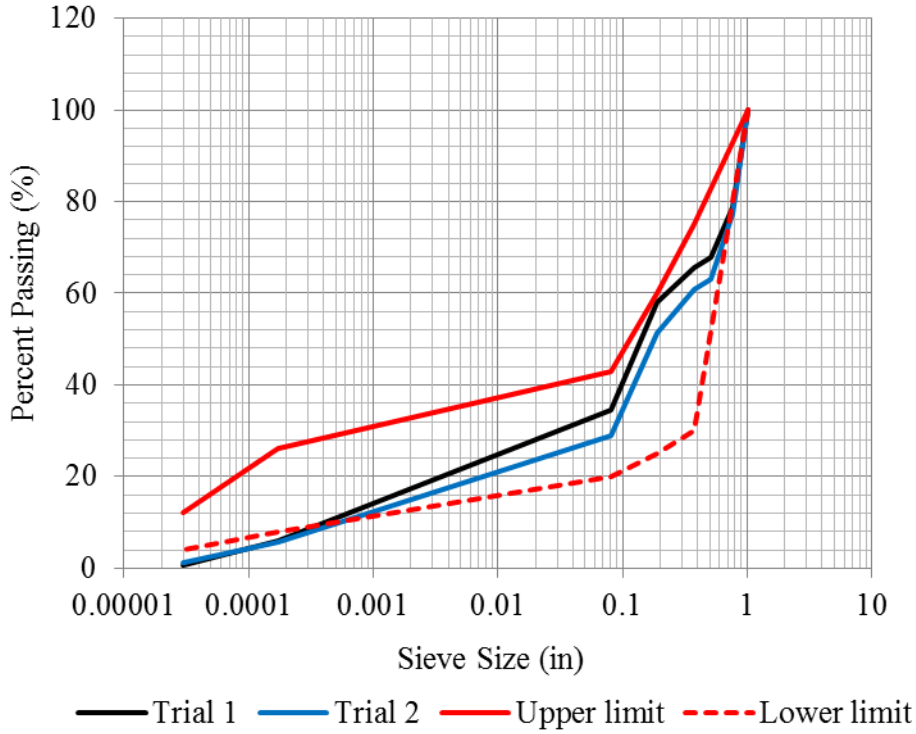

Figure 176. Gradation curves for the ODOT Type-A aggregates used in this study

5.2. Los Angeles (LA) abrasion tests

A series of LA abrasion tests were carried out on ODOT Type-A aggregates as per the ASTM C131-06 test standard to determine their durability (**Figure 177**). This test has been widely used as an indicator of the relative quality of various sources of aggregate having similar mineral compositions. This test also measures the degradation of aggregate minerals due to loading over a project service life. A rotational grinding drum that contained 11 steel balls was used and underwent 500 revolutions to perform the LA abrasion tests. Aggregates were washed and their dry weight after 24 hours was measured. The amount of aggregate weight loss was used to determine the LA abrasion values (**Table 20)**.

Figure 177. Los Angeles (LA) abrasion test

Table 20. LA abrasion test results for ODOT Type-A aggregates

Aggregate Type	Grading Type[1]	% of Loss	% Max Allowable Loss[2]
ODOT Type-A (ODOT Specification)	B	20	50
ODOT Type-A This Study	B	21	50

[1] Type B grading in ASTM C131-01 test standard indicates the use of eleven (11) steel balls. Each load of aggregate for testing should have a mass of 10 ± 03 lbs.

[2] Maximum allowable loss according to ODOT requirements for base aggregates (ODOT 2009, Specification 703.01 C).

6. Plate load tests on aggregate base-subgrade soil models

6.1. Static plate load tests

A total of five static plate load tests were performed and the results were compared to determine the influence of geogrid reinforcement layer and geotextile separator arrangement at the interface between the base course and the sand substrate on the performance of the reinforced base models. The tests were carried out in a 4 ft (L) × 4 ft (W) × 2 ft (H) test box. Styrofoam panels were placed against the walls of the test box on the inside to mitigate boundary effects against the lateral movement of aggregates in the box.

The primary objective of the plate load tests was to compare the reinforcing performance of different geogrids in nominally identical conditions (as opposed to simulating any specific subgrade soils). Therefore, the test box was filled with 14 inches of loose sand (at a relative density of 28%) as the subgrade and 8 inches of base aggregate layer. 4 ft (L) × 4 ft (W) geogrid specimens were placed at or near the base-substrate interface in different reinforced models as summarized in **Table 21**. Details of the plate load test setup, instrumentation and procedure are given by Wang (2009).

Table 21. Summary of static plate load tests

Plate Load Test Number	Sand Thickness (in)	Geotextile Separator	Type of Geogrid	Location of Geogrid	Aggregate Thickness (in)	Descriptions
1	14	Yes	Not Used	-	8	Not loaded. Only for compaction verification purposes
2	14	Yes	Not Used	-	8	
3	14	No	EGG1	On Sand	8	
4	14	Yes	EGG1	1 in above GT	8	1 in aggregate was placed above GT
5	14	No	Not Used	-	8	
6	14	Yes	EGG1	Directly on GT	8	GG and GT were in contact with each other

Figure 178 shows the load-settlement results for the test cases listed in **Table 21**. These results indicate that: 1) the geotextile separator did not provide any significant reinforcing effect within the conditions of the test setup; 2) placing the geogrid at the aggregate-substrate interface without the separator layer improved the interface strength properties and helped mobilize the tensile capacity of geogrid from the start of the test. In other words, adequate interlocking with aggregates is key to achieving effective reinforcement; and 3) placement of a thin aggregate

layer between the geogrid and geotextile layers can be an effective way to provide both the reinforcement and separation functions in roadways. However, practical solutions need to be developed for placing a thin aggregate layer over a separator fabric underlain by a weak subgrade.

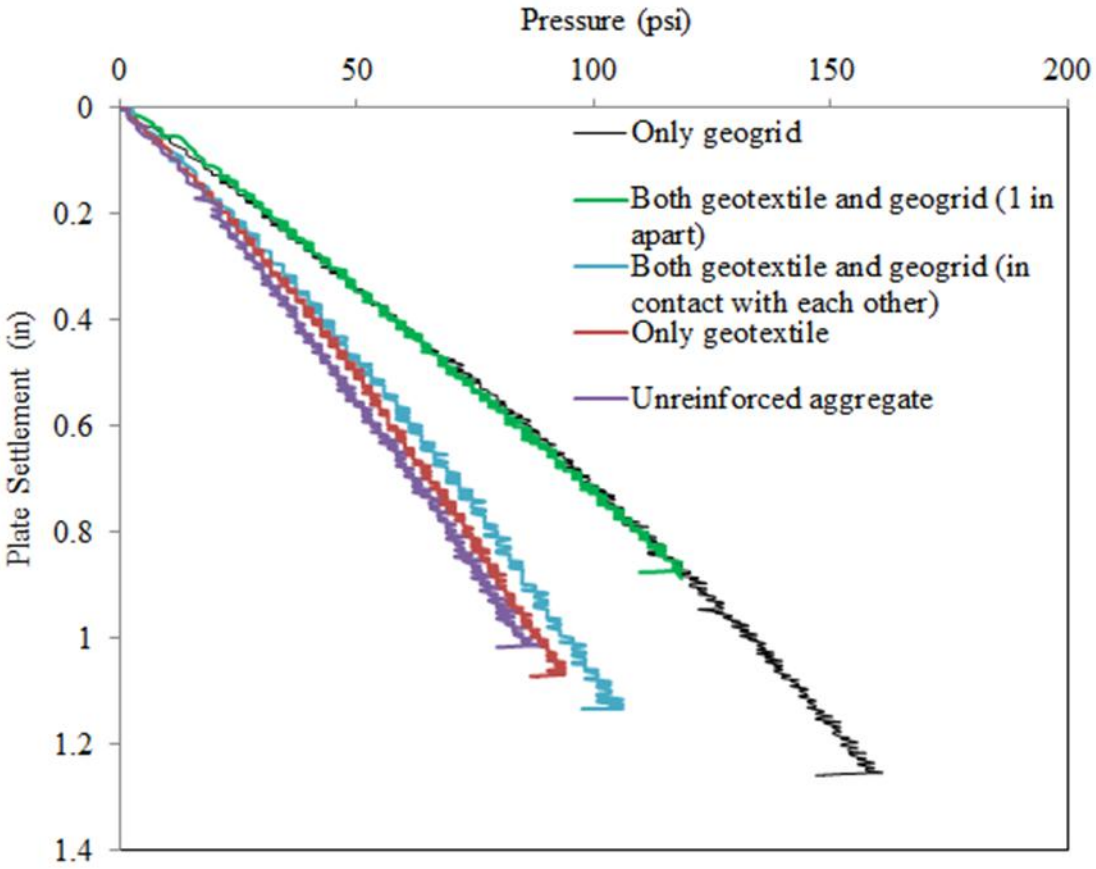

Figure 178. Load-settlement responses of aggregate-sublayer models with and without a geotextile separator

6.2. Cyclic plate load tests

6.2.1. Installation and preparation of new Data Acquisition System

A new data acquisition system with LabVIEW 2010 software was purchased to measure the starin gauge outputs. A graduate student with LabVIEW expertise calibrated the program for the instruments (e.g. load cell, LVDTs, wire potentiometers and strain gauges). A picture of the newly installed data acquisition system is shown in **Figure 179**.

Figure 179. A New Data Acquisition System at the OU Fears Laboratory

6.2.2. A new test station for cyclic plate load tests

The existing loading frame and test box were upgraded and retrofitted to achieve added safety and precision for the cyclic loading tests planned in this study. The structural analysis and design of the testing frame (**Figure 180**) and the new and larger test box (**Figure 181**) were carried out using the computer program SAP 2000.

Figure 180. Redesigned and retrofitted steel loading frame at the Fears laboratory

Figure 181. The newly fabricated large steel test box [6 ft (L) × 6 ft (W) × 3.5 ft (H)] for cyclic plate load tests

6.2.3. Installation and preparation of a new automated dynamic controller unit

A new automated FlexTest 40 dynamic controller unit with a new computer and application software was purchased for the plate load tests (**Figure 182**). The system was calibrated and tuned and a trial cyclic test was carried out in the smaller test box to ensure that the controller system was in a good operating condition.

Figure 182. Cyclic loading tests on reinforced base-substrate models using a new controller system

6.2.4. Strain gauge attachment technique

Strains in geosynthetic reinforcement were measured using model YEFLA-5-3L foil strain gauges (manufactured by Tokyo Sokki Kenkyujo Co., Ltd.) with a gauge factor of 2.14 ± 2% and a gauge length of 0.2-inch. These strain gauges are capable of measuring large strains up to 15%. Wang (2009) found that these foil strain gauges are suitable to measure the strains in both extruded and non-extruded geogrids. The strain gauge installation procedure used for extruded PP (Polypropylene) geogrids is as follows:

a. The geogrid specimen was placed on a smooth and dry surface. The surface of the geogrid rib where the strain gauge needed to be attached was prepared. The outline of the strain gauge was marked on the rib. The surface was cleaned using industrial tissue and/or cotton swabs (**Figure 183**).

b. A piece of 320b grit sandpaper was used to roughen the geogrid surface (**Figure 184**). The surface was then cleaned from any dust and residues due to abrasion using a fine brush (**Figure 185**).

c. A poly-primer (**Figure 186**) was used to clean the geogrid surface at the strain gauge location.

d. The strain gauge was aligned carefully in its position. A piece of Scotch tape was applied to the gauge backing and Cyanoacrylate (CN) adhesive was applied to the gauge (**Figure 187** and **Figure 188**). The Scotch tape helped to fix the gauges in place and adjust their location as necessary (**Figure 189**). The gauges were centered on the prepared ribs and held in place with the Scotch tape while the adhesive was cured.

e. Direct pressure was applied to the gauge (**Figure 190**) for at least one minute and the adhesive was allowed to cure for approximately five minutes before the tape was peeled off the backing (**Figure 191**).

f. The gauge surface was covered with the coating material, M-Coat A (Air-drying Polyurethane coating; **Figure 192**). Wire ties were used to hold the strain gauge wires in position (**Figure 193** and **Figure 194**). The strain gauges were left in air for at least 24 hours.

g. Silicon sealant was injected into a length of flexible tubing (**Figure 195**) that was split open along its length and extended beyond the gauge and its terminal strip.

h. The silicon-filled tube was placed around the gauge (**Figure 196**). It was left for 24 hours in order to dry fully (**Figure 197**). Strain gauge lead wires were then ready to be connected to the readout device.

Figure 183. Cleaning the surface of geogrid with industrial tissue or cloth

Figure 184. Abrasive paper is used to roughen the surface of the extruded geogrid

Figure 185. A brush is used to remove dust due to abrasion

Figure 186. Adhesive, primer and sealant used in this study


Figure 187. Application of adhesive material to the geogrid

Figure 188. Application of adhesive material to the back of the strain gauge base

Figure 189. Gauges are held in place with the Scotch tape while the adhesive is cured

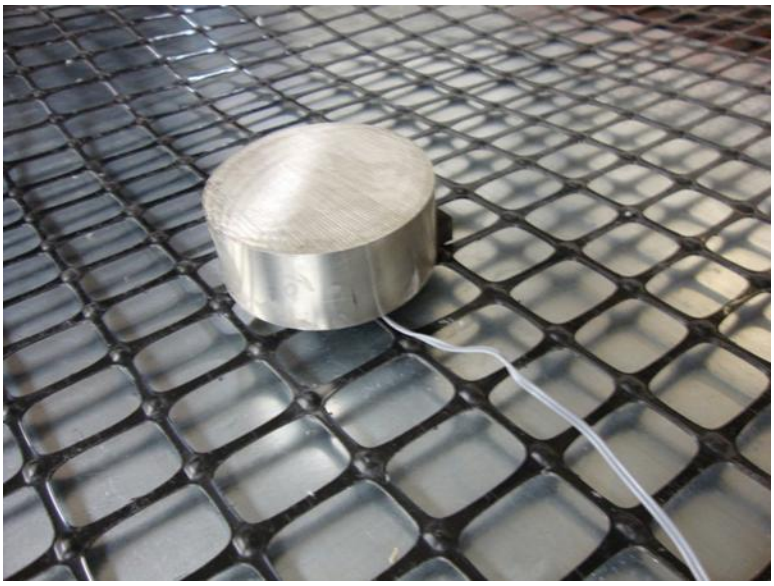

Figure 190. Pressure is applied to the gauge to cure

Figure 191. The tape is peeled off carefully from the strain gauge

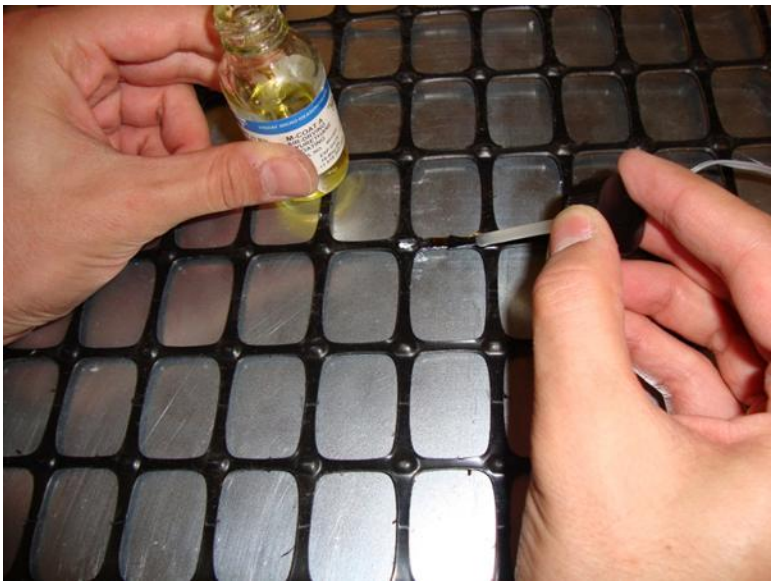

Figure 192. The gauge surface is covered with coating material

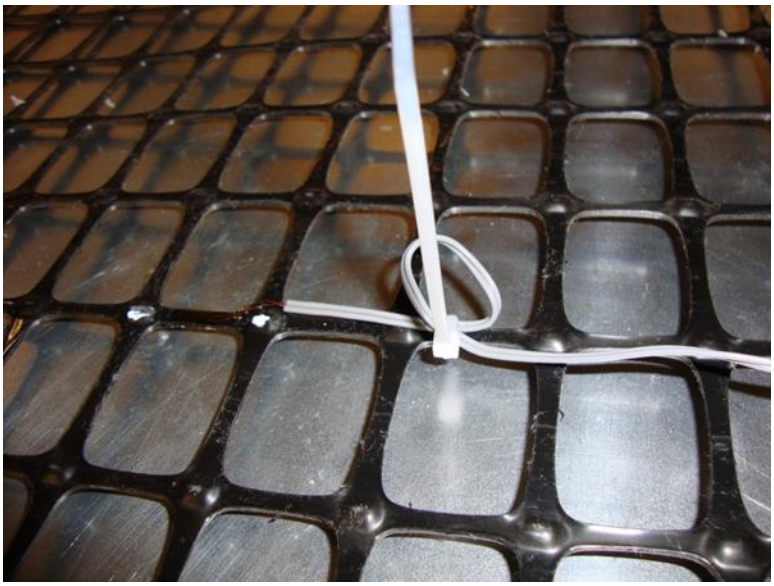

Figure 193. Wire tie is used to hold the strain gauge wire in position

Figure 194. Geogrid with strain gauges attached

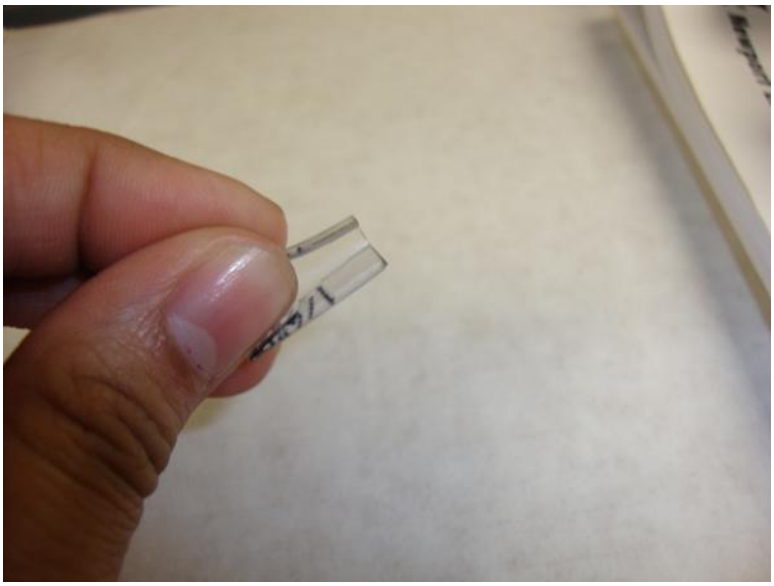

Figure 195. Flexible rubber tube is used to cover strain gauges

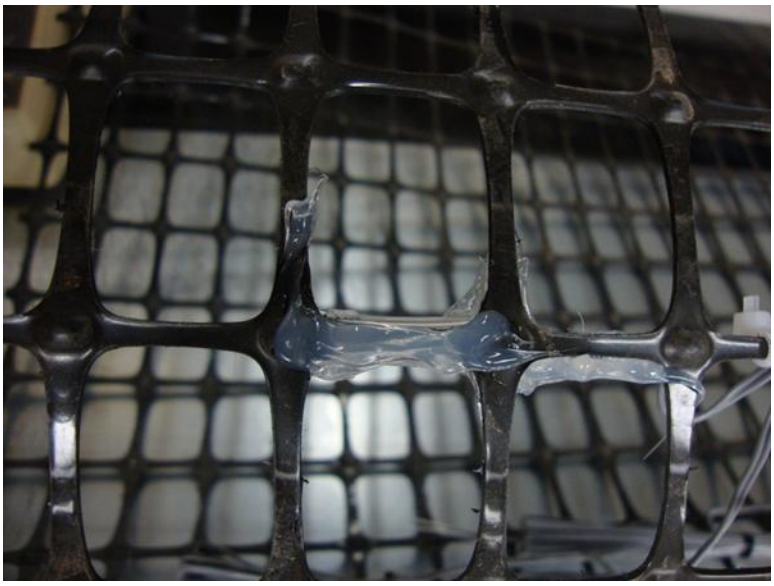

Figure 196. Siliocon rubber sealant is applied on the strain gauge

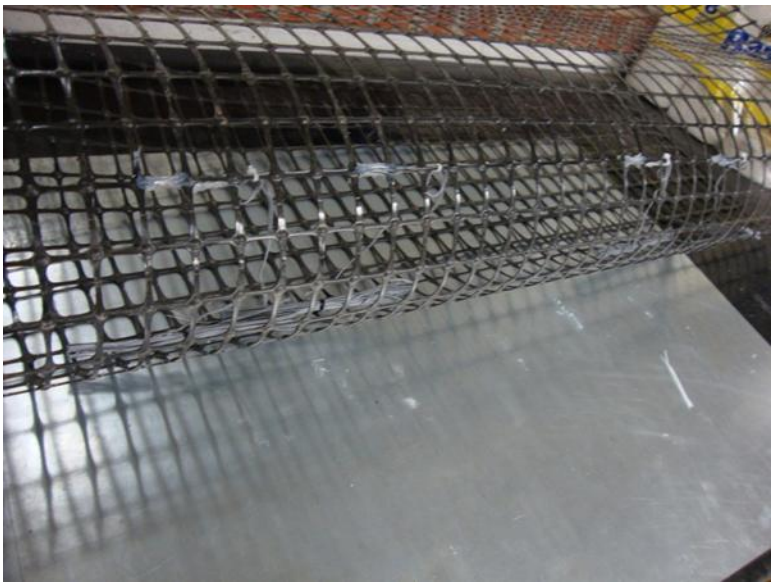

Figure 197. Geogrid sample after the installation of strain gauges

The strain gauge installation procedure used on the polyester geogrid (i.e. WGG1) was slightly different. A small wire brush was used to remove the PVC coating of the geogrid. Then the strain gauge was directly attached to the polyester yarns of the geogrid following the same attachment procedure described for extruded geogrids.

Geogrid specimens were prepared for cyclic plate load tests (**Figure 198** through **Figure 200**). Two 6 ft × 6 ft geotextile layers were also prepared for use underneath the subgrade layer in order to prevent sand from entering the Styrofoam area in the lower section of the test box, and at the subgrade-base interface (**Figure 201**).

Figure 198. EGG1 (ODOT Type-2) geogrid specimen to be used in a cyclic plate load test (before instrumentation)

Figure 199. WGG1 geogrid specimen to be used in a cyclic plate load test (before instrumentation)

Figure 200. KGG1 geogrid specimen to be used in a cyclic plate load test (before instrumentation)

Figure 201. Geotextile for use underneath the subgrade layer in the test box

The local strain recorded by the strain gauge may not be the same value as the average strain over a gauge length. The type of strain gauge, bonding materials, bonding method and the geogrid used could each influence the performance of the strain gauge. Therefore, for each type of geogrid used (i.e. EGG and NEGG), strain gauges were individually calibrated in order to determine the relationship between their local strain and the "global" strain from cross-head displacements in in-isolation tensile tests (ASTM D6637). Two sets of ASTM D6637 tests were carried out using geogrid specimens EGG1 (representing an EGG) and WGG1 (representing an

NEGG; **Figure 202**) with strain gauges attached using the bonding techniques described in **Section Strain** gauge attachment technique**.**

Figure 202. Determination of calibration factor of strain gauges attached to NEGG geogrid products (test setup following the ASTM D 6637 test standard)

Each geogrid specimen was instrumented with strain gauges for the cyclic plate load test. It took typically two days to prepare each specimen as pressure needed to be applied to the gauges to cure for 24 hours (**Figure 203**). It took another 24 hours for the silicon sealant inside the protective rubber tube to dry (**Figure 204**). **Figure 204** and **Figure 205** show the EGG and NEGG geogrid specimens instrumented with strain gauges.

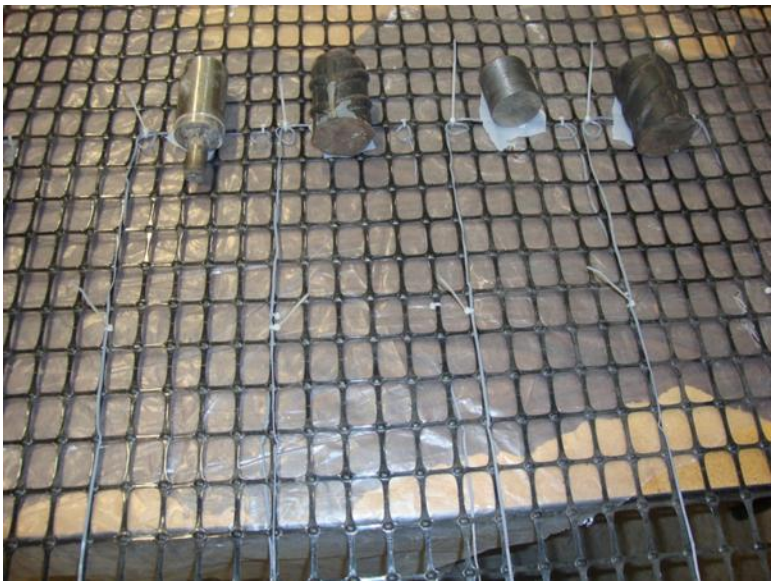

Figure 203. Pressure is applied to the gauges to cure their adhesive layer

Figure 204. EGG1 (ODOT Type-2) geogrid specimen instrumented with strain gauges

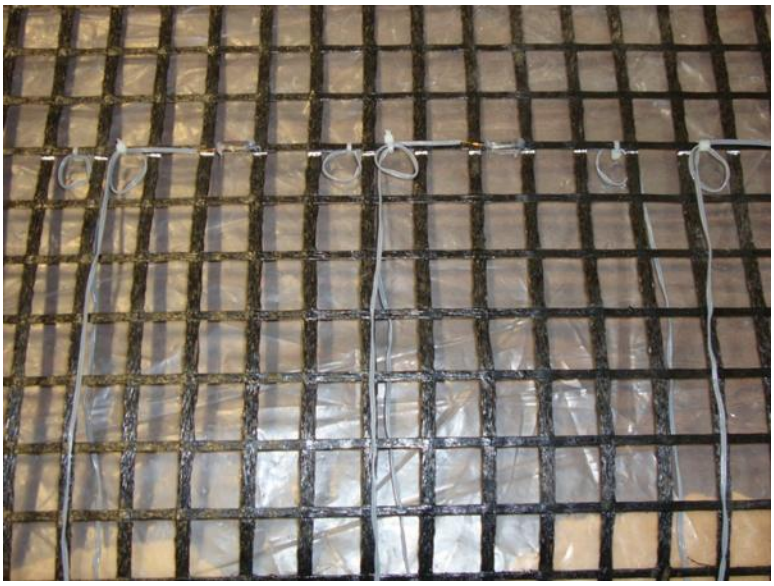

Figure 205. WGG3 geogrid specimen instrumented with strain gauges

6.2.5. Cyclic plate load test setup

Figure 206 through **Figure 222** show different stages of setup and procedure for the large- scale cyclic plate load tests. A horizontal steel beam at the middle of the test frame and spanning the width of the test box served as a reaction beam to apply a concentric load on the test models (**Figure 206**). An actuator was positioned on the middle of the horizontal beam. It was connected to the hydraulic pump and the cyclic pressure controller system. Before placing materials in the test box, the box was lined with Styrofoam panels to reduce the boundary effects (**Figure 207**). A 12-inch block of Styrofoam panels was placed at the bottom of the test box and 1-inch thick panels were placed against the walls of the test box to mitigate the boundary effects against the lateral movement of aggregates. A geotextile layer was placed underneath the subgrade (loose sand) layer to prevent it from entering the Styrofoam block in the lower section of the test box (**Figure 208**).

The test box was then filled with 17 inches of uniformly graded loose sand as subgrade and 17 inches of ODOT Type-A aggregate for the base layer. The aggregate and sand layers were separated using a woven geotextile. The sand unit weight in as-placed condition was 78 lb/ft^3, equivalent to a relative density of 28%. The internal frictional angle of the sand at its as-placed unit weight was determined to be 42º from direct shear tests (Wang 2009). The sand was pluviated in a loose condition to a uniform depth without any compaction to simulate a weak subgrade. A 5.9 ft (L) × 5.9 ft (W) geogrid specimen was placed at 1 in above the sand-aggregate interface inside the aggregate to allow for complete interlocking with the aggregate.

A 12-inch diameter steel loading plate placed was attached to the actuator along with the 20-kip load cell and placed on the aggregate layer directly beneath the actuator. The cyclic load was applied and the settlement of the circular loading plate was measured using the displacement output from the dynamic controller system. In addition, a total of eight extensometers (wire

potentiometers) were attached to the steel cross beam which supported the actuator. The calibration factor for each wire potentiometer was determined prior to the test.

The following information was found useful in developing the instrumentation layout of the cyclic plate load tests: Abu-Farsakh and Chen (2011) found that largest tensile strains developed directly beneath the center of the cyclic loading plate (where the maximum lateral movement of the base course occurred), and became negligible at a distance from the loading plate. This distance was found to be approximately 1.5D (D is the loading plate diameter) from the center of the loading plate for the geogrid placed at the subgrade-base interface and nearly 1.0D from the center of the loading plate for the geogrid placed at the middle of the base layer. Wang (2009) also found that, reinforcement strains become negligible at approximately 1.0D-1.5D from the center of the loading plate. Wang (2009) also reported that the settlement of aggregate layer at the surface was negligible beyond 1.25D from the center of the loading plate.

Each reinforced test model was instrumented to measure the reinforcement strain, top surface deflection and settlements at the bottom of the aggregate layer. The instrumentation in all test cases included eight wire potentiometers (WPs) and eight strain gauges. The strain gauges were attached on the bottom and on the top the geogrid to measure its strains. Four WPs were mounted on one the bottom side of the reaction beam and were connected to the loading plate and the separator geotextile through the aggregate layer at the radial distances of 6 in, 9 in, 12 in and 18 in from the center of the circular loading plate as shown in **Figure 209** and **Figure 210**. This is because the WPs were attached to the bottom flange of one of the two reaction beams that were located on the two sides of the central shaft attached to the loading plate (**Figure 217**).

Four additional extensometers (WPs) were placed on the other side of the reaction beam from the center of the loading plate at otherwise the same distances. The latter four WPs were attached to thin steel plates to form vertical tell-tales to measure the settlement at the top of the aggregate layer at selected locations (**Figure 216** and **Figure 217**). The magnitudes of the cyclic load applied to the circular plate and its settlement were recorded during the test using dynamic controller system software (**Figure 182**). The deformation of the eight WPs and the elongation of the eight strain gauges with time during the test were recorded using the program LabVIEW 2010 of the Data Acquisition System (**Figure 221**).

Figure 206. The redesigned and retrofitted steel loading frame with the actuator, which is connected to the hydraulic pump and the controller system

Figure 207. Styrofoam panels placed at the bottom and against the walls of the test box

Figure 208. Cyclic plate load test box after placing the geotextile separator on Styrofoam panels on the bottom of the test box

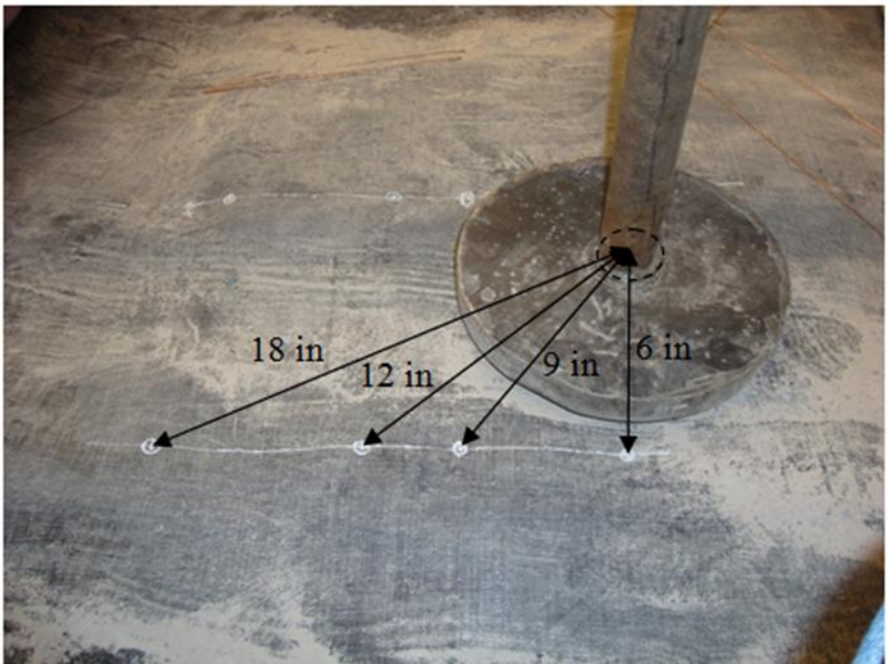

Figure 209. Marked locations of extensometer readings to measure deformation profile of the aggregate layer at the bottom due to cyclic loading

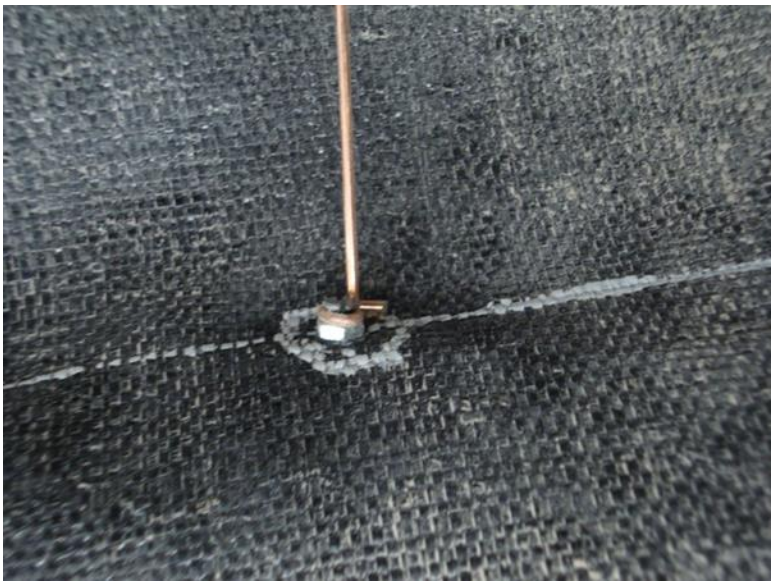

Figure 210. Attachment of brass wires to geotextile separator to measure its settlement

Figure 211. 1-inch-thick aggregate layer placed on the top of the geotextile separator

Figure 212. Placing geogrid reinforcement on the 1-inch-thick aggregate layer

Figure 213. Careful placement of aggregate on the geogrid layer

Figure 214. First 3 inches of compacted aggregate layer placed on the geogrid reinforcement

Figure 215. Brass wires connected to the wire potentiometers to measure the base layer deformation

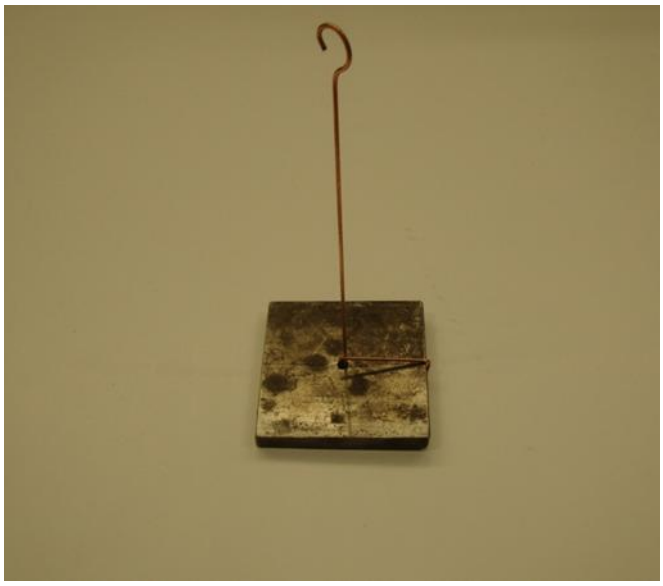

Figure 216. Telltale plates for the wire potentiometers to measure the surface deflection of the aggregate layer

Figure 217. Setup of the wire potentiometers on the top of the aggregate layer

Figure 218. Vertical plate telltale to measure the aggregate deformation near the circular loading plate

Figure 219. Connecting strain gauges to the DAS (Data Acquisition System)

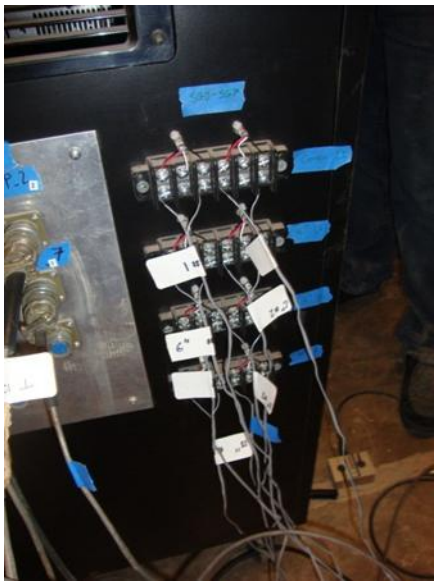

Figure 220. Eight strain gauges connected to the DAS

Figure 221. Monitoring data in the Data Acquisition System while the cyclic plate load test is in progress

Figure 222. The position of the circular loading plate after the test is complete

6.2.6. Cyclic plate loading regime and test results

Prior to carrying out the periodic load tests, a preliminary static test was carried out to check the performance of the loading assembly, controller and the data acquisition system. In this test, a total load of 9 kips was applied monotonically on a reinforced base-subgrade model in 10 equal increments using a 12-inch diameter steel plate. A 9-kip load was selected as the maximum applied load in these tests because it represented a tire inflation pressure of 80 psi which simulated dual tires under an equivalent 18-kip single-axle load (Abu-Farsakh and Chen 2011). A piece of EGG1 (ODOT Type-2) geogrid was used as the reinforcement layer at the interface of the 6-inch base layer and a loose sand substrate. The corresponding load-settlement data are shown in **Figure 223.**

Following the preliminary static test, a series of cyclic plate load tests were carried out on a reinforced model using the BX1200 and SF11 geogrids as the geosynthetic reinforcement. A periodic load with the peak magnitude of 9 kips was applied on the model and the settlement of the aggregate layer at the surface, deformation of the base layer at the bottom, and the strain distribution in the geogrid reinforcement were measured. The following loading regime was used in the cyclic plate load tests**:** First, the load was monotonically increased from an initial seating load of 0.5 kip to the final magnitude of 9 kips in 10 equal increments. Then, a 1-Hz force-controlled periodic load was applied, which included a 0.1-sec loading period followed by a 0.9-sec resting period. The periodic load amplitude varied between 0.5 kip and 9 kips for 1,000 load cycles. **Figure 224** and **Figure 225** show the load-settlement response data for the preliminary periodic plate load tests.

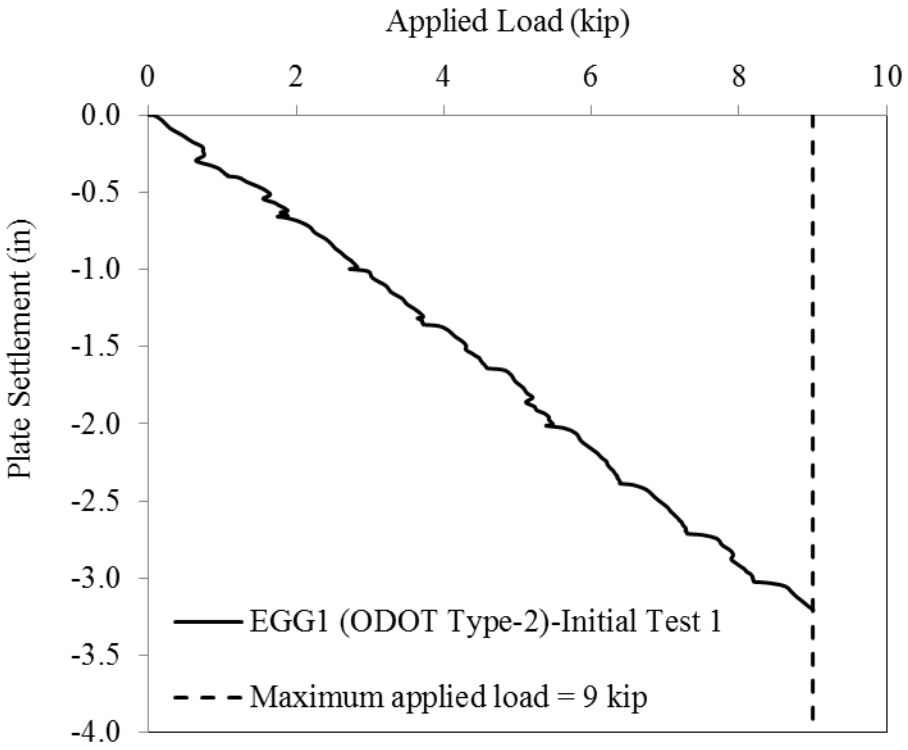

Figure 223. Load-settlement response of the first (incremental static loading) plate load test on an aggregate-loose sand subgrade reinforced with a layer of EGG1 (ODOT Type-2) geogrid at the interface

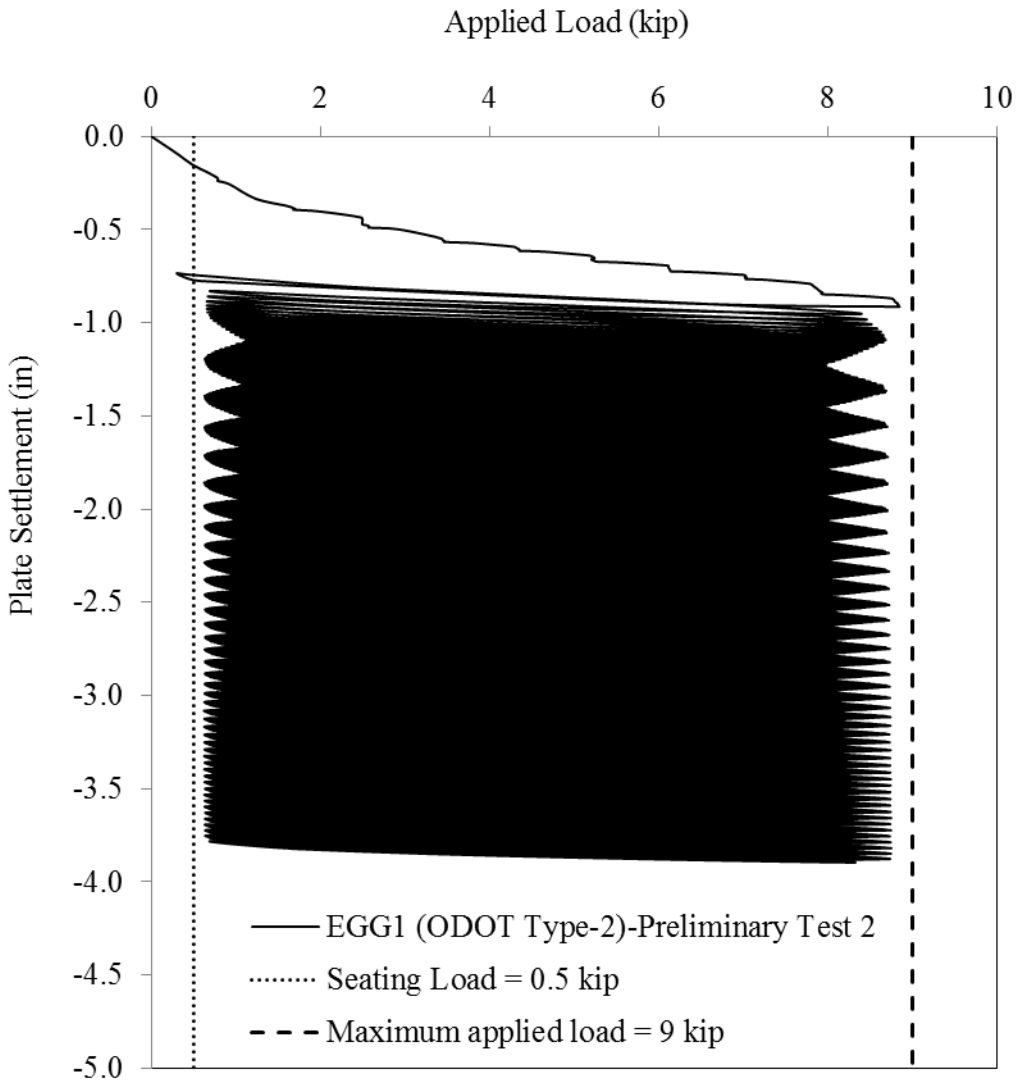

Figure 224. Load-settlement response of the second plate load test (periodic loading regime, number of cycles = 1000). The magnitudes of the target seating load and maximum load are shown with vertical dashed lines on the figure.

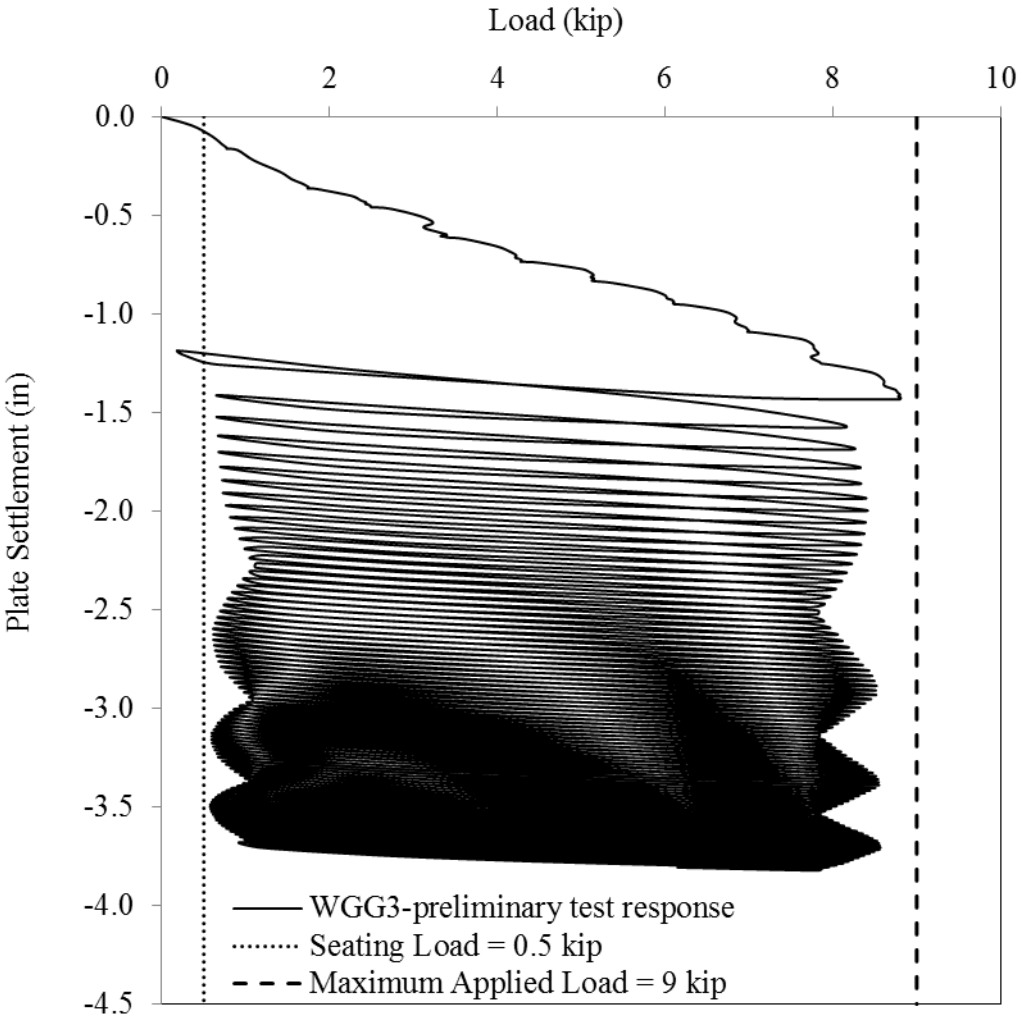

Figure 225. Load-settlement response of the third trial plate load test (periodic loading regime, number of cycles = 1000). The magnitudes of the target seating load and maximum load are shown with vertical dashed lines on the figure

The preliminary tests indicated that the subgrade sand was too weak to support the 1000 dynamic loading cycles. Hence, a series of CBR tests was carried out on the subgrade sand at different compaction levels according to ASTM D1883-07 test protocol to determine a suitable CBR value for the sand in as-placed conditions. From the results of these CBR tests, it was found that a subgrade with CBR value equal to 4 would have adequate strength and stiffness to complete the cyclic plate load tests. **Figure 226** shows the CBR test results for the subgrade sand with a unit weight of 103.50 lb/ft^3.

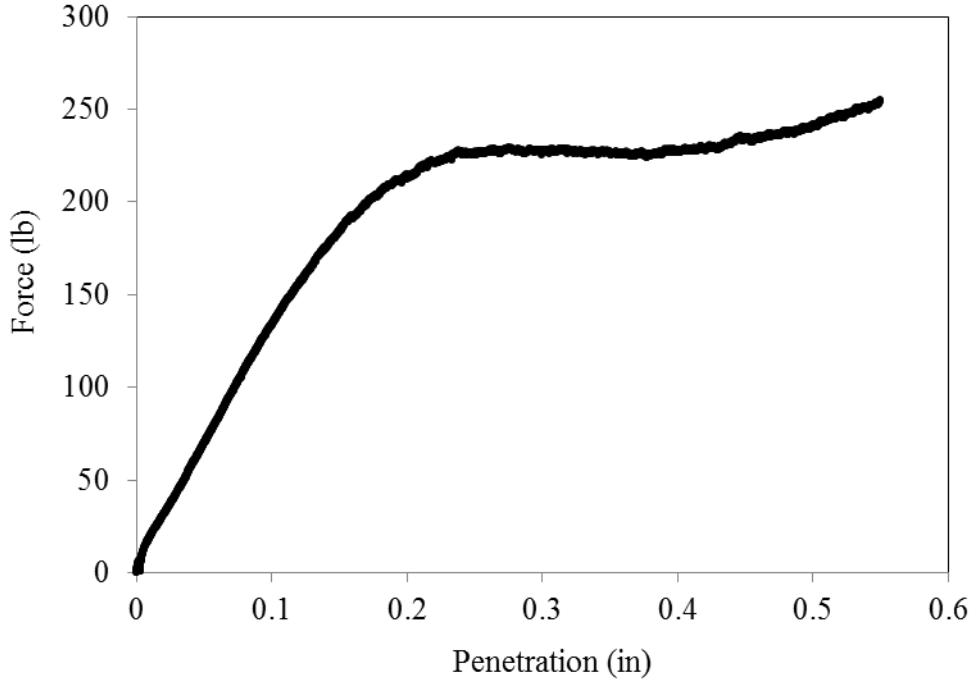

Figure 226. CBR test result for the subgrade sand with unit weight of 103.5 lb/ft^3

Once a suitable CBR value for the subgrade sand was determined, four final cyclic plate load tests were carried out which included three reinforced cases (i.e. using EGG1 (ODOT Type-2), WGG1 and KGG1 geogrids) and an unreinforced case using a new test setup (**Figure 227**). The properties of the geogrids were given earlier in **Table 2**. In these tests, the thicknesses of the aggregate and sand layers were 13 inches and 11 inches, respectively. One inch of aggregate was placed below the geogrid to ensure sufficient interlocking between the geogrid and aggregate interface (**Section 6.1.** Static plate load tests). Afterwards, 12 inches of aggregate was placed and compacted on the geogrid layer in three lifts. The thickness of the base layer in the test models is greater than the minimum six-inch value over soft subgrade and a geosynthetic reinforcement layer as recommended in the current FHWA guidelines (Holtz et al. 2008).

The sand was compacted to a density that corresponded to a CBR value of 4 based on earlier CBR tests. The sand unit weight and water content were 103.5 lb/ft^3 and 0.18%, respectively. The aggregate unit weight and moisture content were 130 lb/ft^3 and 0.02%, respectively. All final four tests ran successfully. A total of 1000 load cycles were applied in each test without any interruption. The corresponding test results are shown in **Figure 228** through **Figure 239**.

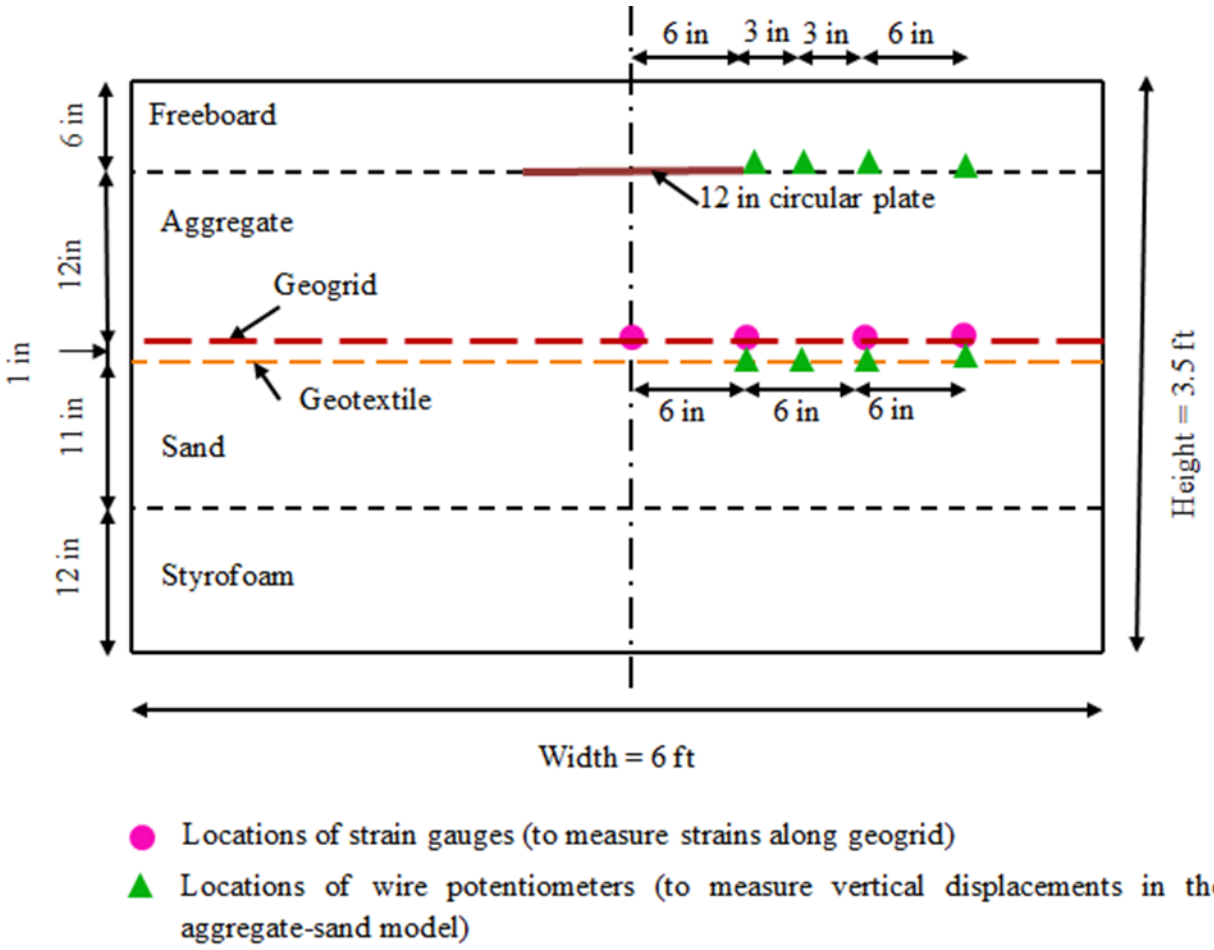

Figure 227. Schematic elevation view of the test box and the instrumentation layout in the final cyclic plate load tests

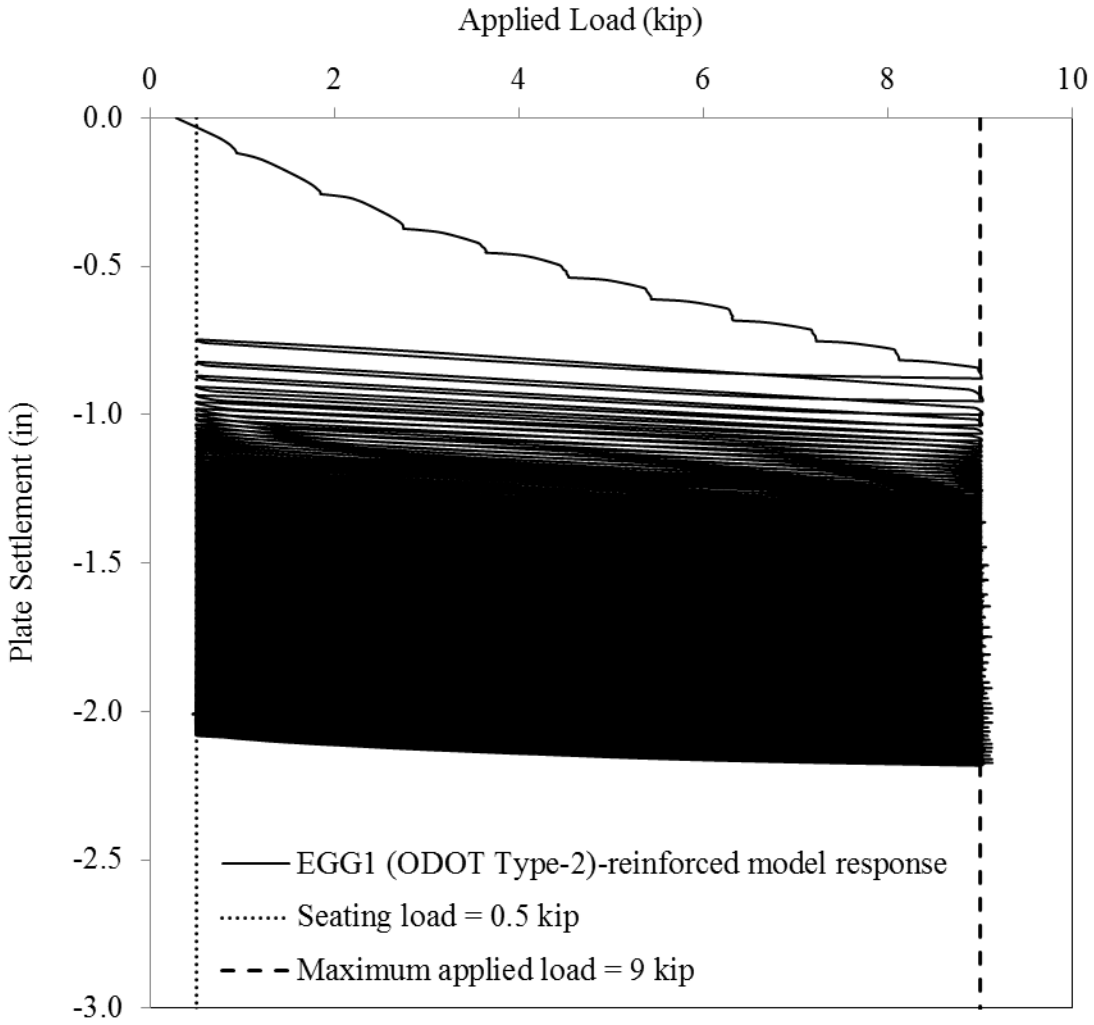

Figure 228. Plate load-settlement response in the test with EGG1 (ODOT Type-2) geogrid (periodic loading regime, number of cycles = 1000)

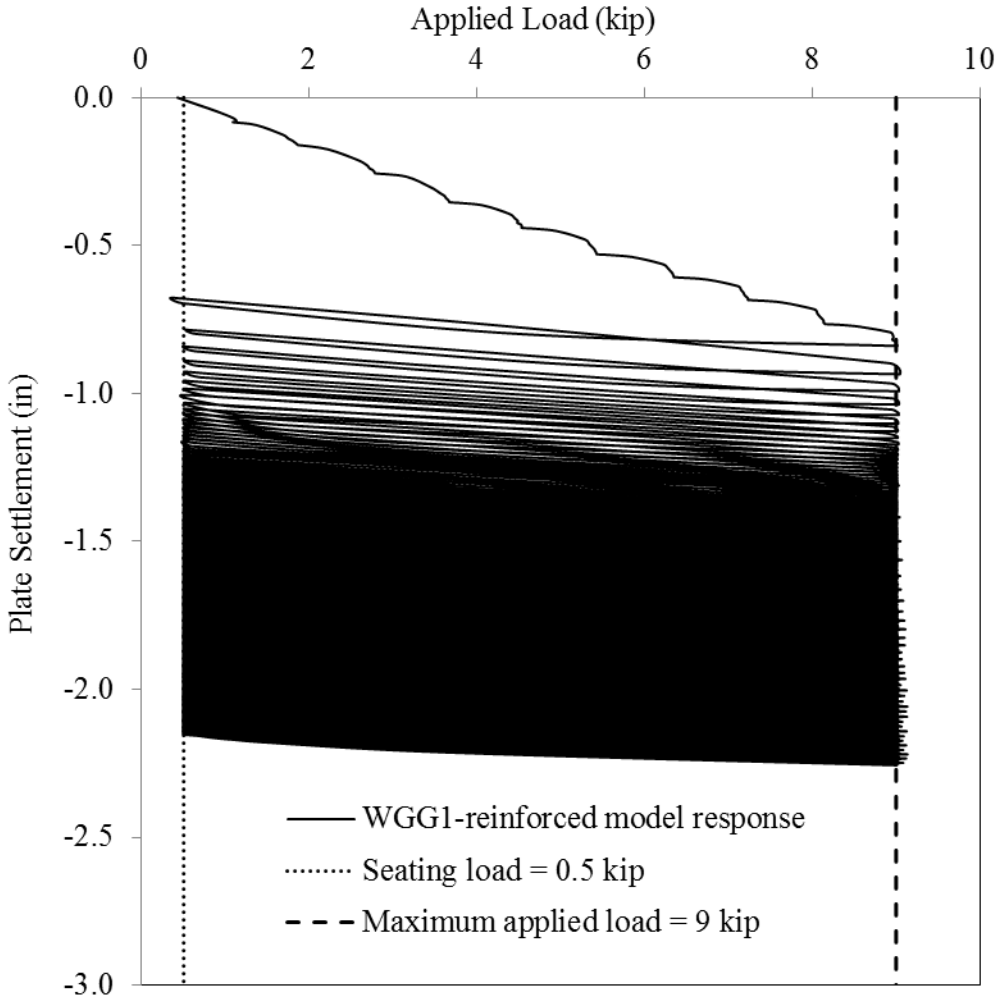

Figure 229. Plate load-settlement response in the test with WGG1 geogrid (periodic loading regime, number of cycles = 1000)

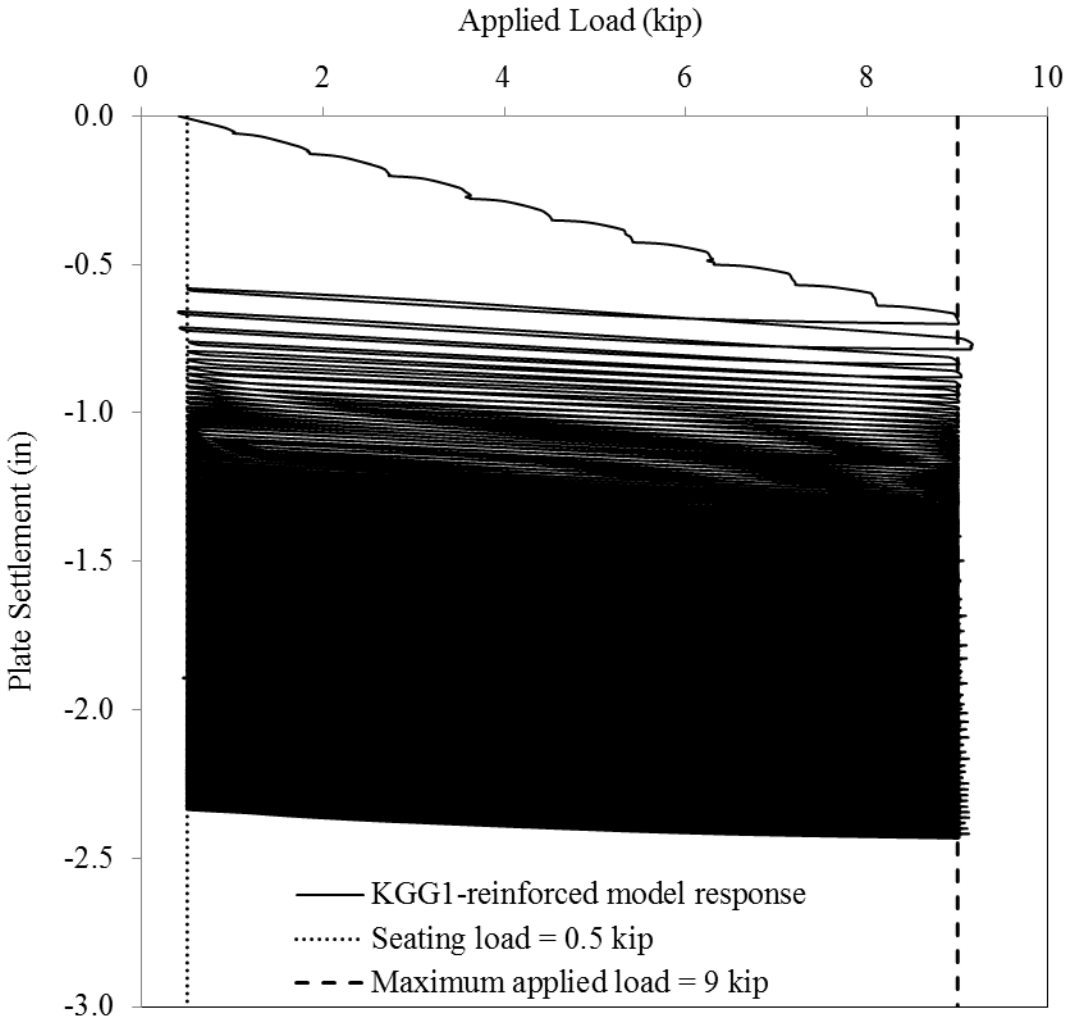

Figure 230. Plate load-settlement response in the test with KGG1 geogrid (periodic loading regime, number of cycles = 1000)

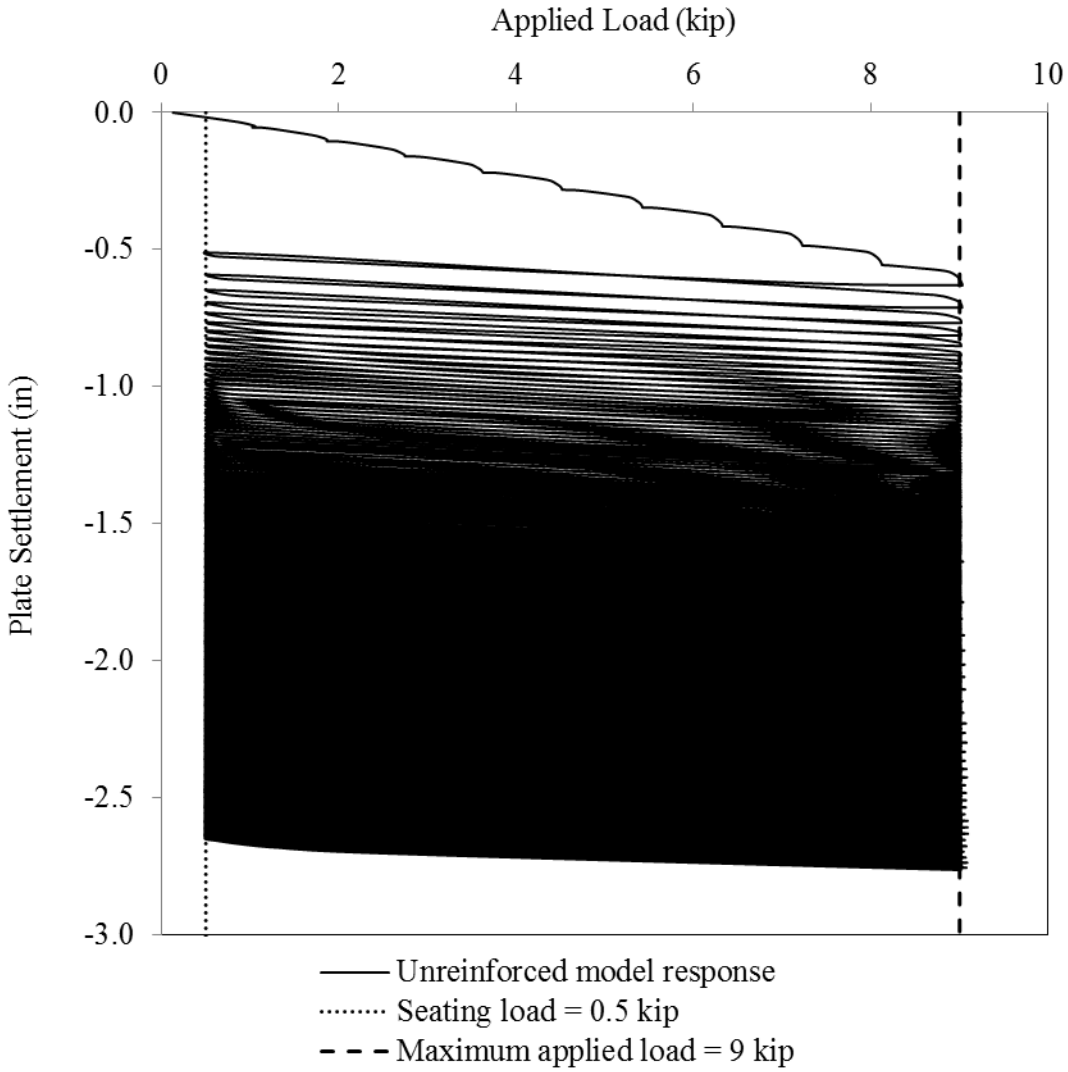

Figure 231. Plate load-settlement response in the test without any geogrids (periodic loading regime, number of cycles = 1000)

Two terms are used in the present study to evaluate the benefits of using geogrids to reinforce aggregate base layers: The Settlement Reduction Factor (SRF) and the Traffic Benefit Ratio (TBR). In this study, the SRF is defined as the ratio of the settlement of a unreinforced aggregate base (S_{ur}) to that of an otherwise identical reinforced layer (S_{gg}) for a given applied load. Therefore, a higher SRF value indicates a more effective reinforcement.

$$SRF = S_{ur}/S_{gg} \quad \text{(Equation 6.1)}$$

The TBR is defined as the ratio between the number of load cycles on a reinforced section (N_R) to reach a defined failure state (e.g. a given rutting depth) and the number of load cycles on an unreinforced section (N_U) with the same geometry and material constituents that reaches the same defined failure state (Berg et al. 2000). The TBR can be defined as:

$$TBR = N_R/N_U \qquad \text{(Equation 6.2)}$$

Therefore, a greater TBR value indicates a more effective reinforcement.

Figure 232a shows that all reinforced cases performed better than the unreinforced case. However, the test section with ODOT Type-2 geogrid base reinforcement performed better than those with WGG1 or KGG1 geogrid reinforcement. **Figure 232b** shows a comparison of SRF values corresponding to different geogrid products tested. **Figure 233** shows a comparison of the corresponding TBR values. The TBR values are larger than 1, which means that the reinforcement layer improved the bearing capacity of the aggregate-sand model.

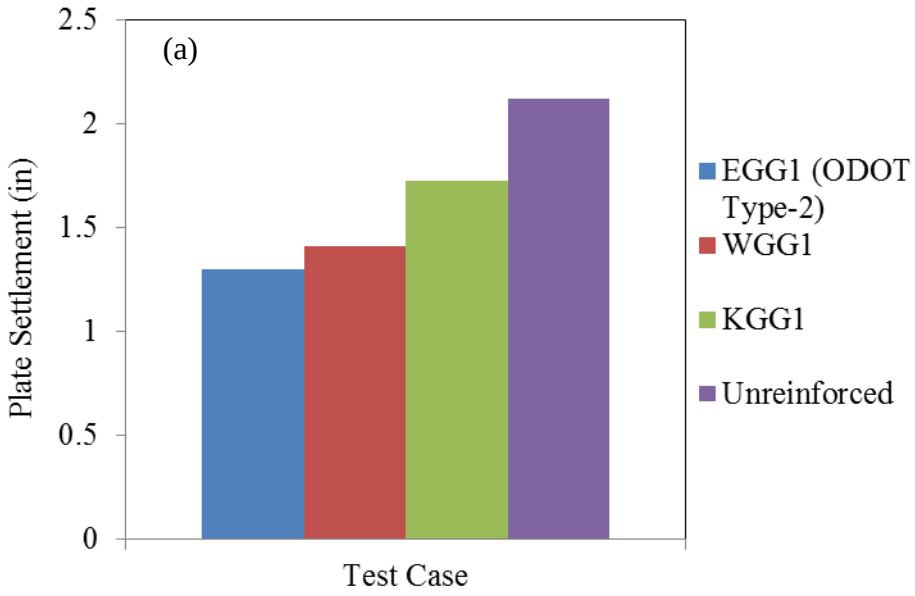

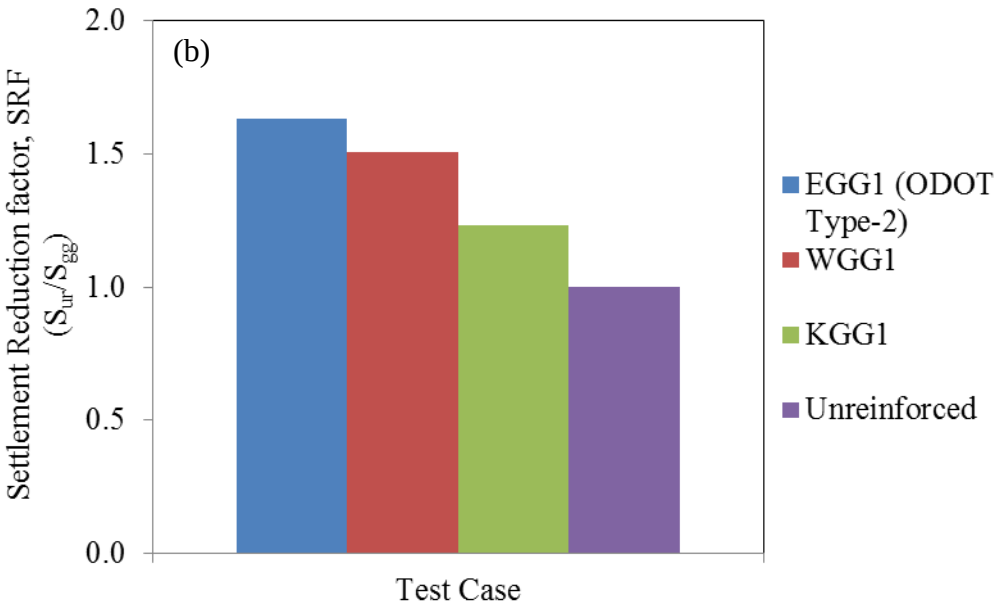

Figure 232. Comparison of (a) plate settlement response and (b) settlement reduction factors

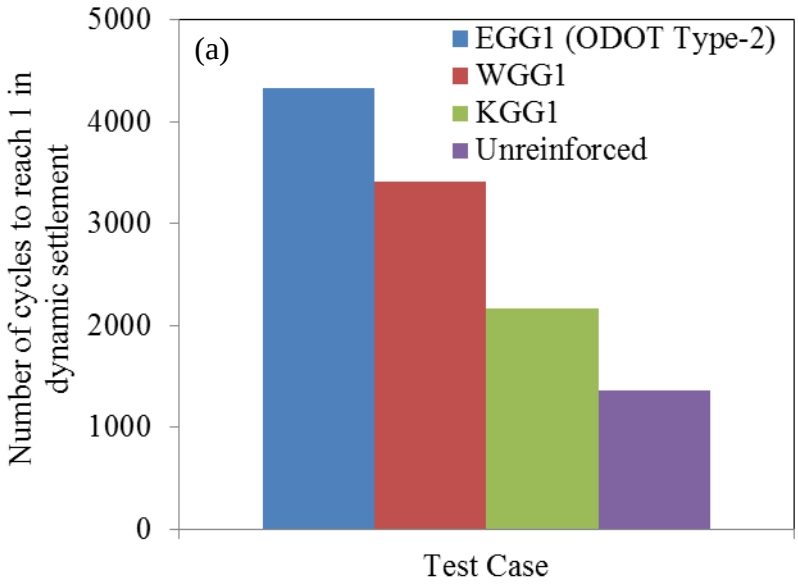

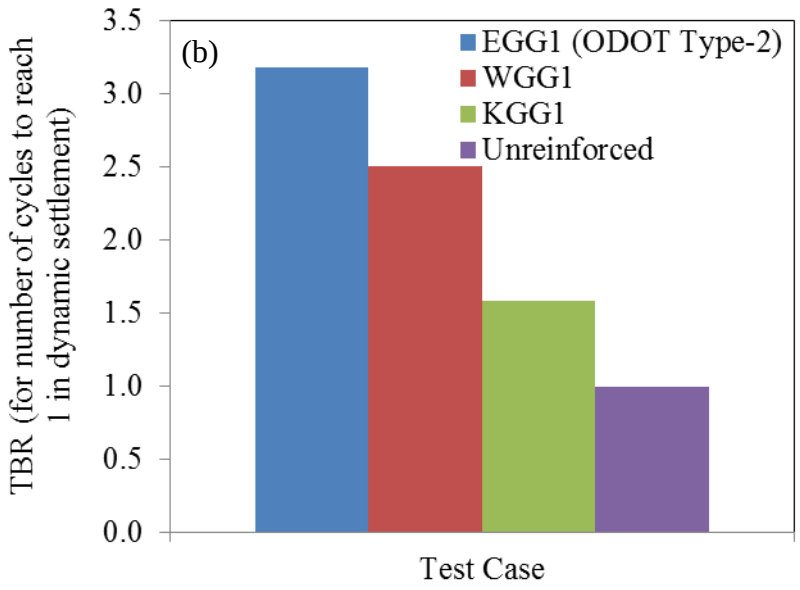

Figure 233. Comparison of (a) number of cycles to reach 1 inch of settlement and (b) traffic benefit ratios (TBR)

Figure 234 represents the top surface deflection profile of the test section reinforced with ODOT Type-2 geogrid at different loading cycles. The results show that permanent deformation accumulated with the number of load cycles. It is also observed that the plate settlement increased at a more rapid rate in the early stages of the loading. These observations are consistent with those reported by Abu-Farsakh and Chen (2011).

Figure 235 shows a comparison of the top surface deflections at the end of 1000 cycles for different test cases. The results show that the test section with EGG1 (ODOT Type-2) geogrid base reinforcement resulted in less deformation than that with WGG1 and KGG1 geogrid reinforcement. They also show that the maximum amount of surface deformation occurred in the unreinforced case.

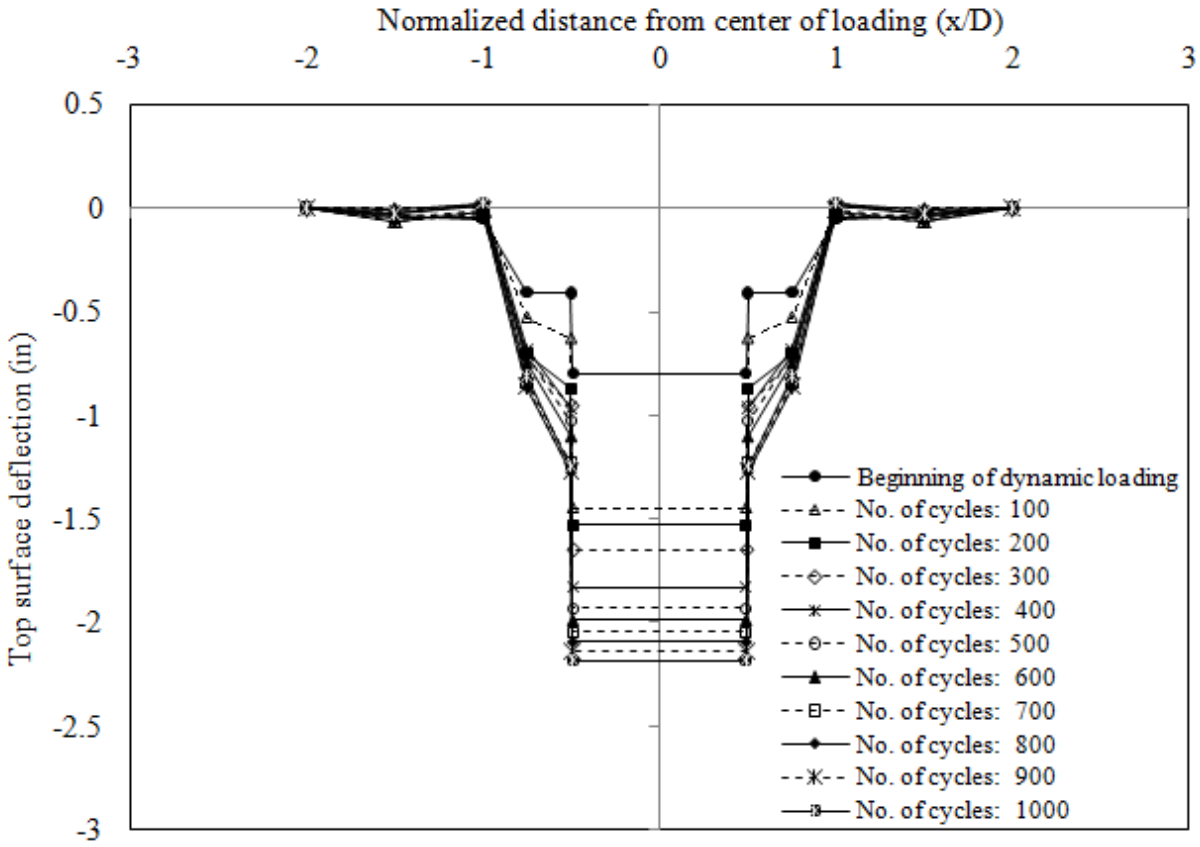

Figure 234. Top surface deflection profile in the test section with ODOT Type-2 geogrid

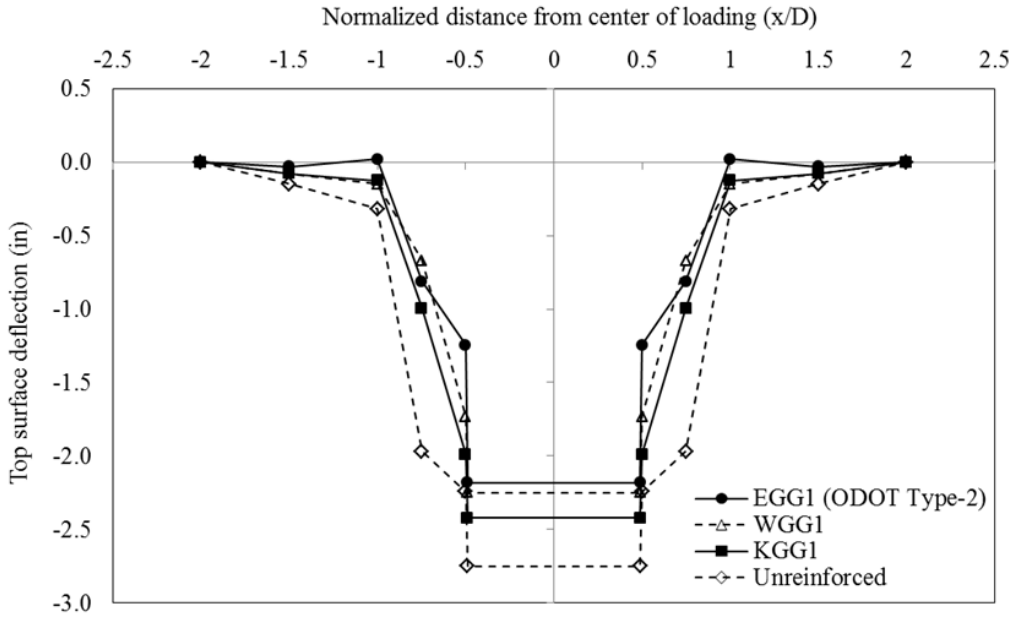

Figure 235. Comparison of top surface deflections at different cases at the end of 1000 cycles

Figure 236 shows the subgrade deflection profile of the test section reinforced with the ODOT Type-2 geogrid at different loading cycles. It was found that the subgrade settlement increased more rapidly during the earlier load cycles. **Figure 237** shows a comparison of the subgrade deflection profiles in different test cases at the end of 1000 cycles. It was found that the test section with the ODOT Type-2 geogrid base reinforcement resulted in the smallest amount of deformation among all cases tested. In contrast, the largest amount of subgrade deformation occurred in the unreinforced case.

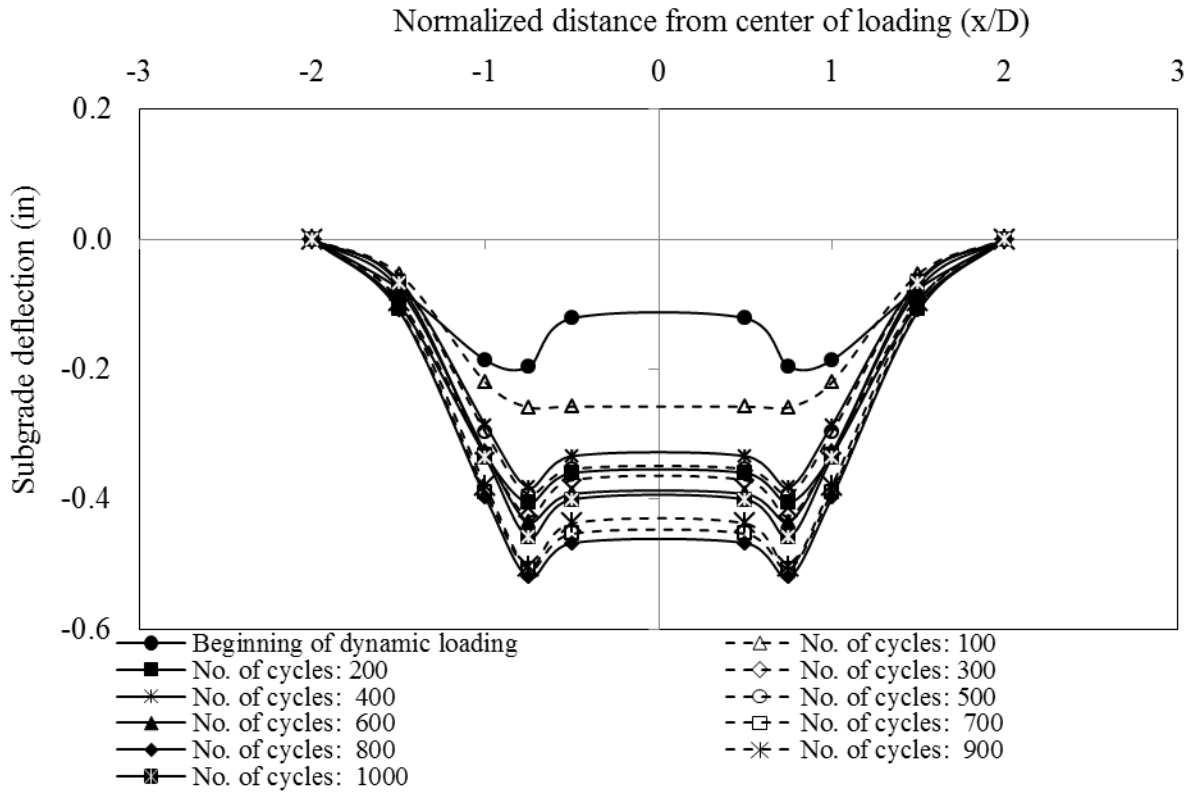

Figure 236. Subgrade deflection profile for the model with ODOT Type-2 geogrid

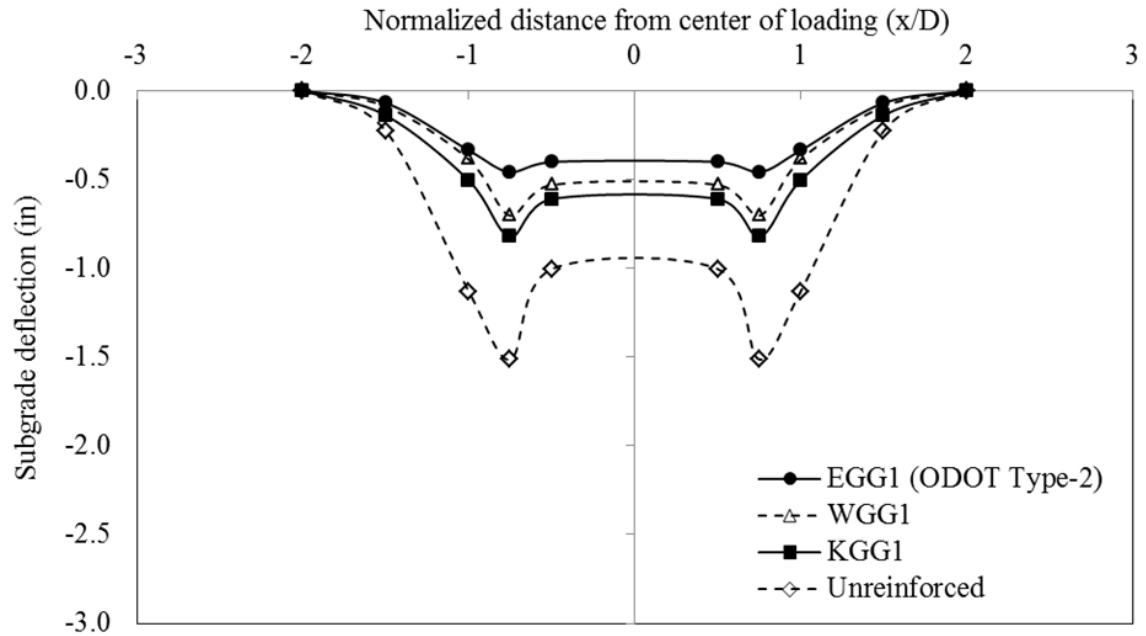

Figure 237. Comparison of subgrade deflection profiles in different test cases at the end of 1000 cycles

The variations of strains along the centerline of the EGG1 (ODOT Type-2) and KGG1 geogrids for different load cycles are shown in **Figure 238** and **Figure 239**, respectively. The highest tensile strains were measured directly beneath the center of the loading plate, where the lateral movement of the base course was expected to be the greatest. Results in **Figure 238** and **Figure 239** indicate that the measured maximum strains in all geogrids were well below the serviceability limit (e.g. 2%; Christopher et al. 2008) and certainly far below the geogrids failure strains. Similar strain distributions were reported by Miura et al. (1990), Perkins (1999) and Abu-Farsakh and Chen (2011).

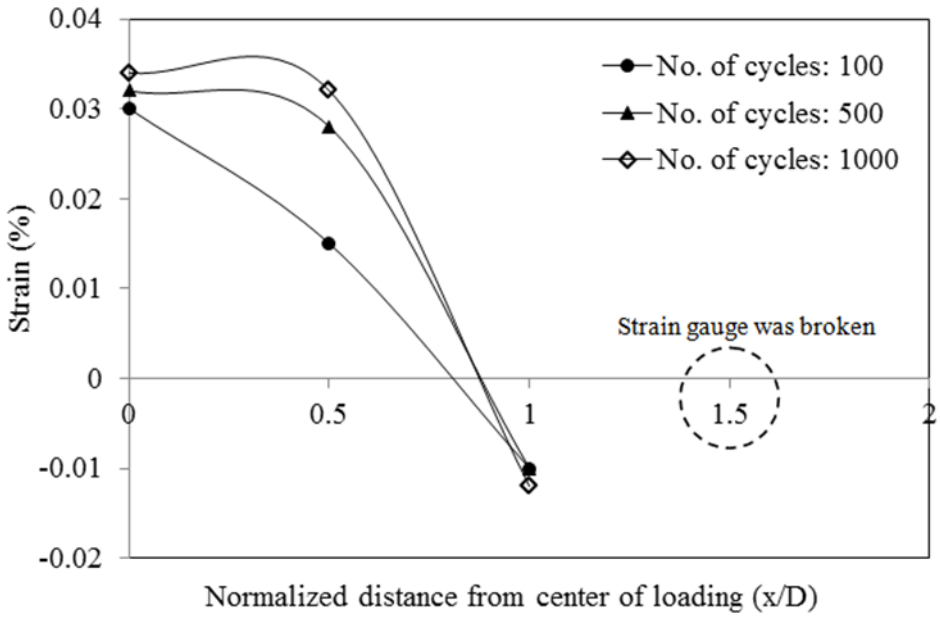

Figure 238. Strain distributions in the ODOT Type-2 geogrid

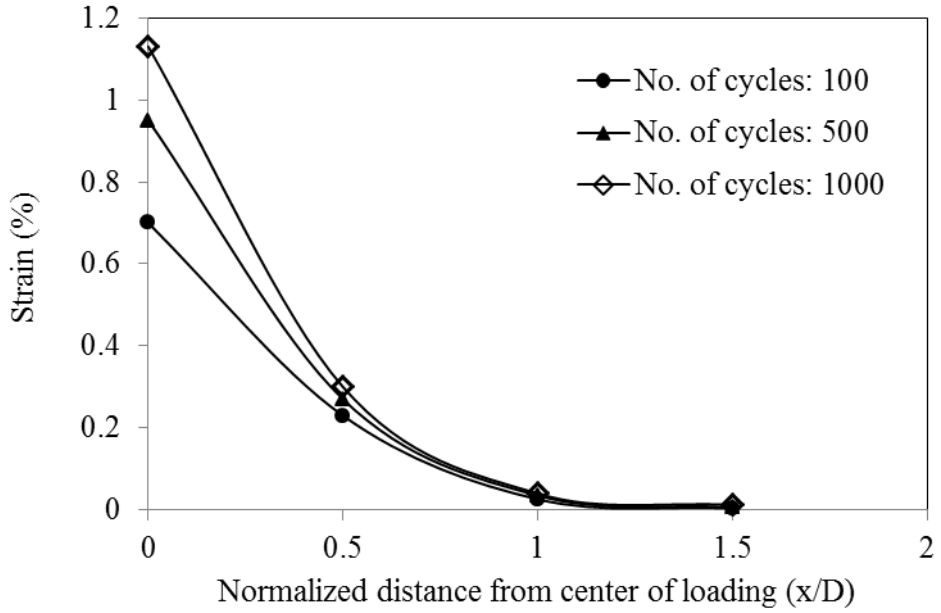

Figure 239. Strain distribution in the KGG1 geogrid

Figure 240 shows the correlations between the SRF values of the test models and the rib strength properties of the geogrids tested. **Figure 240** indicates that the SRF value of a reinforced model increases with the rib strength properties of the geogrid used in the model. **Figure 241** shows the correlations between the SRFs and ultimate junction strength properties of the geogrids tested. Similarly, results shown in **Figure 241** indicate that the SRF value of a reinforced model increases with the junction strength of the geogrid used in the model. However, these results indicate that ultimate junction strength values greater than 25 lb do not result in significant increases in the SFR value for the base-subgrade models tested.

Figure 242 and **Figure 243** show the correlations between the TBR values of the test models and the rib and junction strength properties of the geogrids used, respectively. Similar to the results shown in **Figure 240** and **Figure 241**, the results in **Figure 242** and **Figure 243** show that the TBR value of a reinforced model increases with the rib and junction strength properties of the geogrid used in the model with a diminished return for ultimate junction strength values greater than 25 lbs.

Taken together, the plate load test results indicated that the improvement in the performance of the base-subgrade sections tested was by and large proportional to the rib and junction index properties of the geogrid used. The extruded ODOT Type-2 geogrid performed consistently better than the non-extruded geogrids examined.

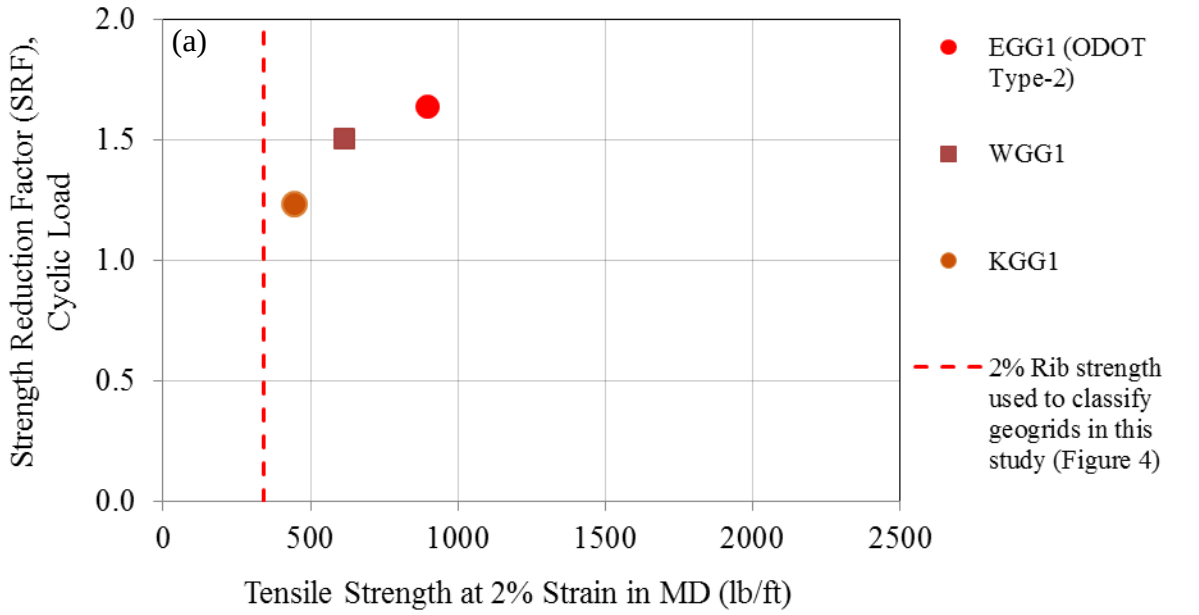
(a)
Strength Reduction Factor (SRF), Cyclic Load
2.0
1.5
1.0
0.5
0.0
0
500
1000
1500
2000
2500
Tensile Strength at 2% Strain in MD (lb/ft)
EGG1 (ODOT Type-2)
WGG1
KGG1
2% Rib strength used to classify geogrids in this study (Figure 4)

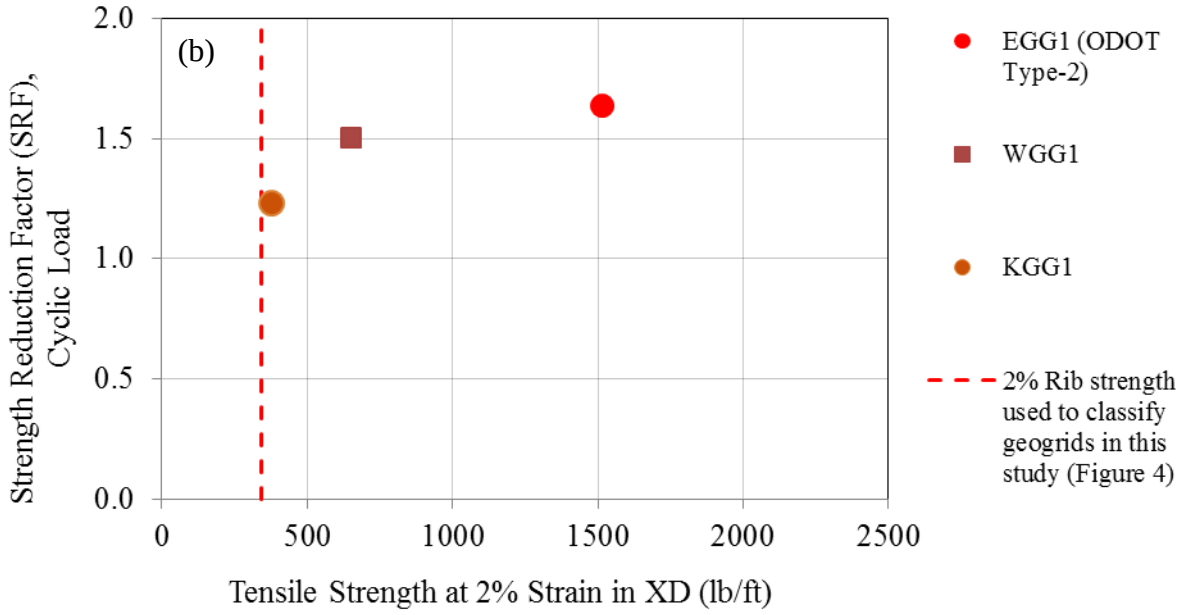
(b)
Strength Reduction Factor (SRF), Cyclic Load
2.0
1.5
1.0
0.5
0.0
0
500
1000
1500
2000
2500
Tensile Strength at 2% Strain in XD (lb/ft)
EGG1 (ODOT Type-2)
WGG1
KGG1
2% Rib strength used to classify geogrids in this study (Figure 4)

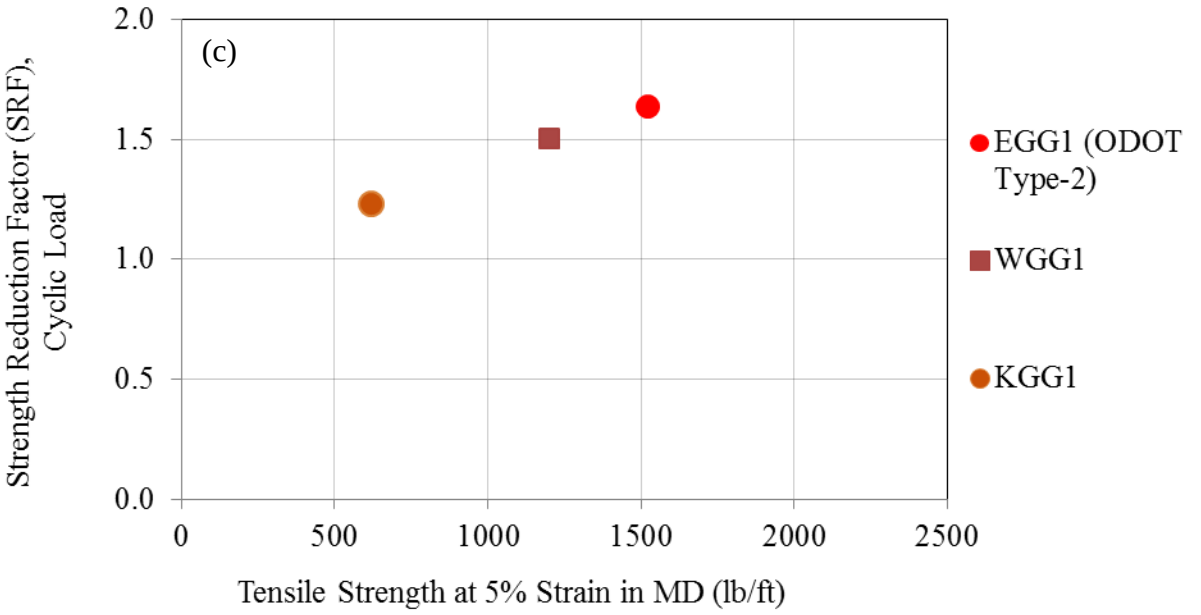
(c)
Strength Reduction Factor (SRF), Cyclic Load
2.0
1.5
1.0
0.5
0.0
0
500
1000
1500
2000
2500
Tensile Strength at 5% Strain in MD (lb/ft)
EGG1 (ODOT Type-2)
WGG1
KGG1

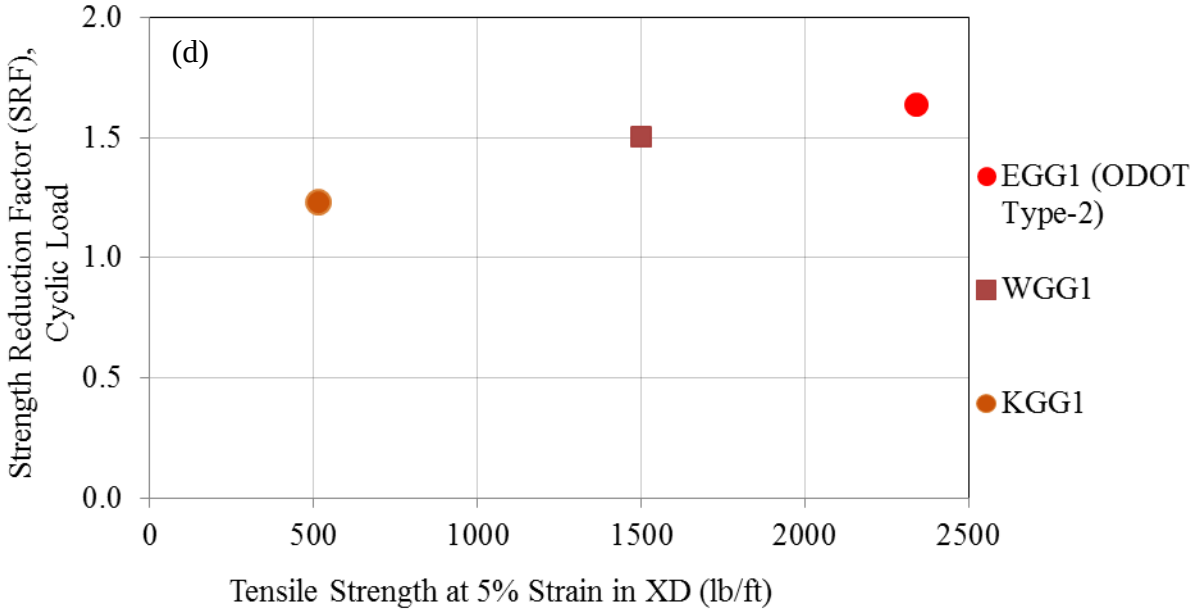
(d)
Strength Reduction Factor (SRF), Cyclic Load
2.0
1.5
1.0
0.5
0.0
0
500
1000
1500
2000
2500
Tensile Strength at 5% Strain in XD (lb/ft)
EGG1 (ODOT Type-2)
WGG1
KGG1

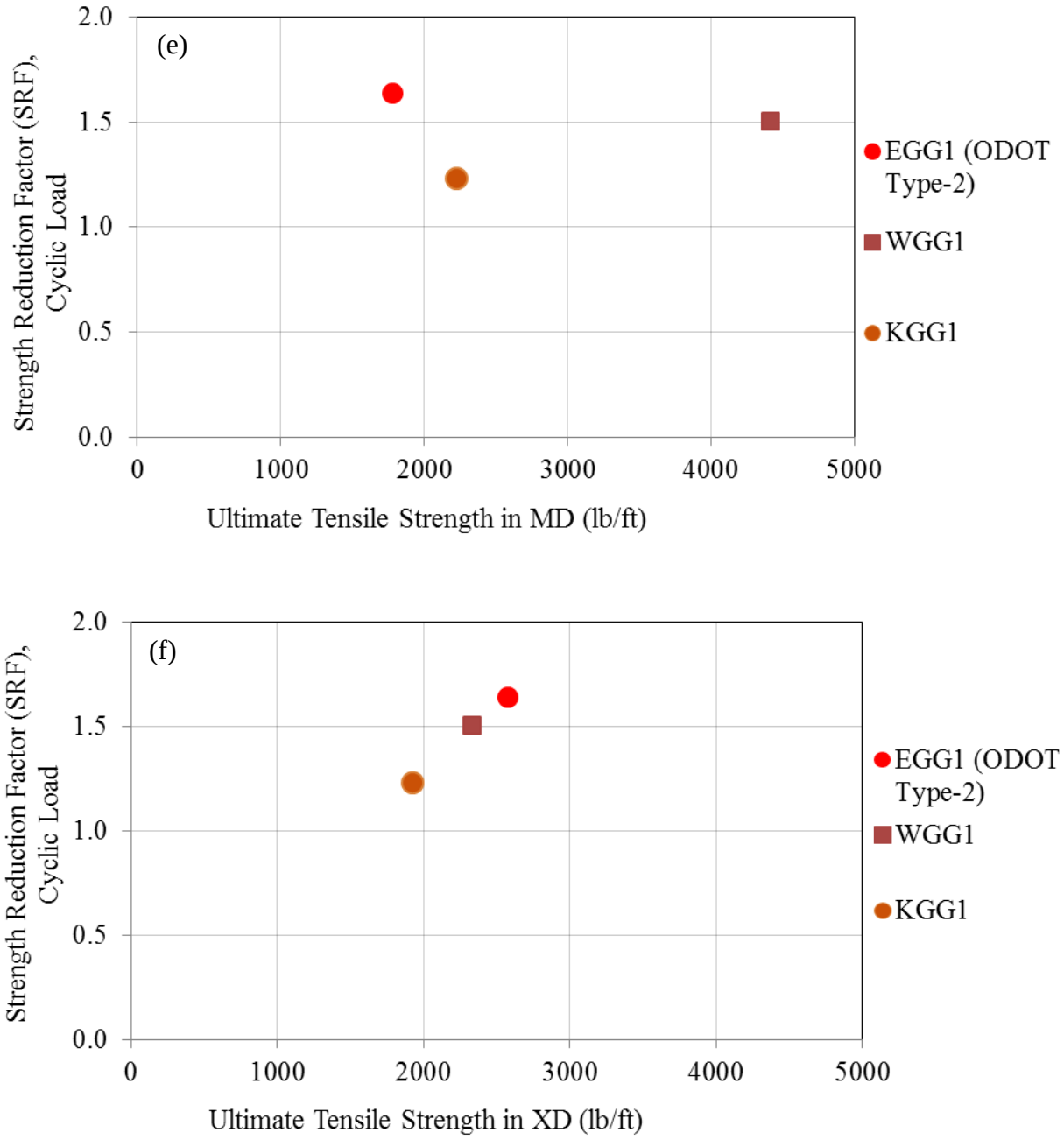

Figure 240. Correlation between SRF from cyclic plate load tests and rib strength values (a) at 2% strain in MD, (b) in XD, (c) at 5% strain in MD, (d) in XD, (e) ultimate rib strength in MD, (f) in XD

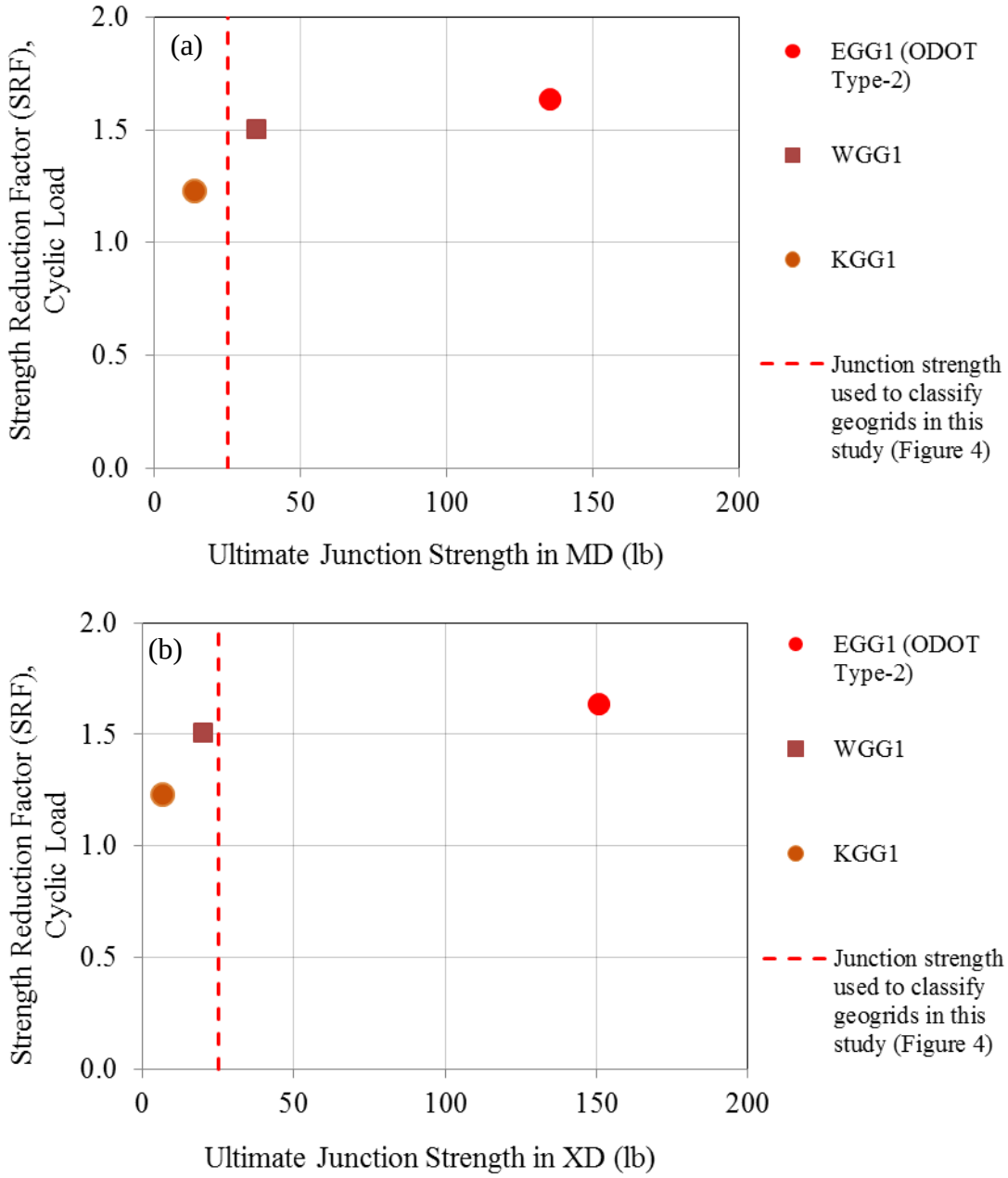

Figure 241. Correlation between SRF and geogrid ultimate junction strength (a) in MD and (b) in XD

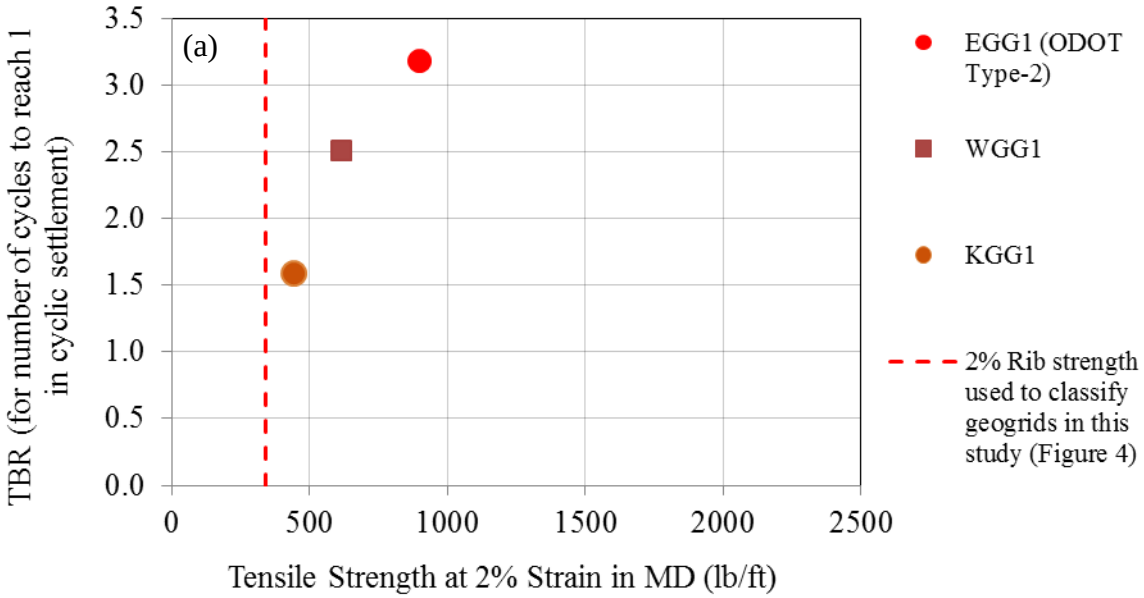
(a)
TBR (for number of cycles to reach 1 in cyclic settlement)
3.5
3.0
2.5
2.0
1.5
1.0
0.5
0.0
0
500
1000
1500
2000
2500
Tensile Strength at 2% Strain in MD (lb/ft)
EGG1 (ODOT Type-2)
WGG1
KGG1
2% Rib strength used to classify geogrids in this study (Figure 4)

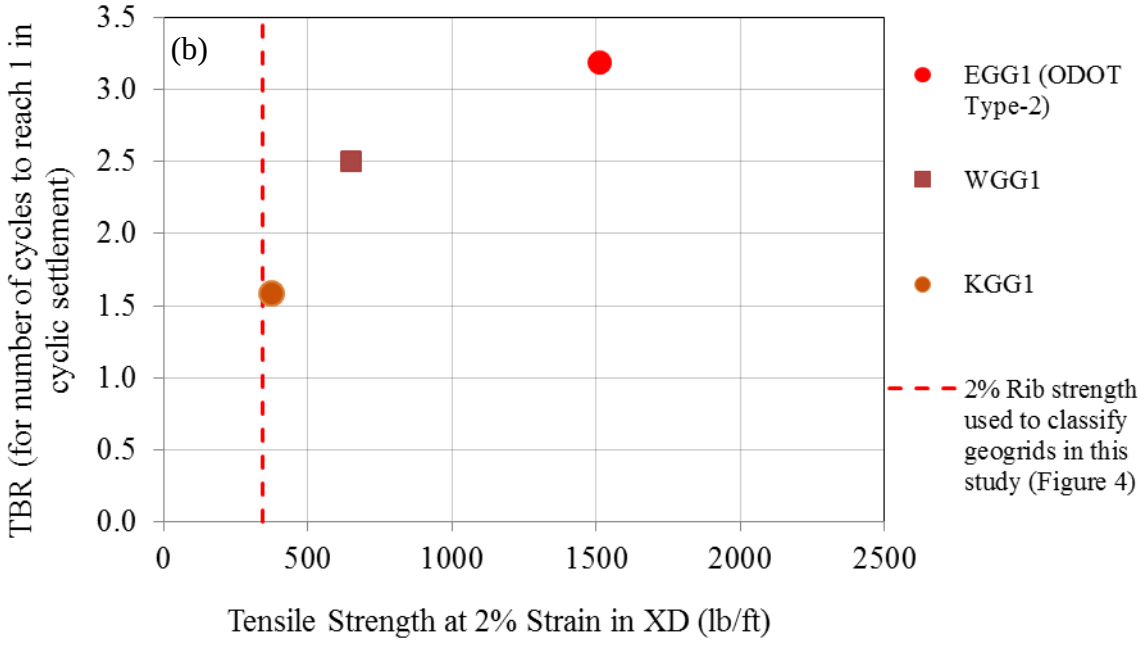
(b)
TBR (for number of cycles to reach 1 in cyclic settlement)
3.5
3.0
2.5
2.0
1.5
1.0
0.5
0.0
0
500
1000
1500
2000
2500
Tensile Strength at 2% Strain in XD (lb/ft)
EGG1 (ODOT Type-2)
WGG1
KGG1
2% Rib strength used to classify geogrids in this study (Figure 4)

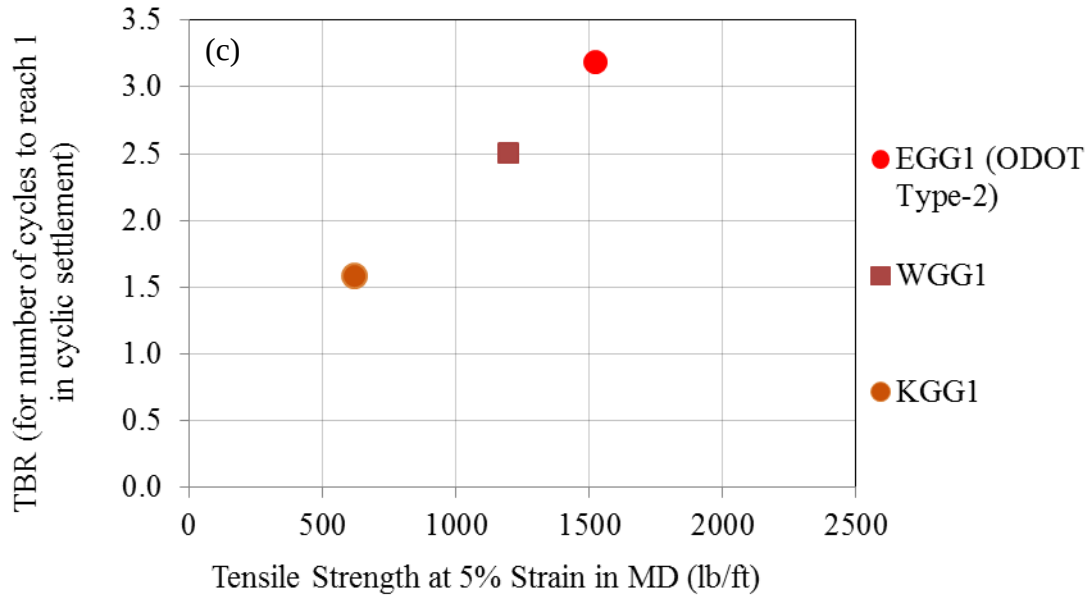
(c)
TBR (for number of cycles to reach 1 in cyclic settlement)
3.5
3.0
2.5
2.0
1.5
1.0
0.5
0.0
0
500
1000
1500
2000
2500
Tensile Strength at 5% Strain in MD (lb/ft)
EGG1 (ODOT Type-2)
WGG1
KGG1

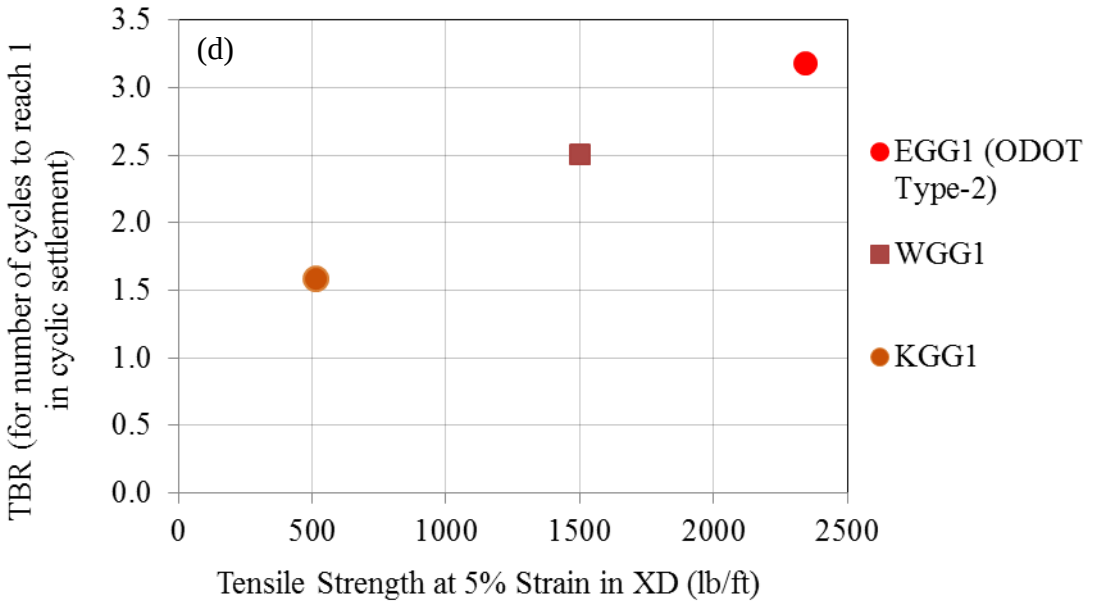
(d)
TBR (for number of cycles to reach 1 in cyclic settlement)
3.5
3.0
2.5
2.0
1.5
1.0
0.5
0.0
0
500
1000
1500
2000
2500
Tensile Strength at 5% Strain in XD (lb/ft)
EGG1 (ODOT Type-2)
WGG1
KGG1

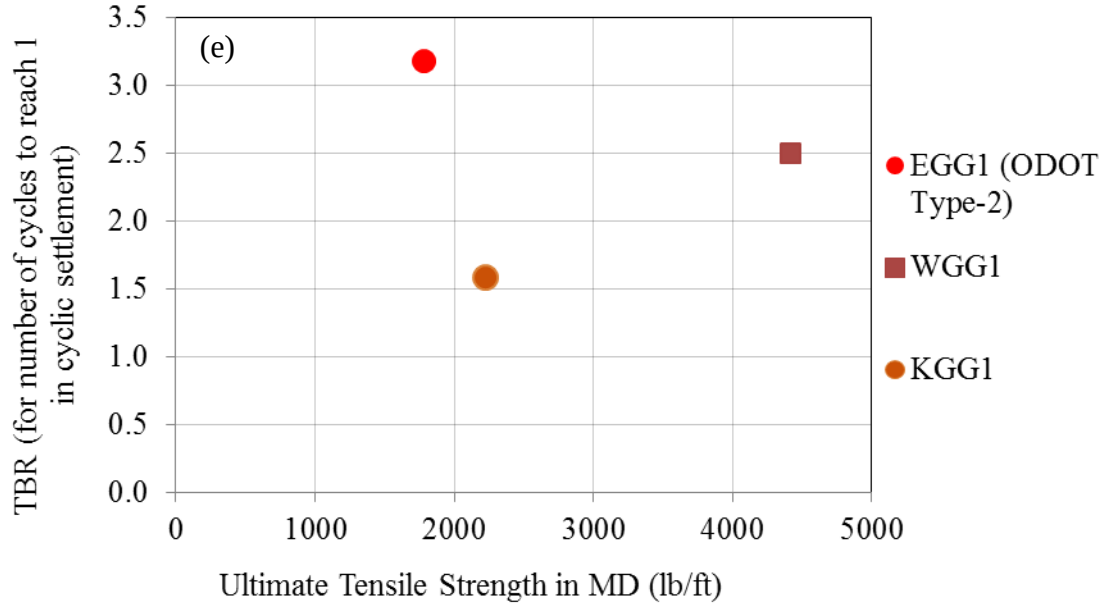

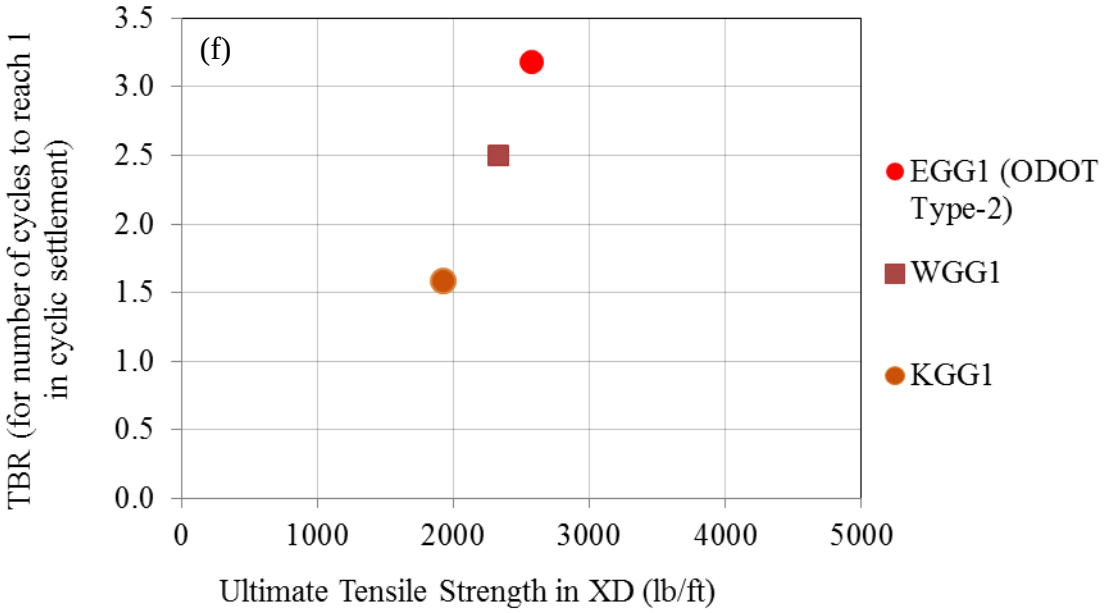

Figure 242. Correlation between (a) TBR and rib strengths at 2% strain in MD, (b) in XD, (c) TBR and rib strengths at 5% strain in MD, (d) in XD, (e) TBR and ultimate rib strengths in MD, (f) in XD

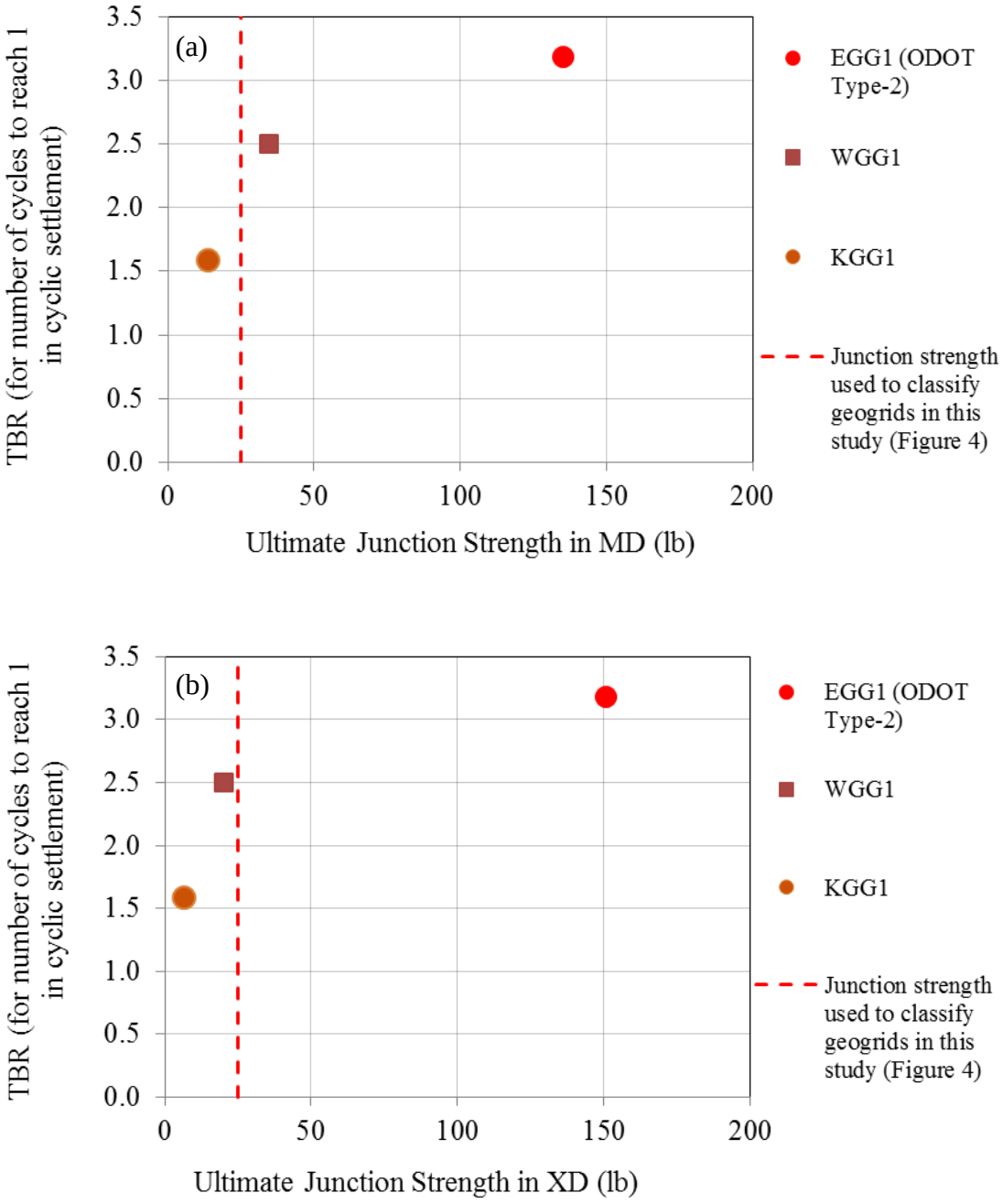

Figure 243. Correlation between TBR and ultimate junction strength (a) in MD and (b) in XD

7. Conclusions of the study and recommendations for future work

The primary objective of this study was to investigate the influence of selected in-isolation properties of geogrids on their in-aggregate performance. The focus of the study was on the rib and junction strength properties of the geogrids. More specifically, the ultimate junction strength, ultimate rib strength and the rib strength values at 2% strain and 5% strain were investigated in machine and cross-machine directions. The geogrids investigated in the study were classified in two basic categories of extruded (EGG) and non-extruded (NEGG) geogrids. The latter category primarily included the woven (WGG) and knitted (KGG) geogrid products.

A comprehensive survey was carried out on the commercially available geogrids and those (or equivalent properties) recommended by the departments of transportation across the United States. The analysis of geogrid properties from this survey resulted in a total of eight geogrid products which were selected for a more detailed study. A geogrid classification table was made using the information gathered from the survey. The geogrid products examined in this study were accordingly classified based on their rib and junction strength properties.

A series of in-isolation and pullout tests were carried out on eight EGG and NEGG geogrids to investigate the significance of junction strength and rib strength properties on their pullout performance in aggregate base layers. The relationship between the in-isolation and in-aggregate properties of geogrid depends on several factors including the geogrid and aggregate properties, their frictional and interlocking interaction mechanisms and the overburden pressure. In order to isolate the influence of geogrid manufacturing technique in this study, the performances of EGG and NEGG products were compared as separate categories. The influence of overburden pressure was also examined. The aggregate used was ODOT Type-A which is a dense-graded aggregate commonly used in ODOT projects.

The pullout test results indicated that geogrids with larger ultimate junction strength values resulted in greater pullout resistance. The 2%-strain rib strength value was found to be better correlated with the pullout resistance at lower confining pressures (e.g. outside of the pressure bulb in the pavement resulting from the wheel load). In contrast, the ultimate rib strength value was found to be a better indicator of the geogrid pullout behavior when subjected to larger overburden pressures. The overall results indicated that as a general rule, greater in-isolation strength properties of geogrids in the pullout direction result in greater pullout resistance.

Installation damage reduction factors (RF_{ID}) were determined for rib and junction strength properties of selected extruded and non-extruded geogrids using outdoor installation damage tests. As a whole, partial reduction factors for the extruded geogrid (EGG) products were found to be larger than those of the non-extruded (NEGG) products. This is somewhat in contrast with the range of values reported in the FHWA guidelines for the PP and PVC-coated PET geogrids

(Berg et al. 2009). However, with only a few exceptions, the RF_{ID} values for all geogrids tested were less than 1.7 as recommended in the FHWA design guidelines (Berg et al. 2009). The installation damage reduction factors for rib strength values at 2% strain were especially found to be significant. This is an important finding which indicates that, the as-placed 2%-strain rib strength of the geogrid reinforcement in the field could be significantly overestimated (and hence would not be available) if the commonly-used, smaller reduction factors for ultimate strength are used for serviceability design. Existing guidelines (e.g. Berg et al. 2009) only specify the RF_{ID} values for the geosynthetic ultimate strength. The RF_{ID} values for the geogrids ultimate rib strength in this study were found to be within the range given in the FHWA guidelines (e.g. Berg et al. 2009). However, as noted earlier, the results of this study indicate that the low-strain rib strength and ultimate junction strength values of the geogrids are important index properties for base reinforcement applications. Therefore, it is recommended that the RF_{ID} values for the low-strain rib strength and ultimate junction strength be also evaluated for any new geogrids and values consistent with those for the ultimate rib strength be specified for design.

Cyclic plate load tests on reinforced aggregate base-loose sand subgrade models indicated that the SRF and TBR values of the models were, by and large, proportional to the rib strength of the geogrid reinforcement. However, increases in the SRF and TBR values in both cases of EGG and NEGG geogrids were not significant for the ultimate junction strength values greater than the 25-lb value recommended in the FHWA guidelines. Overall, the improvement in the performance of the aggregate base-subgrade models tested was found to be proportional to the increase in index properties of geogrid used. The currently specified ODOT Type-2 extruded geogrid (EGG) performed better than the non-extruded geogrids examined in the cyclic plate load tests.

Based on the results of this study, it is concluded that low-strain rib strength and ultimate junction strength of the geogrids are among their most relevant index properties for base reinforcement applications regardless of the geogrid fabrication technique (i.e. extruded, woven or knitted). Therefore, the results of this study suggest that the current ODOT specifications could be revised to include additional extruded and non-extruded geogrids. However, in order for ODOT to consider any new geogrid products for their base reinforcement projects, the 2% and 5% rib strength values of the new geogrids need to be comparable to those of the ODOT Type-2 geogrid. In addition, the ultimate junction strength value of the new geogrids need to be 25 lb or greater as recommended in the FHWA guidelines (Holtz et al. 2008).

The results and the recommendations of this study are based on an extensive series of in-isolation and large-scale in-aggregate tests (i.e. pullout and plate load) in the laboratory. However, based on the observations and findings in this study and survey of literature these results and recommendations need to be validated and expanded with respect to the following items:

(i) Additional in-isolation properties of geogrids need to be investigated in the continuation of this study including the flexural rigidity of transverse members and aperture stability of the geogrids.

(ii) Other reinforcement products such as newer geotextile reinforcement and reinforcement/filter/drainage composite products need to be tested for base reinforcement and subgrade stabilization applications. Clearly, different index properties of such products than those of the geogrids would be relevant to the reinforcement application, which need to be evaluated.

(iii) The findings and conclusions of this study need to be verified or modified through field-scale tests on roadway sections that are subjected to actual traffic load, subgrade types and conditions (e.g. soil type, ground water table, etc.), construction techniques and equipment, and climatic conditions that are representative of roadway projects in Oklahoma and other states.

(iv) The database of laboratory results from this study and the field evaluations in the continuation of this study need to be analyzed and used to develop and validate analytical and computational models for the mechanistic-empirical design approaches for pavements that involve reinforced aggregate bases. These efforts collectively will help ODOT and other state DOT engineers to revise their respective specifications manuals for base reinforcement and subgrade stabilization applications and make them inclusive of a wider range of new products and hence, make them more consistent and cost-effective.

References

AASHTO (2001). “Recommended practice for geosynthetic reinforcement of the aggregate base course of flexible pavement structures”, Designation: PP 46-01, American Association of State Highway and Transportation Officials, Washington, D.C.

AASHTO (2002). “Standard Specifications for Transportation Material and Methods of Sampling and Testing”, American Association of State Highways and Transportation Officials, Washington, D.C.

AASHTO (2007). “LRFD Bridge Design Specifications”, 4th ed., AASHTO, Washington, D.C.

Abu-Farsakh, M. Y. and Chen, Q. (2011). “Evaluation of geogrid base reinforcement in flexible pavement using cyclic plate load testing”, *International Journal of Pavement Engineering*, 12:03, 275-288.

Alzamora, D.E. and Anderson, S.A., 2012, Geogrid Specifications for Base Reinforcement, Presented at the Geosynthetics Committee Meeting at the 2012 Geo-Congress, Oakland, CA, March 2012.

Aran, S. (2006). “Base reinforcement with biaxial geogrid: long-term performance”, Transportation Research Record, Vol. 1975, pp. 115-123.

ASTM (1999). “Annual Book of Standards, Road and Paving Materials”, Vehicle Pavement Systems, American Society of Testing Materials, Vol. 04.03, West Conshohsken, PA.

ASTM D6706-01 (2001). “Standard Test Method for Measuring Geosynthetic Pullout Resistance in Soil”, Annual Book of ASTM Standards, ASTM International, West Conshohocken, PA.

ASTM (2009). "Book of Standards, Volume 4.13: Construction: Geosynthetics”, American Society for Testing and Materials, ASTM International.

ASTM (2009). " Standard Test Method for: Tensile Properties of Geotextiles by the Wide-Width Strip Method.", ASTM International, 100 Barr Harbor Drive, PO Box C700, West Conshohocken, PA 19428-2959, United States, 2009.

Berg, R.R., Christopher, B.R. and Samtani, N.C. (2009). Design and Construction of Mechanically Stabilized Earth Walls and Reinforced Soil Slopes – Volume I, NHI Courses No. 132042 and 132043, Report No. FHWA-NHI-10-024 FHWA GEC 011-Vol I, FHWA, U.S. Department of Transportation, Washington, D.C.

BS8006 (1995). “Code of Practice for Strengthened/Reinforced Soil and Other Fills,” British Standards Institution, Milton Keynes, UK.

Burgess, G.P. (1999). "Performance of Two Full-Scale Model Geosynthetic-Reinforced Segmental Retaining Walls", M.SC. Thesis, Royal Military College of Canada, Kingston, Ontario.

Cuelho, E. and Perkins, S. (2009). “Field investigation of geosynthetics used for subgrade stabilization”, Report No. FHWA/MT-09-0003/8193, Montana Department of Transportation, July 2009.

Chehab, G.R., Palomino, A.M., Tang, X. (2007). “Lab evaluation and specification development for geogrids for highway engineering applications”, FHWA-PA-2007-009-050110, Pennsylvania Transportation Institute, University Park, PA.

Christopher, B.R., Cuelho, E.V., and Perknis, S.W. (2008). “Development of geogrid junction strength requirements for reinforced roadway base design”, Proceedings of GeoAmericas 2008 Conference, Cancun, Mexico, 1003-1012.

Federal Highway Administration (FHWA) (2009). “Design of Mechanically Stabilized Earth Walls and Reinforced Soil Slopes – Volume I”; Report No. FHWA-NHI-10-024 FHWA GEC 011-Vol I, Berg, R. R.; Christopher, B. R. and Samtani, N. C.; Federal Highway Administration, Washington, D.C.

Gabr, M.A., Robinson B., Colin, J.G. and Berg R.R. (2006). “Promoting geosynthetics use on federal lands highway projects”, FHWA-CFL/TD-06-009.

Giroud, J.P. and Han J. (2004). “Design method for geogrid-reinforced unpaved roads I. Development of design method”, Journal of Geotechnical and Geoenvironmental Engineering, 130: 775-786.

GRI (2005). GRI-GG2: “Standard test method for individual geogrid junction strength”, Rev. 3, Geosynthetic Research Institute, Folsom, PA.

Hatami, K., Ghabchi, R., Mahmood, T. and Zaman, M. (2011a). “In-aggregate performance of extruded and woven geogrids in open-graded and dense-graded aggregates”, 90th annual conference of Transportation Research Board, Washington, D.C., 2011.

Hatami, K., Wang Z., Mahmood, T., Ghabchi, R. and Zaman, M. M. (2011b). "In-aggregate testing of unitized and woven Geogrids for base reinforcement applications", Geo-Frontiers Conference, Dallas, Texas, March, 2011.

Holtz, R.D., Christopher, B.R. and Berg, R.R. (2008). "Geosynthetic design and construction guidelines", U.S. Department of Transportation, Federal Highway Administration, Washington DC, FHWA-NHI-07-092, 2008, 592 p.

Huang, B. and Bathurst, R. J. (2009). "Evaluation of soil-geogrid pullout models using a statistical approach"; Geotechnical Testing Journal, Vol. 32, No. 6, September 2009.

IFAI (2009). "Geosynthetics Specifier's Guide." Industrial Fabrics Association International, Roseville, MN.

Jeon, Han-Yong and Bouazza, Abdelmalek (2008). "Analytical consideration of damage tests for geogrids"; the 12th international conference of International Association for Computer Methods and Advances in Geomechanics (IACMAG).

Koerner, R.M. (2005). Designing with Geosynthetics, 5th ed. Pearson, Prentice-Hall, NJ, USA.

Kwon, J. and Tutumluer, E. (2009). "Geogrid base reinforcement with aggregate interlock and modeling of the associated stiffness enhancement in mechanistic pavement analysis", Proceedings of the 88th TRB Meeting, 85-95.

Leng, J., and Gabr, M. A. (2002). "Characteristics of geogrid-reinforced aggregate under cyclic load", Transportation Research Record, 1786: 29-35.

Luo, R. and Prozzi , J. A. (2009). "Combining geogrid reinforcement and lime treatment to control dry land longitudinal cracking", Transportation Research Board, No. 2014; D.C. 2009.

Mahmood, T., Hatami, K., Ghabchi, R. and Zaman. M. (2012). "Laboratory investigation of pullout behavior of non-extruded geogrids in a base aggregate", 91st annual conference of Transportation Research Board, Washington, D.C., 2012.

Mahmood, T., Hatami, K., Ghabchi, R. and Zaman. M. (2012). "Pullout response of geogrids with different junction strength", Geo-Congress Conference, California, March, 2012.

Miura, N., Sakai, A., Taesiri, Y., Yamanouchi, T. and Yasuhara, K. (1990). "Polymer Grid Reinforced Pavement on Soft Clay Grounds", Geotextiles and Geomembranes, Vol. 9, No. 1, pp. 99-123.

National Concrete Masonry Association (NCMA) (1997). "Design Manual for Segmental Retaining Walls", 2nd ed., J. Collin, Ed.; National Concrete Masonry Association, Herndon, VA.

ODOT (2009). "2009 Standard Specification for Highway Construction," Oklahoma Department of Transportation, Section 700: Materials, 2009.

Perkins, S.S. (1999). "Geosynthetic reinforcement of flexible pavements: laboratory based pavement test sections". Report No. FHWA/MT-99-001/8138. US Department of Transportation, Federal Highway Administration, Washington, DC.

Perkins, S.W., Christopher, B.R., Cuelho, E.L., Eiksund, G.R., Hoff, I., Schwartz, C.W., Svano, G. and Want, A. (2004). "Development of design methods for geosynthetic reinforced flexible pavements", FHWA Rep. DTFH61-01-X-00068.

Perkins, S. W., Christopher , B.R., Cuelho, E.L., Eiksund, G.R., Schwartz , C.S. and Svano, G. (2009). "A mechanistic-empirical model for base reinforced flexible pavements"; International Journal of Pavement Engineering, Vol. 10, No. 2, April 2009, 101-114.

Tang, X., Chehab, G. R. and Palomino. A. (2008). "Evaluation of geogrids for stabilising weak pavement subgrade." International Journal of Pavement Engineering Vol. 9, No. 6, December 2008.

Tensar International Corporation. "Product specification - TriAx TX140 geogrid"; "Product specification - TriAx TX160 geogrid" [Online];
Available from: http://www.tensarcorp.com/uploadedFiles/TriAx_140_TX160_Specs.pdf

Tingle, J. S. and Jersy, S. R. (2009). "Full-scale evaluation of geosynthetic reinforced aggregate roads"; Transportation research record, Journal of the Transportation Research Board, D.C. 2009.

TRI/Environmental, Inc. (TRI) (2006). "Carthage Geogrids – Installation Damage Testing", TRI/Environmental, Inc. (TRI), August 10, 2006

Vlachopoulos, N. (2000). "Performance of Two Full-Scale Model Geosynthetic-Reinforced Segmental Retaining Walls: Segmental and Wrapped-Faced" M.Sc. Thesis, Royal Military College of Canada, Kingston, Ontario.

Wang, Z. (2009). "Influence of Geogrids Junction Strength on the Performance of Reinforced Aggregate Base" M.Sc. Thesis, The University of Oklahoma, Norman, OK.

Webster, S. L. (1993). “Geogrid reinforced base courses for flexible pavements for light aircraft: Test section construction, behavior under traffic, laboratory tests and design criteria,” USAE Waterways Experiment Station, Vicksburg, MS, Technical Report DOT/FAA/RD-92/225, 100 p.

Appendix A

Database of Geogrids Properties

Properties of geogrids surveyed in the current study as available in the Geosynthetics Specifier's Guide (IFAI 2009).

Manufacturer	Product Name	Dimensional Properties		Mechanical Propertes ASTM D 6637					
		Aperture Size (mm)		Strength @ 5% Strain (kN/m)		Ultimate Strength (kN/m) / (%)			
		MD	XD	MD	XD	MD		XD	
Tensar Intl. Corp.	BX1100	25	33	8.5	13.4	.	.		.
Tensar Intl. Corp.	BX1200	25	33	11.8	19.6	.	.		.
Tensar Intl. Corp.	BX1300	46	64	10.5	17.5	.	.		
Tensar Intl. Corp.	BX1500	25	31	17.5	20	.	.		.
Tensar Intl. Corp.	TX150	.	.	.	.	.	.		.
Tensar Intl. Corp.	TX160	.	.	.	.	.	.		.
Tensar Intl. Corp.	TX170	.	.	.	.	.	.		.
Tensar Intl. Corp.	CompoGnd CG50	.	.	.	.	50	3%	50	3%
Tensar Intl. Corp.	CompoGnd CG100	.	.	.	.	100	3%	100	3%
Tensar Intl. Corp.	GlassGrid 8501	12.5	12.5	.	.	100	3%	100	3%
Tensar Intl. Corp.	GlassGrid 8502	12.5	12.5	.	.	100	3%	200	3%
Tensar Intl. Corp.	GlassGrid 8511	25	25	.	.	100	3%	100	3%
Tensar Intl. Corp.	GlassGrid 8512	19	25	.	.	100	3%	200	3%
Tensar Intl. Corp.	GlassGrid 8550	25	25	.	.	50	3%	50	3%
Tensar Intl. Corp.	LH800	.	.	.	14	.	.		.
Tensar Intl. Corp.	UX1100HS	.	.	27	.	58	.		.
Tensar Intl. Corp.	UX1400HS	.	.	31	.	70	.		.
Tensar Intl. Corp.	UX1500HS	.	.	52	.	114	.		.
Tensar Intl. Corp.	UX1600HS	.	.	58	.	144	.		.
Tensar Intl. Corp.	UX1700HS	.	.	75	.	175	.		.
Tensar Intl. Corp.	UX1800HS	.	.	95	.	210	.		.
ACE Geos. Inc.	ACE GG30-II	25	28	15	.	30	.	30	.
ACE Geos. Inc.	ACE GG300-II	25	30	120	..	300	.	300	.
ACE Geos. Inc.	ACE GG60-I	24	28	30	...	60	.	30	.
ACE Geos. Inc.	ACE GG100-I	21	28	50	.	100	.	30	.
ACE Geos. Inc.	ACE GG150-I	20	28	75	..	150	.	30	.
ACE Geos. Inc.	ACE GG400-I	23	26	160	.	400	.	50	.
ACE Geos. Inc.	ACE GG800-I	24	24	200	.	800	.	100	.
Cartage Mills	GX-300	22	25	15	.	54.3	.	.	.
Cartage Mills	GX-500	22	25	16.6	..	62.4	.	.	.
Cartage Mills	GX-800	23	23	29.5	.	106.6	.	.	.

Manufacturer	Product Name	Dimensional Properties		Mechanical Propertes ASTM D 6637					
		Aperture Size (mm)		Strength @ 5% Strain (kN/m)		Ultimate Strength (kN/m) / (%)			
		MD	XD	MD	XD	MD		XD	
Checkmate Geo. Inc.	BX1515PP	49	40.4	12.3	12.4	17.7		15.2	.
Checkmate Geo. Inc.	BX2020PP	43.7	41.9	20.7	16	24.8		19.4	.
Checkmate Geo. Inc.	BX2525PP	37.9	37.6	19.5	20.1	28.7		26	.
Checkmate Geo. Inc.	BX3030PP	41.4	38.9	22.7	26.7	33.2		31.1	.
Checkmate Geo. Inc.	BX4040PP	38.7	40.5	28.1	28.8	39.5		38.9	.
Checkmate Geo. Inc.	UX10PET	.	.	14.1	.	31.7		.	.
Checkmate Geo. Inc.	UX20PET	.	.	21.47	.	49.54		.	.
Checkmate Geo. Inc.	UX30PET	.	..	29.82	.	73.68		.	.
Checkmate Geo. Inc.	UX50PET	.	..	40.58	.	102.52		.	.
Checkmate Geo. Inc.	UX70PET	.	..	45.72	.	114.3		.	.
Checkmate Geo. Inc.	UX90PET	.	..	52.54	.	132.4		.	.
Checkmate Geo. Inc.	UX100PET		.	58.8	.	158.8		.	.
Checkmate Geo. Inc.	UX150PET	.	.	70.17	.	203.5		.	.
Checkmate Geo. Inc.	RG5050	25.4	25.4	.	.	51.6		56.4	.
Checkmate Geo. Inc.	RG1010	25.4	25.4		.	103.9		102.1	.
Colbond Inc.	Enkagrid Max 20	44	41	16	16	24	9%	24	9%
Colbond Inc.	Enkagrid Max 30	44	40	23	23	34	9%	34	9%
Colbond Inc.	Enkagrid PRO 40	111	41	33	.	44	6%	.	.
Colbond Inc.	Enkagrid PRO 60	111	37	51	.	70	6%	.	.
Colbond Inc.	Enkagrid PRO 90	111	35	81	.	105	6%	.	.
Colbond Inc.	Enkagrid PRO 120	111	34	87	.	127	6%	.	.
Colbond Inc.	Enkagrid PRO 180	111	34	140	.	199	6%	.	.
Highland Industries	HI-Grid II	23.88	7.11		.	42	.	.	.
Highland Industries	HI-Grid III	21.34	5.59		.	57	.	.	.
Highland Industries	HI-Grid IV	21.34	6.35		.	83	.	.	.
Highland Industries	HI-Grid VIII	22.23	4.06		.	124	.	.	.
TenaxCorp.	LBO 202	28	38	9.5	13.5	13		20.5	.
TenaxCorp.	LBO 302	28	38	14	23	17.5		31.5	.
TenaxCorp.	MS 220	42	50	9	13.42	13.5		20.5	.
TenaxCorp.	MS 330	42	50	13.5	19.6	20		30.7	.
TenaxCorp.	MS 500	60	60	13.5	19.6	22		35	.
TenCate Geos.	Mirafi BXG 11	25.4	25.4	13.4	13.4	29.2		29.2	.
TenCate Geos.	Mirafi BXG 12	25.4	25.4	13.4	19.7	29.2		58.4	.
TenCate Geos.	Mirafi Miramesh	3	3	.	.	21		25.3	.
TenCate Geos.	Miragrid 2XT	22	25	.	.	29.2		29.2	.
TenCate Geos.	Miragrid 3XT	22	25	15.4	.	46		.	.
TenCate Geos.	Miragrid 5XT	22	25	25.4	.	62.7		.	.
TenCate Geos.	Miragrid 7XT	22	25	31.5	.	83.2		.	.
TenCate Geos.	Miragrid 8XT	22	25	36.8	.	102.1		.	.
TenCate Geos.	Miragrid 10XT	22	25	45.5	.	138.6		.	.
TenCate Geos.	Miragrid 20XT	81	7.6	77.9	.	181.2		.	.
TenCate Geos.	Miragrid 22XT	81	7.6	97.8	.	259.1		.	.
TenCate Geos.	Miragrid 24XT	101	17.8	102.1	.	370.3		..	.
Synteen Tech. Fab.	SF 11	25	25	15.2	11.5	34.9		56.5	.
Synteen Tech. Fab.	SF 110	20	20	.	.	150.1		.	.
Synteen Tech. Fab.	SF 12	25	25	15.2	19.9	34.9		76.8	.
Synteen Tech. Fab.	SF 20	20	20	.	.	30		.	.
Synteen Tech. Fab.	SF 35	20	20	.	.	50.2		.	.
Synteen Tech. Fab.	SF 350	20	20	.	.	401.3		.	.
Synteen Tech. Fab.	SF ff	20	20	.	.	68.4		.	.
Synteen Tech. Fab.	SF 80	20	20	.	.	108.4		.	.
Synteen Tech. Fab.	SF 90	20	20	.	.	124.5		.	.

Manufacturer	Product Name	Dimensional Properties		Mechanical Propertes ASTM D 6637					
		Aperture Size (mm)		Strength @ 5% Strain (kN/m)		Ultimate Strength (kN/m) / (%)			
		MD	XD	MD	XD	MD		XD	
TechFab India	Techgrid U-40	30	25	.	.	40		20	.
TechFab India	Techgrid U-60	30	25	.	.	60		20	.
TechFab India	Techgrid U-80	30	25	.	.	80		30	.
TechFab India	Techgrid U-100	30	24	.	.	100		30	.
TechFab India	Techgrid U-120	30	23	.	.	120		30	.
TechFab India	Techgrid U-150	30	23	.	.	150		30	.
TechFab India	Techgrid U-200	30	22	.	.	200		30	.
Samyang	TRIGRID EX 040	34	34	24	.	40		.	.
Samyang	TRIGRID EX 060	33	34	36	.	60		.	.
Samyang	TRIGRID EX 080	32	34	48	.	80		.	.
Samyang	TRIGRID EX 100	31	34	60	.	100		.	.
Samyang	TRIGRID EX 150	30	34	90	.	150		.	.
Samyang	TRIGRID EX 20/20	35	35	14	14	20		20	.
Samyang	TRIGRID EX 30/30	34	34	21	21	30		30	.
Samyang	TRIGRID EX 40/40	34	34	28	28	40		40	.
Samyang	TRIGRID EX 60/60	33	33	38	38	60		60	.
Strata Systems Inc.	Strata MicroGrid	6.35	2.54	8	5.8	29.2		29.2	.
Strata Systems Inc.	StrataGrid SG150	25.4	24.1	9.1	6.2	27.4		27.4	.
Strata Systems Inc.	StrataGrid SG200	18.3	16.5	.	.	52.5		.	.
Strata Systems Inc.	StrataGrid SG350	21.6	14	.	.	72.9		.	.
Strata Systems Inc.	StrataGrid SG500	62.2	25.4	.	.	93.4		.	.
Strata Systems Inc.	StrataGrid SG550	21.6	24.1	.	.	118.9		.	.
Strata Systems Inc.	StrataGrid SG600	62.2	24.1	..	.	132.8		.	.
Strata Systems Inc.	StrataGrid SG700	62.2	24.1	.	.	172.2		.	.
NAUE GmbH & Co. KG	Secugrid 30/30 Q6	34	34	24	24	30		30	.
NAUE GmbH & Co. KG	Secugrid 40/40 Q6	34	33	32	32	40		40	.
NAUE GmbH & Co. KG	Secugrid 60/20 R6	73	31	36	.	60		.	.
NAUE GmbH & Co. KG	Secugrid 80/20 R6	73	30	48	.	80		.	.
NAUE GmbH & Co. KG	Secugrid 120/40 R6	71	28	72	.	120		.	.
NAUE GmbH & Co. KG	Secugrid 200/40 R6	71	25	120	.	200		.	.
NAUE GmbH & Co. KG	Secugrid 20/20 Q1	32	32	16	16	20		20	.
NAUE GmbH & Co. KG	Secugrid 30/30 Q1	32	32	24	24	30		30	.
NAUE GmbH & Co. KG	Secugrid 40/40 Q1	31	31	32	32	40		40	.
NAUE GmbH & Co. KG	Combigrid 30/30 Q1 151 GRK 3	32	32	24	24	30		30	.
St-Gobian Tech. Fab.	CompoGrid CG 100	.	.	.	.	100	3%	100	3%
St-Gobian Tech. Fab.	CompoGrid CG 50	.	.	.	.	50	3%	50	3%
St-Gobian Tech. Fab.	GlasGrid 8501	12.5	12.5	.	.	100	3%	100	3%
St-Gobian Tech. Fab.	GlasGrid 8502	12.5	12.5	.	.	100	3%	200	3%
St-Gobian Tech. Fab.	GlasGrid 8511	25	25	.	.	100	3%	100	3%
St-Gobian Tech. Fab.	GlasGrid 8512	19	25	.	.	100	3%	200	3%
St-Gobian Tech. Fab.	GlasGrid 8550	25	25	.	.	50	3%	50	3%

Manufacturer	Product Name	Dimensional Properties		Mechanical Propertes ASTM D 6637					
		Aperture Size (mm)		Strength @ 5% Strain (kN/m)		Ultimate Strength (kN/m) / (%)			
		MD	XD	MD	XD	MD		XD	
Lukenhaus Tech. Tex. Inc.	RAUGRID 11X3N	20	20	29.3	.	110		.	.
Lukenhaus Tech. Tex. Inc.	RAUGRID 13X3N	20	20	41	.	130		.	.
Lukenhaus Tech. Tex. Inc.	RAUGRID 15X3N	20	20	43.5	.	150		.	.
Lukenhaus Tech. Tex. Inc.	RAUGRID 2X2N	20	20	8	.	20		20	.
Lukenhaus Tech. Tex. Inc.	RAUGRID 3X3N	20	20	9.7	.	30		30	.
Lukenhaus Tech. Tex. Inc.	RAUGRID 4X2N	20	20	11.4	.	40		.	.
Lukenhaus Tech. Tex. Inc.	RAUGRID 5X2N	20	20	16	.	50		.	.
Lukenhaus Tech. Tex. Inc.	RAUGRID 6X3N	20	20	17.9	.	60		.	.
Lukenhaus Tech. Tex. Inc.	RAUGRID 8X3N	20	20	23.5	.	80		.	.
Lukenhaus Tech. Tex. Inc.	STARGrid G+PF	30	30	.	.	50		50	.
Lukenhaus Tech. Tex. Inc.	STARGrid G-PS 100	30	30	.	.	100		100	.
Maccaferri Inc.	MacGrid EB2	42	50	9	13.4	13.5		20.5	.
Maccaferri Inc.	MacGrid EB3	42	50	13.5	19.6	20		30.7	.
Maccaferri Inc.	MacGrid WG5	24	28	28	.	55		.	.
Maccaferri Inc.	MacGrid WG8	24	28	40	.	80		.	.
Maccaferri Inc.	MacGridWG11	21	24	55	.	110		.	.
Maccaferri Inc.	MacGridWG15	21	28	75	.	150		.	.
Maccaferri Inc.	MacGridWG20	19	28	100	.	200		.	.
Maccaferri Inc.	MacGridWG40	24	26	160	.	400		.	.
Maccaferri Inc.	MacGridWG60	34	26	180	.	600		.	.
Maccaferri Inc.	ParaLink 600	931	90	.	.	672		.	.
Maccaferri Inc.	ParaLink 800	931	59	.	.	896		.	.
Linear Composites	ParaGrid 30	426	51	.	.	30		5	
Linear Composites	ParaGrid 50	426	51	.	.	50		5	
Linear Composites	ParaGrid 80	426	51	.	.	80		5	
Linear Composites	ParaGrid 100	426	51	.	.	100		5	
Linear Composites	ParaGrid 150	426	42	.	.	150		5	
Linear Composites	ParaGrid 200	426	42	.	.	200		5	
Linear Composites	ParaLink 200	932	95	.	.	200		.	
Linear Composites	ParaLink 300	932	92	.	.	300		.	
Linear Composites	ParaLink 400	932	90	.	.	400		.	
Linear Composites	ParaLink 500	932	90	.	.	500		.	
Linear Composites	ParaLink 600	932	90	.	.	600		.	
Linear Composites	ParaLink 700	932	89	.	.	700		.	
Linear Composites	ParaLink 800	932	59	.	.	800		.	
Linear Composites	ParaLink 900	932	34	.	.	900		.	
Linear Composites	ParaLink 1000	932	34	.	.	1000		.	
Linear Composites	ParaLink 1250	932	8	.	.	1250		.	
Huesker Inc.	Formit 20	15	15	11	16	17	6%	24	6%
Huesker Inc.	Formit 30	15	15	20	27	27	6%	35	6%
Huesker Inc.	Formit 30/30	35	35	24	24	30	6%	30	6%
Huesker Inc.	Formit 40/40	40	40	32	32	40	6%	40	6%
Huesker Inc.	HaTelit C 40/17	40	40	.	.	50	10%	50	10%
Huesker Inc.	Fortrac 35	20	20	13	.	.	.	.	.
Huesker Inc.	Fortrac 55	20	20	18	.	.	.	.	.
Huesker Inc.	Fortrac 80	20	20	26	.	..	.	.	.
Huesker Inc.	Fortrac 110	20	20	33	.	.	.	.	.
Huesker Inc.	Fortrac 150	30	30	52	.	.	.	.	.
Huesker Inc.	Fortrac 200	30	30	69	.	.	.	.	.
Huesker Inc.	Fortrac 35 MP	20	30	34	.	.	.	.	.
Huesker Inc.	Fortrac 55 MP	20	30	49	.	.	.	.	.
Huesker Inc.	Fortrac 80 MP	20	30	72	.	.	.	.	.
Huesker Inc.	Fortrac 110 MP	20	30	98	.	.	.	.	.